Aptamer functionalized nanobioprobe based sensing platforms for cardiovascular diseases

Munish Shorie

A thesis submitted for the partial fulfilment of
the degree of Doctor of Philosophy

Institute of Nano Science and Technology
Habitat Centre, Sector-64, Phase-10, Mohali, Punjab 160062, India.

Indian Institute of Science Education and Research Mohali
Knowledge city, Sector 81, SAS Nagar, Manauli PO, Mohali 140306, Punjab, India.

February 2021

Dedicated to my parents

Declaration

The work presented in this thesis has been carried out by me under the guidance of Dr. Priyanka Sabherwal & Prof. Deepa Ghosh at Institute of Nano Science and Technology, Mohali. This work has not been submitted in part or in full for a degree, a diploma, or a fellowship to any other university or institute. Whenever contributions of others are involved, every effort is made to indicate this clearly, with due acknowledgement of collaborative research and discussions. This thesis is a *bona fide* record of original work done by me and all sources listed within have been detailed in the bibliography.

Munish Shorie

In my capacity as the supervisor of the candidate's thesis work, I certify that the above statements by the candidate are true to the best of my knowledge.

Dr. Priyanka Sabherwal

(Supervisor)

Prof. Deepa Ghosh

(Co-supervisor)

Acknowledgement

A doctoral thesis is never an outcome of a single individual but represents the efforts of several persons who lend their words, share their wisdom, open the doors and show the right paths at different stages of this long journey. I have tried to acknowledge everyone that played a role in this work in my whole strength however anyone who finds their name mistakenly absent in this exhaustive list is apologized to and assured in advance that their efforts are not forgotten.

I was fortunate enough to have worked under the guidance of Dr. Priyanka Sabherwal, Prof. Ashok K. Ganguli, and Prof. Deepa Ghosh during separate phases of my thesis. I am thankful to Dr. Priyanka Sabherwal for introducing me to my thesis problem and teaching me the nuances of this field of research, while allowing me enough creative freedom to expand my own ideas into publishable outcomes. Her inextinguishable desire for high quality research and clear executional vision shaped my thesis work into its current form and I thank her for steering me in the correct direction whenever I found myself facing a wall. I am also thankful to Prof. Deepa Ghosh for taking me under her wing during the hardest phase of my tenure and guiding me through all obstacles to this culmination point. I highly appreciate her critical thinking, logical inputs and time & discipline that helped me grow both professionally and personally. I will always be indebted for her kindness in and beyond her role as my supervisor.

I express my sincerest gratitude to Directors, Prof. Amitava Patra, Prof. Hirendra N. Ghosh and Prof. Ashok K. Ganguli for their kind help and support. I am deeply obliged especially to Prof. Hirendra N. Ghosh for his constant support and motivation that played a pivotal role in the completion of this thesis. It is not possible to string enough words that may express my gratitude towards him. I would also like to thank my thesis research advisory committee members, Dr. Sharmistha Sinha and Dr. Ramendra Sundar Dey for their valuable suggestions and encouragement.

I gratefully acknowledge the role of my previous group seniors, Dr. Vinod Kumar, Dr. Kulvinder Singh and Dr. Vijay Tomer in teaching me the nano from nanotechnology during the initial years of my thesis work. The efforts of Dr. Vinod Kumar are worth specific mention who exposed me to the world of nanomaterials and never hesitated in sharing the intricacies of research that he gained from his own experience. I highly acknowledge the role of my fellow lab member Ms. Harmanjit Kaur, whose constant questions at times provided me with starkly different perspectives and new insights about things I thought I knew inside-out. I was fortunate for being at the receiving end of her critical reviews and blunt criticisms that shaped my research

Contents

List of figures

xi

List of tables

Abbreviations

×g	Times gravity
μA	Microampere
μg	Microgram
μL	Microliter
μm	Micrometer
μM	Micromolar
0D	Zero dimensional
1D	One dimensional
2D	Two dimensional
3D	Three dimensional
a.u.	Arbitrary units
AuNP	Gold nanoparticle
BET	Brunauer-Emmett-Teller
BLI	Biolayer interferometry
BNP	b-type natriuretic peptide
BSA	Bovine serum albumin
°C	Degree Celsius
cm	Centimeter
CNT	Carbon nanotube
CQD	Carbon quantum dot
CVD	Cardiovascular disease
DMF	Dimethyl formamide
DMSO	Dimethyl sulfoxide
DNA	Deoxyribonucleic acid
fg	Femtogram
GO	Graphene oxide
Hb	Hemoglobin
K_d	Dissociation coefficient
kDa	Kilodalton

kV	Kilovolt
LED	Light emitting diode
LOD	Limit of detection
LPE	Liquid phase exfoliation
M	Molar
mA	Milliampere
Mb	Myoglobin
mg	Milligram
mL	Milliliter
mM	Millimolar
mm	Millimeter
mV	Millivolts
ng	Nanogram
NHS	N-hydroxysuccinimide
nM	Nanomolar
NS-CQD	Nitrogen, sulfur co-doped carbon quantum dot
OD	Optical density
PAGE	Polyacrylamide gel electrophoresis
PCR	Polymerase chain reaction
pg	Picogram
PLL	Poly-L-lysine
PoC	Point-of-care
QD	Quantum dot
R6G	Rhodamine 6G
RFU	Relative fluorescence units
rGO	Reduced graphene oxide
RNA	Ribonucleic acid
rpm	Revolutions per minute
SDS	Sodium dodecyl sulfate
SELEX	Systematic evolution of ligands by exponential enrichment
SERS	Surface enhanced Raman scattering
SPR	Surface plasmon resonance

T_m	Melting temperature
TMB	3,3',5,5'-tetramethylbenzidine
TnI	Troponin I
UV	Ultraviolet
V	Volt
WHO	World Health Organization

"It appears to me a most excellent thing for the physician to cultivate Prognosis; for by foreseeing and foretelling, in the presence of the sick, the present, the past, and the future, and explaining the omissions which patients have been guilty of, he will be the more readily believed to be acquainted with the circumstances of the sick; so that men will have confidence to intrust themselves to such a physician."

Hippocrates, *The Book of Prognostics, ca.* 400 BC

CHAPTER 1

Introduction

1.1. Cardiovascular diseases

1.1.1. Introduction

Cardiovascular disease (CVD) is an umbrella term for multiple interlinked pathological conditions associated to the heart and blood vessels. Atherosclerosis, the term given to build-up of plaque in the blood vessels is the underlying cause of several of the pathologies under CVD. In atherosclerosis, the flow of blood through the blood vessels is restricted due to the narrowing caused by plaques attached to the inner walls, and it can lead to a heart attack or a stroke. Being lifestyle-related slow-onset diseases, there are multiple intertwined processes having a very wide range of causatives that manipulate the disease development in periods spanning from several years to decades (Figure 1-1). [1] It is observed that the prevalence of cardiovascular diseases is rooted in simple environmental factors like higher air & noise pollution levels, less green space and extreme temperature conditions may participate towards the development of such diseases. These factors, in combination with individuals' living standards, level of sanitation and societal factors like lack of education, poverty and lower socioeconomic status create a foundation onto which the progression of CVDs is structured. Such environmental and socioeconomic factors trigger a cascade affecting the physiological pathways of an individual through behavioral factors like poor diet, lack of physical activities, smoking or infections thus generating a metabolic load involving high blood pressure, raised lipid profile, diabetes, thrombosis or cardiac inflammations. This metabolic load caused by over-consumption of rich foods and tobacco products accompanied with decreased labor deteriorates the cardiovascular system slowly over long periods. Further, the disease progression cascade is affected by the genomic & metagenomic composition of an individual and by the prenatal & early years' care, which

ultimately define the overall risk of cardiovascular disease development for a particular individual.
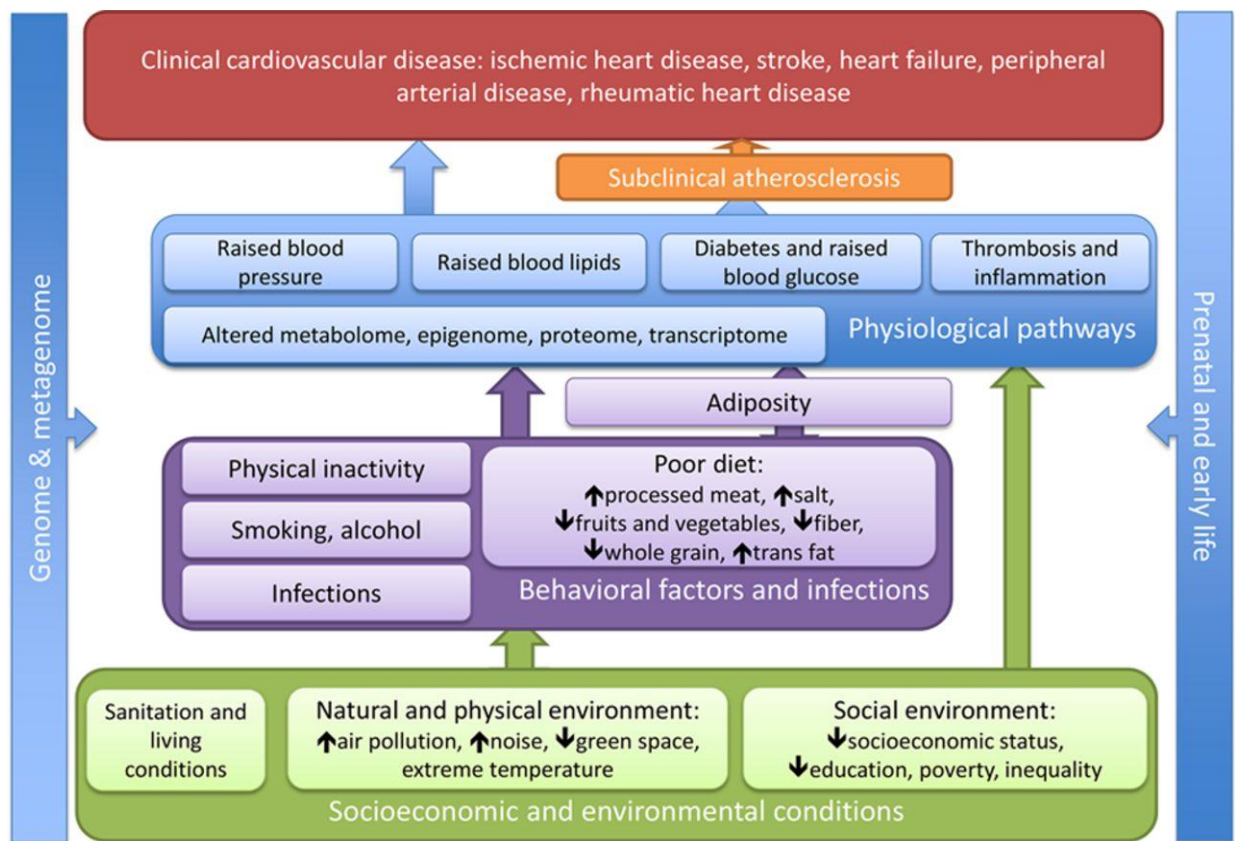
Figure 1-1: Illustration showing the major causations of cardiovascular diseases and their interconnected pathways. Reprinted with permission from Ref. 1.

1.1.2. Classification

Cardiovascular diseases are generally defined as the diseases of heart and blood vessels; however, there are multiple pathologies under this common term, having their unique progression patterns, mechanisms and affected organs. The International Classification of Disease (ICD) classifies the cardiovascular diseases in the following broad categories (Figure 1-2),[2]

i. **Ischemic Heart Disease:** The pathologies associated with the blood vessels supplying to the cardiac muscles are termed as Ischemic heart disease, Coronary heart disease, or Coronary artery disease. The pathology arises when the blood supply to the heart gets blocked due to an atherosclerotic clot, creating an

ischemic state termed as a myocardial infarction or a heart attack. This ischemic state arising from the deprivation of blood supply may cause necrosis of the cardiac myocytes thus affecting its functioning. Myocardial tissue necrosis causes the myocytes to lose their contracting ability, thus affecting their physiological function. This incapacitates the heart in meeting the metabolic oxygen demand of body due to reduction in the volume of blood pumped by the heart, thus generating a clinical condition termed *Cognitive heart failure*.

ii. **Cerebrovascular Disease:** Cerebrovascular disease or Stroke is the term given to lack of blood supply to the brain tissues and is divided in Ischemic and Hemorrhagic stroke depending on the cause. As the names suggest, *Ischemic stroke* is caused when a dislodged clot from an unstable atherosclerotic plaque chokes a capillary in the nervous system, whereas *Hemorrhagic stroke* results from a ruptured blood vessel feeding the brain tissues. Both types of strokes deplete the blood supply to the brain tissues and cause necrosis of the oxygen-deprived neurons. The neural damage may hamper physiological functions depending on the region controlled by the dead tissue. Further, a *Transient ischemic attack* is a term given to a stroke that is temporary and lasts only for a few minutes, during which the expressed symptoms include numbness in limbs and functionality.

iii. **Cardiac Arrhythmia:** Arrhythmia, as the term suggests, is abnormal rhythm of heart, beating too fast, too slow, or irregularly. When the heart is beating at more than 100 beats per minute, arrhythmia is called Tachycardia, and Bradycardia is the term given to an arrhythmia with less than 60 beats per minute. Although different from cognitive heart failure, arrhythmia has similar effects as the irregularity in the beating affects the pumping capacity.

iv. **Valvular Disease:** The abnormalities associated with the valves separating the cardiac chambers are called Valvular diseases. The deformations in the valves can cause failure in generating directionality in the blood flow due to their improper closing, thus leading to a condition called Stenosis. Improper closing of valves
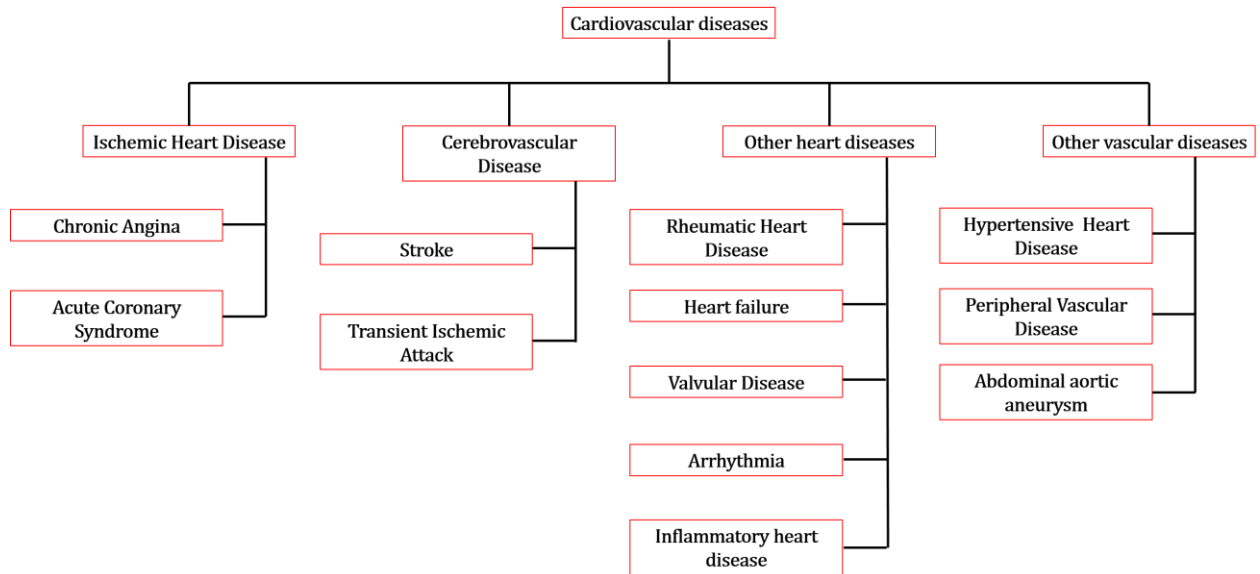
Figure 1-2: Depiction of the classification of various categories related to cardiovascular diseases.

causes the blood to leak in the previous chambers, thus reducing the amount of blood pumped ahead. The valvular diseases are generally congenital, developing during the gestation period in the fetus, and are present in the individual since birth. However, Rheumatic heart disease is a valve-related condition resulting from the damage to the cardiac valves and myocytes from inflammation during a rheumatic fever caused by *Streptococcus* bacteria.

v. **Hypertensive Heart Disease:** Hypertensive heart disease includes heart diseases like ischemic heart disease, strokes, congestive heart failures or hypertrophies *etc.*, where the causative factors are the direct or indirect effects of long-term unmanaged hypertension that cause structural abnormalities in the heart and its vasculature.

Besides the mentioned major diseases, other less prevalent pathological states of the cardiovascular system include cardiovascular neoplasms, inflammatory heart diseases, vascular diseases like peripheral vascular disease & abdominal aortic aneurysm, and some congenital affecting the structure or function of the heart. Such diseases along with valvular disease and arrhythmia are generally innate or represent a smaller fraction of cardiac-associated mortality compared to ischemic heart diseases and cerebrovascular diseases. Further, the diagnosis of these minor cardiac diseases is through measurements of electrical signal conduction, beating pattern of heart, and *via* indirect visualization of heart

5

and vasculature. These methods are starkly different from the diagnosis of ischemic heart diseases, strokes and hypertensive heart diseases that generally rely on blood-based biochemical profiling discussed in detail in the following sections.

1.1.3. Current global scenario

Cardiovascular diseases are the leading cause of mortality throughout the world among all disease categories. The total deaths due to cardiovascular diseases is 32.17% of the annual global mortality, accumulating to *ca.* 18 million worldwide as of 2016.[3–6] According to the recent *Global Burden of Disease* study, ischemic heart diseases are the major contributor for mortality in cardiovascular associated maladies.[3] Among the total deaths, 85.2% of the mortality share is from ischemic heart disease (IHD) and strokes, accounting for 9.5 million & 5.5 million respectively. At the top position in the non-communicable disease category, cardiac diseases are followed by cancer & associated complications having an annual mortality of 8.9 million.

Besides mortality, years of life lost is another important parameter of the severity and burden of a disease, which, as termed, indicate the years deducted from the average life expectancy of an individual due to a diseased condition. Along with their huge death toll, cardiovascular diseases are also the leaders in total years of life lost category, with Ischemic heart diseases being the leading causative of global morbidity among the high to middle-low income countries.

1.2. Disease biomarkers

1.2.1. Introduction

Biomarker (a portmanteau of biological marker) is a biological entity, the presence or concentration of which can be used as an indicator of the presence, or progression of a pathogenic state. As laid by National Institutes of Health Biomarkers Definitions Working Group in 1998, a biomarker is defined as "*a characteristic that is objectively measured and evaluated as an indicator of normal*

6

biological processes, pathogenic processes, or pharmacologic responses to a therapeutic intervention".[7] International Programme on Chemical Safety defines a biomarker as "*any substance, structure, or process that can be measured in the body or its products and influence or predict the incidence of outcome or disease*".[8] Further, WHO provided a more generalized definition of a biomarker as "*almost any measurement reflecting an interaction between a biological system and a potential hazard, which may be chemical, physical, or biological. The measured response may be functional and physiological, biochemical at the cellular level, or a molecular interaction*".[9]

1.2.2. Selection parameters

Although physical parameters like body temperature, pulse, blood pressure *etc.* fall under the definition, disease biomarkers generally refer to quantifiable biochemical molecules resulting from diverse processes in individuals, having an ability to precisely predict complex pathological states.[8,9] Disease biomarkers often are direct products of diseased tissues as in the case of tumors, or are molecules whose expression is affected positively or negatively under the influence of the disease.[10] For a disease biomarker to be beneficial in the screening of the associated disease, it should meet following requirements,[7–14]

i. The biomarker should be specific to a particular disease with little or no interference from other physiological parameters.

ii. The expression levels should be consistent among genders, races and ethnic groups.

iii. There should be ample change in expression level of the biomarker for it to be able to differentiate between diseased and normal condition.

iv. The biomarker should have a wider expression window to allow enough time for its quantification.

v. The biomarker should have the facility of convenient and preferably non-invasive collection. Urine, saliva, sputum and sweat are the body fluids that allow non-invasive measurements, while blood, lymphatic fluid and cerebrospinal fluid offer the invasive route of measurements.

vi. The biomarker should not have any close structural relatives that might interfere in the quantification and generate false results.

vii. The biomarker should be easy to collect, safe to handle for the technician and should have a stable profile for long-term storage.

1.2.3. Classification

Disease biomarkers can range from gene segments, proteins, peptides, small DNA/RNA molecules, to even small inorganic molecules. According to "*Biomarkers and Surrogate Endpoint Working Group*" biomarkers can be classified as,[15]

i. **Type 0 markers**: These are natural history biomarkers, which are clinically established to have direct relevance with a disease. These are characterized *via* clinical trials using assays in a known patient population over a defined period. The state of a disease is correlated with the concentration of such biomarkers, thus these are also termed as "gold standards" for the particular pathological state.

ii. **Type I markers**: These are the drug activity markers, which are measured to assess the effects of drug intervention on a particular disease to predict the clinical outcome. These have concentration-based relation with the state of disease but their underlying mechanistic pathways are not established.

iii. **Type II markers**: These biomarkers are called "surrogate markers" or "surrogate end-points" due to their relevance with clinical end-points. Clinical end-points are not real markers but rather represent how a patient feels. These may or may not

signify the state of disease accurately but still are used as an important parameter in the disease treatment.

Molecular biomarkers used for the monitoring the presence or progression of a disease fall under the Type 0 category and must be highly established in their roles as the severity of disease increases.[7,10] Depending on the involved biochemistries, different biomarkers are expressed corresponding to a particular phase of the disease or a single biomarker may have different expression levels at different stages of the disease.[10] Apart from these, depending on the stage at which the biomarkers are expressed, these can be classified in **Prognostic biomarkers** or **Diagnostic biomarkers**, being active before and after the occurrence of a disease respectively.[10,11] Prognostic biomarkers are used for the risk assessment of the development of a particular disease in an individual, whereas diagnostic biomarkers are the validating signs of the presence of a particular disease. Both types can be used during the therapy monitoring process where their pathological concentrations are scrutinized and decrease in their expression suggests a positive response to the treatment.

1.2.4. Cardiac biomarkers

Cardiac biomarkers are biological molecules associated with the cardiovascular system, which are released in an event of cardiovascular stress or damage and can be quantified to reflect the cardiovascular health.[14,16] In general, the cardiac biomarkers are structural proteins that are released in the blood due to a tissue disintegration following cardiac tissue necrosis.[17] Such proteinaceous markers have the highest cardio-specificity due to their cardiac origins and are the true marker to reflect ischemia-based cellular damage to the cardiac tissues. Examples of such biomarkers are myoglobin, cardiac troponins, heart-type fatty acid binding protein etc. which, depending on their cytosolic concentrations and cellular localization, are released beginning at different intervals from an event of cardiac necrosis. This property, alongside their varying serum expression level helps creating a dynamic kinetics that can be used to precisely locate the cardiac event. Further, several inflammation-related molecules and hormones have been

reported to have a correlation with the onset of disease. These proteins usually are not of cardiac origins though their increased serum expression levels are established to be a direct or associated consequence of the development of a cardiovascular disease. Due to the expression profile, the structural proteins act as the diagnostic markers of a cardiac event, whereas inflammatory molecules and hormones can be utilized as prognostic indicators of the onset of cardiac disease. However, owing to the non-cardiac origins and broader physiological role, their serum concentrations can also be elevated due to non-cardiac issues like inflammatory reactions, cancers, immunogenic processes etc. and thus their expression can not be used for the precise triage of a cardiovascular disease. Examples of such markers are Creatine kinase, IL-6, C-reactive protein, free fatty acids, certain metalloproteinases, myeloperoxidase *etc.* An exception to this list is B-type natriuretic peptide that is a prognostic biomarker with a cardiac origin and thus can be used for the triage of such events with a higher clinical confidence. Besides these, certain DNA based markers have also been reported to be effective in the diagnosis of cardiovascular diseases and usually include microRNAs like miR133-a/b, miR-208a/b, miR-499, miR-1 and miR-145b. However the prognostic effectiveness of such DNA based cardiac biomarkers is yet to be established due to their small physiological half-lives, tedious sample recovery and comparatively lower clinical confidence.

Cardiovascular diseases are slow and progressive disease conditions that include multiple distinct cardiac stages, each having a different biochemical profile.[18] Due to the physiological and biochemical differences in the cardiac events, different biomarkers are released during different phases and thus may act as the indicator molecules of a particular stage of disease. These are further discussed in detail in Section 1.7.

1.3. Biosensors

1.3.1. Introduction

A biosensor is a two-component system comprising of a **bioreceptor** and a **transducer** with the ability to perform a qualitative or quantitative analysis of a

certain target.[19] The bioreceptor is a biological entity, being enzymes, antibodies, host receptors, or nucleic acids, which provides selectivity to a biosensor by specifically binding to the target analyte while the transducer component converts this biorecognition in a readable signal output (Figure 1-3).

1.3.2. History

Sensors were conceived with the invention of pH sensor by Soren Sorenson in the first decade of twentieth century.[20] However, true biosensors were introduced with the work of Leland Clark on Clark electrode, which acted as foundation to develop glucose sensors.[21,22] Their glucose sensor used an enzyme called glucose oxidase as an oxygen electrode acting both as bioreceptor and transducer. The enzyme specifically recognized glucose from blood samples and the consumption of oxygen was used as an indicative of glucose concentration. Initial biosensors relied on the use of enzymes, which provided specificity as well as acted as transducers based on their enzymatic action, however due to their limited repertoire, enzymes were replaced by antibodies that had the ability of generation against a wider range of target molecules.[23] In recent years, nucleic acid-based receptors, called aptamers are being explored as advanced alternatives to the conventional protein-based receptors.[24,25]

1.3.3. Classification

Biosensors can be fabricated using a wide range of bioreceptors or transducers, and thus can be classified based on either of the component in diverse varieties.

1.3.3.1. Classification based on the bioreceptor

Based on the type of bioreceptor used, biosensors can be classified in two major categories, using proteins or nucleic acids as their receptors. Further classification is done based on the origin, properties or application of the bioreceptor as following,
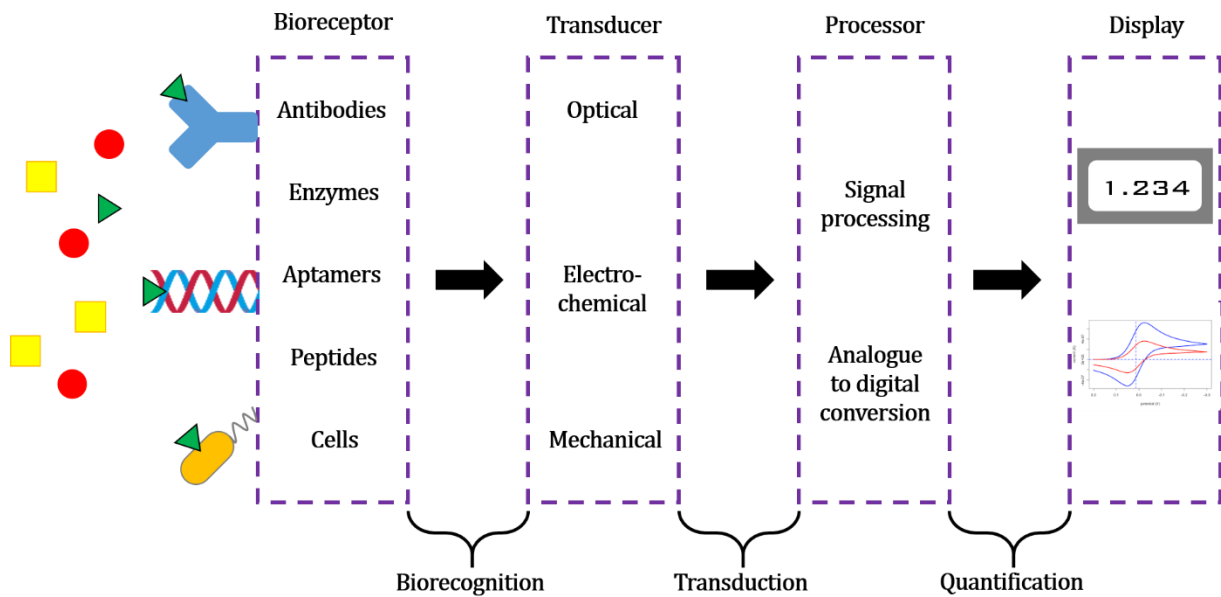
Figure 1-3: Diagram showing general layout and components of a biosensor.

i. **Enzyme-based biosensors**: Enzyme-based biosensors were the first true biosensors to be developed, and as the name suggests, these utilize enzymes as the receptor moiety. The classic and most widely applied example of such biosensors is a glucose biosensor, which uses glucose oxidase as the bioreceptor for the recognition of glucose. However, these type of biosensors do not have a very wide application range due to the limitation posed by the enzymes itself, as such biosensors can be applied to only those targets against which an enzyme is present. Still the unique property of enzymatic action allows these type of sensors to be relevant and operate in a label-free manner.[23,26–28]

ii. **Antibody-based biosensors**: Antibody-based biosensors use antibodies as their receptor molecules. Antibodies are the proteins produced by the immune system of the host organism against any foreign molecules as the general host-defense mechanism. These immunoproteins have a binding pocket which can be modulated by the host cells using a process called V(D)J recombination to yield antibodies with a target range of around 10^{10}. By the development of Hybridoma technique by Köhler and Milstein in 1975 provided the means for generation of antibodies in adequate amounts without continuous requirement of a host

12

organism.[29,30] This lead to the boom in antibody-based technologies including development of immunosensors.[31–34]

iii. **Natural receptor-based biosensors**: As the term, natural receptor-based sensors use the receptor proteins that naturally occur in the host organisms. These type of bioreceptors have the advantage of natural molecular selection, which has mutated such receptors over generations to be a perfectly complimentary to their targets. This property is beneficial in reducing the cross-reactivity of the sensing platforms among closely related species.[35,36]

iv. **Peptide-based biosensors**: Peptide-based biosensors utilize small peptides rather than whole proteins. The peptides either are derived from the binding pockets of their larger counterparts, or are generated by a process called phage-display. The smaller sizes of peptides provide such biosensors with higher stabilities and sensitivities compared to other whole protein-based sensors.[37–40]

v. **Aptamer-based biosensors**: Aptamer-based sensors or Aptasensors use nucleic acid-based receptors called aptamers. An *in vitro* process called SELEX, which is similar to antibody generation by B-cells, is used to generate the aptamers. The process screens a wide library of receptor pool (average 10^{14} molecules) to find the best fitting nucleic acid for the target molecule.[41–44]

vi. **Gene-based biosensors**: These Genosensors have receptors based on nucleic acids but these are not derived by SELEX and thus are different from aptamers. These receptors are produced against genomic nucleic acids specifically, while aptamers can be generated for a wider target range. These type of sensors usually rely on the Watson-Crick complementary bonding between receptor nucleic acid and its target genomic region. Although certain nucleic acid-based sensors have been developed for the detection of small DNA/RNA fragments in biological samples, these do not fall under the category of true genosensors.[45–48]

1.3.3.2. Classification based on the transducer

Depending on the transducing approach, the biointeraction between receptor and target molecules generates an optical response, electronic signal or a mass shift, using which a sensor is classified as Optical, Electrical/Electrochemical or Mechanical broadly (Figure 1-4).

i. **Optical sensors:** Optical biosensors are the most common and highly established approach, which relies on the changes occurring in the spectral properties of the system due to the receptor-analyte interaction.[49,50] Optical biosensors are further classified in Colorimetric, Fluorescent, Surface Plasmon Resonance (SPR)-based, Raman-based or chemiluminescence-based biosensors. Among these, colorimetric, fluorescence- and chemiluminescence-based biosensors function in the visible range of the spectrum. The transducing signal for colorimetric sensors is the change in color or the shift in its intensity,[51–56] whereas for fluorescence- and chemiluminescence-based sensors, the signal is interpreted as the intensity shift in the fluorescence or luminescence respectively (Figure 1-4).[57–62] Surface plasmon resonance-based sensors rely in the changes in the surface plasmon of metallic transducer materials,[63–65] while the Raman-based sensors utilize the characteristic Raman signatures of the analytes due to the Raman scattering.[66–68] In recent times, with the advances in the field of materials technology, Raman-based sensors have gained momentum due to a phenomenon called surface-enhancement which as termed is a surface related phenomenon where the surface topology of the substrates can create multifold enhancement in the Raman signal. This surface-enhanced Raman scattering (SERS) is a method to measure the faintest Raman signals to create a platform for the ultrasensitive detection of analyte molecules. Among the optical sensors, colorimetric are the most common due to their cost-effectiveness, ease of operation and easier signal interpretation without the requirement of any instrumentation.[50]

ii. **Electrochemical sensors:** Electrochemical biosensors are the category of sensors that use an electrode as the transducing element. As the electron transfer is effective *via* the surface of the electrode, any changes occurring on the electrode

14
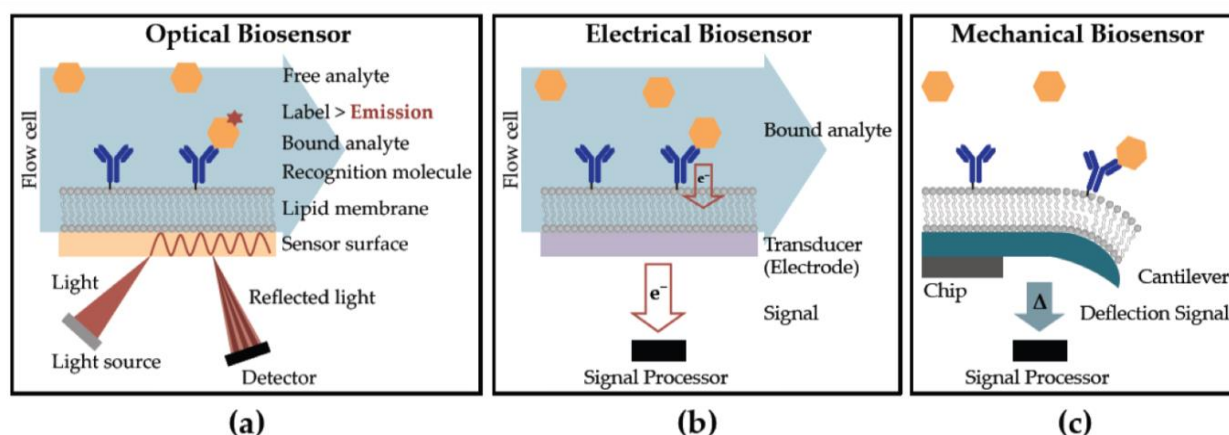
Figure 1-4: Schematic representation of differences in the principles of various transducing approaches. The biorecognition of free analyte by the bioreceptor is translated as the change in the spectroscopic properties (UV, Visible, IR, Raman, SPR) in case of optical biosensors (a), as the change in the charge transfer properties through electrode surface in case of electrochemical biosensors (b) and as the change in the properties of a cantilever by its physical bending (c). Reproduced with permission from Ref. 105.

surface due to the biomolecular interaction change the charge-transfer properties of the electrode, modulating it in either direction.[69–72] This change is correlated to the analyte concentration under a linear working range (Figure 1-4). Depending on the measured parameter, electrochemical sensors are categorized in Amperometric, Potentiometric, Impedimetric and FET-based sensors. Amperometric sensors measure current changes occurring as the effect of another variable, time (chronoamperometry) or potential (voltammetry). Chronoamperometric biosensors measure the changes in current over time at a fixed potential value,[73–75] whereas voltammetric biosensors measure the changes in current over a variable potential range.[76–81] Potentiometric sensors, on the other hand measure the potential between a working and reference electrode in the absence of any current flow, and the potential difference between the electrodes changes in response to the concentration of the analyte.[82,83] Apart from these, Impedimetric sensors operate by measuring the impedance of the system as a function of frequency under a small AC voltage, and monitor the shift corresponding to the analyte concentration.[84–86] The interaction and subsequent binding of the analyte on the electrode surface creates a hindrance to the charge transfer through the surface and is reflected as an increase in the impedance of the system.[87–90] Further Field-effect transistors (FET) are three-terminal systems with the facility of conductivity modulation by the application of electric field to the *Gate* terminal. As sensors, the charge properties of Gate are affected by the binding of analyte molecules, which in turn affects the current flow through the

transistor.[91–94] Owing to their label-free nature, impedimetric sensors and FET sensors have gained much attention in recent years following the advances in the generation of highly sensitive electroactive materials.[93–96]

iii. **Mechanical sensors:** Mechanical sensors are the most sensitive type of biosensors where small changes in mass are measured.[97] These type of sensors generally are fabricated with a very fine cantilever made of silicon, silicon nitride or polymers, which is modified with the receptor molecules. The interaction and binding of analyte changes the mass of the whole system causing a bend in cantilever proportional to the analyte concentration, and this gain in mass is used as the measure of analyte quantity (Figure 1-4).[98,99] Another category of mechanical biosensors is Quartz crystal microbalance, where the changes in the vibrational modes of a quartz crystal are measured as a result of the biointeraction.[100–102] In contrast, piezoelectric mechanical sensors operate by recording the change in the electronic resistance of the cantilever with the analyte binding that is used to quantify the amount of target analyte.[103,104] Methods under mechanical biosensors have the advantage of being highly sensitive and label-free but the techniques require sophisticated instruments for measuring minute changes in mass of the system and can be overwhelmed in the presence of high analyte concentration.[97,105]

1.4. Aptamers

1.4.1. Introduction

Aptamers [from *aptus* (Latin) for fit, and *meros* (Greek) for part] are single stranded sequences of nucleic acids (DNA or RNA) that display unique geometries as a function of their nucleotide sequence .[106] The 3D structures possessed by the nucleic acid strands generate binding pockets complementary to a wide spectrum of target molecules.[107]
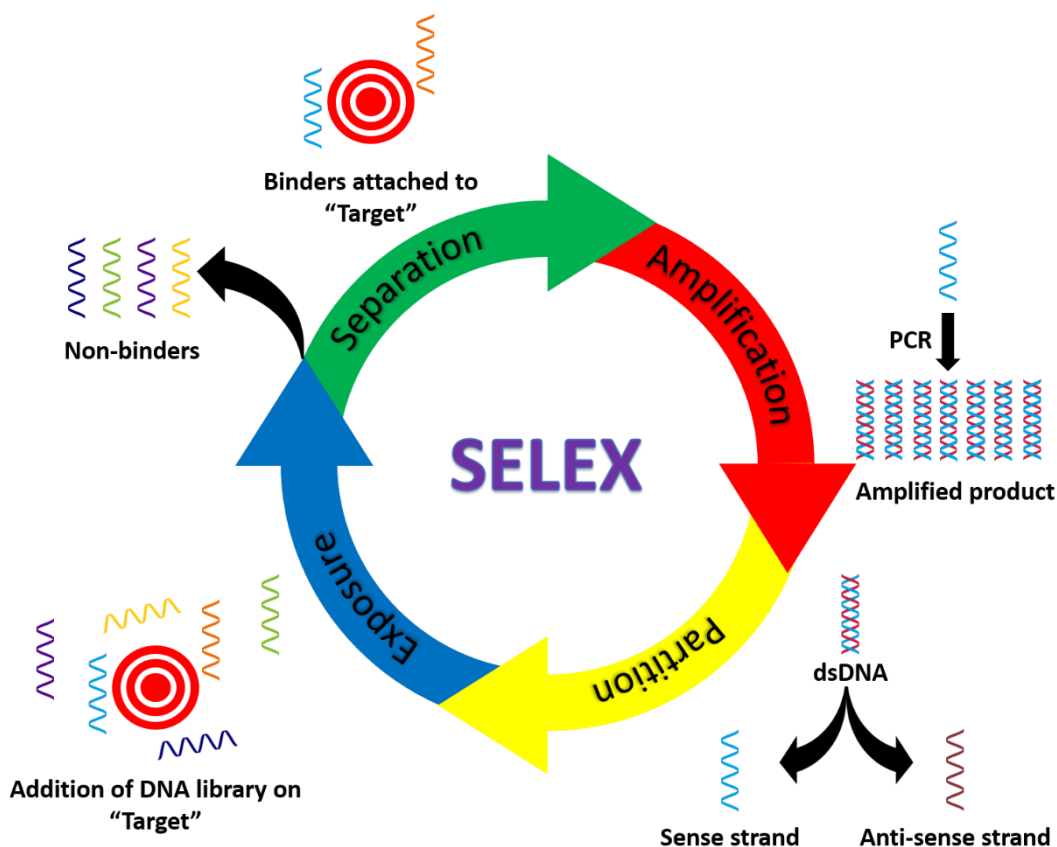
1.4.2. Selection methods

Aptamers have an *in vitro* route of generation termed **S**ystematic **E**volution of **L**igands by **Ex**ponential enrichment, abbreviated as SELEX.[108] Since their inception in 1990, several modifications of SELEX have been invented, however all the methods rely on a simplified 4-step iterative cycle repeated over to create a selection pressure to yield the strongest candidates for binding. SELEX begins with the exposure of analyte to a vast library of single-stranded oligonucleotides to initiate the selection. The nucleotides have different 3D structures as a function of their sequences and the initial selection separates the binding sequences from the non-binding population. This is proceeded by an amplification of the binders' number *via* Polymerase Chain Reaction (PCR) and a last step to generate single strands of oligomers from double-stranded PCR products. These are used to expose the analyte again for second round of SELEX and the process is repeated until the process hits a plateau, where all the sequences in the binding pool have similar affinities and cannot be further differentiated *via* SELEX (Figure 1-5).

Although being a cyclic process, SELEX shares its basic stages with the generation of antibodies *via* immune system that involves an **Exposure step** (antigen presented on antigen presenting cells to naïve B-cells), a **Selection step** (through secretion of chemical messengers), and an **Amplification step** (clonal expansion).

Several alternative methods of SELEX have been developed over the decades with unique properties and advantages.[109,110]

i. **Column-SELEX**: Column-based SELEX is the more employed SELEX technique that functions by trapping the target molecules onto beads of a column acting as the stationary matrix. The DNA library is passed over the column and retention times can be varied as desired. DNA molecules with no affinity pass through the column and the binding populations are harvested by disrupting their interaction by passing buffer of different pH or ionic strength (Figure 1-6). The binding population is amplified and resulting solution is subjected to the column again after generating single strands. Main advantages of column-SELEX are the control over retention time, ability to trap a wide range of target molecules by employing different interaction methods, and a larger surface area offered by different sized beads.[111,112]
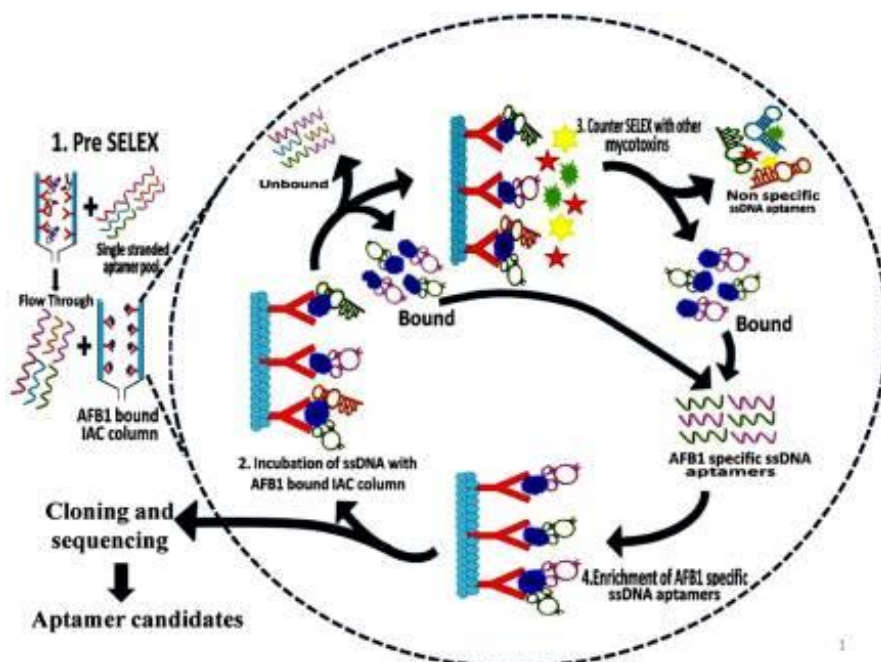
Figure 1-6: Illustration showing the principle and various steps involved in Column-SELEX. Reproduced with permission from Ref. 111.

ii. *in vivo*-SELEX: This is a recent addition towards the development of aptamers where the interaction between the oligonucleotides and the target analyte occurs inside a biological entity. For this, a chemically-modified oligonucleotide library is injected in the host organism, and allowed to distribute in the host system. The organism is euthanized thereafter and the target cells are harvested to recover any interacting oligonucleotides. These binders are amplified to inject in another host, and the process is repeated until the progression saturates (Figure 1-7). This method not only ensures the activity of final aptamers in the biological system but also eliminates any sequences that might be too unstable and vulnerable to the host defenses.[113–115]
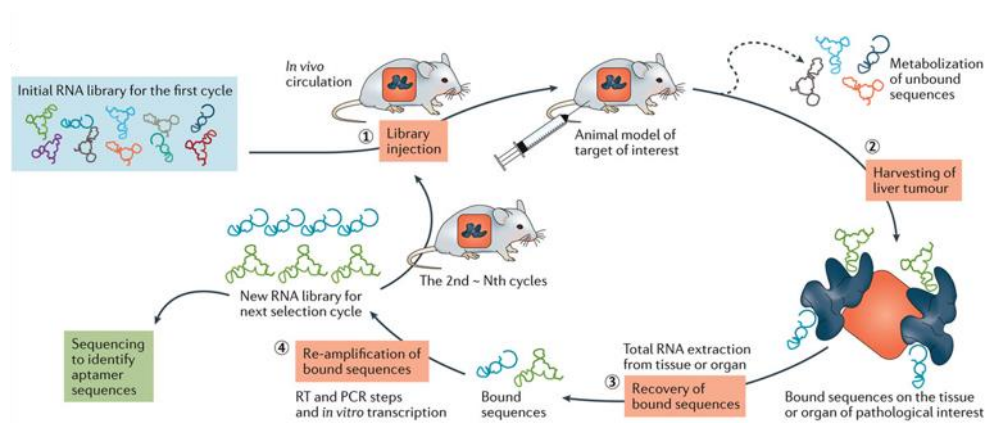
Figure 1-7: Illustration showing the principle and steps involved in *in vivo* SELEX. Adapted with permission from Ref. 115.

iii. **Capillary electrophoresis-SELEX**: Capillary electrophoresis-SELEX is highly sophisticated method of SELEX employing the differences in electro-mobility of molecules during capillary electrophoresis. The DNA molecules bound to the target molecules tend to have slower motilities under applied potential field due to their gained mass. This result in the resolution of the binders from the non-binding species that can be harvested in elutes (Figure 1-8). The most important advantage of CE-SELEX is the ability to capture even the smallest amounts of the binders as well as the benefit of using a mixture of targets differing in masses for a single round multiple selection.[116–118]
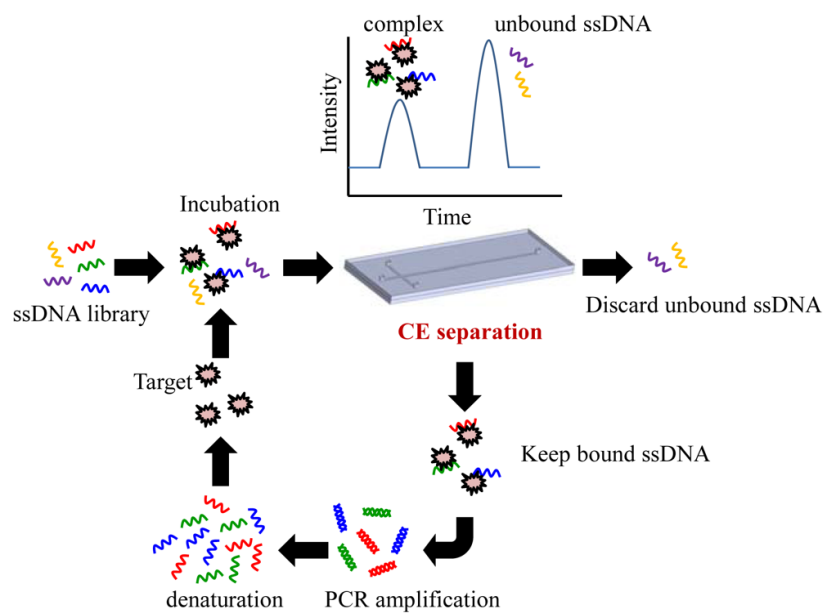
Figure 1-8: Illustration showing principle and steps involved in capillary SELEX. Reprinted with permission from Ref. 118.

iv. **FACS-SELEX**: Fluorescence assisted cell sorting or FACS is a technique used to separate cells based on bound fluorescent label. This method has been applied in SELEX by using a fluorophore modified oligonucleotide library. The sequences
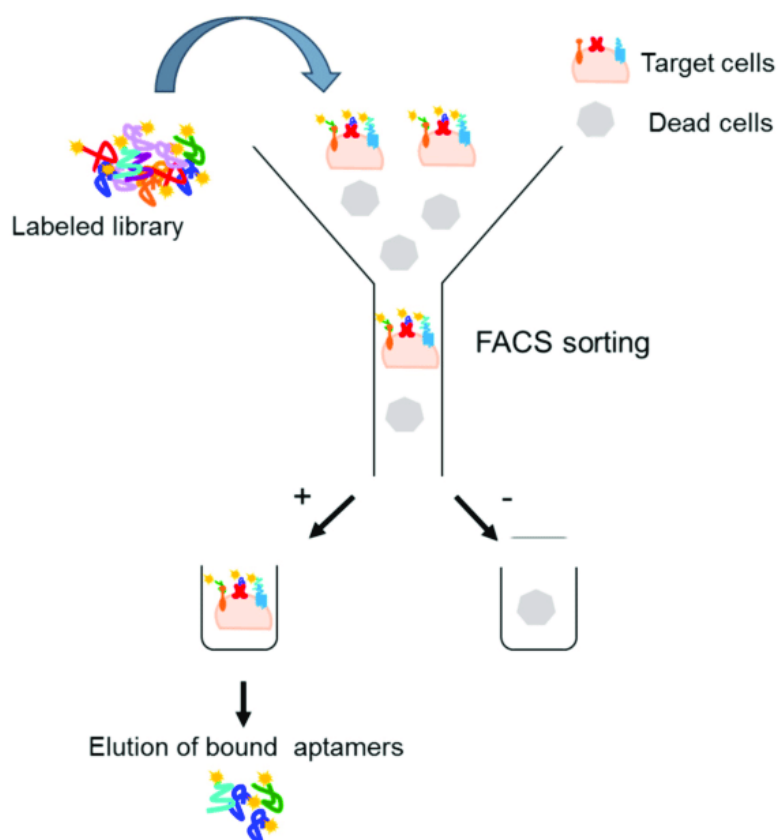
Figure 1-9: Illustration showing the principle of FACS-SELEX along with its various steps. Reproduced with permission from Ref. 124.

interacting with the cells act as a label and are separated from the rest using FACS technique (Figure 1-9). Similar to capillary electrophoresis, usage of sophisticated instrument allows a sensitive separation of sequences at even the smallest quantities.[119,120]

v. **Bead-SELEX**: Bead-SELEX is similar to column-SELEX due to the application of microbeads but unlike columns, in bead-SELEX, the beads are not packed in a column and are kept suspended in the solution by constant agitation. While possessing all the properties of column-SELEX, bead-SELEX offers an additional advantage of improved mixing. The beads can be separated from the solution by settling them using a centrifuge or under external separation forces like magnetic field in case of magnetic beads.[121,122]

vi. **Cell-SELEX**: Cell-SELEX is rather a pseudo-class of SELEX as it is named for the target analyte rather than the method of generation. As named, Cell-SELEX is a SELEX method used generally for whole cells; however, it can also include cellular lysates in some cases. The type is separately classified due to the stark differences in the properties of the cells from other molecules, mainly due to their huge sizes. Cell-SELEX differs from normal SELEX methods as whole cells are hugely affected by surface captures, tend to block columns, have a very large variety of surface molecules and need treatments before application to avoid growth related problems.[123,124]

1.4.3. Advantages over conventional receptors

Conventional antibodies are restricted by the limitations of the host immune system for their production. Hence, antibodies cannot be raised against molecules which are either lethal to the host, or create substantial immunologic pressure thus hampering the antibody production.[125,126] Further, antibodies cannot be raised against whole organisms as they are either managed by the innate system or can have masking mechanisms to avoid immune system, as seen in some pathogens. Aptamers are relieved of this problem due to their *in vitro* mode of generation and have been successfully generated against pathogens and

21

Parameter	Aptamer	Antibody
Molecule type	Nucleic acid	Protein
Molecular size	10-30 kDa	150-180 kDa
Structural complexity	High	High
Route of selection	*in vitro* or *in vivo*	*in vivo*
Target diversity	Very High	Limited
Minimum target size	Small (~60 Da)	Larger (~600 Da)
Thermal stability	High	Medium
Route of production	PCR	Cell culture or animal models
Ease of chemical modification	High	Limited
in vivo stability	Sensitive to DNase action	High
Immunogenicity	Low	High
Production cost	Low	High
Production time	30-60 minutes	Days to months
Batch variation	None	Significant

Table 1-1: Table showing the comparison between several properties of aptamers compared with antibodies. The parameter having a comparative advantage is shown in green.

toxins.[125,127] Further, the *in vitro* generation route is highly cost-effective compared to antibody production that involves rearing and maintaining host animals. While antibodies can be generated only *via* a host organism or by the means of monoclonal immune cell mutants, aptamers have the ease of amplification *via* Polymerase Chain Reaction. Furthermore, their structures can be easily manipulated by controlling the ionic solutions, which allows their *in silico* generation.[107,128] In contrast, the structures of complex proteins like antibodies undergo a sequential route of protein folding involving several assisting proteins and components, which makes the synthetic approach of antibody production infeasible. Immunosensors loaded with antibodies require specific storage conditions due to their temperature-sensitive nature. Antibodies, like other proteins, lose their tertiary structure at higher temperatures and lack the facility to recover thus rendering the sensors useless. Aptamers, in contrast, are more capable in maintaining their structural conformity at a wider temperature ranges and thus provide robustness to the aptasensors.[107,128,129]

1.5. Nanomaterials

1.5.1. Introduction

Nanomaterials are substances that possess at least one structural dimension within 1-100 nm range. The small structure modulates the behavior of materials and its interactions with self and surroundings, producing properties that are starkly distinct from their bulk siblings.[130–132]

1.5.2. Properties arising in nano-regime

There are two main reasons for the remarkable shift in the properties of nanomaterials; change in surface area, and introduction of quantum effects.[133–135] Materials in nano-ranges have very high surface area-to-volume ratio, meaning they have more surface when compared to bulk materials for same unit of mass, allowing nanomaterials to have more sites for interaction, a higher number of surface electrons and higher surface energy. This enhances the surface-dependent properties of materials like plasmons, hydrophobicity/hydrophilicity, charge transfer or catalysis.[136–141] Other more important feature of nanomaterials is the enhancement in quantum effects in comparison to bulks, which become prominent in defining the properties of nanomaterials. One such example is the change in bandgaps of nanomaterials in comparison to their bulk counterparts. The conversion of materials into their nanomaterials has shown to reduce band gaps that turns the nanomaterials into electronically superior materials. Further, is case of nanosheets that usually are generated by the delamination of naturally laminated materials, there is a very beneficial advantage of controlling the number of sheets by optimizing the reaction conditions. This in turn creates a control over the band gap and conductivity of the material and can be utilized in the generation of tunable semi-conductors.[135,140,142]

1.5.3. Classification

1.5.3.1. Classification based on dimensionality

The most basic classification of nanomaterials is on the basis of the number of dimensions occurring in the nanometer regime, and depending on this, these are classified as 0D, 1D, 2D and 3D nanomaterials (Figure 1-10).[143]

i. **0D nanomaterials**: Materials having all spatial dimensions within nano-regime are called 0D nanomaterials. These usually are particles with their longest axis measuring less than 100 nm. The most popular example of such nanoparticles is metallic nanospheres, which is the most common structure attained in an unaided dynamic synthesis.[144–146] Colloidal solutions of gold nanoparticles were synthesized by Michael Faraday in 1857 which was the earliest known example of nanomaterial synthesis.[135] Other 0D structures include nanocubes, nanoprisms, nanotriangles, nanothorns *etc.* that require strict reaction modulation to promote the growth of nanoparticles at specifically defined faces.[144,147,148] 0D nanomaterials can also be obtained by extensive breaking of 2D and 1D nanomaterials, or alternatively higher-dimension nanomaterials can be grown using 0D materials as seeds.[144] Furthermore, another category of very small 0D nanomaterials called Quantum dots (QDs) have been developed that have all spatial dimensions within 5 nm and possess strange properties than larger 0D nanoparticles due to the introduction of quantum confinement effect.[149–153]

ii. **1D nanomaterials**: One-dimensional nanomaterials have a single structural dimension scalable above the nano-range in comparison to their other spatial dimensions. The usual structural features are nanorods, nanofibers or nanowires that are generated by growing the material in a single lattice phase.[154–157] The most common example of such nanomaterials is carbon nanotubes that may measure up to several meters in length while having a diameter of a few nanometers.
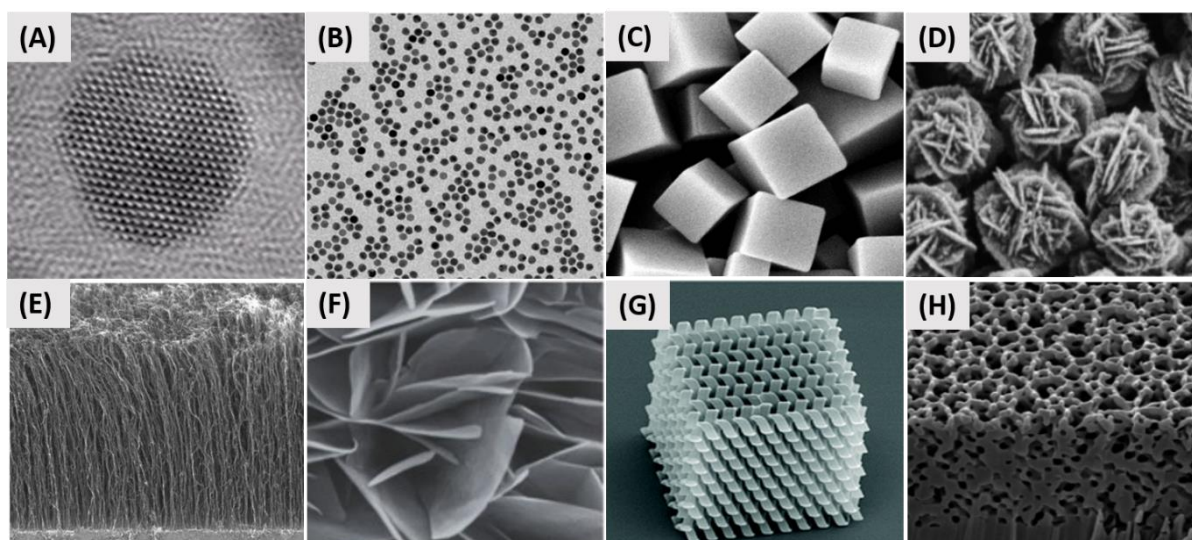
Figure 1-10: Electron micrographs showing different morphologies in nanomaterials; (A) CdSe quantum dot, reprinted with permission from Ref. 153, (B) Spherical gold nanoparticles, reprinted with permission from Ref. 146, (C) $Mn_3[Co(CN)_6]_2$ nanocubes reprinted with permission from Ref. 147, (D) Gold nanoflowers reprinted with permission from Ref. 148, (E) Carbon nanotubes reprinted with permission from Ref. 157, (F) NiO nanosheets reprinted with permission from Ref. 160, (G-H) 3D nanostructures reprinted with permission from Ref. 173 & 174 respectively.

iii. **2D nanomaterials**: These materials have a single dimension in nano-range and resemble with sheets in their geometry. Such nanosheets usually have thickness in nanometers and may span over microns. Graphene was the first 2D nanomaterial generated by Geim in 2004 by mechanical stripping of graphite, and since then several candidates have been added to this list.[158–160] 2D materials are naturally more abundant compared to their siblings, and are found as stacks of single nanosheets resembling a stack of papers.[161–165] A process called Exfoliation that uses physical forces to delaminate the stacks into individual nanosheets can separate these naturally occurring bulk materials in their nanosheets.[166–168]

iv. **3D nanomaterials**: 3D nanomaterials have all three dimensions above nano-range but contain smaller domains with nanoscopic features thus giving them the localized regions possessing properties of nanomaterials.[169–174]

1.5.3.2. Classification based on composition

Another route of classification of nanomaterials is based on the atomic composition of the nanomaterials. Although composition based segregation of

25

nanomaterials is comparatively much diverse due to the presence and possibility of generation of nanomaterials using multiple highly complex atomic structures. Yet, on the basis of the most applied and reported nanomaterials, these can be differentiated in the following classes,

i. **Carbon-based nanomaterials:** Carbon-based nanomaterials are evidently those nanomaterials that are composed solely of carbon or contain carbon as their major atomic constituent by number or weight, and the diversity offered by carbon-based nanomaterials in terms of morphology and dimensionality ensure their classification as a distinct category. Carbon-based nanomaterials can be synthesized to be 0D as fullerenes, 1D as carbon nanotubes, 2D as graphene and its analogues and eventually as 3D nanostructures in the form of graphene aerogels. Further, it was recently reported that the graphene nanosheets can be broken down greatly to generate very small particles where the lateral sizes measure below 10 nm. Such particles display the quantum confinement effects resembling the properties of quantum dots and are evidently called graphene quantum dots.

ii. **Transition metals-based nanomaterials:** Metallic nanomaterials are clearly materials composed solely or mainly of transition metals. Such nanomaterials include monoelemental structure of metals like gold or silver, oxides of metals like iron, manganese or titanium *etc.*, and polyelemental structures possessing components of different metals or their compounds. Such nanomaterials can be generated by several routes including dynamic seed-growth method, electrochemical or photochemical methods, sputter deposition, chemical reduction methods, or even through biological routes of synthesis. Owing to the wide range of synthesis approaches, the metallic nanomaterials demonstrate an elaborate morphological diversity and can be synthesized as nanoparticles, core-shell particles, prisms, rods, cubes, or in the form of nanoscale coatings of single or multiple metals. Such nanostructures display tremendously high & tunable optical, plasmonic, magnetic, electronic and thermal properties and can be functionalized with a plethora of desired modifiers. Metallic nanomaterials have

applications in fabrication of micro- and nano-electronics, biosensing, imaging and therapeutics.

A separate category of transition metals-based nanomaterials is of semiconductor quantum dots derived of metal chalcogens. The general examples of these quantum dots are of CdSe, CdS, CdTe while among the non-transition metal derived quantum dots, InS, PbS, PbSe *etc.* are much researched and applied. These nanomaterials possess very high optical and electronic properties rooted in the quantum properties due to their very small sizes and thus have been applied in biosensing, cellular imaging, optics, micro- & nano-electronics, and therapeutics.

Another major category of metallic nanomaterials is of transition metal chalcogenides. Among the several stoichiometric combinations, the dichalcogenides are naturally lamellar and the individual sheets can be delaminated using physical or chemical methods to generate planer nanosheets with tunable layer number. MoS_2 and WS_2 are currently the most studied & applied examples of such transition metal dichalcogenides although recently trends are shifting towards selenides and tellurides due to the improvement in the electronic properties found in larger chalcogens. These planer nanomaterials have superior semiconducting properties that has enabled their application in photoenergy harvesting, fabrication of micro- or nano-electronics, biosensing and even in therapeutics owing to their thermal properties.

iii. **Polymer based nanomaterials:** Polymer-based nanomaterials are materials that are derived of simpler monomer units through their polymerization or agglomeration, or alternatively by dissolution of larger particles. The polymers used for the synthesis of these particles can be natural, biosynthetic or synthetic; however, the natural polymers are more sought-after due to the environmental-friendly biodegradable properties and biocompatibility. The examples of natural polymers is chitosan, starch, alginates *etc.*, while the biosynthetic polymers used for the synthesis of such nanomaterials is poly-β-hydroxybutyrate, poly(3-hydroxybutyrate-co-3-hydroxyvalerate), polyaminoacids *etc.* The examples of synthetic materials used for preparing polymeric nanomaterials are polylactic acid, polyglutamic acid, poly(lactic-glycolic acid), polyvinyl pyrrolidone *etc.* The

polymer based nanomaterials generally are synthesized in the form of nanoparticles due to the synthesis route restrictions and have found a major role in the development of therapeutics due to their non-toxic & non-immunogenic properties.

iv. **Lipid-based nanomaterials:** Lipid based nanomaterials are evidently materials derived from lipids units. These particularly spherical nanoparticles are generated from phospholipids, fatty acids, sphingomyelins etc. by emulsification, ultra-sonication, or physical homogenization in colloidal systems in the presence of appropriate surfactants. The surfactants act as stabilizers for the nanoparticles and prevent their conversion into mesoparticles due to aggregation. These nanoparticles are generally optimized to be hollow where the core of the particles can be used to load certain molecules, thus creating nanoscale carriers. These lipid-based nanocarriers have demonstrated a profound application in the field of therapeutics where, acting as drug carriers, these nanoparticles can be tuned to disintegrate at specific sites under internal factors or external influence thus enabling site-specific drug delivery.

v. **Inorganic nanomaterials:** This broad category includes nanomaterials that can not be categorized under any of the specific categories on the basis of their elemental composition. This category includes clay & ceramic-based nanomaterials, monoelemental nanosheets of group 14 & 15 elements except carbon and nitrogen. Phosphorene from group 15 is worth a special remark due to its electronic properties comparable to that of graphene while maintaining its semiconducting nature. Phosphorene is a monoelemental nanosheet made of phosphorus atoms and is derived of a phosphorus allotrope called black phosphorus. It was demonstrated in 2014 parallel by several research groups that black phosphorus, a natural lamellar substance can be delaminated into its nanosheets by physical or chemical routes and the nanosheet was given a name phosphorene (phosphorus + -ene akin to graphene). The nanosheets demonstrate heightened electronic properties that are highly dependent on the layer-number and thus provide a route to modulate its properties. This nanomaterial has applications in biosensing, electronics, photo-energy harvesting *etc.* Other similar
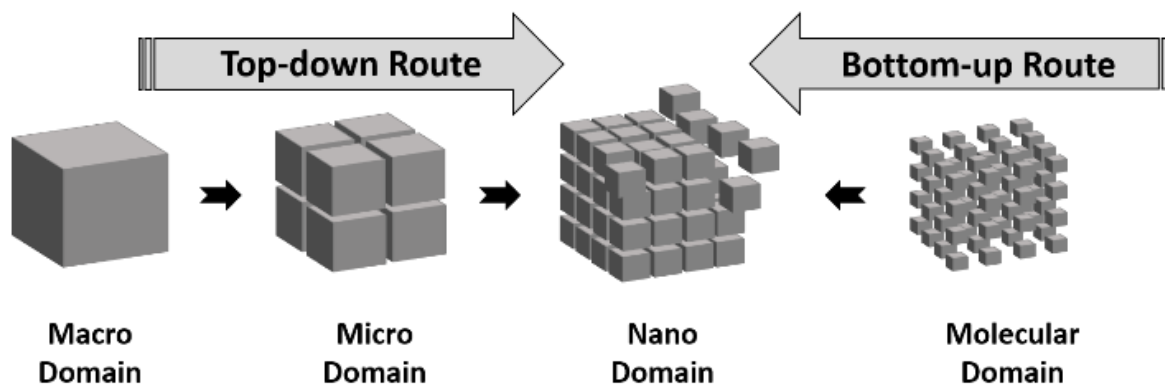
Figure 1-11: Diagram showing routes of nanomaterial generation.

examples include monoelemental nanosheets of silicon (silicene), germanium (germanene), tin (stanene), arsenic (arsenene), antimony (antimonene) and bismuth (bismuthene) however although theoretically predicted, the facile routes to synthesize stable nanosheets of these elements are still under development.

Besides above-mentioned major classifications, the nanomaterials can be classified based on their generation routes, being natural nanomaterials or anthropogenic; based on their morphologies; being nanospheres, nanotubes, nanorods, nanosheets, nanohelices, nanoribbons *etc*.

1.5.4. Generation routes

The synthesis routes for the generation of nanomaterials can be generalized into two categories *viz*. Top-down, and Bottom-up (Figure 1-11).[175,176] As termed, bottom-up approach builds the materials from simpler starting materials using chemical routes in liquid or vapor phases.[175,177] In contrast, top-down approach begins with bulk materials measuring in micro- or millimeters and breaks them down until the sizes reduce to nanoscales. Most popular examples of bottom-up approach are chemical vapor deposition, sputter deposition, electric arc deposition, hydrothermal syntheses, and nucleation & growth methods.[178–182] Most applied routes of top-down synthesis are high-energy ball milling, micromechanical cleavage, and force-mediated liquid exfoliation.[183–187]

1.5.4.1. Top-down methods

i. **High-energy ball milling:** Ball milling is the simplest method of nanomaterial production that generates metal and alloys in the form of nano-powders. The method uses hardened steel or tungsten carbide balls of variable sizes which are rotated along with the substrate in a container to break down bulk materials (<50 μm size) to their nano forms by physically grinding. The method have the advantage of industrial level scale-up and tight control over size, however the balls and container can act as contaminants in some cases. The friction between balls, substrate and container wall due to the milling causes the temperatures to rise up to 1000℃. The temperature is critical in this method as grinding at lower temperature generates amorphous particles. However, this can also cause the gases inside the container to react with the material to change its chemical composition or add chemical functionalities, although it can be reduced by maintaining the milling in inert gases or by using cooling devices to control the temperature. The method is employed for metals like Chromium, Cobalt and Tungsten, as well as for alloys as Nickel-Titanium, Aluminum-Iron and Silver-Iron and can have yields up to few kilograms.

ii. **Micromechanical cleavage:** Micromechanical cleavage is another classic example of exfoliation achieved by application of external forces to bulk materials using scotch tape. The method is best suited for the generation of 2D nanosheets, as demonstrated by Geim for the generation of graphene nanosheets from graphite. For the exfoliation, a scotch tape is repeatedly applied to the bulk material that results in the cleavage of sheets due to adhesion. The freshly cleaved material bound to tape is then applied to suitable flat substrate transferring the nanosheets on to the substrate. The method can be used to generate high quality nanosheets of up to single layer thickness. However the method can not be scaled up thus limiting its applications.

iii. **Liquid phase exfoliation:** Liquid phase exfoliation (LPE) is a top-down approach for the mass scale production of various natural 2D nanomaterials. The method was invented by Coleman and group in later years of 2000s and demonstrated its

applicability on a variety of 2D materials.[168] Natural lamellar materials occur as bundles of singular nanosheets held together by van der Waals interactions, which can easily be broken to strip single nanosheets. As demonstrated by Coleman, if the material is immersed in suitable liquids and subjected to external forces, small bubbles are naturally generated between the sheets. The bubbles may collapse creating shockwaves, which helps separating the nanosheets. Besides force-mediated exfoliation, methods relying on chemical reactions exist for 2D nanosheets exfoliation, however all the methods broadly are based on increasing the inter-sheet distances to generate single or few-layer nanomaterial.

Liquid phase exfoliation using external forces is among the simpler methods of 2D nanomaterial generation in which the main parameter is the selection of liquid phase used for exfoliation. The method relies on exploiting the interactions between the solvent molecules and the bulk material. There are four steps of solvent assisted LPE: immersion, insertion, exfoliation and stabilization, where the best solvent should function in all the steps (Figure 1-12).[188] Immersion is the first step of exfoliation in which the materials interacts with the solvent, "wetting" the material in the process. Immersion guides the exfoliation process and depends on the surface energy of material as well as the hydrophilicity of the solvent. The surface energy and hydrophilicity should be in a close range for a solvent to be efficient in the exfoliation process. Insertion follows immersion and depicts the insertion of solvent molecules in the interlayer spaces. The material is subjected to external force by ultra-sonication that separates the nanosheets due to inserted solvent and the shockwaves arising due to collapsing bubbles. Stabilization refers to the ability of exfoliated samples to remain in their nano-forms by avoiding aggregation and sedimentation. While a good exfoliating agent provides the required stability to exfoliated sheets by decreasing their surface energies, several stabilizing agents can be used to coat the freshly separated sheets to prevent agglomeration. This method can be replicated at mass scales to
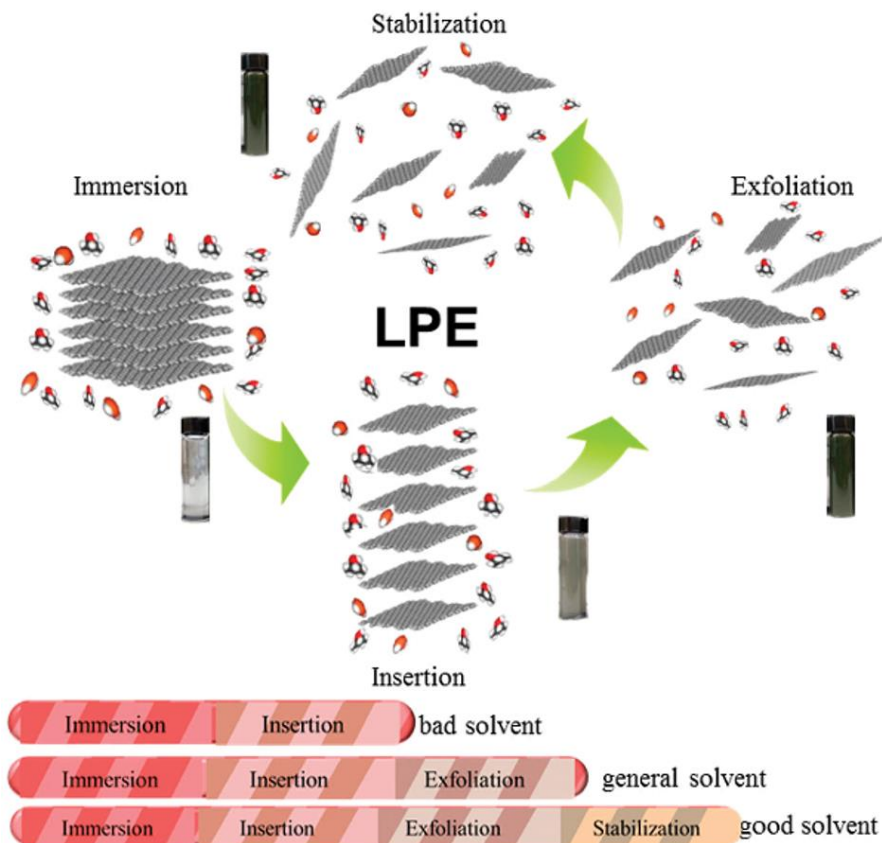
Figure 1-12: Schematic representation of various steps involved in the liquid phase exfoliation of nanosheets highlighting the role of solvent. Reprinted with permission from Ref. 188.

produce large quantities of 2D nanosheets of graphene, TMCs, metal oxides etc. Similar to previous method, Shear force assisted LPE uses high shear forces to separate the bulk materials in nanosheets. However, application of shear force has the advantage of higher yields and production rates thus affecting its industrial application positively. For the shear force assisted exfoliation, bulk material and respective solvent are added to industrial blenders and mixed at very high speeds to generate the nanosheets. With only one process variable, the speed can be modulated to control the extent of exfoliation and the size of exfoliated product. On general, higher speeds generate individual layers of smaller lateral dimensions and vice versa.

The other broad category of LPE utilizes chemical reactions to separate the stacked layers of a material which later can be dispersed in solution using mild forces. The method however is relatively limited and has more specific applications as the involvement of crucial chemical reactions. There are multiple sub-categories of chemical reaction mediated LPE differing in the type of reaction

taking place with the exception of Ion intercalation assisted LPE. Ion intercalation assisted LPE uses small ions like Lithium, which are inserted in the inter-layer spacing due to their small sizes over prolonged incubation times. The inserted ions act like fulcrums, separating the nanosheets as the incubated reaction solution is subjected to mild sonication. This method replaces the force mediated LPE by avoiding the usage of highly toxic solvents however suffers from lower batch size and long reaction times. Other chemical routes of LPE are Ion exchange assisted LPE, Oxidation assisted LPE, and Selective etching assisted LPE where the bulk materials are subjected to various chemical reactions to convert the atoms residing in the middle layers of the lamellar materials. This replacement generates ample spaces between the compounds for the solvent to immerse and separate the material in its nanosheets.

iv. **Microemulsification:** Microemulsification is a method to generate lipid or polymer based nanoparticles. This method is a surfactant-mediated force-assisted homogenization process where large droplets of reaction mixture are vigorously agitated in suitable surfactants to generate small particles ranging between 10-1000 nm in diameters. The method, although simple, is able to optimally generate a homogenous sample of uniformly sized nanoparticles and have an unmatched advantage of nano-carrier function where the solution of choice can be loaded inside these hollow particles. The resulting nanoparticles can be used as prepared solutions or can be evaporated to generate dried nanoparticles.

1.5.4.2. Bottom-up methods

i. **Physical Vapor deposition:** Physical vapor deposition (PVD) is used to synthesize nanoclusters or nanoparticles by depositing evaporating targets on a suitable substrate. The method uses a source to evaporate or sublime bulk material like metals or metal oxides, which generates particles in few nanometers. The formed particles interact with each other to grow in larger particles while travelling to a cold substrate, where the particles condense and are harvested. The method operates at vacuum or in presence of specific gases, and the particle formation can be controlled by maintaining the pressure inside the vessel. This provides PVD

with a high degree of protocol control, which can be tuned to synthesize particles of desired size, shape and phase. PVD method can further be classified in categories like ionized cluster beam deposition, laser pyrolysis or laser ablation which differ in the modes chosen for vaporization like lasers or electron beams, and deposition techniques. The variation allows their application for materials with different properties. ICB deposition is usually used for deposition of thin crystalline films over a substrate. The method uses an electron beam to ionize vaporized material, which directs the material towards the substrate for deposition. Laser ablation and laser pyrolysis use high power laser sources for vapor generation, which are in turn deposited on cooled substrates. Laser ablation have the ability to create phase changes in the material due to their interaction with the contents of chamber in vapor phase and is the industrially used for the mass production of carbon nanotubes (CNTs).

ii. **Sputter deposition:** Sputter deposition is a technique used to generate thin layers of metals, alloys, ceramics or compounds on suitable substrates. The main advantage of this technique is the stoichiometric deposition of materials. The sputtering operates in vacuum chambers where high pressure gas, usually Argon, is used to knock the ions/atoms from the materials called "target", which travel along the chamber to the substrate where thin layers are formed. Among various classes of sputter deposition, DC, RF and magnetron sputtering are more popular. DC sputtering performs by placing the target and substrate at a potential difference of 100-3000 V. Generally applied to conducting materials, the knocked ions/atoms from target kept at negative potential travel to a positive substrate under the influence of potential difference. Insulating materials are coated by using RF sputtering which uses alternating radio frequency in a range of 5-30 MHz to ionize and sputter the targets. Magnetron is an advancement of previous methods where magnetic fields are added and the knocked ions are made to travel in an electromagnetic field guided by Lorentz forces. This allows magnetron sputtering to achieve higher levels of ionization and thus superior coatings. Furthers by introducing reactive gases, controlled chemical reactions can be induced to generate layers oxides, carbides, nitrides and other compounds of targets in a magnetron sputter coater.

iii. **Chemical Vapor Deposition:** Chemical vapor deposition is a widely applied method of bottom-up material synthesis used particularly for the synthesis of planner nanomaterials. The method involves reaction precursors in gaseous phases that react in the reaction chamber and the reaction products get deposited on the surface of a substrate. The reaction vessel remains in a continuous flow to remove the by-products produced in the reaction and can be modulated finely to control the reaction products, their morphologies, chemical compositions *etc.* Chemical vapor deposition is a widely accepted method for generating highly pristine nanomaterials and is specifically used for the deposition of several nanoscale coatings for microfabrication process. The method is commercially used for the production of polysilicon, silicon dioxide, silicon nitride, graphene and several metals like tungsten, niobium, aluminum in their pristine or oxide forms.

iv. **Electric arc deposition:** As evident, this method uses an electric arc as the source of vaporization for the generation of nanomaterials. In a liquid cooled chamber, electrodes made from starting material are set up in vacuum and high voltage is applied to generate an electric arc between the electrodes. The arc vaporizes the electrode material, which in turn is deposited on the inner walls of the reaction chamber. This method is most popular for the mass scale production of fullerenes and carbon nanotubes by using electrodes made of graphite.

v. **Nucleation & growth method:** Nucleation & growth method of nanomaterial production is essentially a thermodynamics-based method of synthesis applied for the generation of a variety of nanomaterial morphologies. The method begins with a nucleation process that is the introduction of small "seeds" in the reaction solution *via* chemical reactions or through manual addition. The reactant species then get deposited on the surface of the seeds following the principles of thermodynamics, thus "growing" in size. This colloidal route of synthesis can be controlled by manipulating the reaction conditions like temperature, concentration of seeds, stoichiometric ratio of seeds respective to reactant species, and with the presence of growth mediators. The method is universally accepted route for the commercial generation of metallic nanoparticles of several

noble metals due to the ease of operation, controllable & optimizable reaction conditions. The method can also be used to produce several diverse morphologies by manipulating the growth dynamics of the nanoparticles during the growth phase by blocking the growth in particular crystal phases with generate shapes like cubes, rods, prisms or even exotic morphologies like urchins & flowers.

vi. **Hydrothermal synthesis:** Hydrothermal synthesis can be traced back to 1839 with its application in the synthesis of crystals as shown by Robert Bunsen. The technique involves reactions of dissolved precursors at high temperature (up to 300 °C) and high pressure (100 bars). The method is especially suitable for materials having low RT reactivity, dissolution, or unstable intermediates at normal conditions. The reaction takes place in reinforced sealed containers called autoclaves, which are fitted with temperature and pressure controllers to maintain the reaction conditions. The method has the advantage of high production rates, control over synthesis and production of novel nanomaterial shapes and phases.

vii. **Micro-reactor based on Lab-on-a-chip:** Lab-on-a-chip based micro-reactors use the principles of microfluidics and is a recent development in the field of nanomaterial synthesis. The method relies on the use of small microfluidics chips into which the reactants are flowed in a continuous or discontinuous flow, are mixed, react and generate nanomaterials following the process of nucleation -&-growth. However the microfluidics-based method heavily varies from the colloidal route of synthesis by presenting a higher degree of control over the reaction parameters like reactant concentration ratio, kinetics, incubation times while also having highly controlled levels of diffusion, thermal uniformity & mixing owing to the advantages offered by miniaturization. The micro-reactor based nanomaterial synthesis shows very small batch variation with high degree of homogenization and can be used to manipulate the nanoparticle morphology however the method currently lacks in the scale-up required for the commercial level production of nanomaterials though this may prove beneficial in future following the advances in the field of microfabrication.

viii. **Biological synthesis:** The biological routes of nanomaterial synthesis utilize biological materials as the reaction vessels. This biosynthesis route utilizes biological entities like bacterial cells, yeast, fungi, cellular lysates or plant extracts *etc.* that possess the ability to convert metallic ions into their respective nanoparticles due to their inherent catalytic properties and reducing potentials. Till now several independent biological routes of nanomaterial synthesis have been found among which generation of gold nanoparticles by *Rhodococcus* sp. and leaf extract of *Pelargonium graveolens*, generation of silver nanoparticles by *Penicillium diversum*, and generation of CdS crystallites by *Candida glabrata* and *Schizosaccharomyces pombe* are note-worthy for their widely accepted applicability.

1.6.   Microfluidics-based biosensors

1.6.1.   Introduction

Microfluidics based devices are defined as microscopic systems that deal with the study, manipulation and control of minute quantities of fluids, generally in microliters or nanoliters.

1.6.2.   Advantages of microfluidics-based devices

Microfluidics based devices display a wide variety of advantages over their bulk scale counterparts due to the two properties named **Miniaturization** and **Integration**. *Miniaturization* provides the benefits by increasing the surface-to-volume, which directly affects the physical properties of the fluids in the micro-compartments. Microfluidics-based devices allow rapid diffusion due to small volumes, which provides superior mixing of the contents. High surface-to-volume also improves heat transfer, which in turn can be used to manipulate the required temperatures for the reactions, and ensure efficient dissipation of heat along the channels, preventing formation of temperature gradients. Another clear advantage of miniaturization is the small size of devices, which helps in reducing the cost of fabrication, and demands lesser functioning sample volumes as

microfluidics-based devices require very small operational sample volumes. *Integration* of the microfluidics chips with multiple inlets, mixers, valves *etc.* creates systems that can harbor multiple steps of a biochemical assay. Further, the microfluidics systems can be equipped with electronics & actuators to generate automated standalone devices called *lab-on-a-chip* or μTAS (Micro Total Analytical System). Such devices benefit from ease of usage, high throughput, rapid analysis, and portability.

Further, microfluidics based devices can be used to develop compartments that facilitate cellular culturing. Such devices, sometimes termed *organ-on-a-chip* are systems where the physiological microenvironment can be replicated at a cellular or tissue level to mimic the *in vivo* conditions.[189-191] Such systems can be used as alternatives to animal models to visualize and understand the physiological mechanisms and pathways. Further, the organ-on-a-chip can expanded into a *disease-on-a-chip* where a diseased condition is induced in a cellular microenvironment for the development of novel therapeutics, and to understand the dynamics of the clinical therapeutic intervention at tissue or cellular levels. These advantages have huge potential in research based on animal models by reducing the number of utilized animals and by introducing a much ethical alternative for conduction of such experiments.

1.6.3. Role of nanomaterials in microfluidics based biosensors

Microfluidics systems especially microfluidics-based biosensors is a field that has tremendously benefited from the advances in the field of materials and nanotechnology. Nanomaterials, owing to their superior optical & electronic properties and huge surface-volume ratio act as tools to further complementing and enhancing the benefits of the microfluidics-based devices.[192-194] In such micro-analytical devices, nanomaterials are used for the purpose of analyte capturing, signal amplification and transduction. Nanomaterials like CNT, nanoparticles with diverse morphologies ranging from simple spheres to exotic structures like nano-urchins derived from metals like gold, silver, titanium, platinum *etc*, magnetic nanoparticles, and quantum dots have been successfully applied for the detection of a wide variety of analytes. Due to their small sizes,

nanomaterials do not pose much resistance to the fluid dynamics and can be used in continuous flow. These nanomaterials can be easily functionalized with receptors like antibodies or aptamers to generate tracer molecules for optical and electrochemiluminescent sensors.[195–200] Among the nanomaterials used, the most prominent examples include gold nanoparticles for the generation of colorimetric or LSPR based optical sensors, and metallic quantum dots for the development of fluorescent biosensors in dynamic modes.[199] Further, nanomaterials can be immobilized to decorate the electrode materials or to generate FETs for the development of electrochemical biosensors.[196,201–203] Besides this, magnetic nanoparticles derived from oxides of iron facilitate the separation of the analyte to bring about enrichment of analyte concentration to improve signal-to-noise ratio.[195,201,204] This property is much sought-after in the detection of early stage disease analytes that are expressed at very small amounts in biological samples.

1.7. Problem definition

1.7.1. Need of cardiovascular diagnosis

Cardiovascular diseases are the leaders in global mortality, a position these have held since the last decade of 20th century.[3,4,6,205] Possessing a huge annual death toll of ~18 million, cardiovascular issues account for one out of every three deaths worldwide. Among the studies initiated to understand the mechanism and causatives of highly lethal cardiovascular diseases, Framingham heart study is the longest running project spanning over 7 decades.[206] Since its inception in 1948, Framingham heart study revealed several cardiac risk factors, including the recognition of hypertension as the indicator for CHD (1957)[207] & stroke (1965)[208], association of diabetes (1974)[209–213] & physiological lipid profile with incidence of heart diseases (1977)[214,215], and the role of smoking and hormonal imbalances in increasing frequency of heart diseases (1985)[206]. The Framingham study shifted the global trend from treatment to prevention in the second half of 20th century.[206] Although the boom in cardiac problems was correlated with the industrial revolution and dramatic shift in urban lifestyle, with its associated risk factors identified and mitigated, there have been no significant decrease in the

mortalities due to cardiac problems in most parts of the world. According to the studies by Feigin *et al* & Roth *et al* performed by accumulating worldwide data including population groups from diverse cultures, races and ethnic groups, the cardiovascular diseases have not shown any decline in either the total number of cases or the number of new cases generated annually.[4,5] During 1990-2010, the mortality associated with cardiac diseases have increased by 33%, and between 2006 & 2016, the annual death count among all ages increased further by 14.5% (Figure 1-13).[3,6] The severity of these diseases is further exaggerated in high-age groups, as seen by the 53.7% increase in mortality in >70 years age group. Along with the mortality, cardiac ailments are the leading cause of morbidity, a position these have held since 1990.[3] The cardiovascular diseases have the highest combined years of life lost (YLL), and ischemic heart disease have been the leading causative of morbidity in high & high-middle income countries since 1990. Similarly, in the middle & middle-low income countries, ischemic heart disease surpassed the communicable disease to become the leader of morbidity in the last
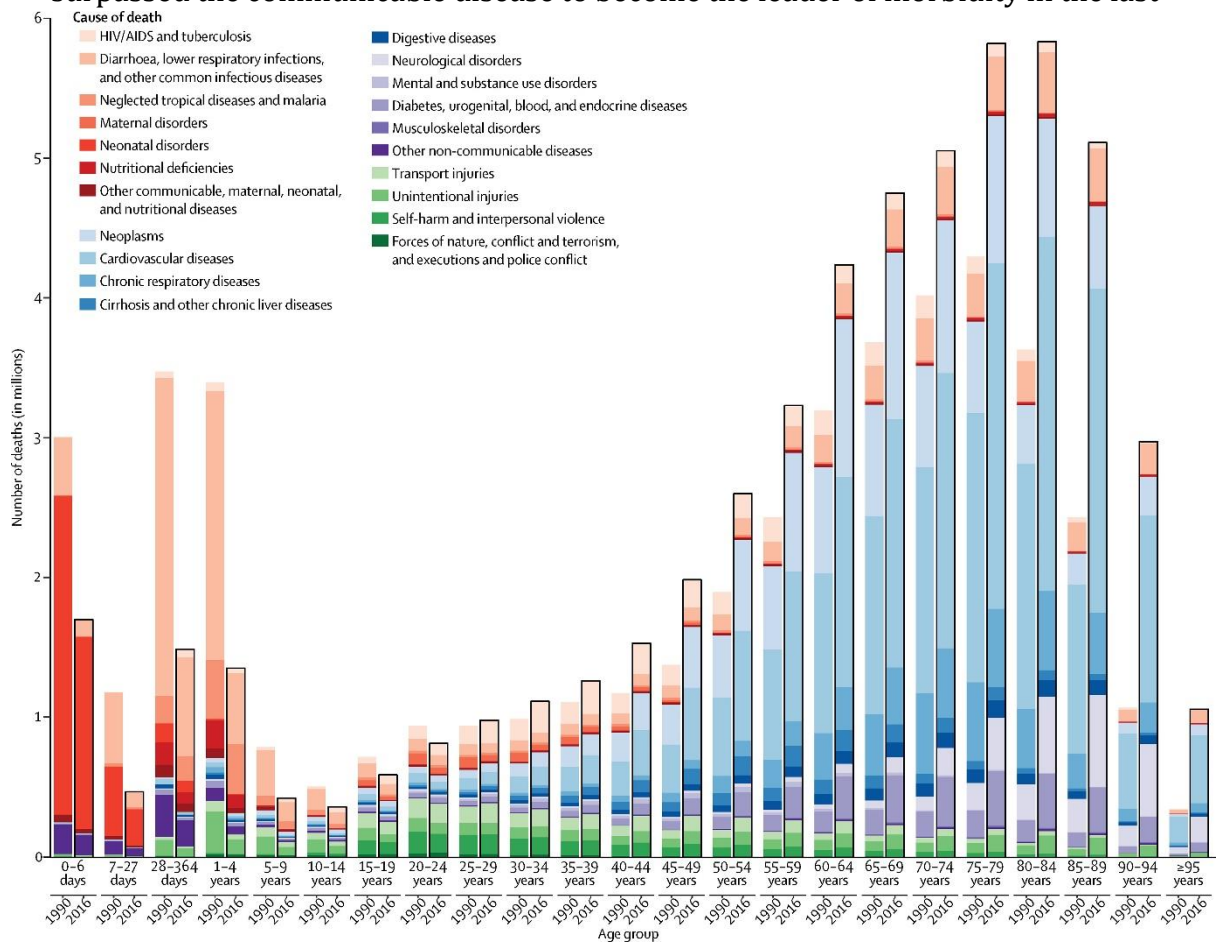
Figure 1-13: Graphical representation of the change in mortality from 1990 to 2016, segregated for different age groups. Reprinted with permission from Ref. 3.

3 decades. Further, even in the lowest income countries, ischemic heart disease is the non-communicable disease causing highest total YLL, and is positioned eighth among top causatives of morbidity as of 2016. This rampant expansion directly reveals the inability of conventional risk scoring in accurately recognizing the possibility of the onset of cardiovascular diseases.[216,217]

1.7.2. Role of cardiac biomarkers in cardiovascular diseases

Although disease risk assessment scoring have been efficient in generating a broader view about the onset of cardiac diseases, its inability in precisely predicting the individual events shifted the attention towards the metabolic and biochemical investigations.[17,206] Therefore, biochemical cardiac biomarkers were included as the critical indicators of a myocardial infarction by the Joint European society of cardiology/ American college of cardiology committee in 2000.[17] Along with their inclusion, the role of multiple cardiac biomarker estimation as a tool to avoid false positives arising from non-specific expression or varying expression periods was also conceptualized.[17] The events of myocardial infarction and myocyte necrosis are completely dependent on the ability of biochemical assays in detecting the presence of such events. Similarly, the lack of cardiovascular health monitoring devices with simpler operation have created an essential window where the serum build-up of cardiac biomarkers is not monitored. Due to these technological gaps, many events of myocardial infarctions are left unaccounted until the clinical endpoints are expressed only after the disease has developed out of its initial stages, thus posing a pressing need for sensitive and simpler assays for the quantification of cardiac biomarkers.

1.7.3. Selected cardiac biomarkers

To address the problem of false negatives, we worked for the development of a sensitive multiplex device with abilities to monitor even faint fluctuations in the serum levels of cardiac biomarkers. As the target proteins, **Myoglobin** and cardiac **Troponin I** were selected owing to their diverse expression profile and retention times. Myoglobin is a 17 kDa heme-containing protein that functions in

oxygen transport in the muscle tissues. It has a physiological threshold of 20-80 ng/mL, which further is higher in case of males than females.[14] The correlation between elevated serum levels of myoglobin and the myocardial infarction was found in 1975 and since then it has been used as a gold standard for the early phase detection of such infarcts.[218] Myoglobin is among the first cardiac markers released after an infarction, a feature that is rooted in its high cytosolic concentration in the myocytes, and the serum levels start elevating around 2 hours from the onset of physical symptoms.[14,219] The elevation peaks around 6-9 hours before returning to the physiological threshold in 24 hours, a period in which myoglobin is the best indicator of a cardiac infarction (Figure 1-14).[14,18,220,221] Myoglobin diagnosis presents a 77-97% sensitivity and 90-98% specificity as a predictor of negative myocardial events during the early phases. The major limitation of myoglobin as a cardiac marker is its lack of specificity to the cardiac tissues, which may create a non-cardiac associated elevation in serum levels of myoglobin and generate false positives.[18,222] Although this can be avoided by careful sample collection and monitoring the patient's history, diagnostic specificity of myoglobin can be increased by combining it with clinical end points or with other more specific cardiac markers.[14] Among the proteins with greater cardiac specificities, cardiac troponins and creatine kinases are the best understood and established cardiac biomarkers.[14,16,18] However, the application of Creatine kinase as the indicator of myocardial events in the multiplex format was ruled out due to its non-specific serum elevations.[14,16,223] Creatine kinases are widely present in the body and may have an increased expression profile due to a variety of non-cardiac reasons including skeletal injuries, muscle diseases, neurological conditions, or usage of alcohol or drugs. In contrast, cardiac troponins are more specific to the cardiac myocytes and possess a similar mid-to-late serum expression profile after the onset of physical symptoms. Troponins exist as a heterotrimeric complex of three proteins *viz.* TnT, TnC and TnI in the muscle tissues, where they act as the regulators of the ionic concentration of calcium and thus act as the regulator of muscle activity.[224] Among the subunits, troponin I has the least sequential homology between cardiac and skeletal versions due to the presence of a specific 31 amino acid chain at its N-terminal in cardiac TnI, and is not expressed in non-cardiac muscles at any stage, thus being
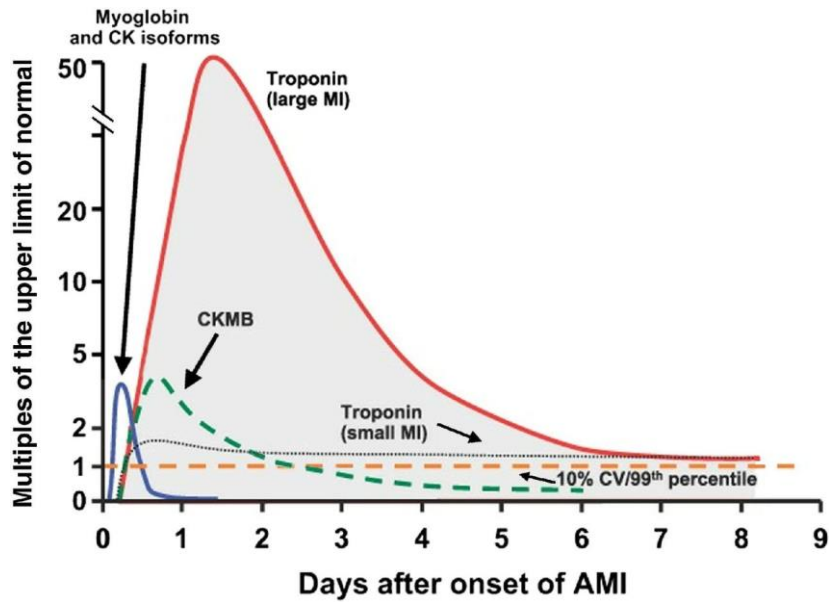
Figure 1-14: Expression profile of cardiac biomarkers over days following an event of acute myocardial infarction. Reprinted with permission from Ref. 219.

the most-specific protein to the cardiac myocytes.[14,225,226] The troponins have a delayed expression, with their serum elevation beginning around 6 hours and peaking during 12-24 hours after the onset of physical symptoms (Figure 1-14). Although the protein itself has a half-life of ~2 hours, the serum levels may remain elevated up to 3-7 days following a cardiac infarction due to continuous release of troponins from the injured cardiac myocytes.[227] The pathological serum range of cardiac troponin I is >0.4 ng/mL, while under normal physiological conditions this is not significantly expressed in the blood of an individual.[14] As a result, troponin I has proved to be the most specific and sensitive cardiac marker for the detection of cardiac infarctions.[17] The combination of myoglobin and troponin I presents an analytical tool having the widest diagnostic window, with myoglobin expressing at the early stage while troponin I acting as delayed stage marker of cardiac infarction.[17] This provides a facility to predict the presence of AMI precisely in support of the rise of clinical symptoms. Furthermore, incorporation of myoglobin to an already established troponin diagnosis allows ability to detect the occurrence of early re-infarctions, which cannot be recognized by troponins due to their very long expression profile.[17] The detection of multiple markers simultaneously provides a method to accurately verify the event of an infarction and benefit the clinicians in the triage of patients for choosing benefitting treatments.[228]
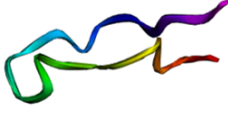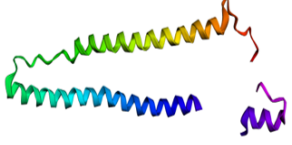
	Myoglobin	BNP	Troponin I
Structure			
Molecular weight	17.18 kDa	3.46 kDa	24 kDa
Chain length	154 aa	32 aa	210 aa
Isoelectric point	7.14	10.95	9.87
Physiological Function	O_2 Carrier	Natriuretic hormone	Contractile protein
Physiological range	20-80 ng/mL	<0.1 ng/mL	<0.4 ng/mL
Physiological half-life	2-3 hours	20 minutes	2 hours

Table 1-2: Table showing the structure and various parameters of the selected cardiac biomarkers.

Besides the diagnostic cardiac markers expressing after a cardiac infarct, certain molecules also have proven to have a correlation with the development of these maladies. Their serum concentrations show a gradual rise in response to the increasing severity of the disease and can be used as prognostic markers for predicting the onset of cardiac diseases.[229–231] Among the recognized markers, B-type natriuretic peptide and inflammatory markers have established as the predictors of cardiac events.[18] However, inflammation-related markers including C-reactive protein, IL-6, myeloperoxidase, matrix metalloproteinases, soluble CD-40L *etc.* have an indirect relation with the cardiovascular system and thus do not have a strict expression profile relative to the cardiac events. Their serum levels may elevate under inflammatory stimulus, and alternatively may be unaffected in several cases of cardiovascular diseases. These markers thus have a lower credulity and lower analytical specificity for cardiac diagnosis. In contrast, **B-type natriuretic peptide** is a direct product of the cardiovascular system and thus possesses high degree of specificity.[232] Under the hemodynamic loading, BNP is produced as pre-proBNP, an inactive form that further is cleaved into BNP & N-terminal proBNP during secretion.[233] Among the pair, BNP is an active hormone that stimulates natriuresis, and decreases the overall volume of blood to relieve

the hemodynamic overloading. Although being regulators of hemodynamic stress, BNP & NT-proBNP have established role in the prediction of heart failures, and are also released by the ventricular tissues in the absence of myocardial necrosis.[16,18,234] The efficacy of BNP diagnosis as the predictor of cardiac-associated mortality is doubled when applied in combination with cardiac troponin I, thus making it a suitable candidate for cardiac prognosis & therapy monitoring. A BNP serum level of <100 pg/mL is considered as the physiological threshold and a serum concentration above 500 pg/mL have proven to be a powerful predictor of heart failure.[235,236] Considering its efficacy, BNP was chosen as the prognostic marker for predicting any looming heart failures in association with myoglobin and troponin I.

1.7.4. Experimental layout and research objectives

As the biorecognition moieties, DNA-based aptamers were explored as alternatives to conventional protein-based bioreceptors. These aptamers are screened from vast library of sequences through a cyclic process called SELEX. A number of SELEX variants were reported, however those lacked in either the convenience of operation or its efficacy. Our intention was to develop a SELEX methodology requiring less cycles to reduce the cost involved in the generation of aptamers while avoiding any compromise in the quality of generated receptors. For the purpose, we developed a plate-based SELEX procedure using a multi-well microtitre plate as the stationary matrix. The microtitre wells allow various surface chemistries for high levels of target analyte binding and allow complete control over the molecular biointeraction. The developed Plate-SELEX method was used for generation of specific aptamers against the cardiac biomarker, myoglobin. To improve the selection procedure further, a single-reaction SELEX procedure was developed based on bio-layer interferometry. The method was applied for the generation of aptamers against B-type natriuretic peptide and troponin I. While the method had the ability of aptamer generation in a single reaction setup, it also possessed the facility to separate the screened aptamers based on their affinities towards the target analyte.
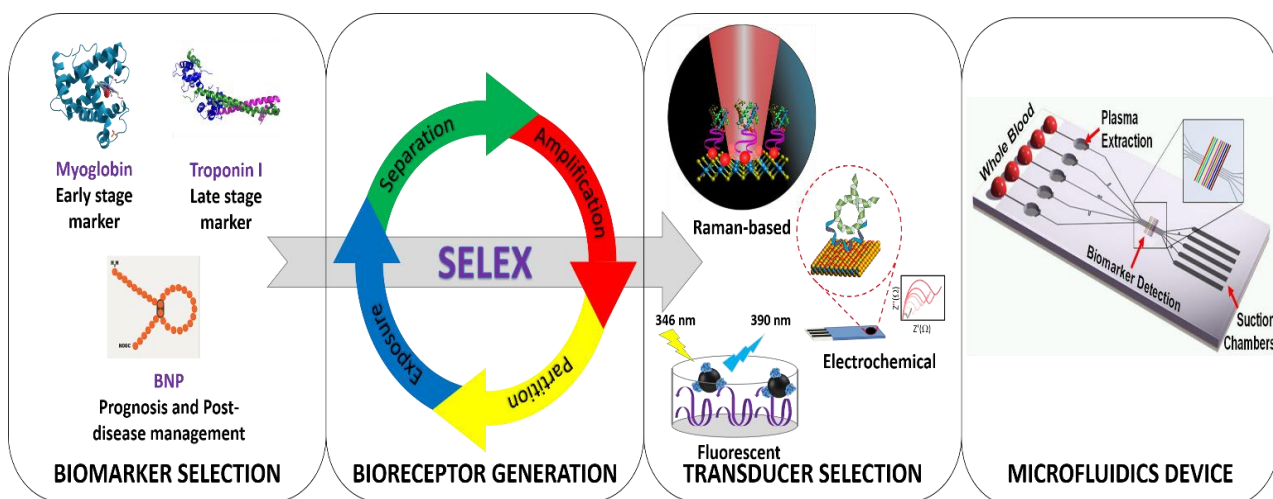
Figure 1-15: Schematic representation of the research plan depicting different stages of multiplex biosensor development for cardiovascular diseases.

As the transducing elements, various nanomaterials were investigated for the development of the diagnostic platforms for cardiac markers. Nanomaterials with distinct physical properties were synthesized to generate fluorescence, electrochemical and Raman-based diagnostic assays. The transducers were utilized towards the detection of myoglobin using its specific aptamers to elucidate the role of different transducers in defining the dynamic range and sensitivity of an assay. As optical transducers, fluorescent Quantum dots were utilized and the role of different starting materials was investigated. Further, the possibilities of developing a Point-of-Care setup from the developed assay were also explored. Another optical transducer in the form of Raman-active AuNP@WS$_2$ hybrid was generated to examine the benefits of label-free SERS-based transducers in shaping the dynamic range of analytical assays. Electrochemical transducers were developed from an rGO/CNT nanohybrid & few-layered phosphorene nanosheets, and different strategies for aptamer modification were investigated (Figure 1-15).

For the development of a multiplex detection platform, a system operating on microfluidics was selected. Microfluidics is the technology dealing with the flow properties and manipulation of fluids in microscopic channels. Microfluidics have played an essential role in the development of independent analytical systems due to the advantages of miniaturization and integration. *Miniaturization* provides the benefits by increasing the surface-to-volume, which directly affects the physical properties of the fluids like diffusion, heat transfer and mass

46

transport in the micro-compartments. Another clear advantage of miniaturization is the small size of devices, which helps in reducing the cost of fabrication, and demands lesser functioning sample volumes. As microfluidics-based devices require very small sample volumes to operate, their application in biological analysis gives an edge over conventional methods requiring larger sample volumes. The effect is further exaggerated if multiple markers are quantified as microfluidics-based devices can be designed to test multiple parameters from the same sample volume. *Integration* of the microfluidics chips with multiple inlets, mixers, valves *etc.* creates systems that can harbor multiple steps of a biochemical assay. Further, the microfluidics systems can be equipped with electronics & actuators to generate automated standalone devices called Lab-on-a-Chip or µTAS (Micro Total Analytical System). Such devices benefit from ease of usage, high throughput, rapid analysis, and portability. Furthermore, the devices can be processed in parallel to perform multiple assays from a single sample under identical experimental conditions, thus highly improving the reproducibility and precision of the assays.

The objectives for this thesis were:

Objective 1: Generation of aptamers against selected cardiac biomarkers

Objective 2: Generation of nanomaterials with superior transducing properties

Objective 3: Generation of nanomaterials-based aptamer functionalized diagnostic platforms for cardiac biomarkers

Objective 4: Development of microfluidics-based multiplex device for multiple marker diagnosis.

CHAPTER 2

SELEX methods for the generation of DNA aptamers against cardiac biomarkers

Aptamers are single-stranded molecules of nucleic acids, possessing unique geometries as a function of their nucleobase sequences, allowing aptamers to bind to their specific targets.[106] These aptamers are screened from a vast library of sequences through a process called SELEX, short for <u>S</u>ystematic <u>E</u>volution of <u>L</u>igands by <u>Ex</u>ponential enrichment.[108] SELEX is a cyclic process involving introduction of target molecules with nucleic acid library and the separation of binding populations from the non-binders. To facilitate the separation process, SELEX is performed over a fixed matrix, which hosts the target molecules *via* covalent or non-covalent interactions. This allows the separation of the sequences able to interact with the target molecules from the remaining library following the principles of chromatography. Several different components have been applied as stationary matrices in SELEX process, thus creating multiple variations of the process itself. Besides these, some dynamic SELEX methods are also developed that function on the gain in mass resulting from the biomolecular interaction acting as the resolving force. However, the methods have very limited application window as these can only work where both nucleic acid sequences and target molecules have high molecular masses to generate an effective dragging force for a high degree of resolution. On the other hand, more sensitive detection methods like capillary electrophoresis can be utilized to recognize pairs with low levels of resolution, albeit this method is costly and requires high skill levels to operate, thus limiting its application.

Our intention was to develop a SELEX methodology requiring less cycles to reduce the cost involved in the generation of aptamers while avoiding any compromise in the quality of generated receptors. For the purpose, we developed a plate-based SELEX procedure using a multi-well microtitre plate as the stationary matrix. The microtitre wells facilitate various surface chemistries for high levels of target analyte binding and also allow complete control over the molecular biointeraction. The developed Plate-SELEX method was used for generation of specific aptamers against a cardiac biomarker, myoglobin. To

improve the selection procedure further, a single-reaction SELEX procedure was developed based on bio-layer interferometry. While the method had the ability of aptamer generation in a single reaction setup, it also possessed the facility to separate the screened aptamers based on their affinities towards the target analyte. The method was applied for the generation of aptamers against B-type natriuretic peptide and troponin I. The generated aptamers were characterized by various methods to confirm their affinities towards selected cardiac biomarkers, and used for the development of sensitive detection platforms for the respective biomarkers.

Objectives:

- Generation of DNA aptamers against cardiac biomarker Myoglobin by using microtitre plate-SELEX method
- Development of alternative methodology for SELEX process by using biolayer interferometry
- Investigation of the ability of affinity-based segregation using the developed SELEX method
- Generation of DNA aptamers against cardiac biomarkers B-type natriuretic peptide and Troponin I

2.1. DNA combinatorial library

2.1.1. Design of DNA library

The DNA combinatorial library was synthesized following the literature report of Sefah *et al.*[123] The library contained a central random region of 45 nucleotides, flanked on each side with primer docking sites spanning 18 nucleotides each. The central random region imparted the library with the ability to generate 1.2×10^{27} unique sequences, while fixed primer-docking sites aided in the amplification of the library through polymerase chain reaction. The reverse primer was modified with biotin at its 5' end to facilitate the separation of strands.

Forward primer was either modified at its 5' end with a fluorophore, a thiol linker or kept unmodified to modulate end modification of the aptamer itself.

Library: 5'-ATCCAGAGTGACGCAGCA-(N ×45)-TGGACACGGTGGCTTAGT-3'
Forward primer: 5'-Modifier-ATCCAGAGTGACGCAGCA-3'
Reverse primer: 5'-Biotin-ACTAAGCCACCGTGTCCA-3'

2.1.2. Preparation of DNA library for SELEX

A combinatorial DNA library stock was diluted from a 100 μM stock to a working concentration of 10 μM by adding 10 μL of stock in 90 μL binding buffer (10 mM Tris-HCl buffer containing 150 mM NaCl & 5 mM MgCl$_2$, pH 7.4). The diluted library contained 10^{14} sequences theoretically. The diluted solution was heated to 95°C to ensure complete disruption of any inter-strand linkages. The library was immediately transferred to ice, and held for 15 minutes to prevent any renaturation. This denatured library was incubated at room temperature for at least 6 hours to allow the strands to fold in the presence of the ionic medium. This folded library was used for the "*Library exposure*" step in all the SELEX protocols.

2.1.3. Cloning and sequencing of aptamers

The sequences of binding pool of aptamers were deduced by cloning the DNA strands in a host cell and sequencing the plasmids through Sanger chain termination method. For preparing competent cells of *E. coli* strain JM107, the lyophilized pure culture (MTCC no. 1669) was procured from microbial-type cell culture repository (MTCC, India), and revived by plating on autoclaved sterile nutrient agar. The plate was incubated at 37°C until the well-grown colonies appeared on the surface of the medium. From this master culture, a single colony was picked and sub-cultured in fresh Luria Bertani growth medium and grown overnight at 37°C with shaking at 180 rpm. Competent cells from this culture were prepared using insTAclone PCR cloning kit (Thermo scientific, USA). From the overnight culture, 150 μL was transferred into warm C-medium and incubated for 20 minutes at 37°C with shaking at 120 rpm. The culture was centrifuged at 2500

×g for 5 minutes, and pellet was re-suspended in 300 μL of T-solution (fresh equivolume mixture of T-solution A & T-solution B). The suspension was incubated on ice for 5 minutes and then centrifuged at 2500 ×g for 5 minutes, and pellet was re-suspended in 120 μL of T-solution followed with a 5 minutes' incubation on ice. The cell suspension was immediately utilized for plasmid transformation after the completion of incubation

For cloning, aptamers were amplified by a polymerase chain reaction using the following protocol,

Reagent	Quantity
Forward primer (10 μM)	1.25 μL
Reverse primer (10 μM)	1.25 μL
Template	1 ng
DMSO	2 μL
PCR master mix (2×)	25 μL
DNase-free water	to make up 50 μL

The primers used for the cloning amplification were not labeled with any linker or modifier. The reaction mixture was prepared onto ice and immediately transferred to a thermocycler pre-heated to 95℃. The reaction mixture was amplified using the following protocol,

Step No.	Step	Temperature	Duration
1	Hot Start	95℃	5 minutes
2	Denaturation	95℃	30 seconds
3	Annealing	56.3℃	30 seconds
4	Extension	72℃	30 seconds
Repeat Step 2-4 × 15 times			
5	Final extension	72℃	20 minutes
6	Hold	12℃	-infinite-

The amplified dsDNA was purified *via* a PCR purification kit to separate the primers and reaction ingredients from the amplified aptamers. The purified

aptamer was quantified using a micro-volume spectrophotometer and 0.52 pmol of this was added into 0.17 pmol of pTZ57R/T vector (Vector map in Figure 2-1). The vector was a linear dsDNA possessing Thymine overhangs on each end that bind to the PCR products containing extra Adenines added due to a limitation of Taq polymerase. The linear vector and purified DNA were mixed according to the following recipe,

Reagent	Quantity
pTZ57R/T vector	3 µL
Insert DNA	28 ng
Ligation buffer (5×)	6 µL
T4 Ligase	1 µL
DNase-free water	to make up 20 µL

The ligation mixture was gently vortexed, and incubated at 4°C overnight to establish efficient ligation. On the subsequent day, 5 µL of the overnight ligation mixture was transferred into a chilled microcentrifuge tube, and 50 µL of fresh competent cells were added. The mixture was incubated for 5 minutes on ice and cultured on warm Luria Bertani agar plates containing ampicillin (100 µg per mL of media), 40 µL of 0.1 M IPTG (isopropyl–β–D–thiogalactopyranoside), and 40 µL of 20 mg/mL of X-gal (5-bromo-4-chloro-3-indolyl-β-D-galactopyranoside). The plates were incubated at 37°C overnight for the colonies to develop. On the subsequent day, white colonies were picked, inoculated in 10 mL sterile LB medium containing 100 µg/mL ampicillin and grown for 6 hours. The samples showing turbidity due to growth were centrifuged at 2500 ×g to harvest the cells and plasmid were extracted from the cells using commercial plasmid isolation kit (QIAprep spin miniprep kit, Qiagen). The plasmids were sequenced *via* Sanger chain termination sequencing method using universal M13 sequencing primers (Figure 2-1).
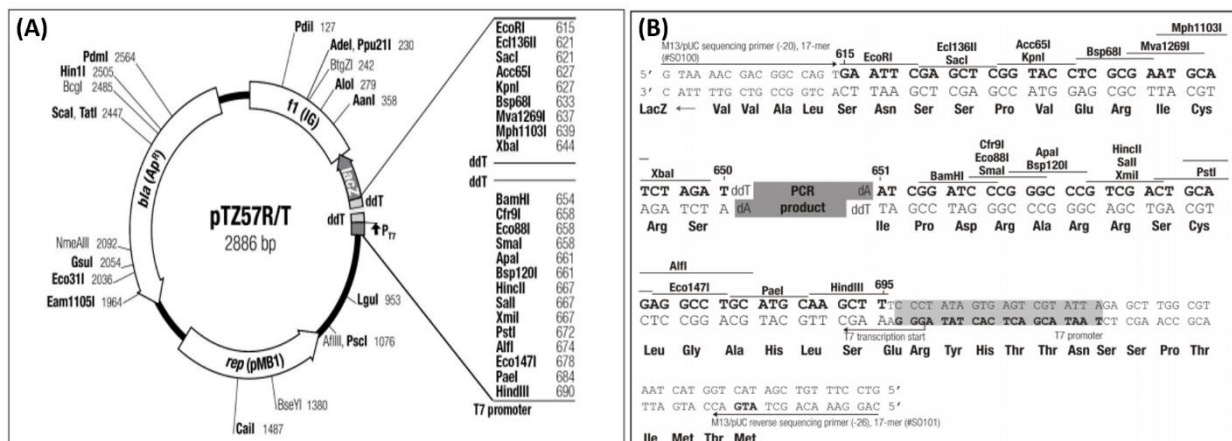
Figure 2-1: (A) Map of pTZ57R/T showing different regions of the vector, (B) DNA sequence of multiple cloning site of the vector along with the primer binding sites for the M13 sequencing primers.

2.2. Microtitre Plate-SELEX method for the generation of aptamers

Myoglobin-specific aptamers were screened from the oligonucleotide library by Plate-SELEX. The method utilized multi-well microtitre plate as the stationary matrix onto which myoglobin molecules were fixed. For the purpose of fixation, myoglobin protein was diluted to a concentration of 5 µg/mL in carbonate buffer (10 mM, pH 9.6), and 100 µL of this dilution was added in a single well of a 96-well polystyrene microtitre plate (Nunc F96 Maxisorp immunoplates, #437111). The plate containing myoglobin was incubated at 4°C overnight to allow binding of protein on the well surface through hydrophobic interactions. On the following day the plate was drained and washed twice with phosphate buffered saline (10 mM, pH 7.4), and the empty sites were blocked by adding 10% skim milk solution prepared in phosphate buffered saline followed by incubation at 37°C for 1 hour. After the incubation, well was washed with phosphate buffered saline twice to remove unbound blocking agent. Onto this well containing bound myoglobin, 100 µL of pre-folded library, prepared as in section 2.1.2, was added and the plate was incubated at 37°C for 1 hour. Following the incubation, the unbound DNA was discarded and the plate was washed with binding buffer twice to remove any loosely bound DNA molecules. The bound DNA were eluted by adding 50 µL of Elution buffer (0.1 M Glycine-HCl buffer, pH 2.5) followed by neutralization with 100 µL of Neutralization buffer (0.1 M Tris base, pH 11). The neutralized sample containing DNA population was passed through a desalting

column equilibrated with Binding buffer (10 mM Tris-HCl buffer containing 150 mM NaCl & 5 mM MgCl$_2$, pH 7.4) to obtain the binder DNA population from cycle 1. The DNA was quantified using a micro-volume spectrophotometer (NanoVue plus, GE life sciences), and prepared for PCR reaction using the following reaction mixture,

Reagent	Quantity
Forward primer (10 µM)	1.25 µL
Reverse primer (10 µM)	1.25 µL
Template	1 ng
DMSO	2 µL
PCR master mix (2×)	25 µL
DNase-free water	To make up 50 µL

The reaction mixture was transferred onto the preheated heating block of thermocycler and amplified using the following protocol.

Step No.	Step	Temperature	Duration
1	Hot Start	95°C	5 minutes
2	Denaturation	95°C	30 seconds
3	Annealing	56.3°C	30 seconds
4	Extension	72°C	3 minutes
(Repeat step 2-4) × 15			
5	Hold	12°C	-infinite-

Double stranded reaction product obtained by amplification of DNA from cycle 1 was converted to single strands by using a streptavidin-gold nanoparticle probe.[237,238] For this, the amplified PCR product was heated at 95°C for 15 minutes and was immediately transferred onto ice after the completion of the incubation. Chilled streptavidin-AuNP probe was added to this heated sample at a final ratio of 1:10 and incubated for 30 minutes. The mixture was centrifuged at 12000 ×g for 30 minutes, and supernatant containing ssDNA was collected. For cycle 2 of SELEX process, two microtitre wells were coated with myoglobin as described earlier, and ssDNA obtained after separation of amplified product was added to

the coated wells at a final concentration of 100 µg/mL. DNA molecules binding to myoglobin were harvested from cycle 2 by following the procedure used for cycle 1. The DNA was quantified, amplified and converted to single strands using streptavidin-AuNP probe. The process was repeated up to 5 cycles by doubling the number of myoglobin coated wells in each cycle. The DNA binders harvested at each step showed a characteristic incremental pattern reflecting an enrichment of DNA binders after each cycle (Figure 2-2). DNA population obtained in the 5th round was analyzed by various means to ascertain its binding characteristics corresponding to myoglobin.

The affinity and subsequent binding of myoglobin with screened aptamers was assessed *via* colorimetric and chromatographic routes. For validating the binding between the biomolecular pair, a colorimetric assay was designed. The assay was based on the peroxidase-like activity of myoglobin[239–241] that was utilized as the colorimetric label to generate a colored product after reacting with TMB/H_2O_2 chromophore with an intensity directly related to the concentration of myoglobin present. For this, myoglobin-specific aptamers were coated onto a clear 96-well microtitre plate by using a DNA coating solution (Reacti-bind DNA coating solution, Thermo scientific, USA). Aptamer solution having a concentration of 250 µg/mL was diluted to 2 µg/mL in DNA coating solution and 200 µL of this mixture was added to each well of the microtitre plate. One microtitre well was prepared as a positive control by coating 100µL of myoglobin (50 µg/mL prepared in 10 mM carbonate buffer, pH 9.6). The plate was incubated at 37°C overnight to allow aptamer binding. On the subsequent day, the plate was
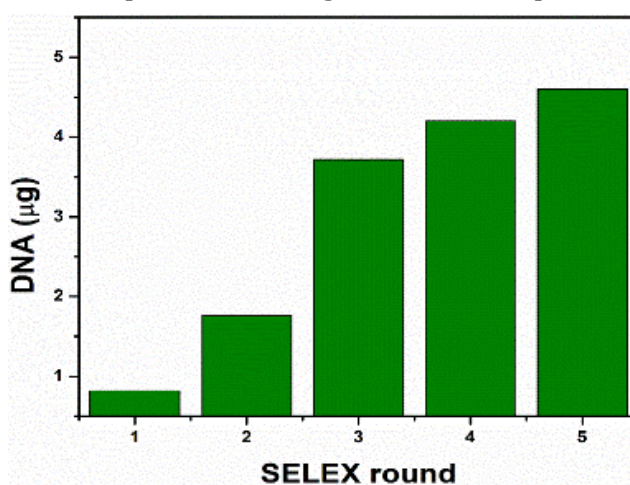
Figure 2-2: SELEX progression showing increase in the DNA harvested at subsequent SELEX rounds.

drained and washed twice with binding buffer to remove any unbound/loosely bound aptamers from the wells. To the aptamer-coated wells, different concentrations of myoglobin ranging from 0.1 μg/mL to 100 μg/mL prepared in phosphate buffer were added and incubated at 37°C for 1 hour. The plate was drained and washed with phosphate buffer to remove unbound myoglobin solution. To quantify the amount of myoglobin bound to the wells, 100 μL of TMB/H_2O_2 solution was added and incubated for 2 hours. The generation of color was measured using a BioTek Synergy H1 multimode microplate reader. The assay showed minimal generation of colored product initially due to the slow enzymatic action of the cardiac protein. However, a colored product was generated with an intensity proportional to the added concentration of myoglobin after incubating for 2 hours in both the positive control and the aptamer bound test wells. The concentration-dependent colorimetric signal confirmed specific interaction between the plate-bound aptamers and myoglobin protein (Figure 2-3).

For the chromatographic analysis of the pair, biomolecules were analyzed for their chromatographic movement by flowing on a BioRad biologic duoflow fast protein liquid chromatography system. For the analysis, a size exclusion column (BioRad SEC70) was prepped by running 2 M NaCl solution and 1 M NaOH sequentially. For this, 1 mL of 2 M NaCl was injected to the column and 1 column volume of ultrapure water (0.2 μm membrane filtered, degassed) was flowed at a flow rate of 0.5 mL/minute. After completion of 1 column volume, 1 mL of 2 M
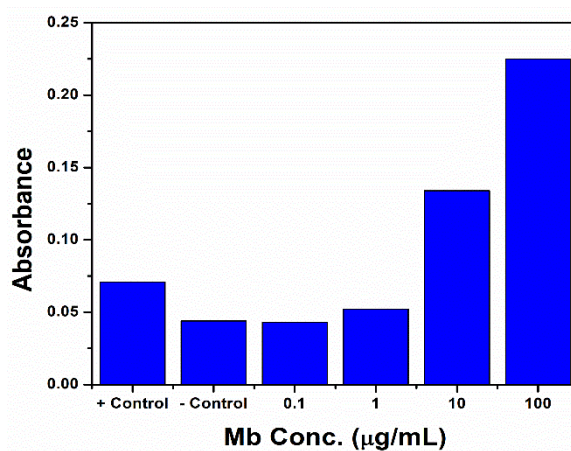
Figure 2-3: Colorimetric assay for the validation of myoglobin-Aptamer biointeraction showing an increase in the averaged absorbance relative to myoglobin concentration (n=3).
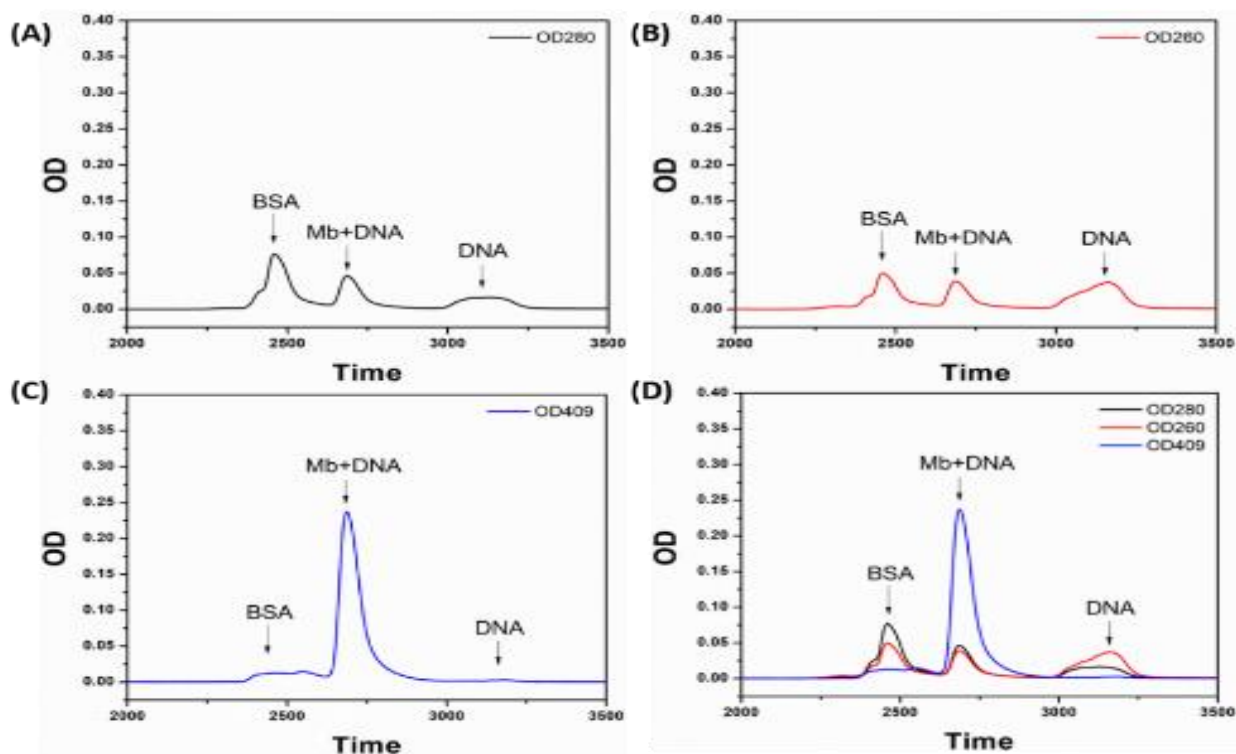
Figure 2-4: Chromatographic analysis of myoglobin:aptamer interaction. (A), (B) & (C) show the absorbance at 280 nm, 260 nm and 409 nm respectively. (D) shows combined absorbance pattern of the chromatogram.

NaCl solution was injected followed by passing 1 column volume of ultrapure water. After this, 1 mL of 1 M NaOH was passed, followed with 2 column volumes of ultrapure water, and this step was repeated again by injecting 1 mL of 1 M NaOH followed with 2 column volumes of ultrapure water. The column was washed with water until the pH returned to neutral and then equilibrated with binding buffer until the pH value stabilized to 7.2. A 1 mL binding buffer containing 200 µg myoglobin, 500 µg bovine serum albumin and 400 µg myoglobin-specific aptamer was injected to the column in continuous flow and binding buffer was flowed at a flow rate of 0.5 mL/minute for 5 column volumes. The movement of biomolecules and their elution profile was monitored by continuous absorbance measurements at 260 nm, 280 nm and 409 nm. The chromatogram showed a weight shift in the sample containing mixture of myoglobin and its aptamer from 16.7 kDa of myoglobin to ~41 kDa suggesting an interaction between the pair. While the peak showed a characteristic Soret absorption confirming the presence of myoglobin, the OD_{260}/OD_{280} ratio showed a higher value (0.83) compared to normal ratio of 0.64 thus confirming the presence of DNA in the elute (Figure 2-4).

To deduce the sequences of the binding population, it was cloned and subsequently sequenced using automated Sanger termination method. For this, DNA pool from the 5th round was amplified using unlabeled primers, purified and cloned in pTZ57R/T cloning vector using InsTAclone cloning kit (Thermo Scientific, USA). The vector was transformed in *E. coli* JM107 cloning host using manufacturer's protocol, and plated on an ampicillin-containing LB agar plate. The recombinants were selected by classic blue-white selection method and individual colonies were picked to grow in LB broth mediums unto an OD of 1. The grown cultures were used to extract plasmids that were sequences were deduced by Sanger sequencing method. The obtained sequences were used to predict their possible secondary structures using mFold webserver.[242] The best sequences was selected using their thermodynamic parameters (T_m above 50°C) and GC content (above 50%) which ensures high stability and binding capabilities in wide microenvironment ranges. The Table 2-1 shows calculated thermodynamic parameters of different possible secondary structures of the deduced sequence. The possible G-quadruplex forming region in the sequence of myoglobin-specific aptamer was mapped using QGRS mapper,[243] which revealed a possible 29 bases long region between 44th and 72nd base. The mapped G-quadruplex region aligned with structure 3 formed considering the Guanine bases found in the loops (Figure 2-5).

Struc.No.	ΔG (kcal/mol)	ΔH (kcal/mol)	ΔS (cal/(K·mol))	T_m
1	-4.58	-76.10	-230.5	56.8°C
2	-4.35	-84.60	-258.7	53.8°C
3	-4.13	-92.70	-285.5	51.4°C
4	-4.08	-95.40	-294.4	50.8°C
5	-3.83	-73.20	-223.6	54.1°C
6	-3.68	-83.40	-257	51.3°C

Table 2-1: Thermodynamic parameters of 2D structures of myoglobin-specific aptamer calculated using mFold.

Position	44
Length	29
QGRS	GGCACGACAGGTTTCCCGACTGGACACGG
G-score	15
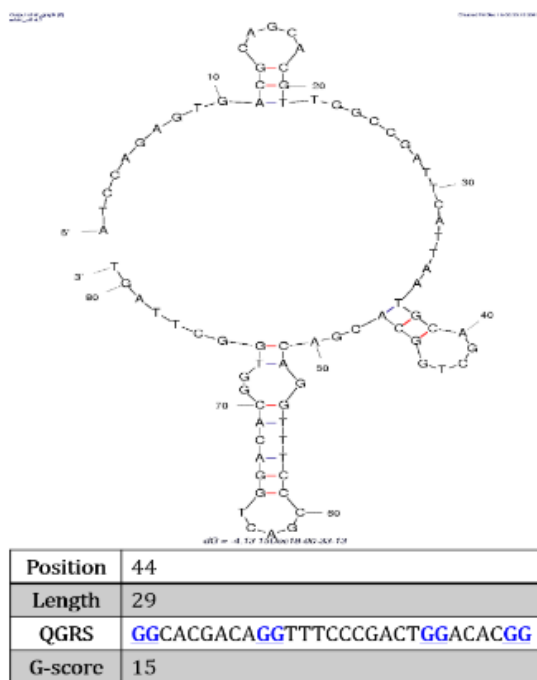
Figure 2-5: Probable 2D structure of the Mb-specific aptamer as deduced from mFold. Bottom table shows probable G-quadruplex forming region in the structure.

2.3. BLI-SELEX method for the generation of aptamers

Aptamers specific to B-type natriuretic peptide (BNP) were screened using a one-pot reaction setup involving biolayer interferometry (BLI). The sensor surface was used as stationary matrix to house BNP molecules. For this, BNP molecules were biotinylated by incubating 100 μg of BNP with NHS-stabilized active ester of biotin for 1 hour. The reaction was purified by spinning at 5000 ×g in a centrifuge-based desalting column that separated the conjugate from unreacted linker molecules. The resulting biotin-BNP conjugate was transferred to a microtitre plate well and Super Streptavidin™ sensor (SSA sensor, Pall life sciences) was dipped in the well for 5 minutes to transfer the conjugate onto the sensor. The sensor achieved 1 nm binding threshold required for biomolecular interactions after 80 seconds, and the step was terminated to prevent any crowding on the sensor surface due to prolonged incubation. The sensor was then washed to remove any loosely bound conjugate from the sensor by dipping it in a well containing phosphate buffer (10 mM, pH 7.2). This BNP-loaded sensor was then equilibrated in Binding buffer (10 mM Tris-HCl buffer containing 150 mM NaCl, 5 mM $MgCl_2$, pH 7.2), and exposed with a pre-folded DNA library by dipping the sensor in the well containing 100 μL of DNA library for 100 seconds. The

60

sensogram showed an increase in signal, which was an indicative of biomolecular interactions between the sensor-bound peptide and probable aptamer candidates present in the combinatorial DNA library. The binding population was harvested by disrupting the interactions between the DNA molecules and sensor bound peptide. For this, the sensor was dipped in wells containing NaCl solutions with ionic strength ranging from 0.01 M to 1.0 M (Figure 2-6). The incremental dissociation strength was supposed to release the aptamers based on their binding strength, with the weakest detaching at lower ionic solution and stronger binders releasing at higher ionic strengths. The hypothesis was confirmed as shown in the dropping pattern in binding intensity as the sensor was dipped in the dissociation solutions. While the drop revealed a release of DNA in the initial step, the intensity was higher than the baseline suggesting that the sensor retained some population of binders. The DNA were released in the later solutions and the sensor returned to the baseline in 0.2 M salt solution suggesting a complete removal of DNA binders from the sensor (Figure 2-7). The increase in the later solutions was due to the change in refractive index of the high strength salt solutions. The sensor was regenerated by dipping it in a 3.0 M NaCl solution. The procedure was repeated for another 4 cycles of gathering the DNA binders from library and releasing in the dissociation solutions. The step was performed to
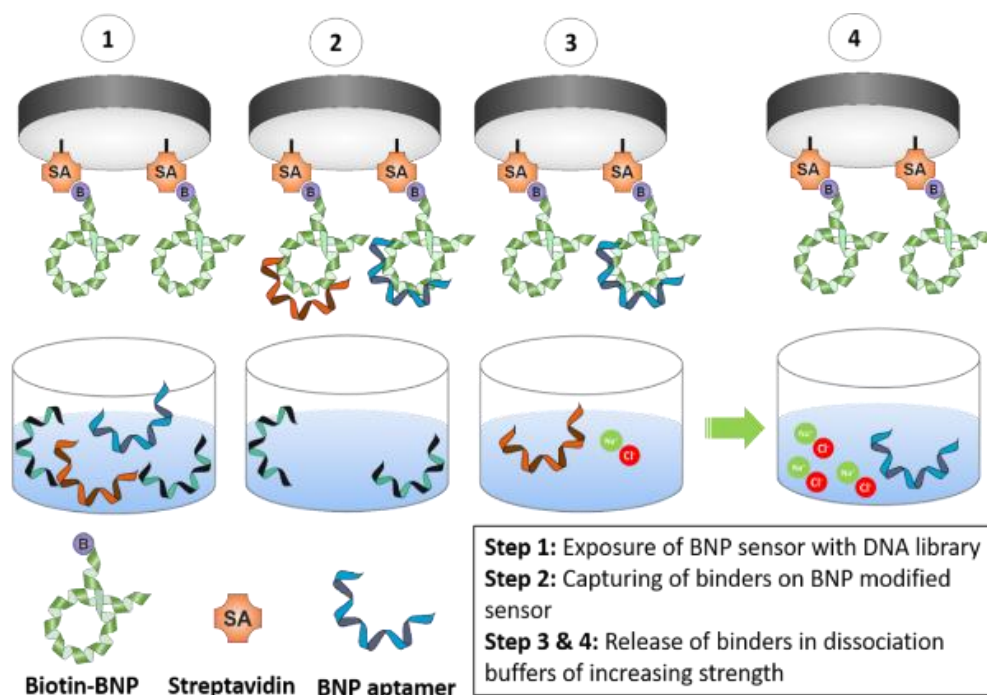
Figure 2-6: Schematic showing the steps of BLI-SELEX involved in the screening of BNP-specific aptamers.

61

ensure the enrichment of DNA species specific to BNP in the elutes. The signal response measured in the *library exposure* step decreased in intensity with each cycle due to depletion of binding candidates gathered from the source library with each proceeding cycle (Figure 2-7C). From the sensogram, it was evident that the strongest binders were released in the 0.2 M solution. Thus, the DNA population present in the 0.2 M salt solution was selected for proceeding experiments. The eluted DNA present in the dissociation solution was amplified *via* a polymerase chain reaction, and single strands were generated from the double stranded PCR product using the streptavidin-gold nanoparticle bioprobe.

BNP-specific aptamers were characterized using biolayer interferometry, and a fluorescence-based microtitre plate assay. For the biolayer interferometry, BNP peptide was loaded on the sensor surface and was allowed to interact with different concentrations of amplified aptamer pool eluted in 0.2 M NaCl. For this, five super streptavidin sensors were dipped parallel in 100 μg/mL biotinylated BNP molecules taken in a microtitre well. The incubation was set on a threshold value of 1 nm response units in the sensogram. After the incubation, the sensor
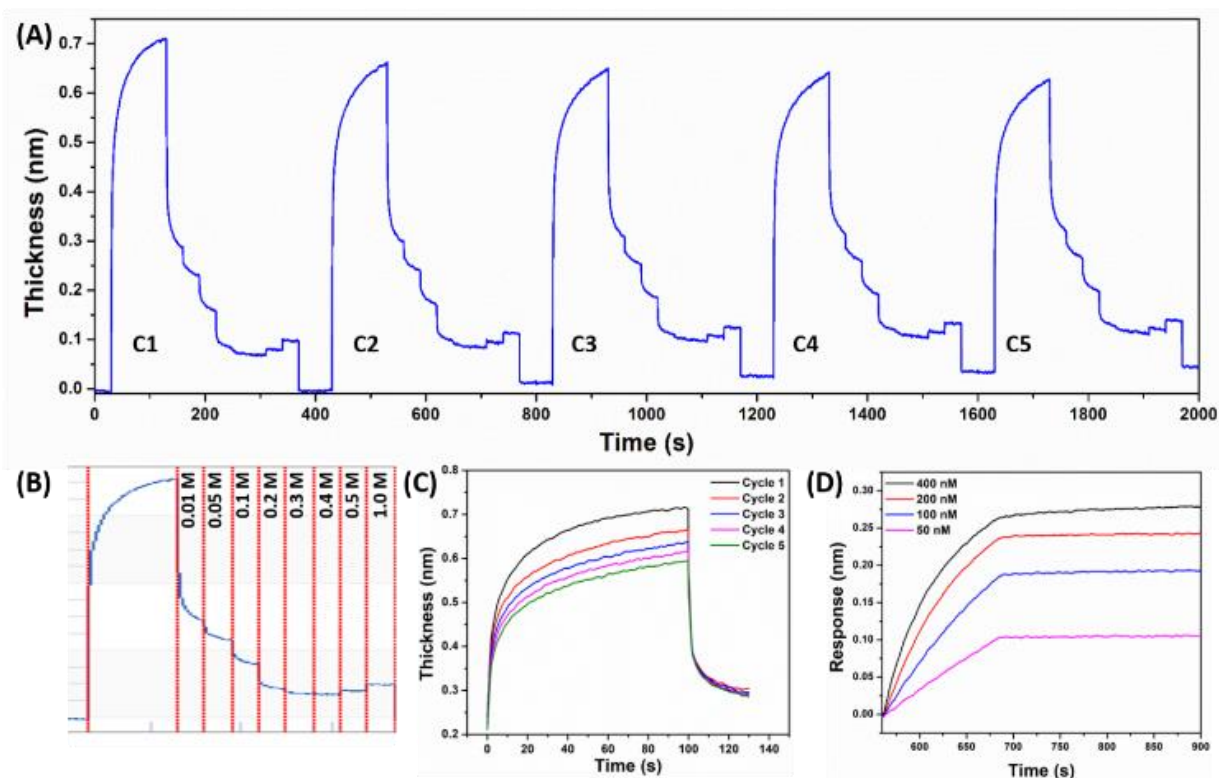
Figure 2-7: (A) Biolayer interferometry showing the changes in bio-layer thickness during the progression of one-pot BLI-SELEX. (B) Zoomed-in view of a single cycle to highlight different steps involved. (C) Overlay of association response from consecutive cycles showing drop in binder populations. (D) Affinity confirmation of final selected aptamers using biolayer interferometry.
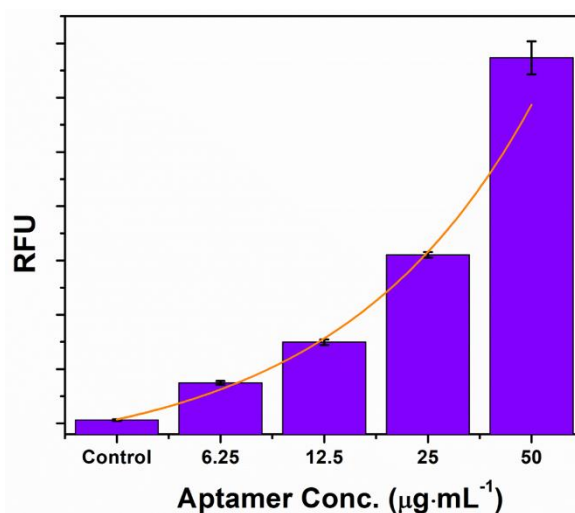
Figure 2-8: Fluorescent plate binding assay based validation of biointeraction between BNP and its aptamer.

was dipped in phosphate buffer (10 mM, pH 7.2) to remove any unbound peptide molecules and then equilibrated in binding buffer. The sensors were dipped in aptamer concentrations (0 nM (Control), 50 nM, 100 nM, 200 nM, and 400 nM). The response was recorded as change in thickness of the biolayer on the sensor surface and analyzed using ForteBio Analysis 9.0 software. As the sensors were dipped in the aptamer solutions, the recorded response showed an increasing pattern respective to the aptamer concentrations (Figure 2-7D). However, when the sensors were dipped in the binding buffer for dissociation, the response curve showed insignificant change which can be attributed to high strength binding between the biological pair.

For the microtitre plate-binding assay, BNP-specific aptamers were amplified using forward primers modified at their 5' ends with a green fluorophore TET (Tetrachlorofluorescein), and single strands were generated using streptavidin-AuNPs bioprobe. A black 96-well microtitre plate was coated with BNP molecules by adding 100 μL of 5 μg/mL BNP solution prepared in carbonate buffer (10 mM, pH 9.6), and incubated at 4°C overnight. On the subsequent day, the wells were washed with phosphate buffer (10 mM, pH 7.2) twice to remove any loosely bound BNP molecules. Different aptamer concentrations prepared in binding buffer were added to the wells as 0 μg/mL (negative control), 6.25 μg/mL, 12.5 μg/mL, 25 μg/mL, 50 μg/mL, and 100 μg/mL. The microtitre plate was incubated at 37°C for 6 hours to achieve binding between free aptamers and BNP molecules bound onto the surface of the wells. After the

incubation, the wells were washed with binding buffer twice, and 100 μL phosphate buffer was added to the wells. The fluorescence of the wells was recorded using a BioTek synergy H1 multimode microtitre plate reader. The fluorescence signal showed an incremental pattern respective to the concentrations of fluorophore-labelled aptamer confirming a specific interaction between the peptide and its screened aptamer (Figure 2-8).

The aptamers were sequenced using a Sanger chain termination method to elucidate the sequences and structural properties of the aptamers. The secondary structures of the sequences were deduced by running the sequences through mFold webserver.[242] Further, the sequences were screened for the presence of G-quadruplex forming regions by using QGRS online tool.[243] The mapping tool showed the presence of probable G-quadruplex forming regions in the aptamers itself, which was used to generate the probable tertiary structure of the aptamer shown in the Figure 2-9.

ATCCAGAGTGACGCAGCAGTGTCGAGTGGGAAGAGGTGGGGACGGCCGGTGGGGGTGGGGTGGTGGACACGGTGGCTTAGT

Position	Length	QGRS	G-score
30	13	GGAAGAGGTGGGG	17
45	23	GGCCGGTGGGGGTGGGGTGGTGG	23

Predicted 2D structure

Parameter	Structure 1
ΔG	-4.90 kcal/mol
ΔH	-111.50 kcal/mol
ΔS	-343.7 cal/(K·mol)
T_m	51.2 °C
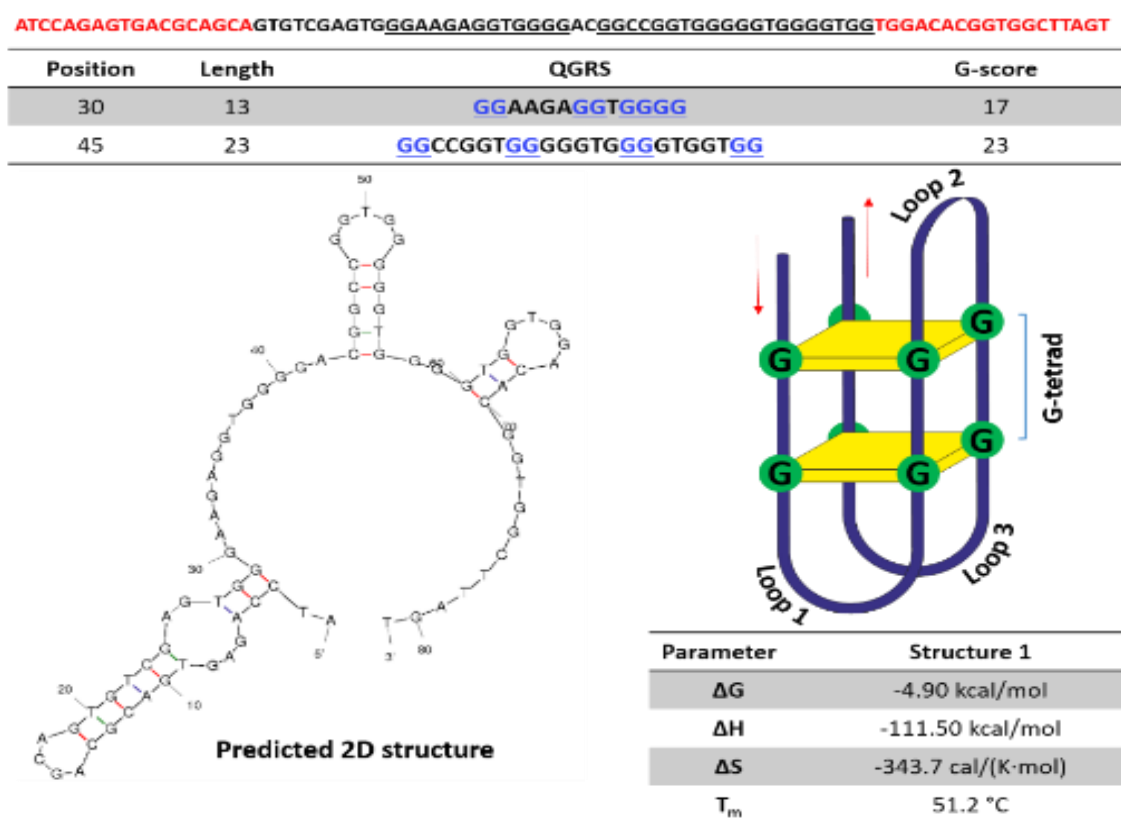
Figure 2-9: Structure prediction of BNP-specific aptamer. Top table shows the QGRS mapping of the sequence. Bottom left shows the predicted 2D structure. Right side shows the probable G-quadruplex forming region and the thermodynamic parameters.

For Troponin I aptamer, the stationary matrix for SELEX method is prepared, a BLI sensor was modified with troponin I (TnI) protein. For this, TnI molecules were covalently linked onto the surface of the AR2G sensor (Amine Reacting 2nd Generation sensors, Pall life sciences, USA) through carbodiimide-based conjugation method. Carbodiimide-based conjugation uses a carbodiimide linker that specifically attacks protonated carboxyl groups to generate an intermediate ester, which can react with a primary amine group to form an amide bind. For this, fresh dried AR2G sensor were regenerated by dipping in 200 μL water for 15 minutes. The sensor was dipped in a solution containing 400 mM freshly prepared solution of EDC (prepared in 50 mM sodium acetate buffer, pH 5.2) and 100 mM NHS. The sensor was incubated for 200 seconds during which EDC reacted with the carboxyl group present in the sensor surface. The sensogram showed an increase in signal during the activation step, which reflects the increase in mass due to the generation of intermediate species in the sensor surface. After the incubation, the sensor was dipped in 100 μL water briefly to remove any unbound molecules on its surface. The sensor was then moved to a well containing troponin I solution (2 μg/mL) and incubated for 10 minutes. The binding of troponin molecules on the surface was indicated by an increase in the signal response in the sensogram. After the binding, the sensor was dipped in 1M ethanolamine for 300 seconds to quench any unreacted intermediates present on the sensor surface. The prepped sensor was kept hydrated by dipping in a well containing water to prevent any damage to the bound protein. For the SELEX procedure, the TnI-bound sensor was equilibrated by dipping in binding buffer for 120 seconds, and exposed to 100 μL of 10 μM pre-folded library. The sensor was incubated with the library until the sensogram showed a stabilization of the signal response, implying the stage where all the present binders were bound to the sensor, or the sensor surface was saturated with the bound DNA molecules. The sensor was dipped in binding buffer for 45 seconds to remove any non-specifically bound molecules, and then proceeded with the incremental dissociation step. For this, the sensor was incubated for 45 seconds in NaCl solutions with concentrations ranging from 0.01 M to 2.0 M. The salt stripping step revealed a gradual decrease in the intensity originating from the release of DNA molecules bound on the sensor-bound TnI molecules (Figure 2-10A). The sensor was dipped
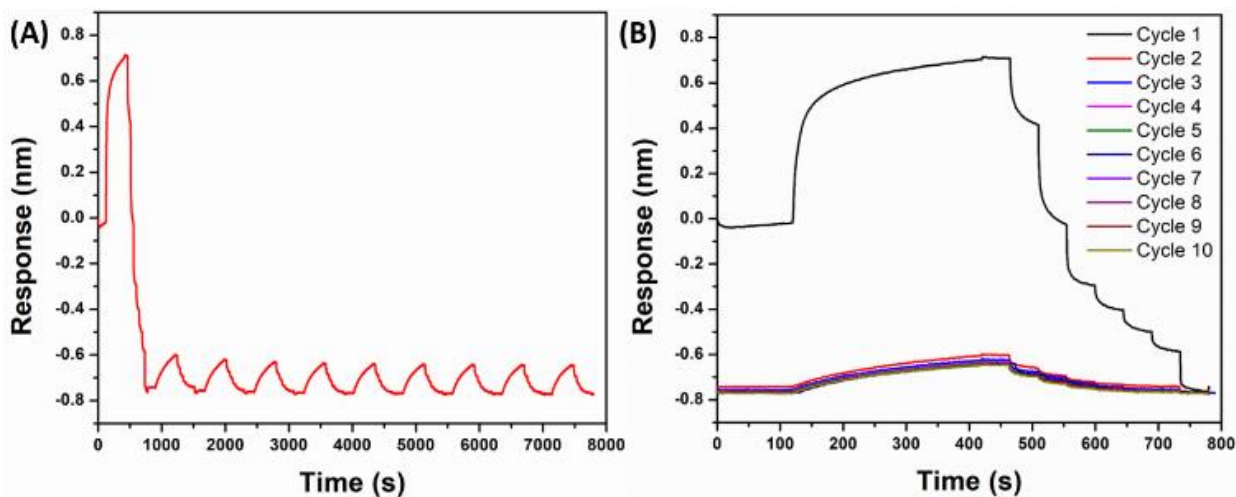
Figure 2-10: (A) Biolayer interferometry showing the change in signal response during the SELEX progression. (B) Overlaid signal responses showing the decrease in response from cycle 1-10.

in binding buffer for equilibration, and exposed to the library by dipping the sensor in the well containing folded library. However, the sensogram displayed no significant change in the signal response suggesting that major binding population was extracted in the first cycle. The process were repeated for 9 more cycles, however the signal intensity in the binder selection step did not show a downward shift in the subsequent SELEX rounds (Figure 2-10B). The DNA molecules present in the salt solutions were recovered and quantified by using a micro-volume spectrophotometer (NanoVue spectrophotometer, GE life sciences, USA). For the selection of binders with best affinity towards TnI, the binding population was subjected to a thorough affinity investigation using BLI. For this, the DNA recovered in 0.3 M, 0.4 M and 0.5 M dissociation solutions were amplified using a polymerase chain reaction and ssDNA were generated using a streptavidin-AuNP bioprobe. Troponin I molecules were loaded onto an AR2G sensor as described previously. Amplified DNA from 0.3 M elute was diluted in a concentration range of 5 µg/mL to 40 µg/mL, and TnI-loaded sensor was dipped in the dilutions of DNA for 240 seconds following with a dissociation step for 120 seconds. The process was repeated for the DNA recovered from 0.4 M & 0.5 M, and response were analyzed. The comparison of the binding revealed that the binders recovered in 0.4 M dissociation solution had the highest response for all the DNA concentrations, followed by 0.3 M and 0.5 M dissociation solutions (Figure 2-11).
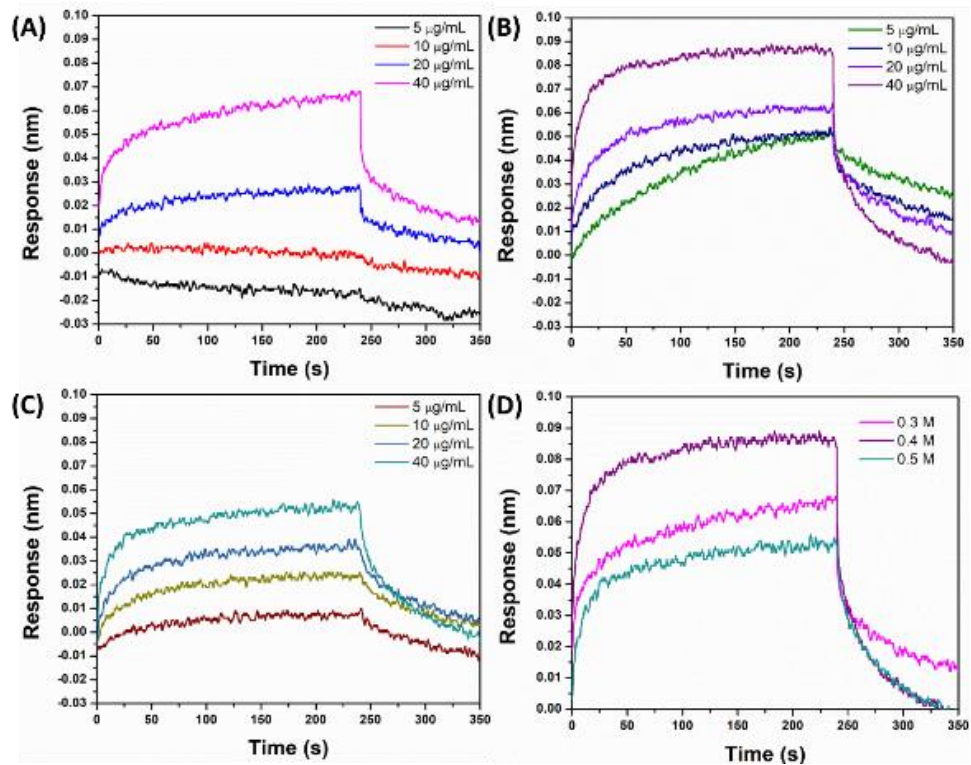
Figure 2-11: Analysis of affinity of TnI-binding DNA sequences collected from (A) 0.3 M, (B) 0.4 M, and (C) 0.5 M NaCl dissociation solutions. (D) shows the overlaid sensogram for 40 µg/mL DNA solutions depicting the difference between bindings.

The trend was also repeated in the dissociation constants of the bio-interactions, where DNA from 0.4 M had a K_d value of 0.3 µM whereas that of 0.3 M & 0.5 M was found to be 0.6 µM & 1.7 µM. The DNA recovered in 0.4 M dissociation buffer was labeled *TnI-specific aptamer*, and used for further experiments. The sequence of the TnI-specific aptamer was resolved by cloning the aptamers in a pTZ57R/T cloning plasmid and sequencing using Sanger chain termination method. The deduced sequence was run through mFold online DNA folding tool to find the probable 2D structures.[242] It showed a diversity of 2D structures with a variety of

| ΔG -3.85 kcal/mol | ΔG -3.3 kcal/mol | ΔG -3.12 kcal/mol | ΔG -2.91 kcal/mol |
| T_m 47.3 °C | T_m 44.5 °C | T_m 43.5 °C | T_m 45.4 °C |
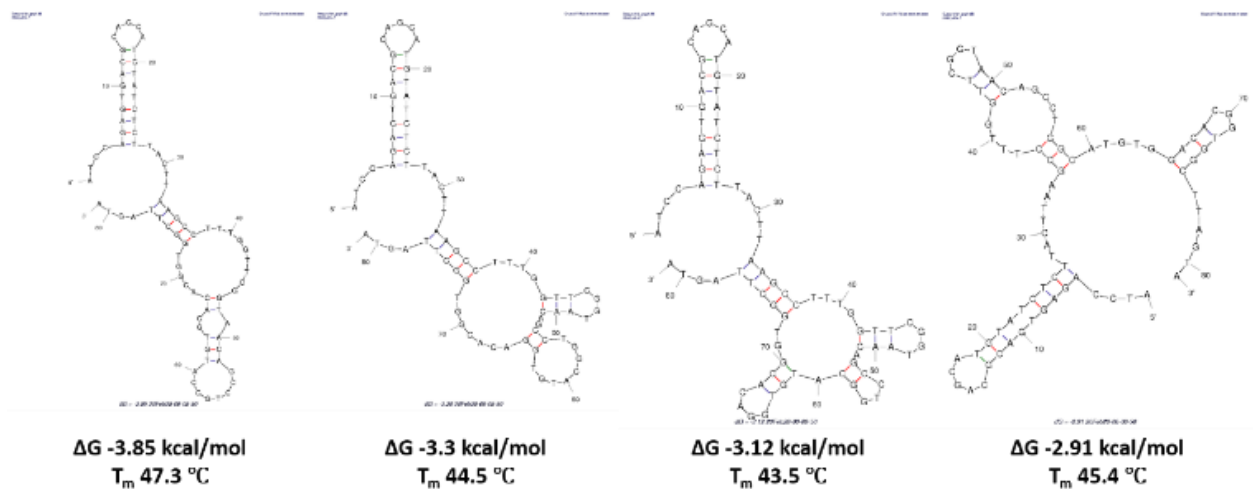
Figure 2-12: Selected probable aptamer secondary structures interpreted using mFold webserver.

loops suggesting presence of several domain-rich regions in the aptamer (Figure 2-12). The structural complexity of the aptamer was also revealed in the QGRS mapping for checking presence of G-quadruplex forming regions in the sequence.[243] The mapping showed presence of six such possible regions mostly having a high G-score (Table 2-2). Furthermore, the region between 46th and 73rd base is noteworthy for having 4 possible G-quadruplex forming regions, suggesting the presence of the binding pocket focused in or around this region of the aptamer.

Position	Length	QGRS	G-Score
41	25	GGTTCGGTAACAGCCTGGCATGTGG	15
46	26	GGTAACAGCCTGGCATGTGGACACGG	16
46	29	GGTAACAGCCTGGCATGTGGACACGGTGG	17
46	29	GGTAACAGCCTGGCATGTGGACACGGTGG	11
46	29	GGTAACAGCCTGGCATGTGGACACGGTGG	6
57	18	GGCATGTGGACACGGTGG	17

Table 2-2: Table showing the QGRS mapping of the aptamer sequence to locate possible G-quadruplex forming regions.

2.4. Conclusion

The SELEX methods for the generation of aptamers were improved by the introduction of different stationary matrices. The introduction of polystyrene surface in form of a microtitre plate provided a route of efficient control over the reaction parameters, as reflected in the reduction in cycle number. The method was employed for the generation of specific aptamers against cardiac biomarker myoglobin. Further, by utilizing Biolayer interferometry, the SELEX process was drastically changed to generate a method able to screen specific aptamers in a single cycle. The process enabled control over the separation of screened binders based on their inherent binding strengths. The method was utilized in the generation of specific aptamers against cardiac markers troponin I and BNP.

CHAPTER 3

Quantum dots based point-of-care platform for myoglobin quantification

Among the different transducing approaches, optical transducers possess the unmatched ability to be converted in the simplest point-of-care devices. Further, colorimetric, fluorescence and chemiluminescence-based sensors are sought-after, as the signal in these transducers is the change in the intensity of light in the visible range. This property supports the production of devices that can be used with the naked eyes without requiring any sophisticated instrumentation. This ability of optical sensors was first realized in 1950s with the development of paper-based optical sensor for detecting glucose in urine samples.[244,245] Recently, the incorporation and further improvement in the cameras available in smartphones have opened up an avenue for the development of handheld sensors where the smartphone acts as the detector as well as analyzer.[245,246] For the development of an optical detection platform for the diagnosis of myoglobin, fluorescent quantum dots were synthesized. Among the optical transducers, fluorescence-based platforms are sensitive enough to be perturbed by small changes in the analyte concentrations, while still possessing the ease of usage due to the presence of a visual signal. As fluorescent probes, carbon-based quantum dots selected owing to a plethora of benefits like their high photoluminescence alike semiconductor quantum dots, biocompatibility, relative ease of synthesis and surface modification, higher aqueous solubility and chemical & photo-stability.[247–249] Carbon quantum dots were synthesized from different starting materials as to assess the role of chemical composition of source material on the fluorescent properties of the nanomaterial. Finally, the designed fluorescent platform was developed into a handheld Point-of-Care device by amalgamation of the fluorescence-based system with the portability of a smartphone.

Objectives
- Synthesis of carbon-based quantum dots as fluorescent probes

- Investigation of the role of elemental composition on the fluorescence properties of the quantum dots
- Development of fluorescence based assays for the detection of cardiac biomarker
- Development and validation of the developed fluorescence assay on a smartphone based readout module

3.1. Carbon quantum dots as fluorescent probes for myoglobin estimation

3.1.1. Synthesis of carbon quantum dots

Quantum dots were synthesized *via* thermal carbonization, which is a method of bottom-up synthesis through carbonization of relatively simpler organic sources into carbon dots at temperatures around/above 200°C.[250–253] We synthesized carbon quantum dots from L-glutamic acid used as the starting material and carbon source. For this, 0.75 g of L-glutamic acid taken in 10 mL of 45% glycerol containing 5 M HNO_3 was heated at 300°C for 6 hours. Heat treatment of the organic substance changed the color of the solution from clear to dark brown, which suggested successful carbonization of the starting material into carbon quantum dots. After the completion of reaction, the vessel was cooled and 10 mL of ultrapure water was added to the reaction mixture, followed by stirring for 30 minutes. After the stirring, the material was centrifuged at 40000 ×g for 1 hour and the resulting pellet was re-suspended in 10 mL water to obtain an aqueous suspension of the carbon quantum dots.

3.1.2. Characterization of carbon quantum dots

The quantum dots showed a bright blue fluorescence under UV light, suggesting the emission band of quantum dots to be lying in 400-500 nm range with a possible excitation maximum in near-UV range. The prepared carbon quantum dots were analyzed for their fluorescent profile on a BioTek Synergy H1 multimode microplate reader. A 10% aqueous dilution of prepared quantum dots was measured by exciting at 350 nm and recording the emission spectrum, which

generated a strong emission in the blue range with the peak maximum at 424 nm. Lower dilutions of the quantum dots generated peak intensities beyond the detection range of plate reader and thus 10% or higher dilutions were used for the experiments involving measurements with the multimode plate reader. The emission peak recorded at 424 nm was used to find the excitation maximum of the QDs by measuring the quantum dots under excitation mode. The excitation wavelength of the nanomaterial was found to be 346 nm and was used for all the following experiments involving fluorescence measurements. Transmission electron microscopy of the quantum dots was performed by drop-casting a highly diluted sample of the quantum dots (1%) on a 200-mesh Cu TEM grid to avoid aggregation on the grid, and visualizing under a JEOL 2100 Transmission electron microscope operating at 200 kV. The selected area diffraction (SAED) pattern and energy-dispersive X-ray (EDX) spectroscopy of the mounted sample was recorded to analyze its crystal structure and elemental composition. The size of carbon quantum dots was measured from the transmission electron micrographs, which showed particles with an average size of 3 ± 0.6 nm diametrically. SAED pattern showed several diffraction rings suggesting the quantum dots to possess a polycrystalline character.

3.1.3. Development of fluorescence-based assay

Fluorescence-based diagnostic assay for the detection of myoglobin was developed to generate a platform with ability to quantify the concentration of a cardiac biomarker, myoglobin in solutions. Carbon quantum dots prepared from glutamic acid as carbon source were conjugated with myoglobin protein to generate a fluorescent nanoprobe. For this, prepared carbon quantum dots were centrifuged at 40000 ×g for 1 hour and the supernatant was discarded. The pellet containing quantum dots was re-suspended in 10 mL of 5 wt% solution of nafion, and incubated overnight at 4°C to allow surface functionalization of quantum dots with nafion. The specific concentration of nafion was chosen following the study of Wang et al reporting highest wettability and solubility of carbonaceous materials in 5 wt% nafion solution.[254] Nafion presented a non-selective method of linkage to further bind myoglobin molecules onto carbon quantum dots in a
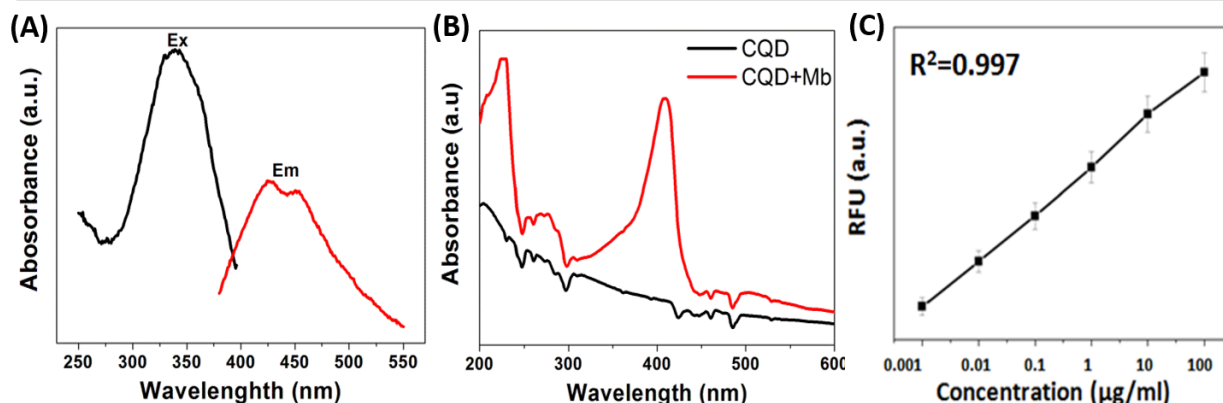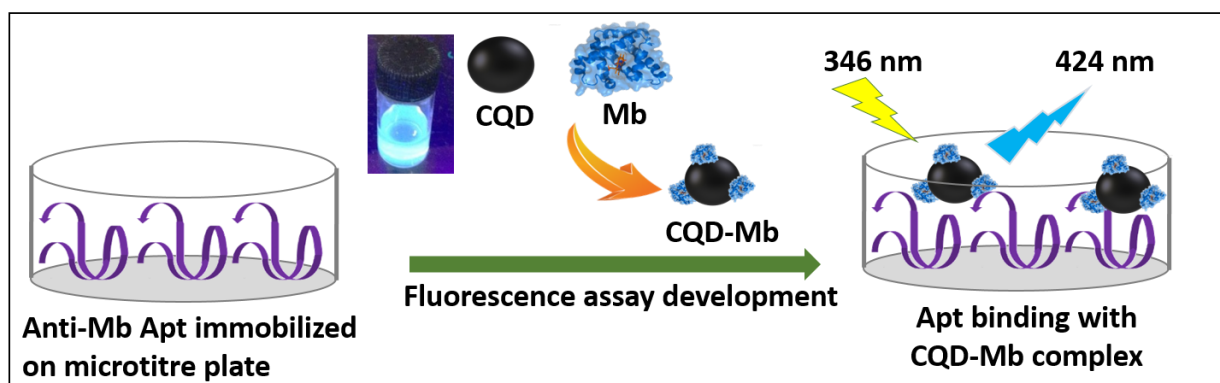
Figure 3-1: Graphic schematic showing the stepwise working of the designed fluorescent assay (Above). (A) Absorbance and fluorescence spectrum of the carbon quantum dots. (B) Comparative absorbance spectra of CQDs before and after the modification of myoglobin. (C) Linear fitting of the peak intensities of carbon quantum dots in response to added myoglobin concentration.

controlled manner. The coating of nafion on the quantum dots was confirmed from the presence of elemental signature of fluorine in the EDX spectrum of the nafion-coated carbon quantum dots. The resulting solution containing CQDs coated with nafion was further used to conjugate with myoglobin by incubating 1 mL of nafion-CQD conjugate with 1 mL of myoglobin solution (4 mg/mL, prepared in 100 mM phosphate buffer, pH 7.2) for 2 hours. The concentration of myoglobin was taken in excess to ensure sufficient amount for binding with nafion-coated quantum dots. After the incubation, the mixture was added in a dialysis bag (3.5 kDa cut-off), and dialyzed against ultrapure water at 4°C for 24 hours. The conjugate was characterized by optical absorption spectroscopy, and fluorescence spectroscopy (Figure 3-1A). The binding of myoglobin molecules onto the carbon quantum dots was confirmed from the presence of characteristic absorptions at 230 nm and 280 nm originating from peptide bond & aromatic amino acids respectively. Furthermore, the conjugated was checked for the presence of Soret peak, a characteristic absorption of heme containing proteins around 400 nm due to the π-π* electronic transitions in the porphyrin ring.[255,256] The presence of an

absorption peak at 409 nm corresponding to the Soret peak in the absorbance spectrum of the Mb-CQD conjugate specifically validated the presence of myoglobin in the conjugate (Figure 3-1B).

For developing the assay, anti-myoglobin aptamer was diluted in DNA binding solution (Reactibind DNA coating solution, Thermo Fisher Scientific) to a concentration of 2 µg/mL and was used to functionalize a 96-well black microtitre plate using the manufacturer's protocol for DNA binding.[257] The aptamer solution was added to the microtitre plate (200 µL/well), and incubated overnight at 4°C to achieve uniform coating of aptamers on the well surface. The microtitre plate was washed with ultrapure water twice to remove unbound/loosely bound aptamer molecules. The Mb-CQD nanoprobe generated above was added to the aptamer-coated microtitre wells in a concentration range of 1 ng/mL to 100 µg/mL estimated in respect to myoglobin. The plate was incubated at 25°C for 2 hours, and rinsed twice with ultrapure water to remove unbound moieties. 100 µL of ultrapure water was added to each well of microtitre plate and the fluorescence spectrum was recorded on a Biotek synergy H1 multimode microtitre plate reader in the range of 380 – 450 nm. The fluorescence spectra showed a linear increase in the fluorescence at 424 nm respective to the concentration of myoglobin-CQD conjugate with a lower limit of detection of 1 ng/mL. The fitting of emission maximum of CQDs showed a linear relation with the concentration of myoglobin added with regression of 0.997 and presents an efficient method of myoglobin estimation optically (Figure 3-1C).

3.2. Nitrogen, sulfur co-doped carbon quantum dots based direct quenching assay

3.2.1. Synthesis of NS-co-doped carbon quantum dots

Nanomaterials are often doped by incorporating different elements in their structure to enhance their properties. Synthesis of doped nanomaterials is usually done by performing the synthesis process in presence of defined concentrations of particular dopant. For the synthesis of doped carbon quantum dots, a protein source was chosen as the starting material as their elemental composition leads to incorporation of mainly nitrogen as dopant in the final structure of quantum

dots. To create carbon quantum dots with both nitrogen and sulfur as dopants, a sulfur-rich protein, Keratin was used. Nails and chicken feathers were used as different sources of Keratin containing starting material differing in the keratin amounts (80-90% in nails versus >90% in feathers) and the type of keratin (α-keratin in nails versus β-keratin in feathers).[258–260] The keratin sources were carbonized in the presence of a strong acid along with vigorous stirring to maintain high level of homogenization and to prevent generation of large particles. For the synthesis, 50 mg of nails were washed with acetone and ethanol respectively, and air-dried. These were then added to 25 mL of H_2SO_4 and heated at 180°C for 2 hours with vigorous stirring. After the completion of reaction, the solution was cooled to room temperature and used for further characterizations. Alternatively, chicken feathers were used as the starting material for the synthesis of NS-co-doped carbon quantum dots due to their higher sulfur content than nails. Chicken feathers were collected from the local market and barb was removed from the rachis of feathers. The barb of feathers was soaked in absolute ethanol for 1 hour to decontaminate the feathers and dried at 40°C in an oven for 30 minutes. 100 mg of barb was added in 50 mL H_2SO_4, and heated at 180°C for 4 hours along with vigorous stirring. After the incubation, the reaction was cooled to room temperature, followed with various characterizations to assess the synthesis of quantum dots. The color of the reaction changed from pale to dark brown suggesting the completion of carbonization and formation of quantum dots.

3.2.2. Characterization of NS-co-doped carbon quantum dots

i. Fluorescence spectroscopic analysis

To check the fluorescence properties of the nanomaterial, an Excitation-Emission matrix was generated (Figure 3-2). The matrix is a 3D plot involving extensive profiling of a fluorophore in which the material is excited at a range of wavelengths and emission is monitored. For this, 100 µL of 10% aqueous dilution of the quantum dots was added to a 96-well microtitre plate and its fluorescence spectra was read by exciting the material at different wavelengths ranging from 290 nm to 470 nm at a pitch of 10 nm. The fluorescence intensity at each excitation
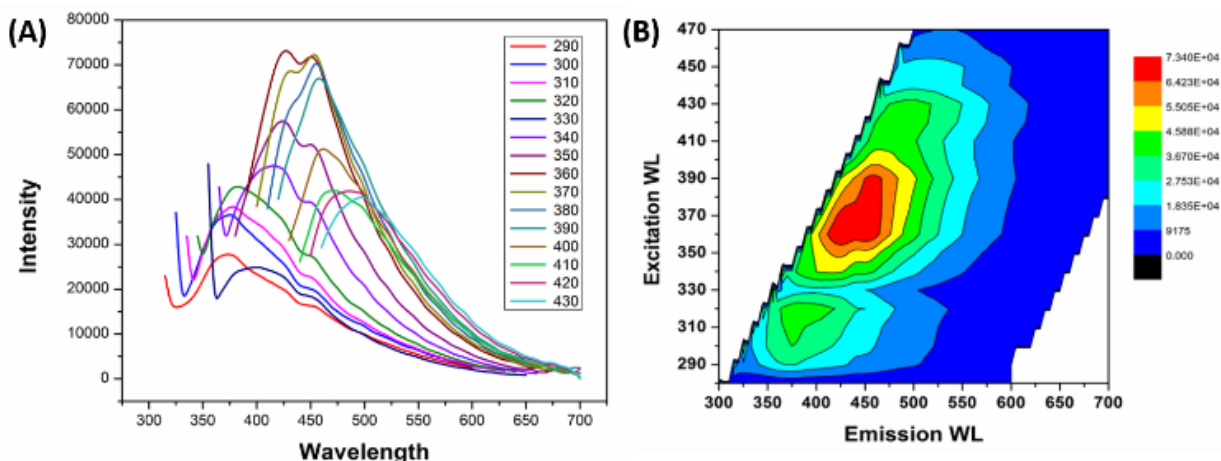
Figure 3-2: (A) Excitation-dependent fluorescence emission spectra of the quantum dots. (B) Excitation-Emission matrix (EEM) showing the centralized region with highest fluorescent intensity.

wavelength was plotted as the z-axis while taking excitation and emission wavelengths at xy-axes. The EEM of these quantum dots showed a fluorescence patch focused between 440 - 450 nm for NS-CQDs generated from nails. The EEM of quantum dots generated from feathers showed a comparatively compact profile suggesting a relatively better conversion of raw material into homogenous quantum dots. This directly reflected in the fluorescence of the quantum dots where the QDs generated from feathers showed higher fluorescence intensity than those generated from nails. Absorption spectrum of the quantum dots was recorded using Shimadzu UV2600 spectrophotometer between a range of 280 nm to 650 nm. Optical absorption spectrum of the carbon dots proved less informative as it showed a typical scattering pattern characteristic of quantum dots (Figure 3-3A).

ii. Elemental analysis

For the elemental analysis of the quantum dots, the 5 mL of quantum dots solution was diluted in water and dehydrated in a rotary vacuum concentrator (CVE-3000, Eyela). The resulting solid sample was collected and its elemental constituents were estimated using a Thermo scientific FLASH2000 CHNS elemental analyzer, which revealed presence of both nitrogen and sulfur in the quantum dots (Figure 3-3B).

iii. Raman spectroscopic analysis

For the Raman analysis, quantum dots solution was dropped onto a clean Si substrate and dried at 60°C in a hot-air oven. The sample was analyzed under a Witec alpha300R spectrometer operating with a 532 nm laser and showed presence of Raman signatures at 1385 cm^{-1} and 1570 cm^{-1} referring to D and G bands of the carbonaceous material respectively (Figure 3-3C). The bands represent the structural disorder and the extent of graphitic nature of the nanomaterial respectively.

iv. Electron microscopic analysis

Transmission electron microscope was used to quantify the size of the quantum dots by dropping a 1% aqueous dilution of the nanomaterial onto a Cu TEM grid to avoid aggregation, and visualizing under a JEOL JSM2100
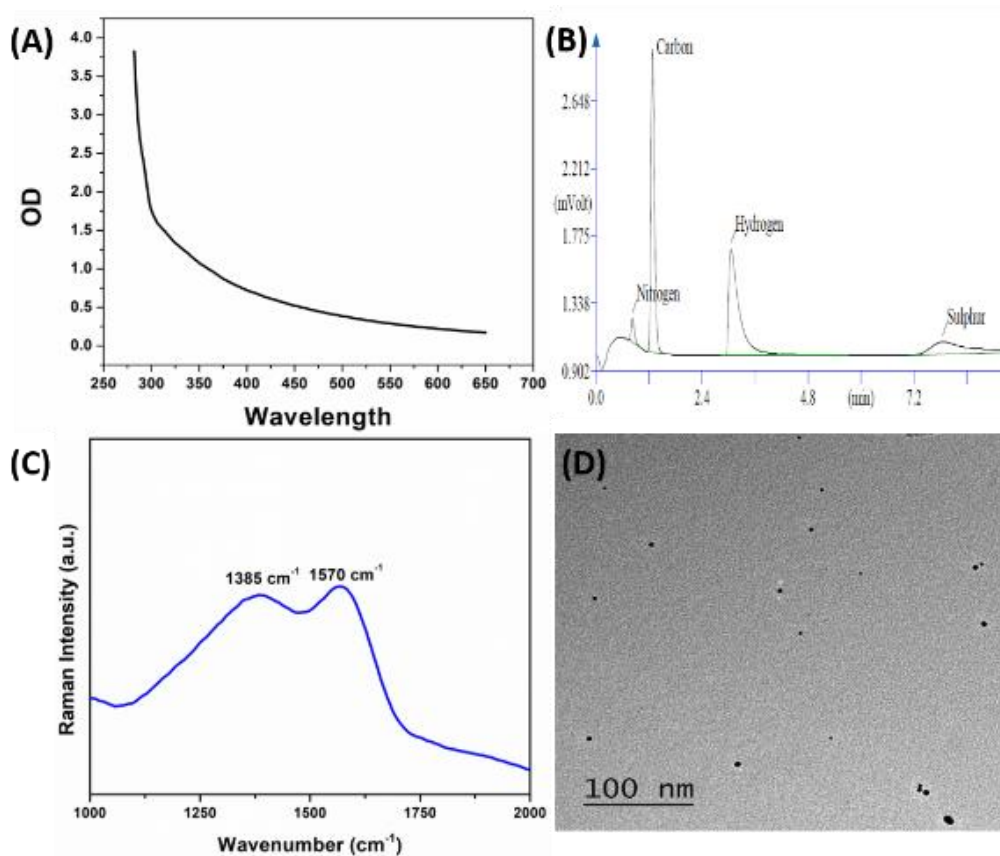
Figure 3-3: Characterization of NS-CQDs *via* (A) optical spectroscopy, (B) CHNS elemental mapping, (C) Raman spectroscopy, and (D) Transmission electron microscopy.

transmission electron microscope after drying under vacuum. The micrograph showed quantum dots having an average diameter of 3.55 nm (Figure 3-3D).

3.2.3. NS-CQDs based direct quenching assay

To develop a fluorescence-based assay using carbon quantum dots doped with nitrogen and sulfur, the effect of various objects on the fluorescence profile of CQDs was assessed. To visualize the effect of various metal ions, the quantum dots were incubated with several different metal ions (Ca^{2+}, K^+, Mg^{2+}, Na^+, Zn^{2+}, Fe^{2+}, Mn^{2+}) in a concentration range of 3.125 µM to 200 µM. The CQDs were diluted to 5% aqueous dilutions for the experiments to prevent the possibility of material leeching from the microtitre plate surface due to very low pH of as-prepared dispersion. For this, 90 µL of metal ion solution was added to 10 µL of 50% aqueous dilution of CQDs in a black 96-well microtitre plate well. The mixture was incubated for 5 minutes with double orbital shaking at 110 rpm and fluorescence was measured between 405 nm to 700 nm using an excitation wavelength of 375 nm. The peak maxima found at 452 nm was plotted for different concentrations and patterns were scrutinized. The NS-CQDs showed no or insignificant changes in its fluorescence in response to the metal ions suggesting no interaction and influence of metal ions on the quantum dots.

To analyze the effect of myoglobin on the fluorescence of quantum dots, co-incubation followed with fluorescence measurements was performed. Myoglobin solution were prepared at different concentrations (ranging from 2.5 µM to 160 µM) in phosphate buffer (10 mM, pH 7.2), and 90 µL of each solution was added into a microtitre well of 96-well black microtitre plate. To the wells, 10 µL of 50% aqueous solution of CQDs was added to create a 5% final dilution, and the mixture was incubated for 5 minutes with stirring to ensure complete mixing of the components and to ensure completion of the reaction to avoid any drift during measurements. After the completion of incubation, the fluorescence was measured in a range of 405-700 nm with excitation wavelength of 375 nm. The fluorescence of the quantum dots was compromised linearly in response to the added concentration of myoglobin from 2.5 µM to 160 µM (Figure 3-4). The effect of myoglobin on the fluorescence of quantum dots was attributed to the Soret

absorption of myoglobin that overlaps with the emission of the quantum dots. As the Soret absorption is a property of heme-containing proteins, it was expected that the similar quenching effect could be seen with hemoglobin. The effect of hemoglobin on fluorescence of quantum dots was analyzed by following the same protocol by using hemoglobin solutions of 2.5 µM to 160 µM. The fluorescence of quantum dots decreased with increase in the concentration of hemoglobin in the solution thus confirming the basis of fluorescence quenching. To validate the phenomenon further, aqueous solutions of hemin were used to recreate the quenching effect, as the Soret absorption originates from the heme component of such proteins. Fluorescence quenching by hemin was tested by incubating aqueous solutions of hemin (2.5 µM to 160 µM) with quantum dots. A mixture of 90 µL of each hemin concentration and 10 µL of 50% aqueous solution of quantum dots taken in a black 96-well microtitre plate was incubated for 5 minutes in a plate shaker and fluorescence spectra were recorded between 405 nm to 700 nm. The presence of hemin brought a similar reduction in the fluorescence of the quantum dots in a strong concentration-dependent manner, thus validating the hypothesis (Figure 3-4).
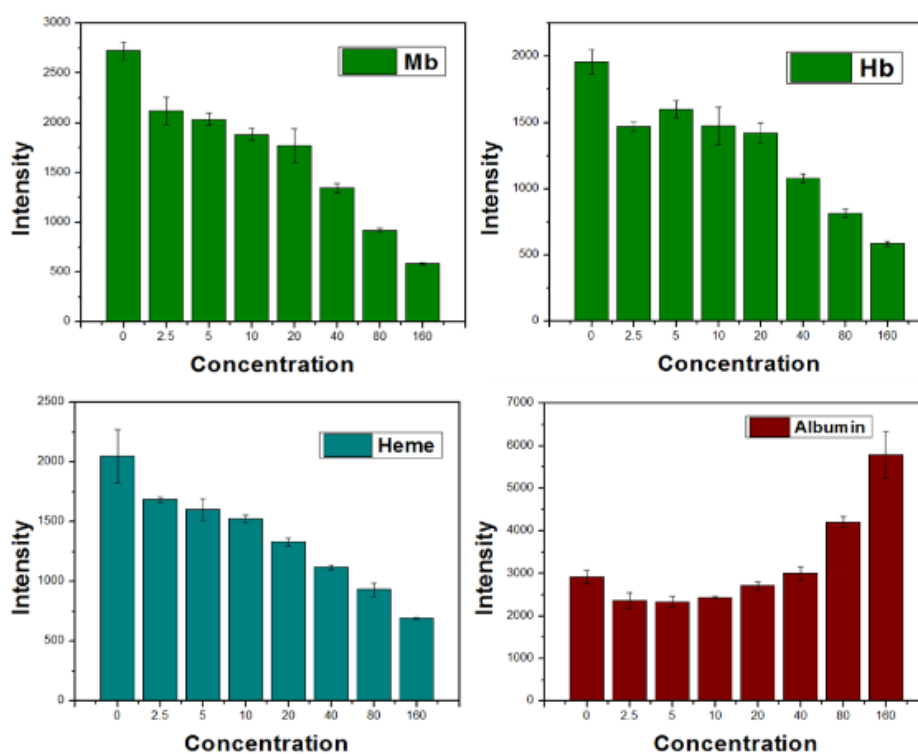
Figure 3-4: Effect of various proteins on the fluorescence of the NS-CQDs

To analyze the effect of serum albumin on quantum dots, several concentrations of bovine serum albumin (BSA) ranging from 10 µM to 160 µM were prepared in phosphate buffer (10 mM, pH 7.2). Into 90 µL of each concentration, taken in a microtitre well, 10 µL of 50% aqueous dilution of quantum dots was added, and incubated for 5 minutes before taking fluorescence measurements. In the presence of BSA, the fluorescence of the quantum dots showed insignificant change up to 40 µM of BSA. However, BSA at concentrations beyond 40 µM created a stabilizing effect in the solution, which was shown as an increase in the fluorescence of the quantum dots. For recording the effect of myoglobin in presence of serum albumin, myoglobin concentrations ranging from 1.25 µM to 80 µM were prepared in 0.6 mM solution of BSA (prepared in 10 mM phosphate buffer, pH 7.2). The concentration of BSA was chosen to recreate the amount of albumin present in the serum in physiological conditions. The effect of these myoglobin concentrations on the CQDs was tested by using the protocol followed for myoglobin earlier. As BSA showed a stabilizing effect in the earlier experiments, its presence curbed the quenching effect of myoglobin up to 10 µM of myoglobin. In solutions containing myoglobin concentration above 10 µM, the stabilizing effect of BSA was overcome by the increased concentration of myoglobin and the fluorescence of the quantum dots was accordingly reduced in a concentration-dependent manner (Figure 3-5A).

To tackle the problem of compromised detection range towards lower concentrations of myoglobin caused due to albumin, a method to isolate myoglobin from the albumin was devised. To separate myoglobin from serum albumin, selective protein precipitation was done utilizing the effect of salting out. Saturated solution of ammonium sulfate (pH set at 9) was used for selective precipitation of a mixture of myoglobin & BSA at final concentrations of 100 µg/mL and 10 mg/mL respectively. To this mixture, saturated ammonium sulfate was added while stirring to increase its weight component from an initial concentration of 20% to 80% gradually with a rise of 5% at each step. The mixture was stirred for 15 minutes at each step and any precipitate was removed by centrifuging the solution at 12000 ×g. After achieving 80% ammonium sulfate concentration, the solution was stirred for 6 hours for complete precipitation. The pellets removed were pooled, re-suspended in 1 mL phosphate buffer (10 mM, pH
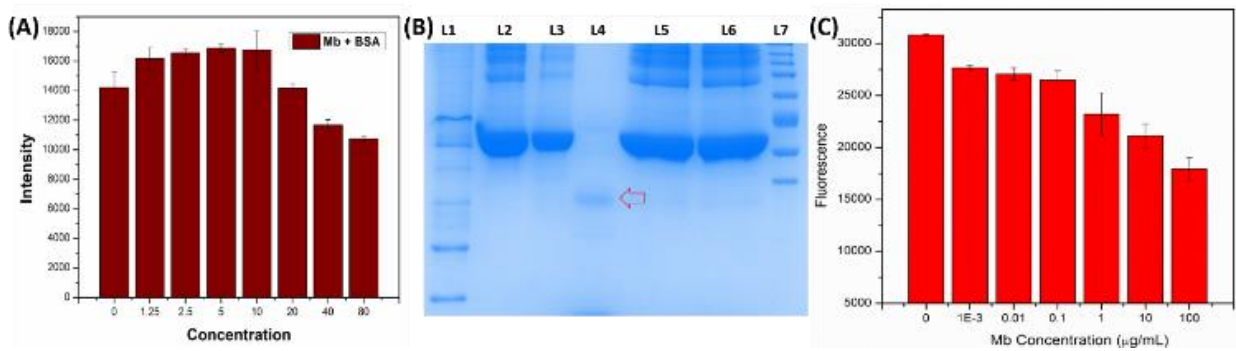
Figure 3-5: (A) Fluorescence of the quantum dots in presence of various concentrations of myoglobin in BSA. (B) Polyacrylamide gel showing separation of myoglobin from BSA. L1 & L7: protein ladders; L2-3: BSA; L4: Mb; L5-6: Precipitate. (C) Fluorescence of quantum dots in the presence of various concentrations of myoglobin separated from BSA *via* selective precipitation.

7.2) and the extent of selective precipitation was monitored by examining the pellet through 15% SDS-PAGE. The pellet showed absence of any band corresponding to myoglobin in the pellet whereas presence of a band around 17kDa confirmed complete separation of albumin from myoglobin (Figure 3-5B). The harvested myoglobin was diluted in 80% ammonium sulfate in a concentration range of 1 ng/mL to 100 µg/mL, and its effect on the fluorescence of the quantum dots was tested. The plot showed a concentration dependent decline in the fluorescence of the quantum dots in presence of myoglobin between 0.01 µg/mL to 100 µg/mL thus providing a dynamic range required for the clinical applicability of the developed assay (Figure 3-5C).

3.3. Smartphone-based PoC device for myoglobin detection

A Point-of-Care device is any equipment that can be used at places like the patients' bedside, or clinical emergencies, unlike conventional time-consuming laboratory setups.[261–265] Besides the portability, the other essential feature of such devices is the ease of usage, which allows any untrained person to understand and utilize such devices. In diagnostics, such devices allow convenient quantifications of biomarkers and help in the regular screening of diseases without the requirement of professionals thus creating long-term routine monitoring feasible. In recent times, the rise of smartphones have breached every sector of our lives and the field of diagnostics falls in the category that have benefitted from this feature positively.[266–270] While the smartphone's camera can be used as the detector for quantification signals, the signal can also be processed and converted

16.3mm

45.5mm

142.5mm

63mm

73mm

53mm

70mm

A

B

C

Front View   Section across yz-plane   Outer Shell
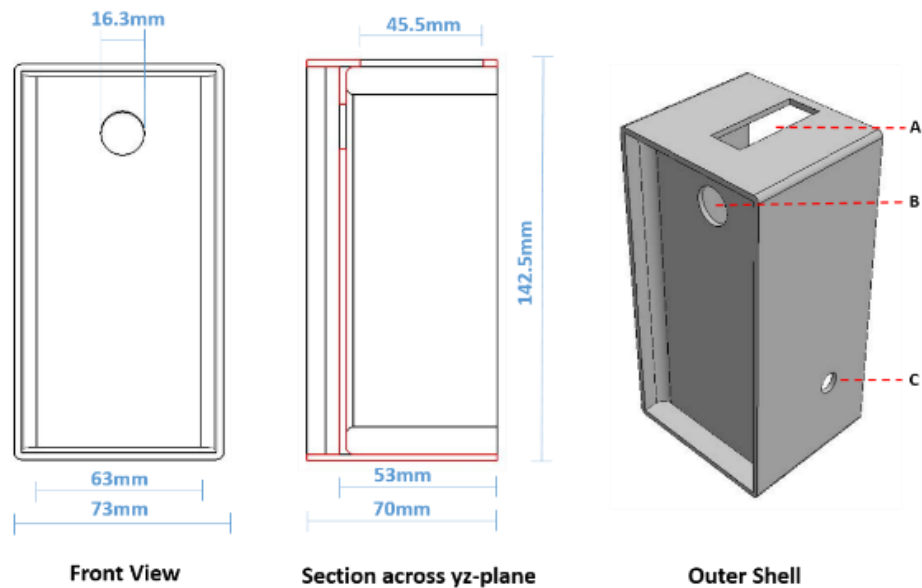
Figure 3-6: Diagram showing the physical dimensions of the Outer Shell of device and its cross sections. "A" denotes the space for inserting the cuvette holder, "B" denotes the aperture for visualization, "C" denotes opening for inserting potentiometer.

in graspable figures, record and save trends over extended periods, and may relay the trends to the clinicians or related personnel in case of any deviations away from the threshold.

The fluorescence-based method developed for the quantification of myoglobin was developed into a smartphone-based Point-of-Care (PoC) device considering its advantages. A Motorola G3 smartphone was selected for the initial prototype and the device was designed in accordance to the physical dimensions of the selected smartphone (142.1 mm × 72.4 mm × 11.6 mm). The device was

16mm

13mm

16mm

35mm

5.1mm

10mm

35mm

45mm

38mm

20mm

D

E

F

Section across xy-plane   Section across yz-plane   Cuvette Holder
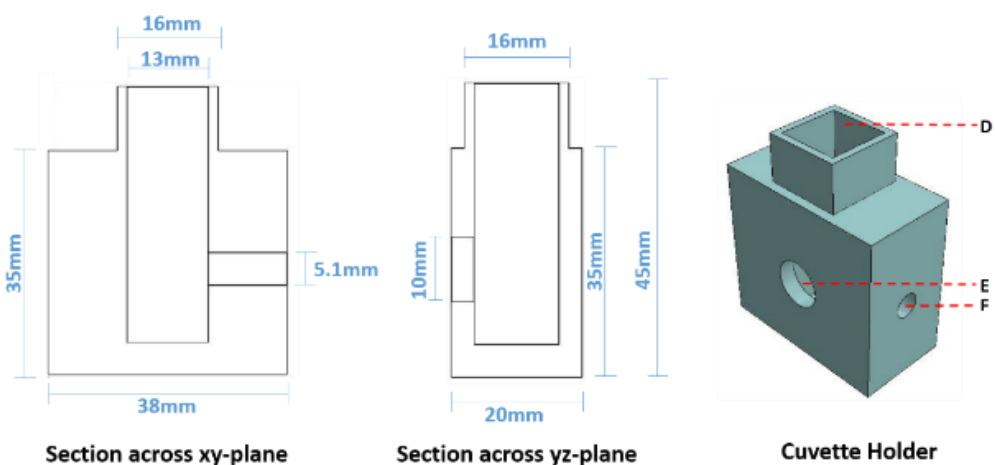
Figure 3-7: Diagram showing the physical dimensions of the Cuvette Holder of device and its cross sections. "D" denotes the shaft for inserting the cuvette, "E" denotes the aperture for visualization, "F" denotes opening for inserting LED source.

designed to cradle the smartphone inside, to provide a stable platform for optical measurements. The device was fabricated from a thermoplastic polymer by 3D printing the designs. The smartphone housing contained an aperture that was aligned with the camera of the smartphone. A cuvette holder was aligned directly beneath the aperture that possessed a shaft for inserting the sample cuvette. The sample in the cuvette was illuminated by a UV-emitting LED source inserted perpendicular to the optics of the smartphone camera to avoid the need of inserting optical band filters in the device. The UV source was powered with a 9V battery fixed inside the housing. A potentiometer was connected in series to the circuit, to control the intensity of the UV source. For the measurements, a quartz cuvette containing mixture of sample & QDs was inserted in the cuvette holder, and illuminated with the UV source (Figure 3-8A). The fluorescence originating from the QDs was recorded by the smartphone's camera, and processed using an android application (Color Grab, Loomatix, Israel https://play.google.com/store/apps/details?id=com.loomatix.colorgrab) that provided the RGB content of the signal from the selected region (Figure 3-8B). The RGB component of the optical signal were plotted individually for the changes in the fluorescence of the QDs from myoglobin in the sample. It was observed that the green component of the quantum dots reacted more linearly to the alterations in the fluorescence, than red or blue components, although blue component was supposed to prove critical in the measurements owing to the blue fluorescence of the quantum dots.

Figure 3-8: (A) Actual photographs of the working of device showing fluorescence signal from Quantum dots. (B) Close-up image of the smartphone application showing the RGB content of the fluorescence from the selected area. The RGB values are marked with a yellow dashed rectangle.
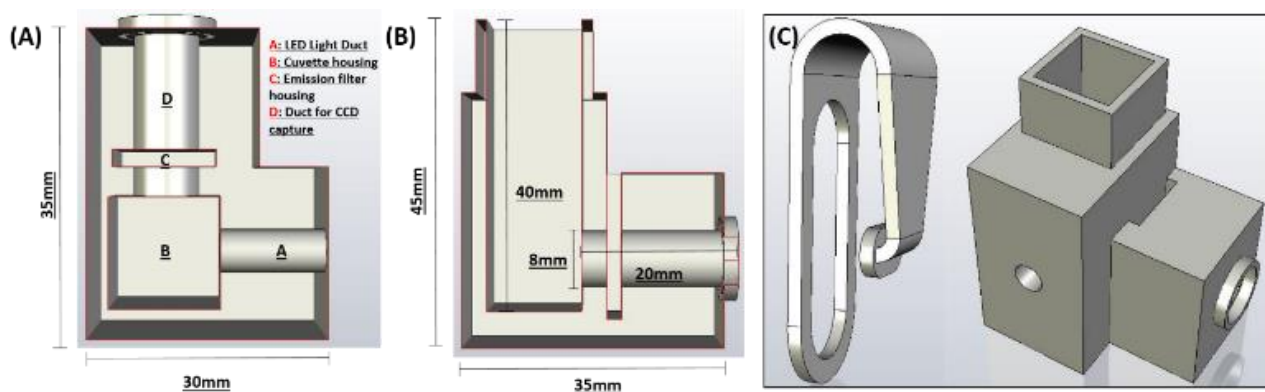
Figure 3-9: (A) Cross-section of Cuvette holder of Prototype 2 showing the inner optics and individual parts. (B) Diagram showing the physical dimensions of the cuvette holder. (C) Complete design of the cuvette holder and the clip-on connector

The initial prototype was limited to function on a single type of smartphone due to the constraint put by the physical dimensions of the smartphone and the position of its camera. The alignment of camera with the camera aperture was the paramount requirement of the device for its functioning. To improve on this, a second prototype was designed containing a single fully enclosed *cuvette holder* (Figure 3-9). The cuvette holder could attach to any device through a *clip-on* allowing complete spatial freedom to the device. Further, the enclosed nature of the device prevented any interference by ambient light. The device was fabricated by 3D printing the designs and was successfully tested on a smartphone to investigate its functioning (Figure 3-10A-B). The working of the device was assessed by adding different concentrations of myoglobin in 5% NS-co-doped CQDs and visualizing through the device. The RGB intensity was recorded for each concentration under constant parameters of the device, and green component of the signal was plotted (Figure 3-10C). The plot showed a concentration-
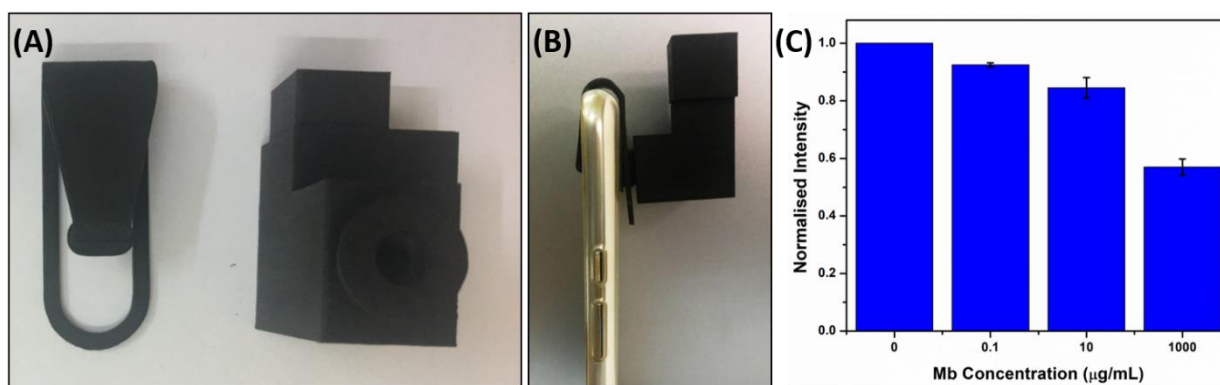
Figure 3-10: (A) Photographs of the individual parts of the fabricated prototype. (B) Photograph showing the device mounted on a smartphone. (C) Normalized fluorescence of the quantum dots in the presence of different concentrations of myoglobin as captured with the device.

84

dependent decrease in the fluorescence of the Quantum dots thus establishing the applicability of the device in a PoC scenario.

3.4. Conclusion

Carbon-based quantum dots were synthesized from various starting materials to assess the role of composition on the fluorescence and functional properties of the nanomaterial. It was revealed that incorporation of sulfur and nitrogen in the skeleton of the nanomaterial improves the fluorescent properties of the quantum dots. The synthesized quantum dots were utilized in the development of optical assays for the quantification of a cardiac biomarker myoglobin. Further, the developed assay was applied on a smartphone-based handheld point-of-care system to harvest the potential of these optical assays for generating a field-applicable device.

CHAPTER 4

Electrochemical platforms for ultra-sensitive quantification of myoglobin

Electrochemical biosensors are the class of biosensors that use an electrode as the transducer and measure the voltage/current changes in the chemical reactions occurring on the electrode surface.[69,271] The electrodes in the biosensor are generally fabricated from conductive materials like carbon or metals like gold, silver or platinum. The signal generated in the sensors is directly affected by the electrode materials and can be manipulated by changing the electrode material. Nanomaterials like graphene, transition metal chalcogenides, metallic nanoparticles *etc.* with exceptional electronic properties compared to conventional electrode materials are hence employed for the development of sensitive sensing platforms.[165,272,273] While a characteristic of nanomaterials is the increase in the surface area that leads to augmented electron transfer through the surface of electrodes thus leading to a higher signal, hybrid composites can be generated to further modulate the surface area and the resulting electron transfer.[71,274,275] For our study, we synthesized a reduced graphene oxide based 2D nanomaterial onto which 1D carbon nanotubes were decorated to prepare a 1D@2D nanohybrid, and a 2D material prepared out of few-layered phosphorene. The nanomaterial was tested against its parent entities to understand the changes in the electronic properties resulting from the modifications in topology. Further, the role of specific aptamer binding in improving the analyte quantification was assessed. The developed nanomaterials were used as electroactive modifiers to generate electrochemical platform for myoglobin using myoglobin-specific aptamers.

Objectives:

- Synthesis of carbon nanotubes & reduced graphene oxide based electronically active nanohybrid
- Development of electrochemical aptasensor for the detection of cardiac biomarker myoglobin using synthesized nanohybrid

- Investigation of the role of poly-L-lysine as immobilization agent for the binding of aptamers
- Development of few-layered phosphorene nanosheets based electrochemical platform for the detection of cardiac biomarker myoglobin

4.1. rGO/CNT nanohybrid for myoglobin quantification

Van der Waals heterostructures are the most common kind of heterostructures that rely on the van der Waals interactions between two or more different constituents to create a structure having superior enhanced properties owing to the synergism between the components.[276–279] Such nanomaterials are highly sought-after in applications like electrochemical diagnosis, which requires high surface areas for interactions and subsequent transfer of signal in a readable manner. A van der Waals heterostructure composed of one-dimensional carbon nanotubes and two-dimensional reduced graphene oxide (rGO) was synthesized by the method of co-incubation. The developed rGO/CNT nanocomposite was a 1D@2D heterostructure that displayed decoration of linear nanotubes onto flat two-dimensional surface thereby increasing the surface area, and contributing towards multifold enhancement in the electrochemical response.

4.1.1 Synthesis of rGO/CNT nanohybrid

For this, first graphene oxide was synthesized from graphite powder by using a modification of Hummer's method developed by Marcano *et al.*[280] For this, 1.5 g graphite powder and 9 g $KMnO_4$ was added to 200 mL solution of H_2SO_4 and H_3PO_4 taken in 9:1 volumetric ratio (H_2SO_4:H_3PO_4 180 mL:20 mL v/v). The mixture was heated to 50°C and stirred for 12 hours. After the completion, the reaction was cooled by adding ice made from 200 mL DI water. To the reaction, 1.5 mL of 30% H_2O_2 was added to quench the reaction by reacting with free $KMnO_4$ and the resulting mixture was centrifuged at 7000 ×g to separate the synthesized nanomaterial from the solvent. The pellet was re-suspended in ultrapure water and the process was repeated thrice with water, once with 30% HCl and twice with

absolute ethanol. The suspended nanomaterial was coagulated in diethyl ether by incubating overnight, filtered and vacuum dried. The resulting graphene oxide (10 mg) was suspended in 10 mL solution of water:DMF (v/v 9:1) to achieve a concentration of 1 mg/mL, and sonicated for 30 minutes to disperse completely.[281-285] To the resulting suspension, 10 mg of multi-walled carbon nanotubes (MWCNT) were added to create a mixture of rGO:CNT with 1:1 w/w ratio, and mixture was sonicated for 1 hour to obtain GO/CNT nanohybrid.[286] To reduce the prepared GO/CNT nanocomposite to rGO/CNT, 2 mL of 0.1 M ascorbic acid solution was added and the concoction was stirred vigorously for 4 hours while heating at 90°C.[287-289] Incubating the reaction for a longer period while heating ensured complete utilization of ascorbic acid and thus allowed omitting the addition of H_2O_2 for quenching of reaction. The resulting reduced nanomaterial was washed with ethanol thrice and dried in a vacuum oven to obtain rGO/CNT nanocomposite.

4.1.2 Characterization of rGO/CNT nanohybrid

i. Electron microscopic analysis

The decoration of nanotubes onto rGO surface was validated by directly visualizing the nanocomposite under electron microscopes. For scanning microscopy, a dilute aqueous suspension of the nanocomposite (2.5 μg/mL) was drop-casted on a clean Si wafer and visualized under a JEOL-1T300 scanning electron microscope. For transmission electron microscopy, aqueous suspension of the nanocomposite was put on a carbon-coated 200-mesh Cu TEM grid, and dried under vacuum before visualizing under a JEOL JSM2100 transmission electron microscope operating at 200 kV. Bundles of carbon nanotubes latching onto the surface of nanosheets were revealed in scanning electron micrographs as well as under high-resolution transmission electron microscope, thus confirming the successful generation of the nanohybrid (Figure 4-1A-B).
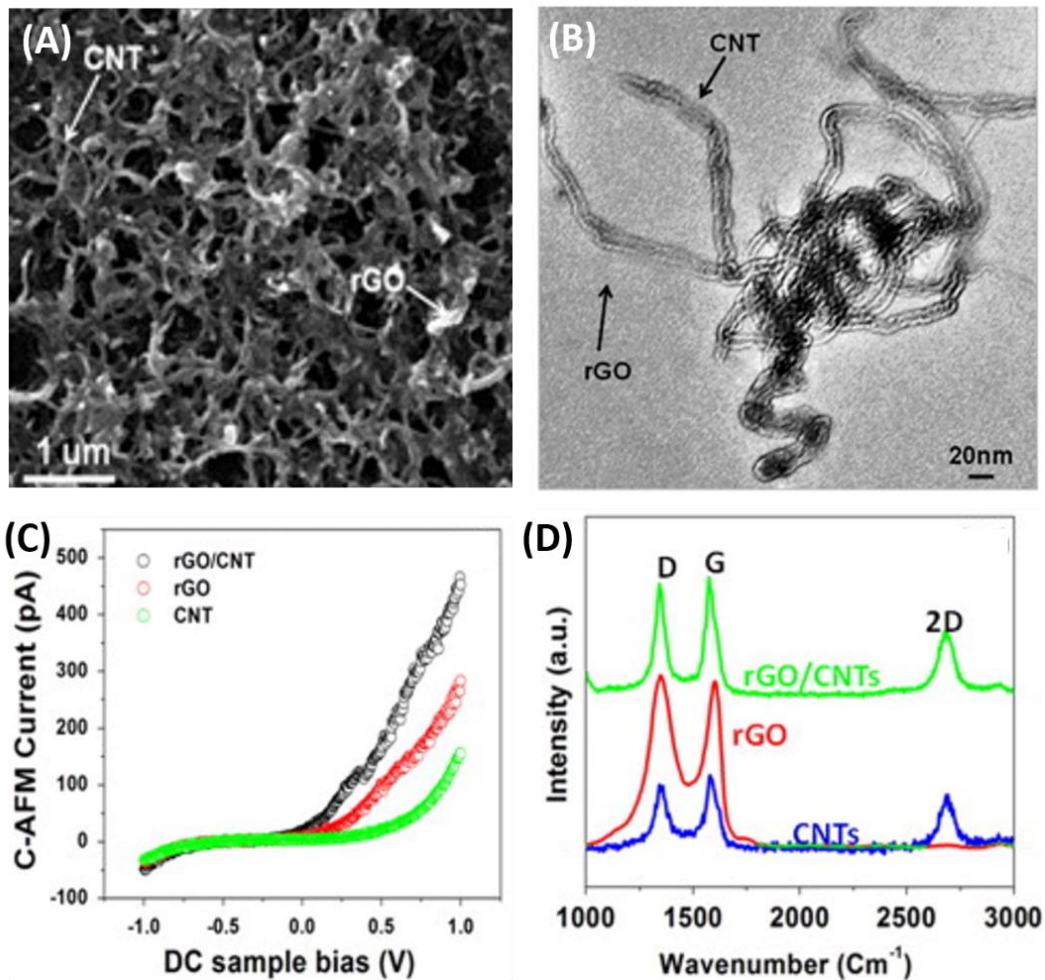
Figure 4-1: Characterization of rGO/CNT hybrid using (A) Scanning electron microscopy, (B) Transmission electron microscopy, (C) Conductive AFM, and (D) Raman spectroscopy.

ii. Conductive-AFM studies

Conductive atomic force microscopy was carried out on a 0.1 µg/mL sample drop-casted onto a fresh Si wafer by applying a bias voltage between sample and the cantilever. The enhancement in the electrical properties was observed in conductive-AFM where the nanocomposite outperformed its constituents tested individually. The nanocomposite showed a steeply rising current value even at a lower potential, higher than individual rGO and nanotubes (Figure 4-1C).

iii. Raman spectroscopic analysis

Raman spectroscopic analysis of the sample drop-casted on a Si wafer was done on a Witec alpha300R Raman spectroscope using a 532 nm laser. The rGO/CNT nanocomposite showed Raman peaks at 1340 cm^{-1} and 1576 cm^{-1} corresponding to D (structural disorder) and G (degree of graphitization) signature bands depicting A_{1g} and E_{2g} vibrational modes respectively (Figure 4-1D). The vibrational modes produced the signature bands in both rGO and CNT as shown in their individual spectrum as 1580 cm^{-1} (CNT) & 1595 cm^{-1} (rGO) showing G band, and as 1345 cm^{-1} (CNT & rGO) showing D band. The 2D signature band corresponding to material stresses was shown at $\sim$2685 cm^{-1} in CNT and in rGO/CNT composite only, suggesting the incorporation of the nanotubes with rGO nanosheets in composite state.[286,290]

iv. BET surface area analysis

Surface area analysis of the composite *via* BET showed contradictory observations in the surface areas of the materials. The calculated surface area of rGO (266.7 m^2/g) and CNT (18.9 m^2/g) showed a decrease in their nanocomposite form (81.3 m^2/g). However, the observations can be due to the masking of rGO caused by the overlapping of CNT bundles onto the nanosheets.[291]

4.1.3 Electrochemical characterization of rGO/CNT nanohybrid

The electrochemical properties of the nanocomposite were checked by comparing the nanocomposite against its parent components. The nanomaterials were individually bath-sonicated in ultrapure water at a moderate concentration of 1 mg/mL for 1 hour. The resulting dispersions were checked for presence of any visible aggregates and the resulting stable dispersions were further bath-sonicated for 5 minutes before drop-casting for electrode modification. For the
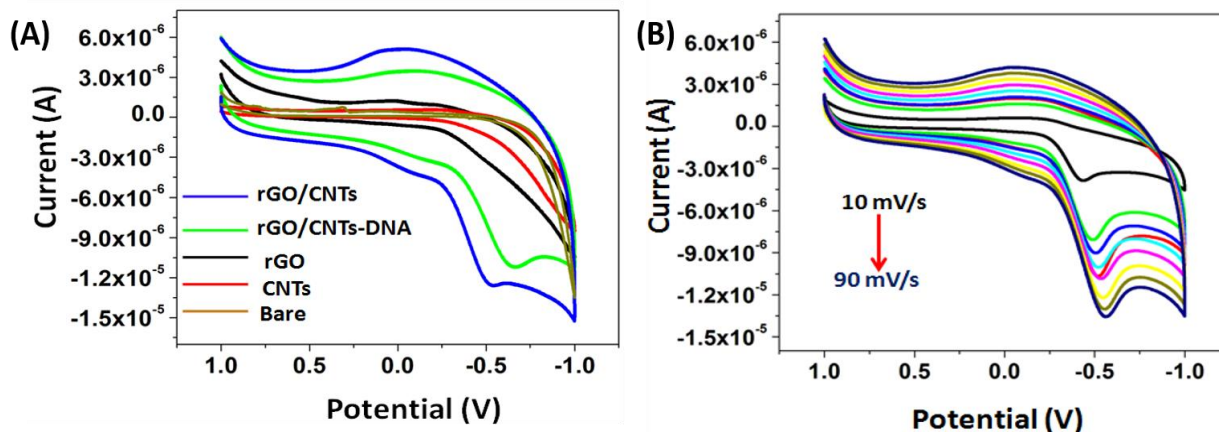
Figure 4-2: (A) Cyclic voltammograms showing the superior electroactivity of rGO/CNT hybrid. (B) Scan-rate dependent cyclic voltammetry showing linear relative increase in the current response.

electrochemical measurements, a screen-printed electrode (TE100, Zensor USA) comprising of 3-electrode system was used. The commercial electrode system consisted of carbon-based working and reference electrodes, and a silver-based reference electrode. The background current response of the electrode was measured by adding 50 µL of phosphate buffered saline (100 mM, pH 7.2) and recording the current response *via* cyclic voltammetry. The nanomaterials were drop-casted on the working electrode of the system by adding 2.5 µL drop of the nanomaterial and baking at 60°C for 5 minutes.[286] The electroactivity of the electrodes was measured by recording the cyclic voltammograms for each nanomaterial. In comparison to the bare current response from the unmodified electrode, the electrodes modified with nanomaterials showed a heightened response. Further, the nanocomposite of rGO/CNT showed a superior current response than its parent entities (Figure 4-2A). This increment in the electrochemical response can be attributed to the synergism between the nanomaterials that created a novel and better topological properties in the composite. The rGO/CNT nanocomposite modified electrode was further analyzed for the properties of the composite *via* various electrochemical examinations. For the rGO/CNT modified screen-printed electrode, repeated scans (25 repetitions) were performed to analyze the stability of the electrode. The current response showed insignificant changes among the scans, and the observation suggested that there was no leeching of nanomaterial from the electrode during the scans. Scan-rate dependent cyclic voltammograms were recorded by changing the scan rate from 0.01 V/second to 0.09 V/second, and recording the CV responses for

each scan rate. The current response in scan-rate dependent scans is indicative of the electron diffusion properties of the system, and showed a direct correlation between scan-rate and current response with very high linearity (Figure 4-2B).

4.1.4 Assay development

For the development of a sensitive quantification method for the estimation of myoglobin, an electrochemical platform was developed by employing a conducting nanocomposite of reduced graphene oxide and carbon nanotubes (rGO/CNT). To generate a platform for the detection of myoglobin, the rGO/CNT modified electrode was further decorated with myoglobin-specific aptamers. The concentration of aptamers required for optimum coverage of the electrode surface was calculated by visualizing different concentrations of aptamer on the working electrode. For this, FITC-labelled aptamer was dropped onto the working electrodes of SPE at 0.1 µg, 0.5 µg, 1 µg & 1.5 µg, and incubated for 30 minutes at room temperature. The electrodes were then washed and visualized under a fluorescent microscope (BX-53F, Olympus Corp.) using a green filter with an exposure time of 5 seconds. The fluorescence images revealed that
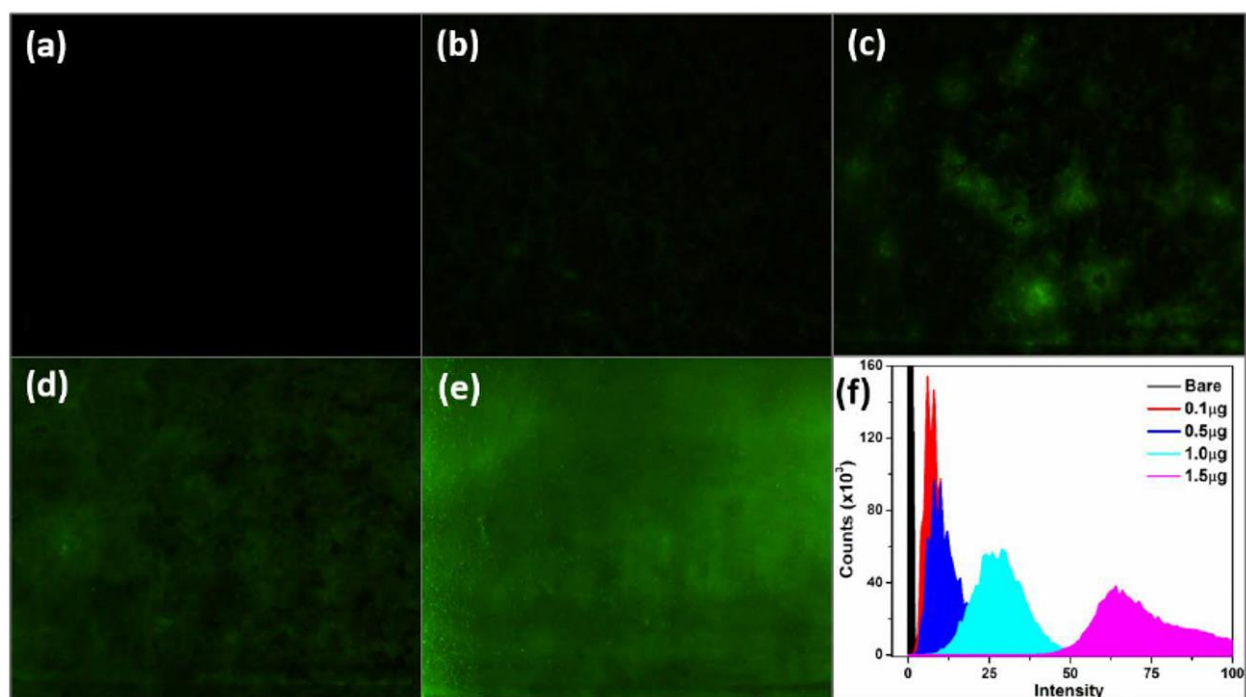
Figure 4-3: Optimization of aptamer concentration (**a**: 0 µg, **b**: 0.1 µg, **c**: 0.5 µg, **d**: 1 µg, **e**: 1.5 µg) for immobilization on working electrode through fluorescence microscopic analysis of FITC-modified aptamer. **f** shows fluorescence intensity plot derived from ImageJ image analysis software.

the electrode surface showed a gradual increase in the fluorescence arising from the aptamer binding as the dropped amount of aptamers was increased, and showed a near complete coverage at 1 µg (Figure 4-3). Although 1.5 µg showed a higher fluorescence intensity, a lower amount was chosen to avoid layering of aptamers that may lead to highly insulating behavior and may cause leeching of material during measurements.

For developing the assay, 5 µL of the aptamer stock (230 µg/mL) was drop-casted onto the surface of nanocomposite modified working electrode to achieve an effective aptamer amount of 1.15 µg. The electrode was incubated at room temperature for 30 minutes to allow binding of the aptamers. The electrode was washed with ultrapure water once to remove unbound aptamer molecules, and cyclic voltammetry was used to check the binding of the aptamer on the surface of electrode. The binding was confirmed from the slight decrease in the current response in the voltammogram, which is due to the disruption of electron diffusion originating from the DNA binding on the surface of electrode. The aptamer-enabled rGO/CNT-based electrode system was exposed with linearly increasing concentrations of myoglobin, prepared in binding buffer, ranging from 1 ng/mL to 4 µg/mL. For this, a 10 µL drop of myoglobin concentration was added on the surface of working electrode and incubated for 15 minutes to allow the aptamers to capture the protein molecules. After the incubation, the electrode surface was washed with binding buffer, and the CV response was measured in 50 µL of phosphate buffered saline. The current response in the voltammograms showed a gradual increase in its response respective to the concentration of myoglobin added (Figure 4-4A). The basis of this increase in current lies in the phenomenon of direct electron transfer (DET) of redox-active myoglobin, which gives a direct upsurge in the current of the system due to the redox switching of iron in the metalloprotein. The process was repeated thrice with the myoglobin concentrations to analyze the reproducibility of the system. The developed system showed a high linearity in the current signal relative to myoglobin concentration in the solution displaying very high reproducibility (Figure 4-4B). The specificity of the developed platform was tested against hemoglobin (Hb) and serum albumin (bovine) by analyzing the current response of 64 ng/mL concentrations of each
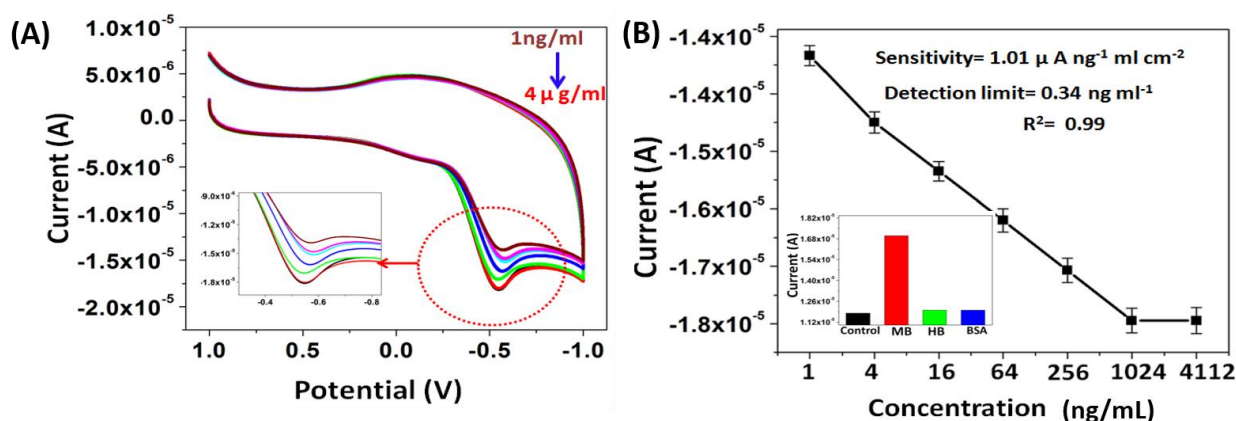
Figure 4-4: (A) Cyclic voltammograms showing increase in the current response corresponding to increasing Mb concentrations. (B) Peak current responses showing a highly concentration-dependent relation. Inset shows the specificity analysis of the platform.

protein on an aptamer-modified rGO/CNT electrode system. The system showed superior specificity towards myoglobin as demonstrated by the absence of any significant change in the current of the system in presence of albumin or hemoglobin in comparison to myoglobin at same concentration.

4.2. Few-layered Phosphorene for myoglobin quantification

Phosphorene is a term given to two-dimensional nanosheet made of phosphorus.[292,293] The nanosheet is derived from black phosphorus, the most stable allotrope of phosphorus. The orthorhombic single sheets, which are held by weak van der Waals forces can be stripped in the form of phosphorene nanosheets by mechanical stripping or through liquid phase exfoliation in suitable solvent mediums.[292,294] Unlike graphene, phosphorene is not truly planer and has a puckered structure that generates its superior mechanical properties including high tensile strength and high flexibility.[293] Phosphorene is also a direct band gap nanomaterial (~0.3 eV as bulk, ~2 eV as single sheet) which is highly tunable in response to number of layers and applied strain and electric field.[292,295–297] This tunable semiconductor behavior makes phosphorene a more suitable nanomaterial for diverse applications. Phosphorene also possess very high electron mobility (1000 cm^2/Vs) and has remarkable optical and thermal properties that are highly dependent on the number of phosphorene layers and externally applied parameters.[296,298,299] Keeping all the mentioned facts in purview, Phosphorene nanosheets have emerged as a candidate with all the pros

of the wonder material graphene while lacking its cons. Due to these properties, phosphorene is highly sought-after in fields like energy, solar cells, nano-electronics, FETs, photo-catalysis, biosensors, optoelectronics, therapeutics *etc.*

Exfoliated 2D nanosheets of phosphorene with the coating of poly-L-lysine were explored as alternative to rGO/CNT nanocomposite in the development of electrochemical detection platform for the quantification of myoglobin. Phosphorene nanosheets coated with poly-L-lysine were received from Dr. David J. Lewis, University of Manchester, UK. Poly-L-lysine (PLL) is a member of cationic polymer family that also includes poly(ethyleneimine), poly[2-N,N-dimethylamino)ethyl methacrylate and chitosan among others. PLL is a homo-polypeptide made of a basic amino acid, L-lysine containing two amino groups and one carboxylic group. Either of the amino group can participate in the polymerization process which may result in the formation of α-polylysine or ε-polylysine (Figure 4-5). Due to the presence of additional amine groups that remains free in its polymer form, poly-L-lysine has a net positive charge at above pH 5. PLL is a natural polymer and due to its biocompatibility it is used as food preservative, as binding agent to promote cellular adherence in cultures and as coating agent in therapeutics. In our study, this cationic polymer was used to facilitate the electrostatic interaction between negatively charged aptamers and positive polymer coated nanosheets.
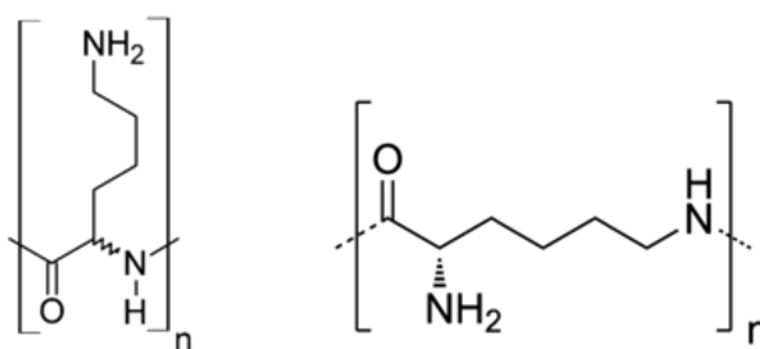
Figure 4-5: Structure of α-polylysine (left) and ε-polylysine (right).

4.2.1 Characterization of PLL-modified phosphorene nanosheets

i. Raman spectroscopic analysis

Raman spectroscopy was used to analyze the characteristic Raman signature of Phosphorene sheets and the changes arising in the signatures due to the modifications were monitored. For the measurement, 5 µL of each sample was dropped on a fresh Si substrate and dried at 50°C for 5 minutes. The samples were mounted on a Witec Raman spectrophotometer and scanned using a 532 nm green laser. From the Raman spectra, it was observed that the Raman signature at ~370 cm^{-1} corresponding to A^1_g phonon mode remain unchanged, whereas the signature peaks at 440 cm^{-1} and 470 cm^{-1} corresponding to B_{2g} and A^2_g modes respectively showed a slight decrease in their intensities with modification with PLL and subsequently with aptamer (Figure 4-6).
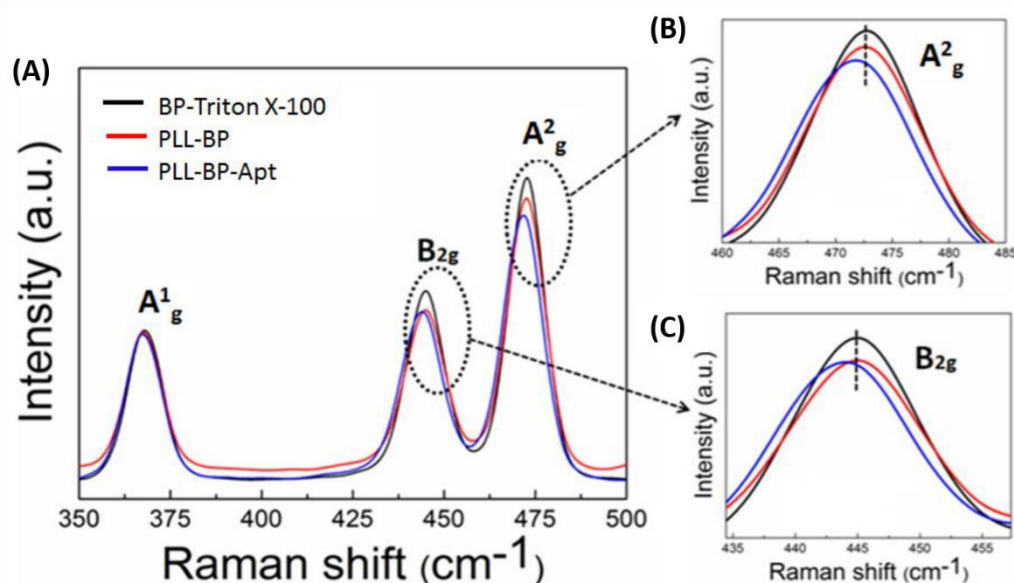
Figure 4-6: (A) Raman analysis of the Phosphorene nanosheets at different levels of modifications showing shifts in A^2_g and B_{2g} bands (B-C)

ii. Zeta potential analysis

The interaction was confirmed by measuring the zeta potential of the nanosheets before PLL modification and after interaction with the aptamers. The zeta potential of the polymer-coated nanosheets showed a sharp shift in its zeta potential from -23.4 mV to +13.5 mV. The interaction with aptamers shifted the

zeta potential to -12.1 mV due to partial neutralization of ammonium groups of PLL upon binding with aptamers (Figure 4-7A). The effect of solvent pH on the aptamer modification over PLL-modified nanosheets was observed to find the optimum conditions. For this, the PLL-modified Phosphorene nanosheets and aptamers were incubated in buffers differing in their pH being 3.4, 7.4 and 9.5. The nanosheets were then recovered, re-suspended and their zeta potential were measured. The zeta potential values for the pH was found to be -4.57, -12.1 and -11.7 respectively, suggesting the highest binding at pH 7.4 (Figure 4-7B). The lower extent of aptamer binding at pH 9.5 is attributed to the deprotonation of the amine groups on PLL whereas that at pH 3.4 is due to the instability of single-stranded aptamer in acidic medium.
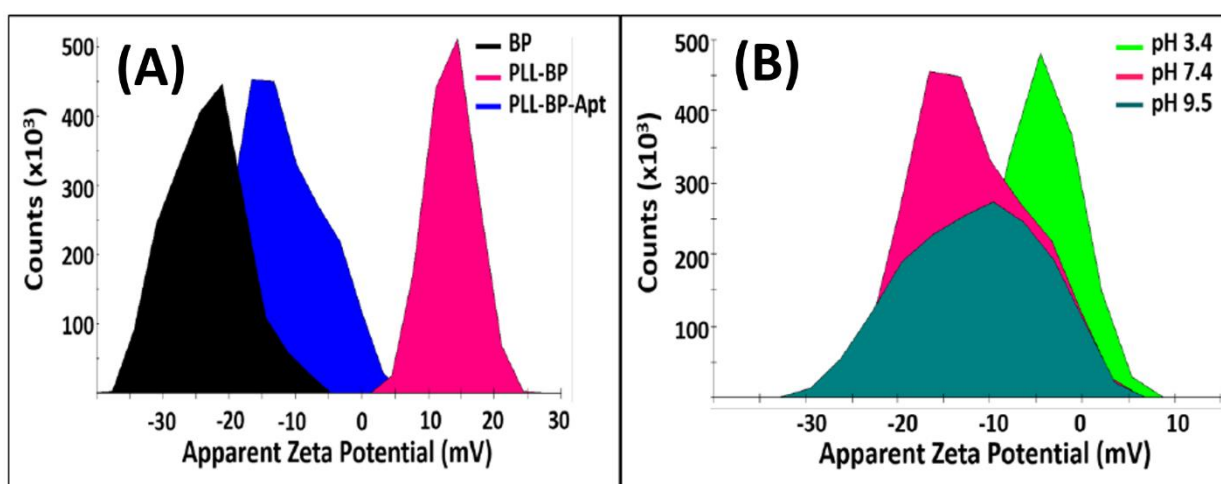
Figure 4-7: (A) Zeta potential measurements of Phosphorene nanosheets at different levels of modifications. (B) Zeta potential measurements of phosphorene nanosheets after aptamer binding at different pH.

iii. Contact angle studies

To validate the immobilization of the nanomaterial and aptamers on the surface of electrode, contact angle measurements were carried out to reveal the hydrophilicity of the surface. The measurements were carried out using the sessile drop method (DSA 100, DSA/V 1.9, Kruss GmbH, Hamburg) where a 1 µL drop of water was dropped onto the surface of the electrode at various degrees of modifications and its contact angles were measured. It was observed that the mean contact angle decreased from 117.55° in bare electrode to 88.60° for

Modification	Contact angle (Left)	Contact angle (Right)	Contact angle (Mean)
(A) Bare electrode	118.4°	116.7°	117.55°
(B) Phosphorene	88.5°	88.7°	88.6°
(C) Aptamer	84.1°	84.2°	84.15°
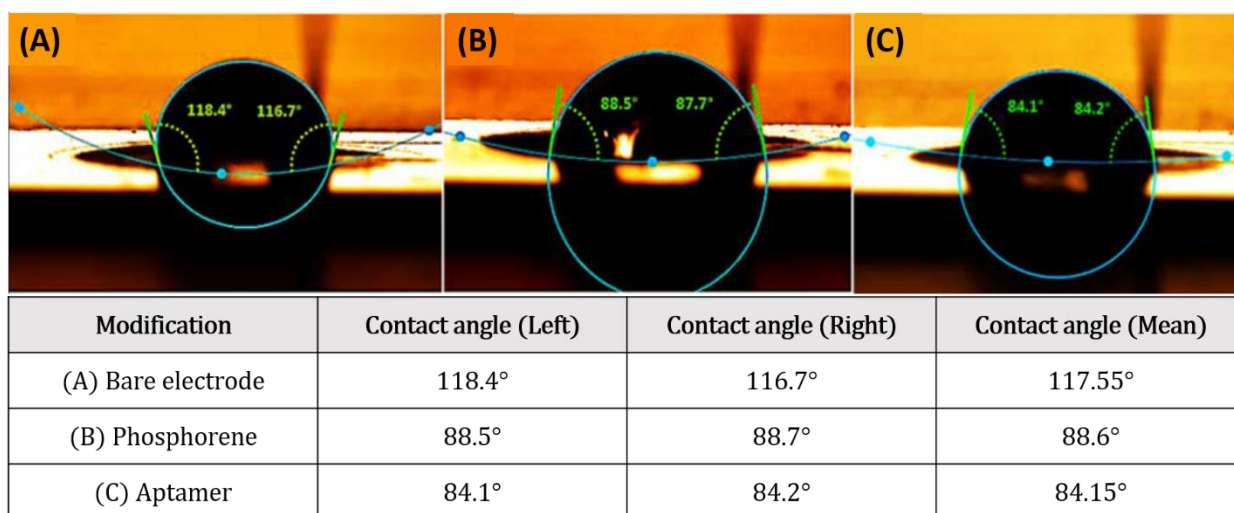
Figure 4-8: Contact angle measurements at various levels of modifications.

phosphorene-modified electrode, which indicates efficient surface modification of SPE (Figure 4-8). The modification with aptamer further decreased the mean contact angle further to 84.15° validating its binding onto the surface of electrode and suggesting the development of an effective bio-interface.

4.2.2 Electrochemical characterization

The electroactivity of the nanomaterial was validated by modifying the working electrode of a screen-printed electrode and comparing the current response against an unmodified electrode system. For this, 50 µL of ferricyanide-ferrocyanide electrolyte (5 mM equimolar solution, prepared in 100 mM phosphate buffered saline, pH 7.2) was dropped onto a fresh screen-printed electrode and current response was measured by recording cyclic voltammograms between -1.0 V to +1.0 V at a scan rate of 0.1 V/second. The electrode was washed with ultrapure water and dried. Onto the working electrode of dried SPE, 3 µL of PLL-coated phosphorene nanosheets were dropped, and the electrode was dried at 50°C for 2 hours in an Argon environment. The current response of the electrode was measured after the incubation by recording the cyclic voltammogram at a sweeping potential between -1.0 V to +1.0 V. The current response showed significant enhancement upon the modification of the working electrode with phosphorene nanosheets (0.64 µA in bare *versus* 1.3 mA in phosphorene modified), owing to their superior electronic properties (Figure 4-9A). The electron transfer abilities of the system were tested by recording

current responses between a potential range of -1.0 V to +1.0 V at different scan rates varying between 25 mV/second to 300 mV/second (Figure 4-9B). Scan rate dependent CV measurements showed linear increase in the current signal in response to the changing scan rates, which can be due to the rapid diffusion controlled electron transfer at the electrode surface. The CV measurements were validated *via* scan rate dependent electrochemical impedance spectroscopy by measuring impedance of the system at scan rates varying between 25 mV/second to 300 mV/second in ferricyanide-ferrocyanide electrolyte solution (10 mM equimolar solution). The impedance of the system decreased as the scan rate was changed from 25 mV/second to 300 mV/second, validating the voltammetric measurements. The stability of the generated nanomaterial modified electrode system was evaluated by recording multiple cyclic voltammetric scans (100 repetitions) in 50 µL of ferricyanide-ferrocyanide electrolyte. Repeated scans showed insignificant change in the current response, suggesting generation of a stable nanomaterial-modified electrode system (Figure 4-9C).
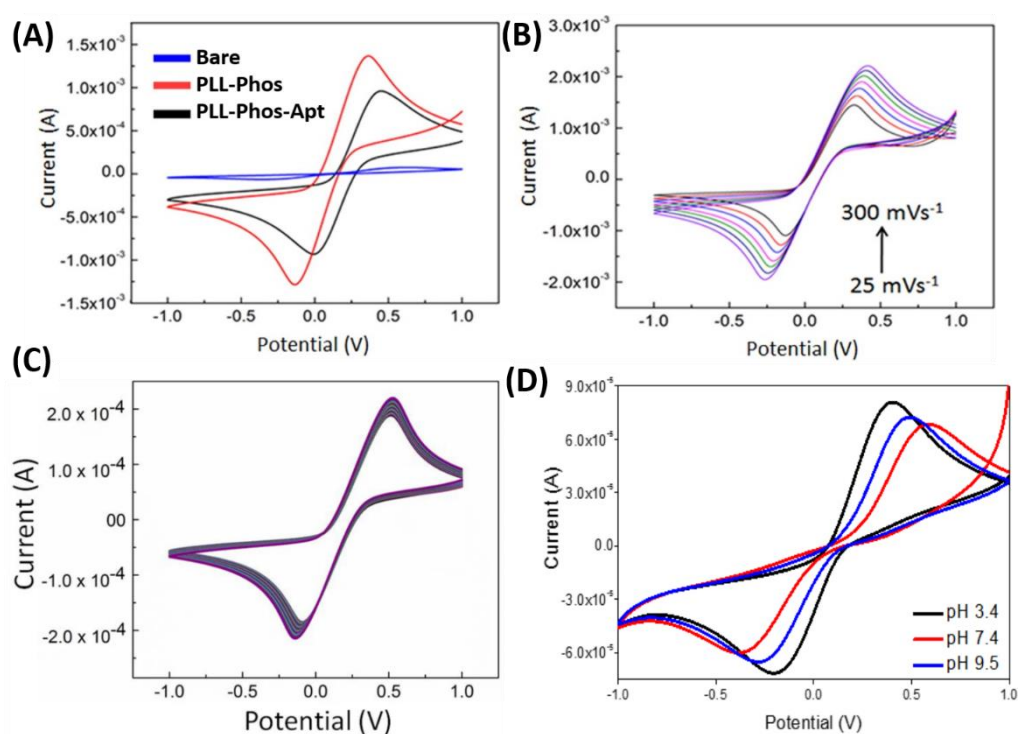
Figure 4-9: (A) CV showing the electrochemical response of screen-printed electrode after phosphorene and aptamer modification. (B) Scan-rate dependent CV response of the phosphorene-modified electrode. (C) Electrode stability studies using multi-scan CV measurements. (D) Effect of pH on aptamer binding on the PLL-modified phosphorene nanosheets decorated electrode.

4.2.3 Assay development

Aptamers screened for myoglobin were used to decorate the nanomaterial-modified electrodes to prepare a detection platform specific towards myoglobin. For this, anti-myoglobin aptamer from a 200 µg/mL stock prepared in binding buffer (10 mM Tris buffer with 150 mM NaCl, 5 mM MgCl2, pH 7.2) was drop-casted on the working electrode to achieve a final amount of 1 µg per electrode. The electrode was incubated at room temperature for 30 minutes to create enough coating of aptamer and the binding was confirmed by cyclic voltammetry. The current response showed a decrease in value after incubating with myoglobin-specific aptamer, confirming successful binding of aptamers on the nanostructured electrode surface (Figure 4-9A). To calculate the optimum conditions for aptamer modification, anti-myoglobin aptamer was diluted at different pH (3.4, 7.4 and 9.5) and dropped on the nanosheets –modified electrode and CV measurements were taken. It was observed that the highest level of current reduction was observed at pH 7.4 (Figure 4-9D), which also validates the zeta potential studies. Based on this, pH 7.4 was chosen for decorating the anti-myoglobin aptamers on the sensor surface. Myoglobin was exposed on the prepared electrode between a concentration range of 1 pg/mL to 16 µg/mL by adding 10 µL of each concentration on the modified working electrode and incubating at room temperature for 30 minutes. The electrode was washed with
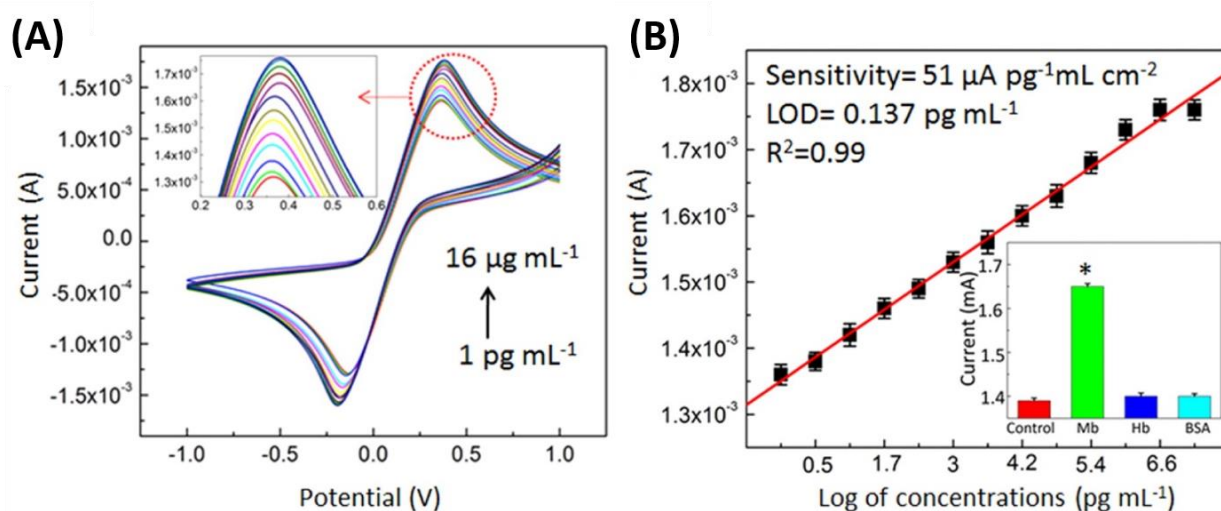
Figure 4-10: (A) CV measurements showing the increase in the current response respective to the increase in myoglobin concentration. (B) Peak currents showing a linear relation between current response and concentration. Inset shows the cross-reactivity studies using hemoglobin and serum albumin.
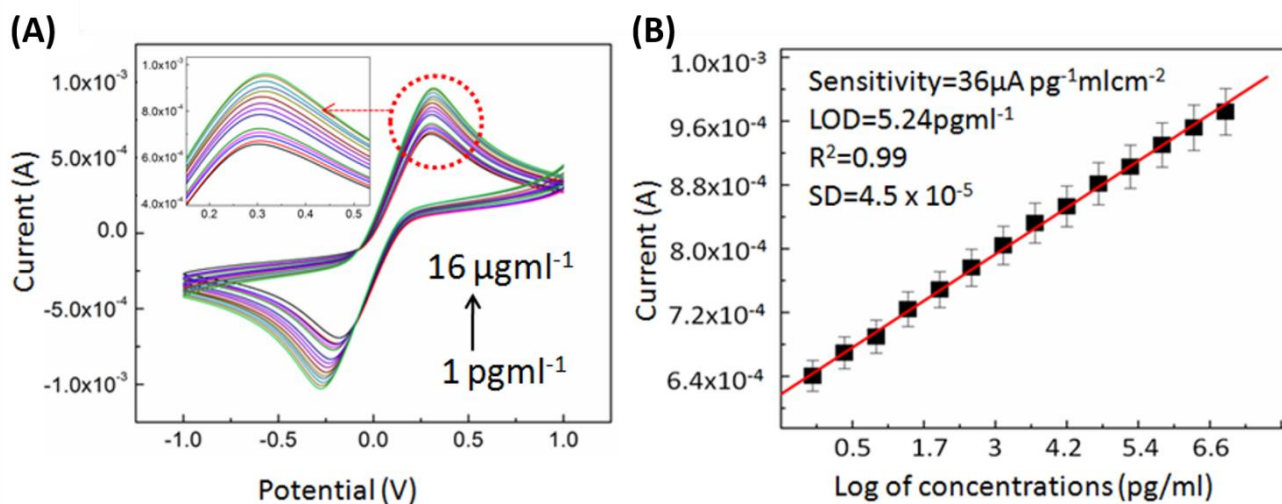
Figure 4-11: (A) CV showing the validation of the analytical ability of developed Phosphorene-modified platform for detection of myoglobin concentrations spiked in serum samples. (B) Fitting of peak currents showing linear concentration dependent increment in the current values.

ultrapure water to remove unbound protein and binding was confirmed by measuring the current response in cyclic voltammetry at a sweeping potential in a range of -1.0 V to +1.0 V at a scan rate of 0.1 V/second. The current response showed a linear elevation in the signal in a highly concentration-dependent manner (Figure 4-10A). Specificity of the developed platform was assessed by comparing the current responses of the system in presence of 1 µg/mL of serum albumin (bovine) and hemoglobin. The current response showed insignificant variation in the presence of cross-reactive proteins, thus establishing the specificity of the developed platform towards myoglobin (Figure 4-10B). This specificity was further validated by scrutinizing the developed myoglobin-specific detection platform for myoglobin concentrations spiked in serum. For this, myoglobin was added into the serum to a final concentration ranging from 1 pg/mL to 16 µg/mL and the electrochemical response was measured *via* cyclic voltammetry. The developed platform demonstrated concentration-dependent increase in the current values as the concentration of myoglobin was increased (Figure 4-11). The dynamic range of the sensor remained uncompromised although a slight decrease in sensitivity was recorded (51 µA/(pg/mL)·cm^2 for myoglobin in buffer *versus* 36 µA/(pg/mL)·cm^2 for myoglobin in serum). The stability of the developed platform was analyzed by performing the CV measurements at different intervals over time. This was done by preparing six electrodes under similar conditions and recording the change in current response in presence of 256 pg/mL myoglobin at 0th, 1st, 3rd, 7th, 14th and 21st day. The loss

of peak current was within 5% of the initial value during the period, suggesting a very stable platform for the detection of myoglobin(Figure 4-12).
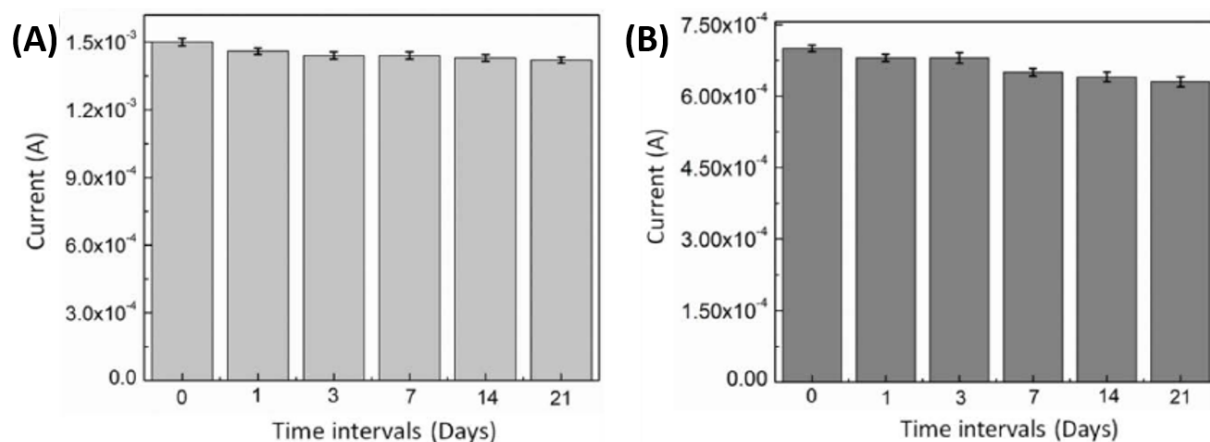
Figure 4-12: Stability studies of the developed phosphorene based aptasensor showing the change in peak current over various days' intervals in response to 256 pg/mL myoglobin in buffer (A), & serum (B) samples.

4.3. Conclusion

In this chapter, the role of electronically advanced nanostructures was investigated for the generation of electrochemical platforms for myoglobin quantification. The electrochemical platform developed using a nanocomposite prepared from two-dimensional rGO and one-dimensional CNTs possessed the ability to measure the presence of myoglobin in a range of 1 ng/mL to 4 μg/mL. The developed platform was improved by replacing the nanomaterial with few-layer phosphorene and by introducing a stringent binding strategy for aptamer immobilization. This improved platform showed a multifold enhancement in the dynamic range of the assay and was able to quantify the presence of myoglobin in both buffer and serum samples in the range of 1 pg/mL to 16 μg/mL. The developed platforms showed superior potential as sensitive detection modules for the estimation of myoglobin.

CHAPTER 5

Gold nanoparticle decorated WS$_2$ nanosheets based Raman-active platform for SERS-based quantification of cardiac marker

Raman spectroscopy is the technique that measures inelastic scattering of incident light showing a spectroscopic shift due to the Raman effect. This spectroscopic shift originates from the vibrational modes specific to the structure of a molecule and thus functions as characteristic Raman signatures of the respective molecule. The Raman signatures allow implementation of Raman spectroscopy as a powerful label-free analytical tool.[300–304] Although Raman spectroscopy is a sensitive technique that can be used for solid, liquid or gas samples, its sensitivity can further be enhanced by generating stronger signals. This Raman enhancement is a surface phenomenon and was firstly observed by Fleischmann in 1974 for the detection of pyridine over roughened surface of silver metal.[305–307] The enhancement is featured mostly due to metallic surface roughness or more recently due to nanoscopic metallic features like junctions, crevices or edges *etc*, and thereafter the technique is termed Surface-enhanced Raman spectroscopy or SERS. The increase in the Raman signals is critically due to the generation of *plasmonic hotspots*, either originating from the morphology of the plasmonic materials, as the plasmon is stronger at features like tips, edges, boundaries *etc*, or due to the interaction of closely lying plasmonic features.[306–311] Being a topology-dependent feature, SERS-based enhancement can be manipulated by organizing the nanoscopic features on a material. Several methods of nanomaterial arrangement have been reported which involve 0D core-shell nanohybrids[312,313], 1D structures like nanorods, nanotubes with surface decoration of metallic nanoparticles[314,315]; 1D or 0D plasmonic nanostructures on 2D planner sheets like GO, rGO, MoS$_2$ *etc*[316–318]; or 3D structures involving 2D nanohybrids of different nanosheets or 2D nanosheets separated with other non-planner nanostructures.[319–321] Among the reported methods of generation, spontaneous *in situ* assembly of such plasmonic nano-features has several

advantages over others, including the ease of synthesis, control over reaction parameters, rapid and cost-effective synthesis *etc*.

Objectives:

- Generation of WS$_2$ nanosheets using liquid phase exfoliation method
- Investigation of the reducing ability of WS$_2$ nanosheets for the *in situ* synthesis and decoration of gold nanoparticles on the nanosheet surface
- Investigation of the SERS abilities of the generated AuNP@WS$_2$ heterostructure using a Raman-active label molecule rhodamine 6G (R6G)
- Development of a Raman-based aptasensor for the specific detection of cardiac biomarker myoglobin

5.1. Generation of WS$_2$ nanosheets *via* LPE

A Raman-active nanocomposite was generated through *in situ* decoration of gold nanoparticles over the nanosheets of tungsten disulfide (WS$_2$). The nanosheets of transition metal chalcogenides have shown to possess reducing abilities centered around their edges and surface defects. This reducing ability can be utilized for the conversion of metals into their nanoparticles, which in turn are deposited over the nanosheets to create active plasmonic centers. Nanosheets of WS$_2$ were generated by force-assisted liquid phase exfoliation as this route generates nanosheets with several surface defects and morphological anomalies.[167] For this, 10 mg bulk WS$_2$ powder was soaked in 10 mL solution of N-methyl-2-pyrrolidone (NMP) and isopropyl alcohol (IPA) taken at a volumetric ratio of 3:1. This solution was sonicated using a horn-type probe sonicator operating at 30% amplitude for 2 hours with a pulse cycle of 5 seconds. The resulting solution was centrifuged at 10000 ×g for 30 minutes and supernatant was separated. The exfoliation of bulk WS$_2$ converted the solution from black to green suggesting the conversion of WS$_2$ from bulk into nanosheets. The exfoliated WS$_2$ suspension was characterized using various techniques to assess the presence of exfoliated nanomaterial.

5.2   Characterization of WS₂ nanosheets

i.   Morphological analysis

Morphological analysis of the nanosheets was done by directly visualizing the material under electron microscopes. Scanning electron micrographs were recorded by visualizing the nanomaterial drop-casted on Si substrate under a JEOL JSM-1T300 scanning electron microscope. Transmission electron microscopy of the sample dropped on a carbon-coated Cu TEM grid was performed on a JEOL JSM-2100 transmission electron microscope attached to an energy-disruptive X-ray spectrometer. The exfoliated material showed presence of nanosheets of few-layer status under both scanning and transmission electron microscope (Figure 5-1).
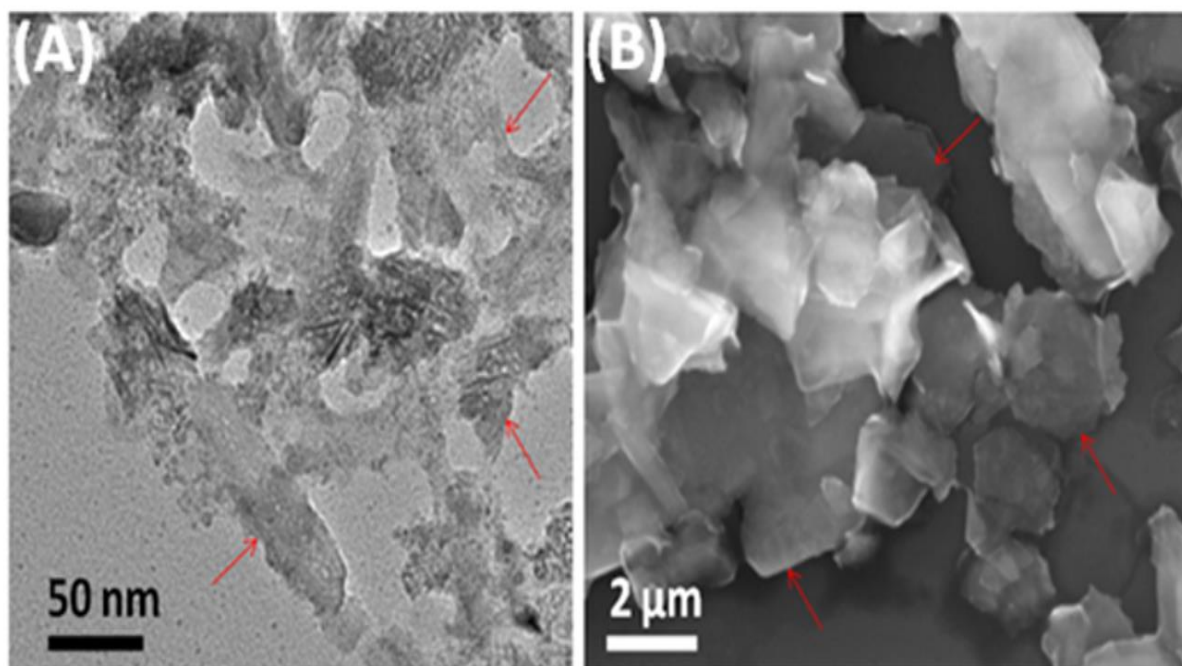
Figure 5-1: Morphological analysis of exfoliated WS₂ nanosheets through (A) Transmission electron microscopy, (B) Scanning electron microscopy.

ii. XRD analysis

The crystal structure of the nanomaterial was determined by analyzing the exfoliated nanomaterial against its bulk counterpart using a Bruker powder X-ray diffractometer. The X-ray diffraction pattern of the bulk WS₂ showed the presence
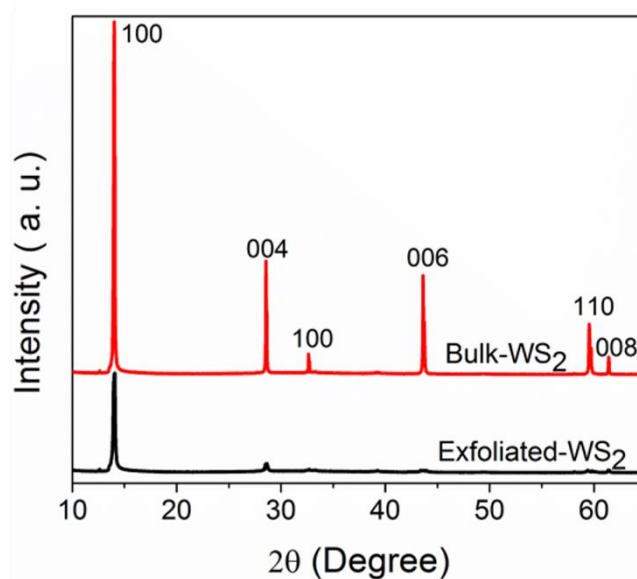
Figure 5-2: X-ray diffraction spectra of bulk and exfoliated samples of WS_2

of peaks at 14.364°, 28.959°, 32.769°, 44.055°, 57.495° and 60.010°, referring respectively to [002], [004], [100], [006], [110], and [008] phases of various lattice planes present in multi-layered WS_2 (Figure 5-2). The exfoliated sample of WS_2 showed absence or weakening of most phases except [002] phase at 14.2° referring to the planner nature of the material. The loss of major lattice phases suggested the stripping of multi-layered material into its few-layer form during the exfoliation process.

iii. Spectroscopic analysis

Spectrometric analysis of the exfoliated WS_2 was done by recording the absorbance spectrum of the suspension on a Shimadzu UV2600 spectrophotometer for a range of 300 – 750 nm. The baseline was corrected for the solvent by measuring 1 mL of NMP:IPA (3:1) mixture before recording absorbance of the nanomaterial. Absorbance spectrum of the nanosheets showed the presence of its signature peak around 628 nm that depicts the absorption arising from the excitonic transition of electronic bands (Figure 5-3A).[322]

Raman spectra of the nanosheets was recorded by drop-casting the exfoliated sample of WS_2 on a clean Si substrate, drying in a hot-air oven and analyzing under a WITEC alpha300R Raman spectrometer using a 532 nm laser. The Raman spectrum showed characteristic signature modes of WS_2 nanosheets

located at 352 cm^{-1} and 417 cm^{-1}. The modes correspond to E^1_{2g} and A_{1g} phonon modes for 352 cm^{-1} and 417 cm^{-1} respectively, which represent in-plane and out-of-plane vibrations (Figure 5-3B).[323]
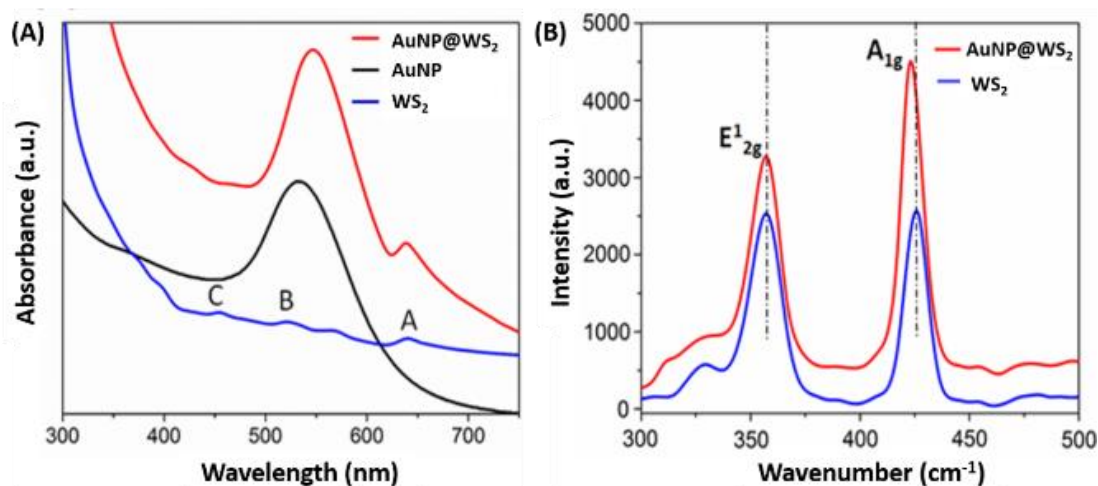
Figure 5-3: (A) Spectra showing visible-range absorbance of WS$_2$ nanosheets and AuNP@WS$_2$ nanohybrid. (B) Raman spectra of WS$_2$ nanosheets and AuNP@WS$_2$ nanohybrid showing the Raman enhancement.

5.3 Generation of gold nanoparticle decorated WS$_2$ nanosheets

The characterized nanosheets of WS$_2$ were used as reducing agents for generation of plasmonic nanocomposite by incubating in the presence of gold ions. To optimize the concentration of HAuCl$_4$, different concentrations ranging from 0.8 mM to 4 mM were added to the WS$_2$ suspension utilizing the reducing ability of the nanosheets in creating plasmonic nanocomposite. The concentration of gold ions in the solution act as a regulatory mechanism for controlling the size and inter-particle spacing of the gold nanoparticles, where high concentration tends to make multiple closely placed seeds in the beginning of the reaction that ultimately lead to creation of plasmonic hotspots. However, a very high concentration may cause aggregation of the particles that negatively affects the enhancement factor, which can occur only with the interaction of surface plasmons of particles. For the decoration of gold nanoparticles on these nanosheets, multiple reaction vials containing 1 mL of WS$_2$ nanosheets were heated at 80°C with vigorous stirring. To the stirring suspensions, 0.5 mg of

carboxy-methylcellulose was added as a stabilizing agent for the reaction. Different concentrations of HAuCl$_4 \cdot$3 H$_2$O (0.8 mM to 4 mM) were added in the reaction mixtures, and stirred for 30 minutes. The color of the reactions changed from greenish to red indicating the generation of nanocomposite (Figure 5-4). The mixture was removed from the stirrer, cooled and used without any further processing.
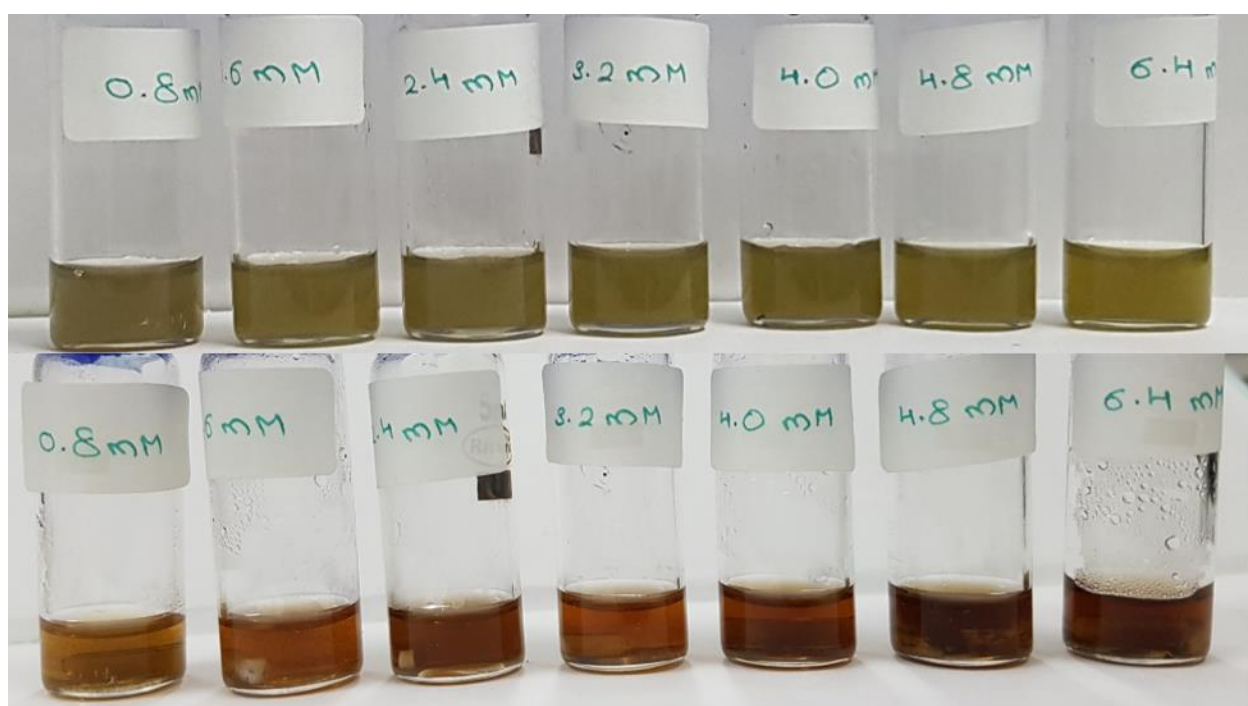
Figure 5-4: Images of different ratio of WS$_2$:HAuCl$_4$ before (above) and after (below) the completion of reaction.

5.4   Characterization of AuNP@WS$_2$ nanocomposite

i.   Spectroscopic analysis

The as-prepared samples of different reactions were analyzed on a Shimadzu UV2600 spectrophotometer by recording their absorbance spectra in a range of 300 – 750 nm. Absorption spectra of the nanocomposite showed characteristic absorption signature of WS$_2$ along with a new absorption band arising due to the plasmon of the nanoparticles (Figure 5-3A).[324]

Raman spectra of the nanocomposite and WS$_2$ nanosheets were recorded on a Witec alpha300R Raman spectrometer using a 532 nm laser source. For this,
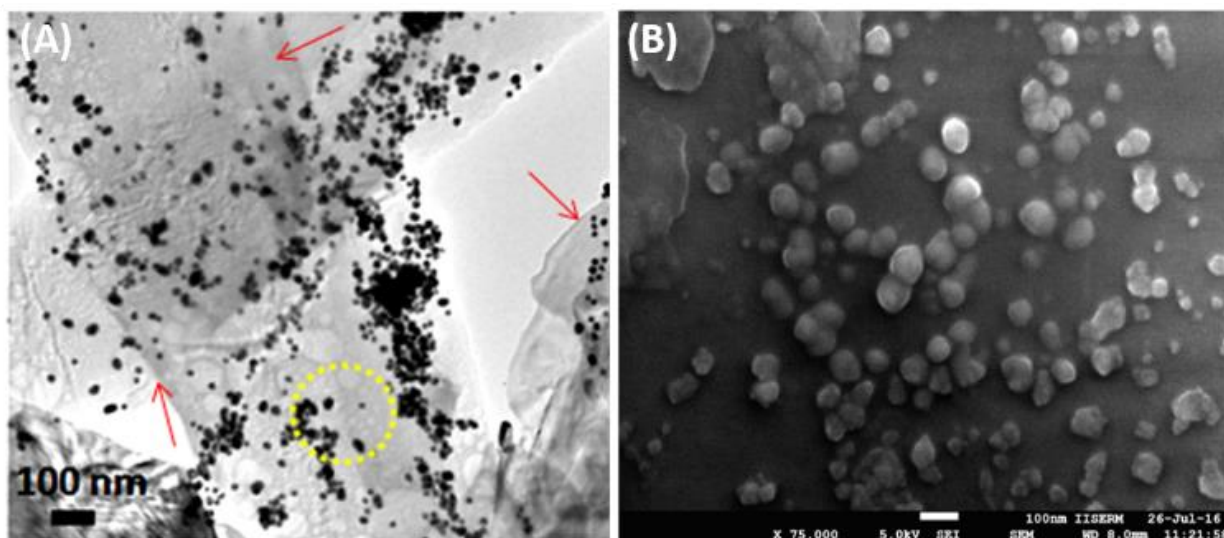
Figure 5-5: Morphological characterization of AuNP@WS$_2$ nanohybrid using (A) Transmission electron microscopy, and (B) FE-Scanning electron microscopy.

5 µL sample was drop-casted on a clean Si wafer, dried by heating at 60°C and observed under the spectrometer. The Raman spectra showed enhancement in the signature modes of WS$_2$ in case of the nanocomposite compared with the Raman spectrum of WS$_2$ nanosheets alone, creating an impression of the generated Raman enhancement by the nanocomposite (Figure 5-3B).

ii. Morphological analysis

Morphological characterization of the nanocomposite was done by electron microscopy. For transmission electron microscopy, 5 µL of 10% aqueous dilution of sample was dropped on a carbon-coated 200-mesh Cu TEM grid and dried under vacuum. The prepared sample was visualized under a JEOL JSM-2100 transmission electron microscope operating at 120 kV along with its elemental mapping and energy-disruptive X-ray spectrometry. The micrographs showed presence of metallic nanoparticles in the surface of WS$_2$ nanosheets, and its elemental mapping showed uniform signal of gold from the surface of nanosheets, suggesting an optimum coverage of the nanosheets surface with gold nanoparticles (Figure 5-5A). Field-emission scanning electron microscopy was done for 5 µL sample drop-casted on a fresh Si wafer using JEOL JSM-7600F FE-scanning electron microscope. The morphological analysis of the nanocomposite using FE-scanning electron microscope showed clusters of gold nanoparticles

lying on linear sheets of WS_2 (Figure 5-5B). The size of gold nanoparticles was measured using ImageJ image analyzing software, and an average size of 29 nm was obtained from 50 different points, and the inter-particle distance of closest gold nanoparticles was measured to be ~10 nm from the micrographs (Figure 5-6).
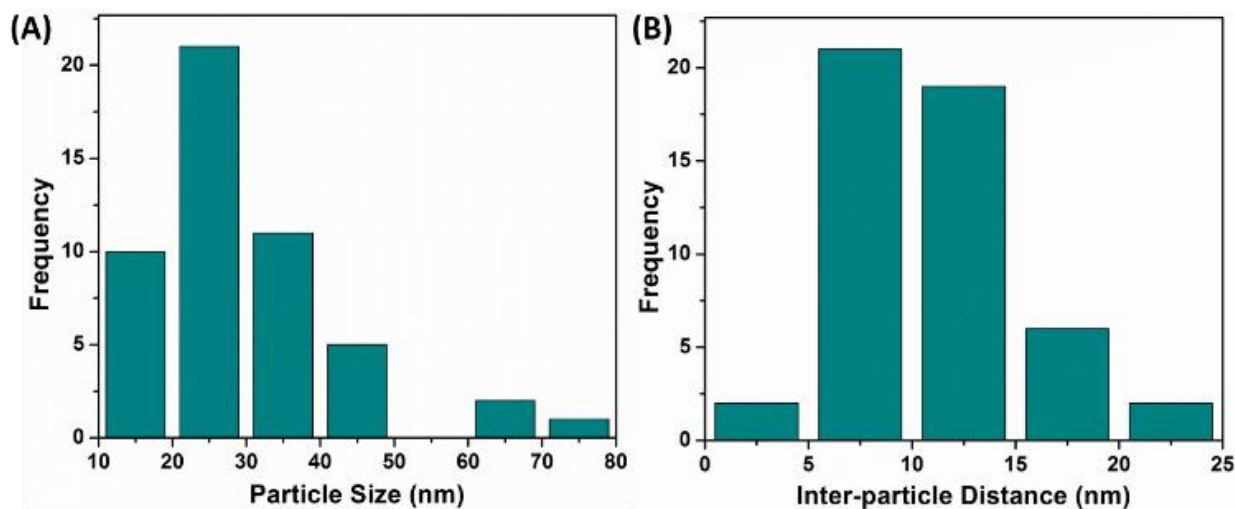
Figure 5-6: Particle distribution data, calculated from the FE-scanning electron micrograph, based on: (A) Particle size, and (B) inter-particle distance.

5.5.   Characterization of the Raman enhancement

The SERS effect generated by the plasmonic arrays is highly dependent on the spatial arrangement of the nanoparticles on the substrate's surface. However, in SERS platforms using isotropic metallic nanostructures, the generation of plasmonic hotspots majorly depends on the inter-particle distance than their orientation. The inter-particle distance of the plasmonic domains present in the array requires an optimum distance for the individual plasmons to interact and create an enhancement effect. The particles separated by large distances are unable to generate *surface enhancement* as their individual plasmons are not able to interact, however if the particles are arranged too close, they act as single unit and generate a single merged plasmon rather than creating an enhancement. Thus, there is an optimum distance range that is required for the arrangement of nanoparticles to generate an efficient enhancement effect and be utilized as substrates for SERS.

To understand the effect of distances on the surface enhancement by the gold nanoparticles, a theoretical model was generated by manipulating the inter-particle distances of the nanoparticles. To optimize the range under which the AuNP@WS₂ nanohybrid efficiently produces the hotspots, the plasmon of Gold nanoparticles separated by varying distances on WS₂ nanosheets was predicted using CST microwave studio (CST studio suite, Student edition). The optical constants for Gold nanoparticles and few layer thick WS₂ nanosheets were taken as $\mathcal{E} = 6.9$; $\mu = 0.467 + 2.415i$; and $\mathcal{E} = 6.86$; $\mu = 2.62$ respectively.[325,326] WS₂ sheet (500 nm × 500 nm × 10 nm) was modeled with longer axes on the x-y plane, having gold nanoparticles (30 nm) lying on top and a 532 nm light propagating along the z-axis from top (Figure 5-7 Right-top). The inter-particle distance was varied from 1 nm to 30 nm and the generated electric field was calculated along the longer axis for AuNP@WS₂ hybrid. As observed, the predicted electric field was highest when AuNPs were lying closest to the neighboring particle (~1 nm), which decreased subsequently with increase in the inter-particle distance up to ~15 nm (Figure 5-7 Left). As control, the simulations were repeated for AuNPs alone to assess the role of WS₂ on the plasmonic effect generated in AuNP@WS₂ hybrid (Figure 5-7 Right-bottom). In contrast to nanohybrid, the field for AuNPs was calculated to be 73%, and decreased sharply to 23% as the distance increased
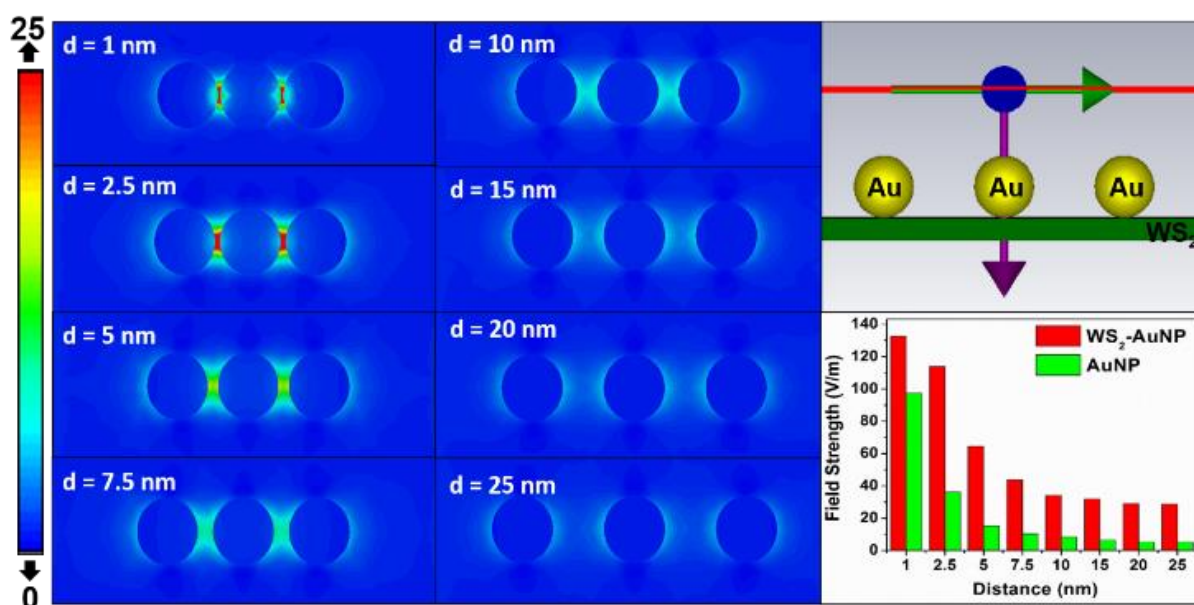
Figure 5-7: 2D representation of theoretical calculations showing the effect of inter-particle distance on the interaction of individual plasmons (Left). Right-top shows the model used for the calculations. Right-bottom shows comparison in the field strengths of AuNPs and AuNPs placed on a WS₂ nanosheet.

beyond 2.5 nm. This established the role of WS_2 in generating 4-folds enhancement in the field strength, while also creating a stabilizing effect for the plasmon.

Furthermore, a cluster of closely lying plasmonic nanoparticles generate a localized electric field in their inter-particle space that is a function of their distance.[327,328] The generated electric field was calculated from a form of Poynting vector while omitting the generated magnetic field.

$$E_{loc} = E_0 \ (D+d)/d \ .....[1]$$

Where E_{loc} is the localized electric field generated in the inter-particle space of closely lying particles, E_0 is the applied electric field, D is the particle diameter and d is the inter-particle distance.

Also from Poynting Vector, Electric field, $E^2 = P_{av} \times 2\eta \ .....[2]$

Where P_{av} is Laser power per unit area and η is characteristic impedance of air (376.73 Ω). For a Laser operating at a power of 45 mW at the fiber end with a waist of 354 nm after focusing through a 60× objective lens, the value of E_{loc} is calculated to be 39146.66 V/m for 30 nm AuNPs separated by a distance of 10 nm.

5.6. Validation of SERS effect of nanocomposite

The plasmonic nanocomposites generated spontaneously by chemical reactions are highly susceptible to the substrate ratios for generating an optimum effect. To optimize the substrate ratio for synthesizing AuNP@WS_2 nanocomposite, different concentrations of gold ions were added to a fixed concentration of WS_2 nanosheets. The reactions were processed simultaneously under identical conditions and the generated enhancement in the Raman signal was experimentally investigated for the composites. The different reactions were tested for their ability to enhance the signal of Rhodamine 6G. Rhodamine 6G is a member of xanthene based Rhodamine family of fluorophores (Figure 5-8) having
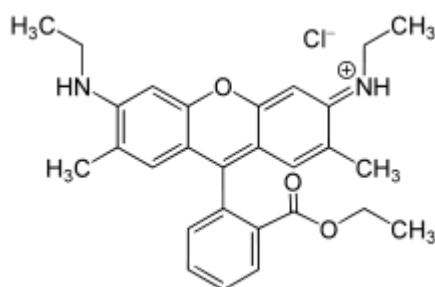
Figure 5-8: Structure of Rhodamine 6G

a strong resonance Raman absorption in the visible region. Due to the established, well-characterized and highly sensitive Raman signature of R6G upon excitation with a 532 nm green laser, it is generally used as a Raman-active label molecule for Raman measurements involving surface enhancements.[329–332] For the measurements, 10^{-5} M of R6G was added on different AuNP@WS$_2$ nanostructured substrates, and the signal intensity of the signature peaks of R6G at 1136 cm^{-1}, 1175 cm^{-1}, 1311 cm^{-1}, 1343 cm^{-1}, 1362 cm^{-1}, 1589 cm^{-1} and 1644 cm^{-1} was measured under constant parameters over the different synthesized nanocomposites.[333] The intensity of these signature peaks of R6G increased up to WS$_2$-Au$^{2.4}$ (composite generated by adding 2.4 mM HAuCl$_4$) after which it declined (Figure 5-9). The found pattern aligned with the hypothesis that aggregation caused at high concentrations of gold acts as a self-limiting factor in the reaction. Further, significant enhancement in Raman signal for R6G was observed within concentration range of 10^{-4} M to 5×10^{-8} M over WS$_2$-Au$^{2.4}$ nanocomposite with a highly linear concentration-to-signal relation (Figure 5-10). In contrast, AuNPs
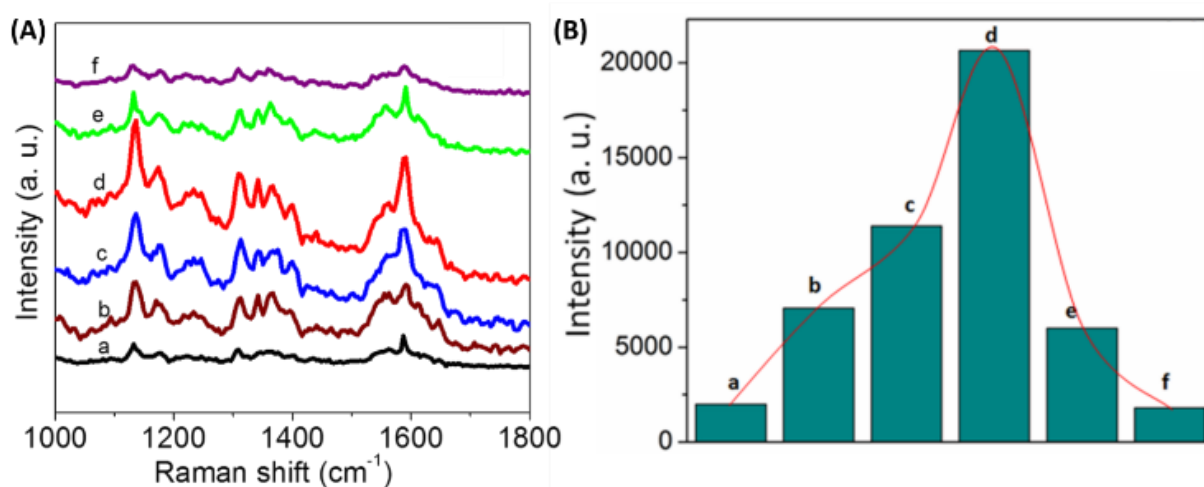
Figure 5-9: (A) Raman spectra of R6G molecules collected on different AuNP@WS$_2$, where a-f represents concentration of HAuCl$_4$ from 0.8 mM to 4 mM (B) Histograms showing Raman intensity of 1175 cm^{-1} signature peak.

115
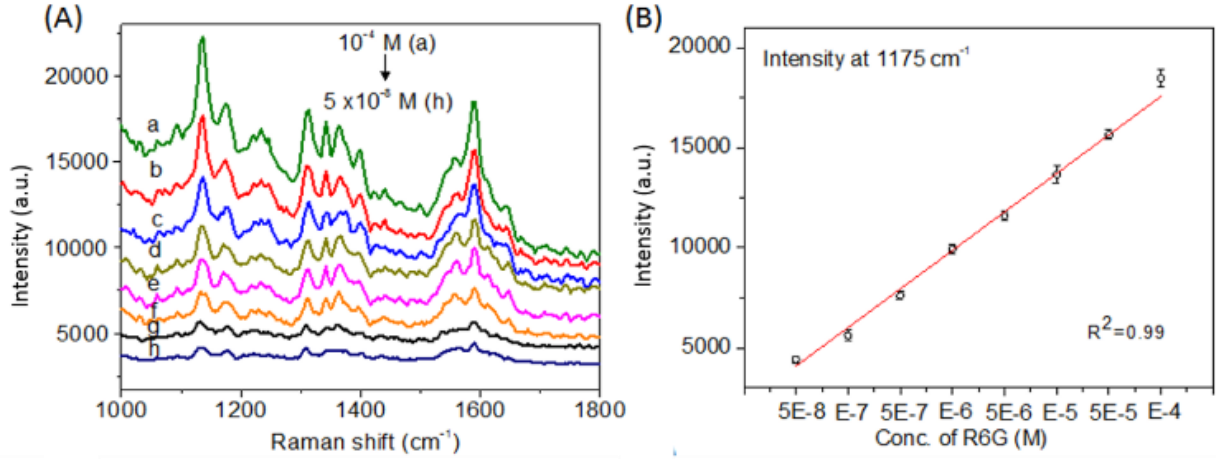
Figure 5-10: (A) Raman spectra of R6G molecules from 10^{-4} M to 5×10^{-8} M collected over AuNP@WS$_2$-modified substrate. (B) Fitted Raman intensity of 1175 cm^{-1} signature peak of R6G showing linear concentration-dependent increase.

alone displayed a weaker Raman signal for R6G than that of the multifold enhanced signals on nanohybrid SERS platform.

The Raman enhancement factor (EF) of developed WS$_2$-Au$^{2.4}$ SERS-active platform for R6G was measured experimentally by a direct comparison of Raman intensity of 1135 cm^{-1} vibrational band in the presence and the absence of WS$_2$-Au$^{2.4}$ nanohybrid using following equation[334–339]:

$$EF = I_{SERS}/I_{bulk} \times N_{bulk}/N_{SERS} \ .....[3]$$

Where I$_{SERS}$ is the intensity of 1135 cm^{-1} vibrational mode in the presence WS$_2$-Au$^{2.4}$ nanohybrid and I$_{bulk}$ is the intensity of the 1135 cm^{-1} vibrational mode in the bulk Raman spectrum from only R6G. N$_{bulk}$ is the number of R6G molecules used in the bulk, and N$_{SERS}$ is the number of R6G molecules used for the SERS experiment using WS$_2$-Au$^{2.4}$ nanohybrid surface. Further, N is calculated by the following equation,

$$N = A \times D \times C \times Av \ .....[4]$$

Where A is the area of laser falling on the substrate, D is the depth achieved by the laser, C is concentration of the analyte used and Av is Avogadro's number. However, for measurements having identical experimental conditions, the equation can be rewritten as,

116

$$N_{bulk}/N_{SERS} = C_{bulk}/C_{SERS} \ .....[5]$$

Using equation [5] and incorporating the effect of different laser power, Equation [3] can be rewritten as,

$$EF = I_{SERS}/ I_{bulk} \times C_{bulk}/C_{SERS} \times P_{bulk}/P_{SERS} \ .....[6]$$

From the experimental data, the enhancement factor was estimated to be approximately $\sim 6.78 \times 10^6$ in the case of WS$_2$-Au$^{2.4}$ nanohybrid.

5.7. SERS-based quantification of myoglobin

To develop a SERS-based aptasensor for detection of myoglobin, AuNP@WS$_2$ SERS platform was functionalized with anti-myoglobin aptamer and different myoglobin concentrations were exposed onto the sensor. For SERS measurements, 50 μL of prepared AuNP@WS$_2$ nanohybrid was drop-casted on a clean Si substrate and dried in ambient conditions. The dried sample was washed with ultrapure water to remove any residual nanomaterial and Raman measurements were recorded to confirm nanohybrid coating. Thiol-labelled single-stranded DNA (ssDNA) aptamer diluted in Binding buffer (Tris-HCl 10 mM, NaCl 150 mM, MgCl$_2$ 5 mM, pH 7.2) was immobilized on the AuNP@WS$_2$ modified Si substrate by drop-casting 10 μg DNA per 50 μL nanohybrid. The resulting sample was incubated in ambient conditions for 60 minutes, and washed with binding buffer to remove unbound DNA molecules. For this, 10 μL of each myoglobin concentration, ranging from 0.1 fg/mL to 10 μg/mL, were incubated on aptasensor surface for 15 min, washed with binding buffer and used for Raman measurements. A significant concentration-dependent enhancement in Raman signal was noticed within a concentration range of 10 fg/mL to 0.1 μg/mL (Figure 5-11A). The characteristic vibrational bands for myoglobin, positioned at 1126 cm^{-1} (due to C-N stretching), 1373 cm^{-1} (oxidation marker of heme, Fe) and 1560 cm^{-1} (C-C vibrations) were observed in Raman spectra.[340,341] Other bands in SERS spectra of myoglobin at 760, 1011, 1365 and 1554 cm^{-1} arise due to numerous
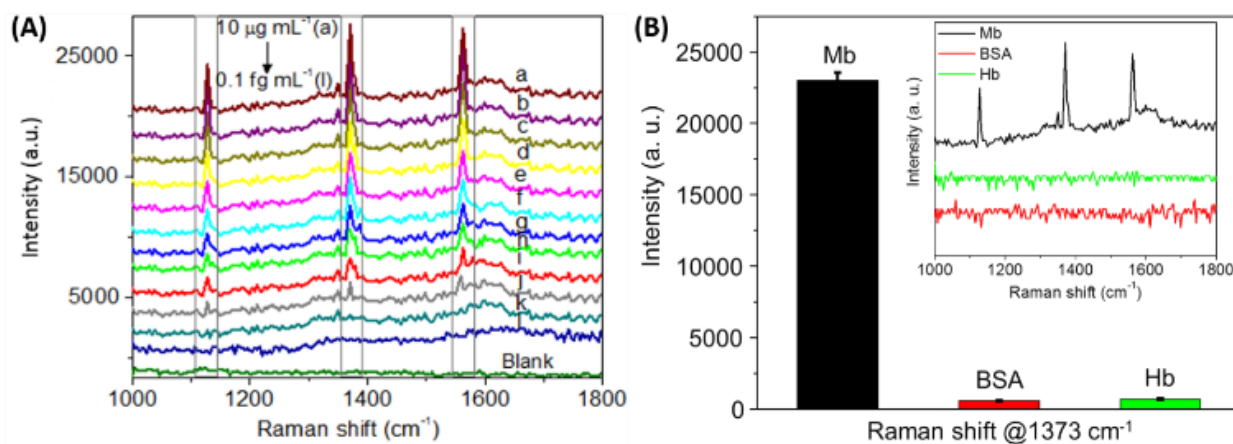
Figure 5-11: (A) Raman spectra of myoglobin molecules bound on the SERS-active platform showing an increase in the signature peaks. (B) Cross reactivity studies showing high selectivity of the developed platform towards myoglobin (Mb) in comparison to BSA and hemoglobin (Hb).

vibrational modes of tryptophan residues and some less intense bands at 1005 cm^{-1} and 1034 cm^{-1} were also observed due to phenylalanine residues of myoglobin respectively.[341]

The detection limit (LOD) of the developed SERS aptasensor was found to be 10^{-2} pg/mL, which is significantly low for the efficient quantification of Mb in clinical diagnosis. The formula used for the calculation is, LOD $= 3\sigma/m$, where σ is the standard deviation of the blank and **m** is the slope of the curve. To check the specificity of the developed aptasensor, a comparative study was done for the enhancement of signal in the presence of other serum proteins, Hemoglobin (Hb) and Bovine Serum Albumin (BSA). The signals produced in the presence of these protein molecules were negligible, which can be attributed to the use of screened aptamers specific to myoglobin (Figure 5-11B).

5.8. Conclusion

A SERS-active nanohybrid was generated by *in situ* growth of gold nanoparticles on the defected nanosheets of WS_2 utilizing their inherent reducing properties. The reaction was optimized to achieve an efficient enhancement in the signal of R6G, a Raman-active molecule. The morphological characteristics of the nanohybrid were validated through theoretical modelling, and the role of inter-particle distance as the decisive factor for the generation of a SERS-active substrate was established. The developed platform was successfully employed

for the ultra-sensitive quantification of myoglobin by using myoglobin-specific DNA aptamers.

CHAPTER 6

WSe₂ nanosheets-based impedimetric sensing platform

Among the electrochemical methods, Impedimetry is the technique that can be employed in a true label-free manner.[84,95,96,342] The basis of the technique is the obstruction to the current flow through electrode surface, as a function of applied frequency under a small AC voltage.[84] The impedance of the system fluctuates as a variable dependent on the binding of moieties over the electrode surface. The application of bioreceptors imparts the impedimetric sensors their required specificity, however the modification of sensor surface with high molecular weight bioreceptors generates high base impedance, thereof decreasing the sensitivity of the sensor towards the binding of analytes. The application of small weight bioreceptors like aptamers or peptide as an alternative to large bioreceptors have proved to be of higher potential in case of impedimetric biosensors.[343] Furthermore, the exploitation of highly electroactive nanomaterials as electrode materials provides a way to increase the sensitivity of the impedimetric biosensors towards the changes occurring on their interface respective to the analyte binding.[344,345]

As the electrode material, 2D nanosheets of tungsten diselenide (WSe₂) were generated by force-mediated solvent-assisted liquid phase exfoliation. The method utilizes physical forces to delaminate stacked nanosheets in naturally lamellar materials to single or few-layered state by vigorously shaking in presence of a solvent.[166,167,346] The use of an appropriate solvent is much sought-after in such procedures as the solvent assists in the delamination by seeping between the layers and weakening the inter-layer non-covalent bonds. The solvent further may act as a stabilizing agent for the freshly exfoliated nanosheets by preventing their interaction and subsequent restacking.

For the generation of WSe₂ nanosheets, a variety of solvents were evaluated to obtain a favorable exfoliation medium able to produce a stable nanomaterial. The nanosheets were thoroughly characterized, and implemented as electrode material for the development of an impedimetric biosensor for the detection of B-type natriuretic peptide (BNP), a cardiac biomarker.

Objectives:

- Optimization of solvents for the liquid phase exfoliation of WSe$_2$
- Investigation of the ability of poly-L-lysine as exfoliating agent
- Development of an impedance based platform for the detection of B-type natriuretic peptide

6.1. Generation of WSe$_2$ nanosheets *via* LPE

To find the best solvent for the liquid phase exfoliation of tungsten diselenide (WSe$_2$), exfoliating ability of different solvents *viz.* acetone, cyclohexanone, dimethyl formamide, dimethyl sulfoxide, water, isopropanol, methanol, N-methyl-2-pyrrolidone, and N-vinylpyrrolidone were tested. For this, 10 mg of bulk WSe$_2$ powder was soaked in the 5 mL of each solvent and sonicated for 1 hour with a horn-type probe sonicator operating at 30% amplitude in pulses of 5 seconds. The resulting solution was centrifuged at 1500 ×g, and the supernatant was collected for further characterizations. The extent of exfoliation was quantified by measuring the absorbance spectrum for each solvent and comparing the intensity of absorbance signature of WSe$_2$ nanosheets at 759 nm. The signature absorbance of WSe$_2$ occurs due to the A1 and B1 direct excitonic transitions existing due to the energy splitting of the valance band of WSe$_2$, and its spin orbital coupling.[347] For this, 1 mL of each exfoliated solution was measured for its absorption between a range of 200 - 900 nm on a Shimadzu UV2600 spectrophotometer after correcting the baseline for individual solvents. The solvent-corrected spectra showed the highest signature intensity for nanosheets of WSe$_2$ exfoliated in cyclohexanone, followed with isopropanol. Alternatively, an aqueous solution of poly-L-lysine (PLL) was used to exploit DNA binding owing to its ability to provide a cationic charge onto the exfoliated nanosheets following our previous studies on the application of PLL as an ionic mediator for the binding of DNA (Chapter 4, Section 4.2).[76] For exfoliation, WSe$_2$ was sonicated in aqueous solution of poly-L-lysine (0.1% w/v) using the parameters set for other solvents previously. The solution containing the nanomaterial was centrifuged at 10000 ×g and the pellet was washed twice with water to remove any free PLL, and finally suspended in water. The aqueous PLL solution was found to be the best medium
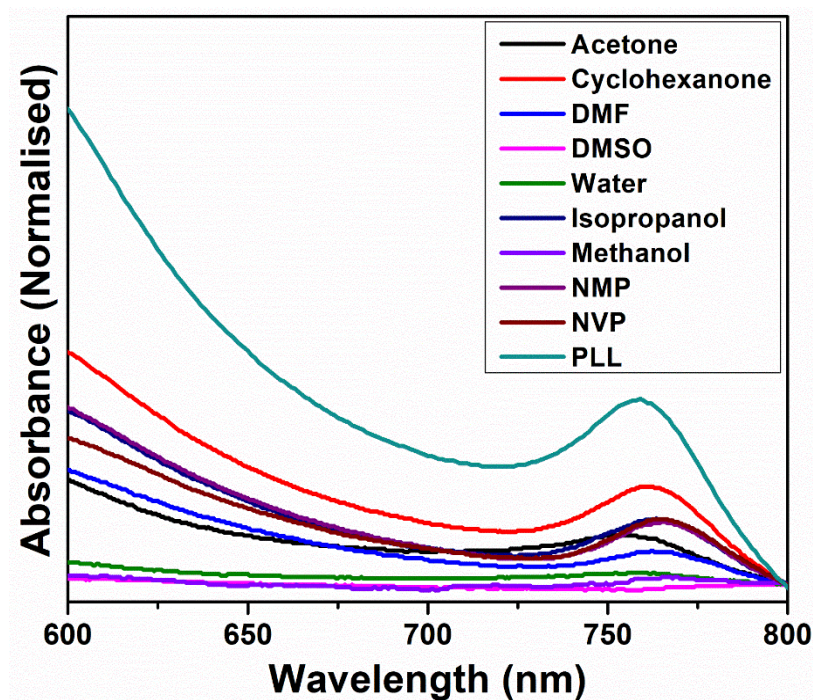
Figure 6-1: Comparative spectra showing normalized visible-range absorbance of WSe_2 nanosheets exfoliated in different solvents.

for exfoliating WSe_2 into nanosheets, as displayed by its signature absorbance that measured higher than WSe_2 nanosheets exfoliated in cyclohexanone, suggesting an efficient suspension with higher concentration of nanosheets (Figure 6-1). This finding was expected from the ability of PLL in creating a charged layer around the nanosheets, which in turn prevents the restacking of the nanosheets due to electrostatic repulsions.

6.2. Characterization of WSe_2 nanosheets

i. Zeta potential measurements

To confirm presence of cationic PLL on prepared nanosheets, zeta potential of the nanomaterial was measured using a Malvern Zetasizer. The nanosheets' suspension showed a net positive charge of +26.8 mV in the zeta potential measurements, which was attributed to the surface modification of nanosheets with PLL (Figure 6-2). To confirm the role of PLL as the origin of positive charge, WSe_2 nanosheets exfoliated in isopropanol were taken as a control for zeta charge analysis. The isopropanol-exfoliated nanosheets displayed a near neutral charge of +1.26 mV, thus validating the hypothesis.

123
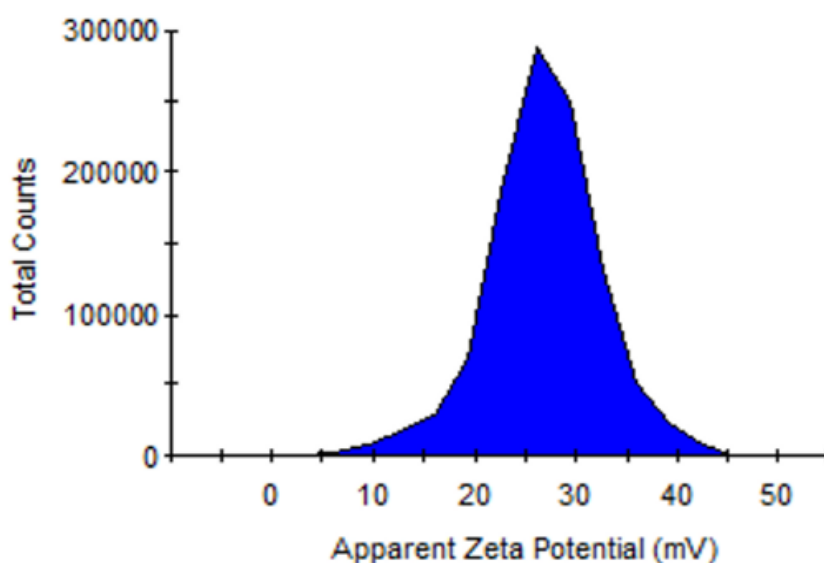
Figure 6-2: Zeta potential measurements of WSe$_2$ nanosheets exfoliated in PLL showing net positive charge.

ii. Raman Spectroscopy

Raman spectroscopy of the WSe$_2$ exfoliated in PLL (WSe$_2^{PLL}$) was performed using a Witec alpha300R Raman spectrometer. The sample was prepared by dropping a 5 µL drop of prepared exfoliated material over a clean Si wafer and drying in hot-air oven at 60°C. The drop-casted material was located
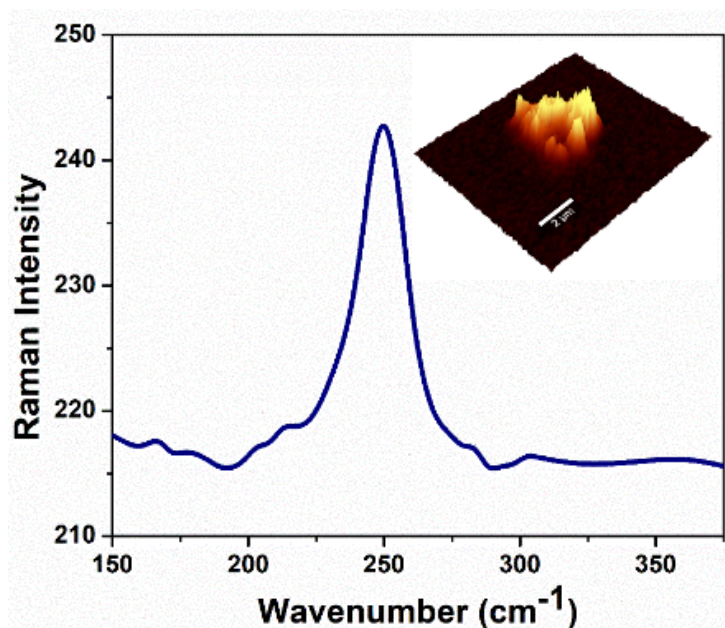
Figure 6-3: Raman spectrum of WSe$_2^{PLL}$ showing the characteristic signature absorption the nanosheets. Inset shows a 3D Raman mapping image depicting the Raman intensity from the selected area.

124

using the visible microscope assembly of the spectrometer and Raman signal was recorded at designated spots using a 532 nm green laser. The Raman mapping of the same spot was done for a 12 μm × 12 μm area by scanning the area for Raman signal and intensity was plotted as z-axis over the xy-image of the spot. Raman spectroscopic analysis showed a single degenerate band at 250 cm^{-1} depicting two signature phonon modes of E^1_{2g} (248 cm^{-1}) and A_{1g} (250 cm^{-1}), which appear as a merged band in case of WSe_2 nanosheets (Figure 6-3).[348,349]

iii. Morphological characterization

To understand the morphological characteristics of the exfoliated material, several microscopic techniques were utilized. For scanning electron microscopic analysis of the sample, 10 μL of as-prepared sample was drop-casted over a clean Si wafer, and visualized under a JEOL JSM-1T300 scanning electron microscope. The micrograph of the sample revealed nanosheets measuring around 300 nm at their longer axis having a characteristic signals of tungsten and selenium in EDX spectrum (Figure 6-4). For the transmission electron microscopy, 5 μL drop of 5% aqueous dilution of the sample was dropped on a carbon-coated 200-mesh Cu grid and dried under vacuum. The sample-containing grid was visualized under a JEOL JSM-2100 transmission electron microscope operating at 200 kV. The high-resolution transmission electron micrographs revealed small nanosheets measuring <100 nm at their longest axis (Figure 6-5A). The thickness of the nanosheets was investigated using an atomic force microscope operating in
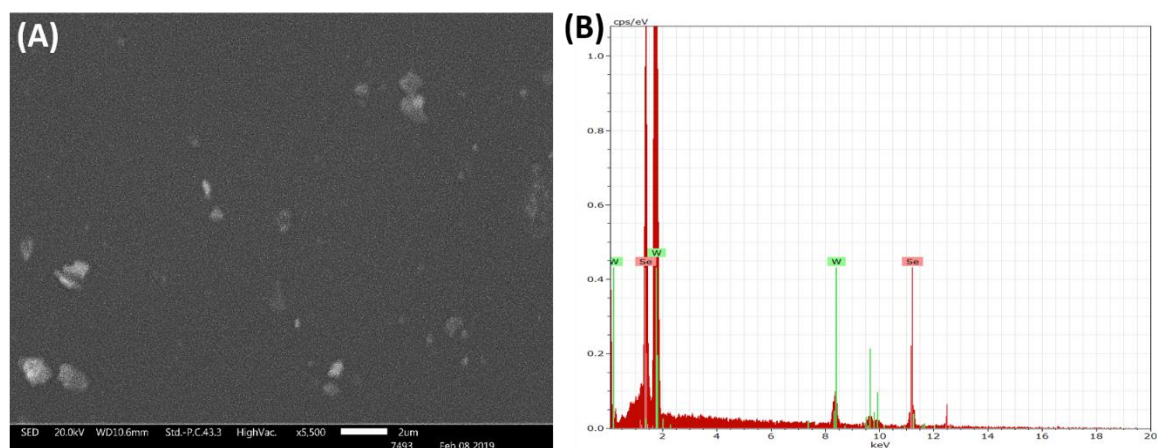
Figure 6-4: (A) Scanning electron micrograph showing exfoliated nanosheets of WSe_2. (B) EDX spectrum showing characteristic elemental emissions from Tungsten and Selenium.
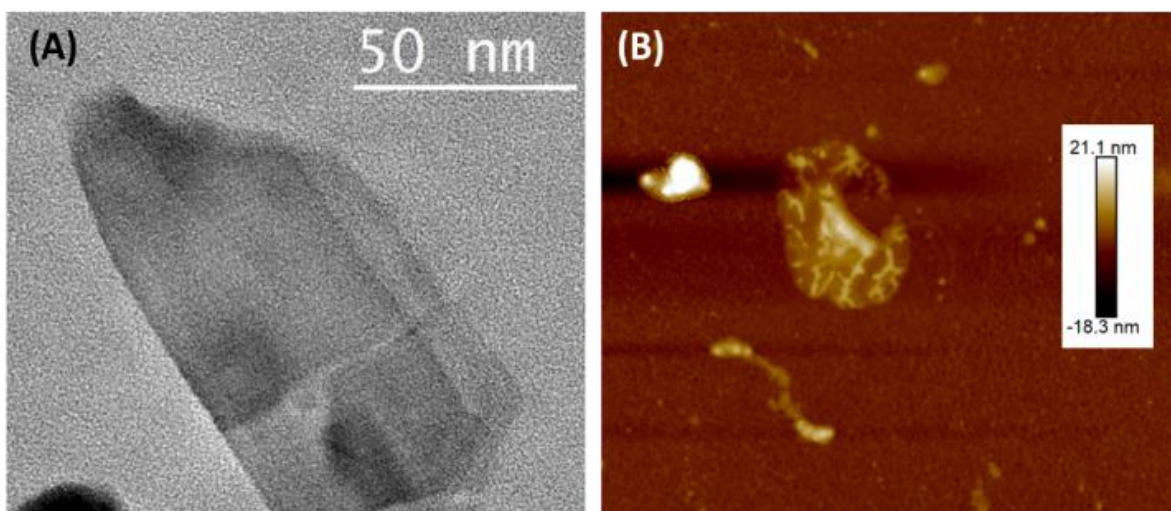
Figure 6-5: (A) Transmission electron micrograph showing the morphology of the exfoliated nanosheets. (B) Atomic force micrograph showing the height of the nanosheets.

tapping mode. The sample was prepared by dropping a 5% aqueous dilution of exfoliated sample on a fresh Si wafer, and washed with ultrapure water after incubating for 5 minutes. The thickness were found to be around 6 nm corresponding to nanosheets comprising of around 5-7 layers, considering the thickness added by the polymer coating onto the nanosheets (Figure 6-5B).[349]

6.3.   Development of impedimetric platform for BNP quantification

To generate a diagnostic platform for the detection of B-type natriuretic peptide, an electrochemical impedimetric system was developed. 2D nanosheets of tungsten diselenide (WSe_2) were utilized as the electroactive material for modifying the electrode surface. The optimum amount of WSe_2 nanosheets required for electrode modification was calculated *via* sequential loading of the electrode surface while monitoring the change in current response by recording cyclic voltammograms in a potential range of +1.0 V to -1.0 V. For this, PLL-exfoliated WSe_2 nanosheets were drop-casted onto the surface of working electrode of a screen-printed electrode in increments of 4.5 µg. Each increment was followed with baking at 60°C for 5 minutes to fix the material onto the surface and CV response was measured by adding 50 µL of ferricyanide-ferrocyanide electrolyte system. The current response in the voltammograms increased gradually with the addition of nanomaterial on the working electrode until 22.5 µg of the material was added (Figure 6-6). Addition of any nanomaterial beyond

126
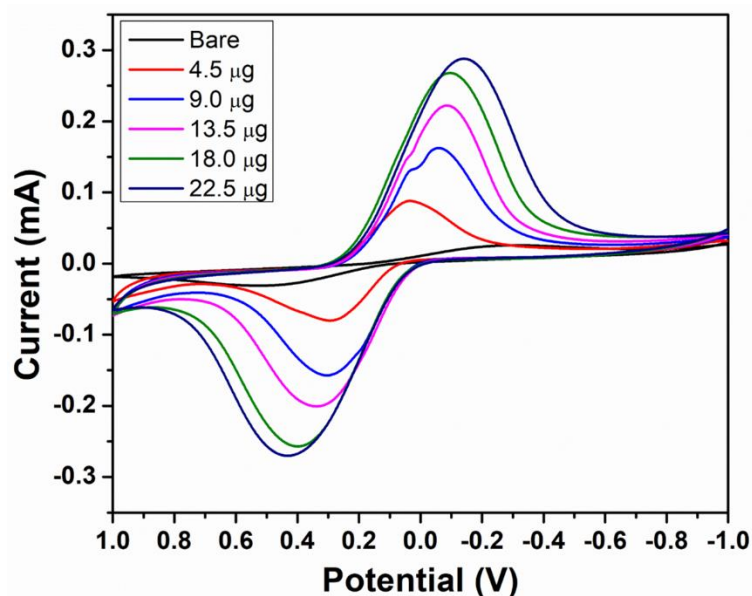
Figure 6-6: Cyclic voltammograms showing the increase in current response respective to the nanomaterial concentration on the electrode surface.

22.5 µg decreased the current response, which can be due to the overloading of the material on the electrode creating masking effects. The loading of nanomaterial was repeated thrice more and had similar results regarding the amount of nanomaterial added versus current response. For all further experiments, 22.5 µg of nanomaterial was added for the modification of the electrode in stepwise increment of 4.5 µg. Scan-rate dependent voltammograms were recorded between a fixed potential range by increasing the scan-rate from 0.01 V/s to 0.1 V/s. The response showed linear correlation with increasing scan-rate suggesting good electron diffusion properties of the developed system (Figure 6-7A). Stability of the modified electrode was tested by performing
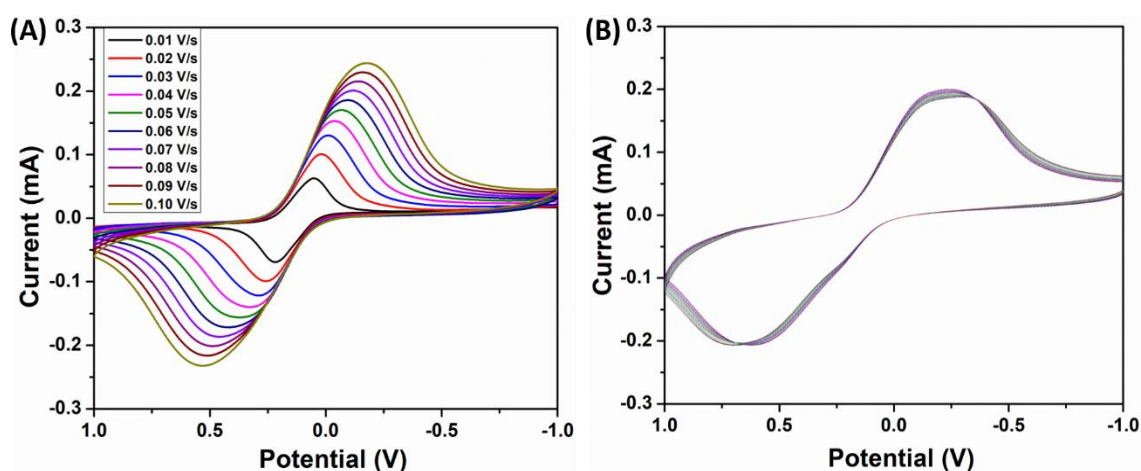
Figure 6-7: Characterization of nanomaterial-modified electrode through (A) variable scan-rate cyclic voltammetry, and (B) multi-scan cyclic voltammetry.
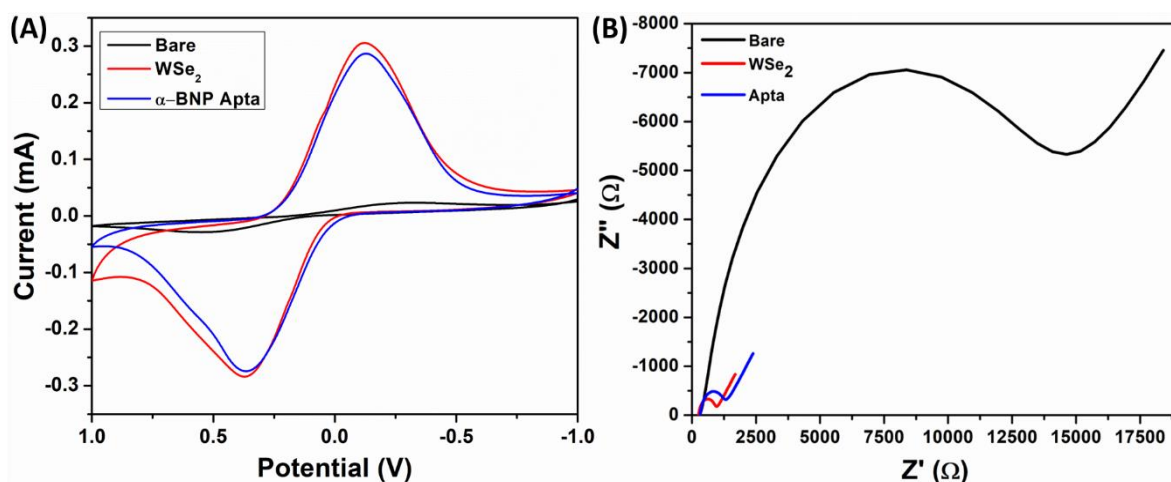
Figure 6-8: Validation of aptamer binding over nanomaterial-modified electrode surface *via*: (A) decrease in current response in cyclic voltammetry, and (B) increase in impedance in electrochemical impedance spectroscopy.

repeated scans (25 times) over the potential range of +1.0 V to -1.0 V at a scan rate of 0.1 V/s. The nanomaterial-modified electrode showed insignificant change in the current response suggesting formation of a stable layer on the electrode with no leeching of the material during voltammetric measurements (Figure 6-7B). The impedance of generated system was measured *via* electrochemical impedance spectroscopy for a frequency range of 1 Hz to 100 kHz using an alternative voltage with amplitude of 5 mV. The comparison of impedance of the nanomaterial-modified electrode showed very high reduction in the comparison to the unmodified electrode system, thus validating the findings from CV measurements (Figure 6-8B).

To generate a BNP-specific platform, WSe$_2$ modified electrode was further decorated with anti-BNP aptamer. After the coating of nanomaterial, the SPE was dried and 5 µL of aptamer stock (230 µg/mL) was added on the working electrode following the protocol for aptamer immobilization from previous studies (Chapter 4, Section 4.1), and incubated at room temperature for 15 minutes. Following the incubation, the electrode was washed with ultrapure water and binding was confirmed through electrochemical measurements in 50 µL of electrolyte. The current response in the cyclic voltammetry showed a decrease in current due to the binding of insulating aptamers on the electrode surface (Figure 6-8A). The observation was further validated by electrochemical impedance spectroscopy that showed an increase in impedance after aptamer modification (Figure 6-8B), which is consistent with our previous studies where successful modification with
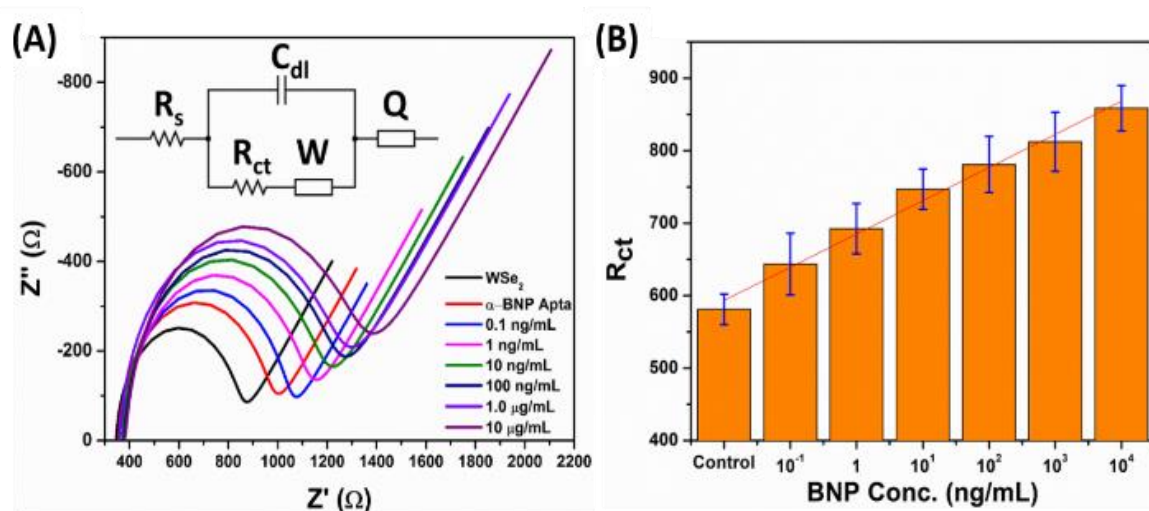
Figure 6-9: (A) Fitted Nyquist plots showing increase in impedance signal as a function of increasing analyte binding on the developed aptasensor. Inset shows the circuit diagram used for signal fitting. (B) Linear increase in the charge-transfer resistance (R_{ct}) as obtained from the Nyquist plots.

aptamers is seen to hinder the charge transfer by occupying some portion of the active surface (Chapter 4, Section 4.2).[343,350,351] The extension in the incubation time beyond 15 minutes did not yield any drift further and thus 15 minutes' incubation was maintained for the subsequent experiments. For the detection of B-type natriuretic peptide, different concentrations of the peptide were prepared by diluting the peptide stock (10 mg/mL) in binding buffer. 20 µL of each peptide concentration was added on the modified electrode to cover the entire electrode surface on the screen printed electrode. The chosen sample volume was limited by the physical dimensions of the electrode as the electrode area could hold only up to 25 µL of aqueous samples and volumes above 25 µL tend to spill over thus not contributing to the biointeraction process. The sample containing electrode was incubated at room temperature for 15 minutes. The electrode was washed with binding buffer once to remove unbound peptide molecules from the surface, and the amount of bound peptide was estimated by measuring impedance using electrochemical impedance spectroscopy. The impedance curves was fitted using Randles Sevick circuit to generate the Nyquist plots, which were overlaid to visualize the changes in response. The impedance of the system showed linear increase in its value with subsequent addition of the peptide concentrations (Figure 6-9A). Resistance to charge-transfer (R_{ct}) was calculated from the Randles Sevick circuit, and plotted against the concentration of the peptide added, which showed high linearity in the concentration range of 0.1 ng/mL to 10 µg/mL

129

(Figure 6-9B). The assay was repeated thrice and R_{ct} values were subsequently plotted showing less than 5% deviation thus establishing the reproducibility of the developed platform. The specificity of the developed platform was assessed by performing the impedance spectroscopy in the presence of 100 ng/mL of bovine serum albumin, hemoglobin and myoglobin. The reacting proteins brought insignificant changes in the impedance of the system in contrast to the B-type natriuretic peptide that created a surge in impedance (Figure 6-10). This observation confirmed the selectivity of the developed impedimetric platform towards BNP owing to the application of specific aptamers.
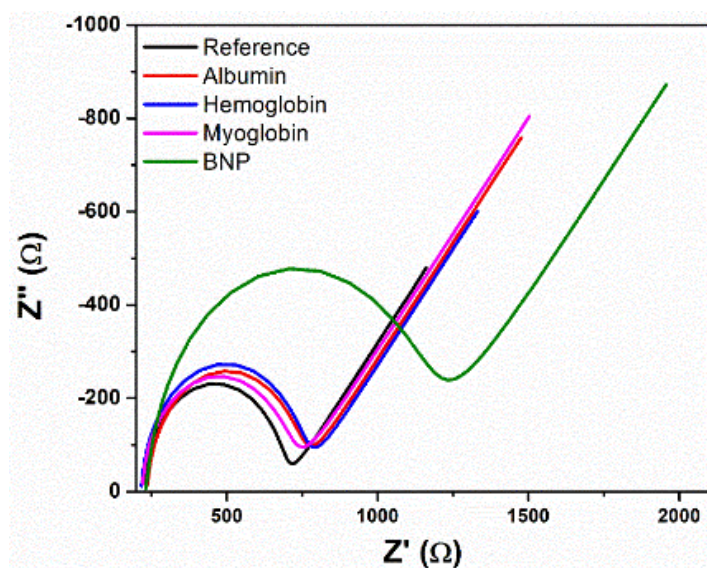
Figure 6-10: Cross reactivity validation of the developed platform in presence of different blood proteins.

6.4. Conclusion

A comparative analysis of the role of a solvent in the exfoliation of WSe_2 into its nanosheets was carried out, which showed the superior ability of polymers as the exfoliation agents. The exfoliated nanosheets were utilized as electroactive materials for the development of a specific impedimetric platform for B-type natriuretic peptide. The developed platform is sensitive towards the interfacial changes brought due to the presence of BNP in a concentration range of 0.1 ng/mL to 10 µg/mL with high degree of specificity.

CHAPTER 7

Microfluidics-based device for multiple cardiac biomarker diagnosis

A diagnostic device operating on whole or diluted blood requires a means of separating plasma from the cellular contents.[352–355] The separation step is essential to reduce to the interference by the cellular components with the analytical system. The conventional methods of plasma separation are either gravity-driven sedimentation of the blood cells, or centrifuge-based separation. While the former method is archaic, insufficient in complete removal, and highly time-consuming, the latter method requires special instrumentation, involving multiple steps and care for efficient separation. Therefore, the trend has shifted to *in-chip* plasma separations in a Lab-on-a-Chip assembly. In general, the in-chip separation strategies are either Passive flow dynamics-based, or Active methods using acoustics, electrophoresis or magnetic separation assemblies.[353,354,356] The active modes of separation require special equipment to achieve the separation, which although being efficient, decreases the applicability of the device by increasing the complexity of the system.

Among the passive flow-based separation methods, the most basic cellular separation is achieved by **Filtration** through a physical membrane with a pore size smaller than the erythrocytes.[357–361] The blood samples are passed through the membrane that retains the cells and only strained cell-free plasma is processed further. However, the method is restricted by the efficiency of membranes that affects the overall device performance. As the cellular content is not actively removed from the membranes during the operation, these can easily be clogged by the cellular overload, limiting the volume capacity of the device. Further, the membranes are prone to physical damages, desiccation and are not reusable. Alternatively, micro-sized beads or porous gels have also been employed as physical filtration units in place of filtration membranes, however these methods also have the same limitations as paper membrane-based filtration.[362–365] The advancement over cellular straining by a physical membrane is the application of microfluidics-based plasma separation by the incorporation of a **microscopic**

132

strainer in the microfluidics channels itself.[366-372] This type of separation uses channels or structures that are designed to be smaller than the physical dimensions of the blood cells. Upon the sample injection, only solution passes through the channels, separating them from the cells. However, this method is also prone to choking by the components of biological samples, which either affects the yield or can render the device inoperable. Further, several complex modes of microfluidics-based cellular separation have been devised employing cellular dynamics. Certain microfluidics devices involve a large blood channel (> 300 μm width) and based on the **Fahraeus-Lindqvist effect**, the cellular content tends to move towards the center of the channel thus creating cell-free zones near the walls to separate cell-free plasma.[373,374] This effect is further explored in devices involving the bifurcation of microfluidics channels containing blood into channels having different flow rates due of their design and construction. In such devices the cellular content of the blood, flowing through the central region of the channel due to Fahraeus-Lindqvist effect, tends to move through the wider channel having high flow rate based on the phenomenon of **Zweifach Fung effect** and cell-free plasma can be harvested from the narrower channel having slower flow rate.[355,375-377] Another type of plasma separation method called **Pinch-&-Expand method** is an advancement of the bifurcation method. Pinch-&-Expand method consists of a narrow channel through which the blood samples are passed at high flow rate.[354,378-380] The channel is immediately increased in width, creating a pinch junction where the blood sample experiences a rapid expansion. Owing to the differences in the dynamics of cell from plasma, cellular content tends to move out quicker, thus generating cell-free voids at the edges of the pinch junction from where plasma can be harvested by adding drain channels. Other separation methods use spiral channels through which the cells can separate *via* either centrifugal forces or the inertial forces. **Inertial force mediated separation** is a sophisticated method of cell sorting that allows the segregation of various type of cells according of the differences in their movement dynamics based on the acting inertial forces.[381-383] Whereas devices using **centrifugal forces** are only able to remove cells from the plasma without offering any cell sorting abilities.[384-387] Such devices are usually circular disc shaped systems that can be spun at their axis. The blood sample is introduced at the center of the disc and upon spinning the disc,

the blood sample experiences centrifugal forces. The movement of blood sample under the centrifugal forces causes separation of cellular content from the medium (plasma) due to the weight and dynamics differences. The discs can just be used for the purpose of plasma separation or may contain the analytical system integrated into them to create a Lab-on-a-Disc assembly.

While the cell straining method clearly has the limitation of cellular clogging, channel bifurcation and Pinch-&-Expand modules suffer from a narrow range of flow rate due to their dependency on high flow speeds to achieve separation. At slower flow rates, the cells do not experience enough forces or expansion to move in separate channels, causing cellular leakage in the plasma channels and affecting separation yields. Whereas the centrifugal devices based on spinning discs have less control over the dynamics, may cause cellular damage if large forces are applied thus contaminating the plasma, and are essentially not true microfluidic devices.

To overcome this limitation, we tried a hybrid system functioning on both microfluidic centrifugation and pinch-&-expand methods. For this, we fabricated an outward spiral channel that ultimately opened in a wider channel in a pinch-&-expand manner. The device intended to utilize the benefits of both methods to create a pre-separation based on centrifugal forces before entering the pinch module to generate a higher separation ability preventing any cellular leakage. The hybrid system allowed a wider range of operational flow rate and is found to be apt for plasma separation from diluted as well as whole blood.

Objectives:
- Photolithography based generation of microfluidics device for plasma separation
- Investigation of the improvement in cellular separation from whole and diluted blood by employing dual separation approach
- Development of a microfluidics based device with facility of multiplex diagnosis
- Generation of MoSe$_2$ nanosheets based electrochemical platform

- Development of microfluidics based multiplex detection device for the dual detection of cardiac biomarkers myoglobin and troponin I

7.1. Photolithographic microfabrication

7.1.1. Design of microfluidics device

The device was designed to have a central inlet (A) that wound out in circular channels for 9 turns (Figure 7-1). In contrast to the reported devices, this design allowed the control over the centrifugal force experienced by the contents of blood by varying the flow rate. The channel width in the centrifugal zone (B) was designed to be 100 μm, 200 μm & 300 μm to explore the effect of channel width on the plasma yield & separation efficiency. The channel from the centrifugal zone opened up in a wide channel (460 μm wide) and a plasma channel (100 μm wide) to generate a Pinch-&-Expand module (C). While the centrifugal zone was designed to put enough outwards pressure on the heavier cellular content during movement, the Pinch-&-Expand module was added to ensure the movement of only cell-free plasma in the plasma channel. Further, by incorporating two different dynamic separation strategies, the device was expected to function efficiently without necessitating very high flow rates. The plasma channel opened into a plasma reservoir (D, 4 mm diameter) that further lead through a 200 μm
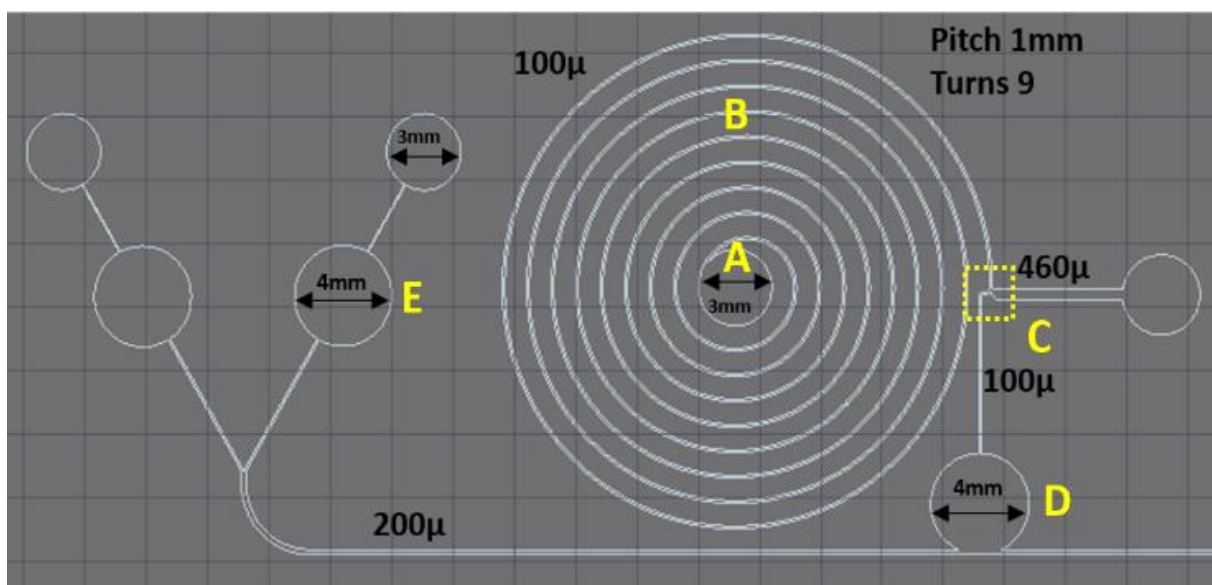
Figure 7-1: Diagram of the microfluidics pattern as designed in AutoCAD showing the location and dimensions of various features.

wide channel into the detection zones (E, 4 mm diameter), and finally exited through the final outlets.

7.1.2. Photolithography mask generation

The microfluidics pattern was designed in AutoCAD (Autodesk Inc., USA) keeping a minimum of 5 mm distances between different microscopic features of the designs. The designs were transferred to CleWin layout editing software (CleWin 4.0, WieWeb software), and used to create a *photolithography mask* on a chrome-coated glass *via* direct writing using Heidelberg µPG-501 mask writer. The mask itself was a square piece of soda-lime glass having a uniform coating of chromium on top. The chromium coating was etched using a laser beam to recreate the design onto the glass. The generated mask was a negative imprint of the design whereas the areas containing design features were etched off to create a transparent patterning on the chrome glass (Figure 7-2). The mask was cleaned by treating the mask in acetone & isopropanol for 8 minutes each and finally in a fresh piranha solution for 10 seconds. The mask was rinsed in DI water to clean the acid and blow dried using N_2 gas.
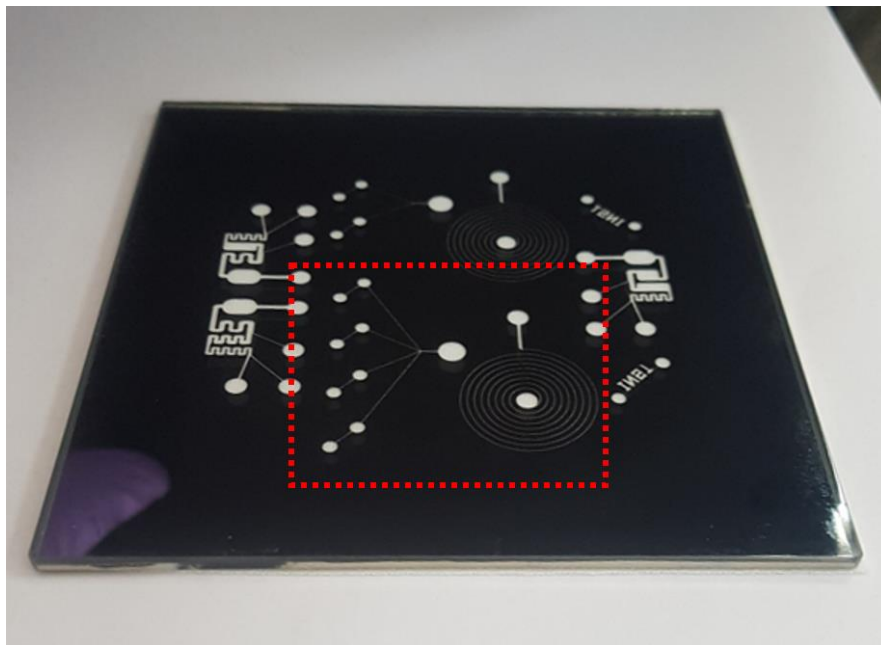
Figure 7-2: Photograph of the photolithography mask showing microfluidics patterns etched on the chrome-coated glass.

7.1.3. Microfluidics Master generation

The designed microfluidics patterns were replicated on a Si substrate to generate a microfluidics *Master* using a negative photolithography method.[388–390] The method uses a negative photoresist coated on a Si substrate, which is illuminated with UV light source through the photolithography mask. The region containing the designs on the mask are transparent and allow the UV light to pass and react with the photoresist underneath. The photoresist hardens in the presence of UV light and the structures are revealed upon subsequent washings. For this, a fresh p-type Si substrate was cleaned using acetone and isopropanol for 8 minutes each, and 10 seconds in a piranha solution. The substrate was dehydrated by heating for 10 minutes on a hot plate set at 250°C. This dehydration bake step removes any absorbed surface moisture that can hinder the binding of photoresist. A SU-8 2035 resist was spin-coated on the cooled Si substrate using a spin coater (Laurell spin processor Model: WS-650-MZ-23NPP) operating at 3000 rpm for 30 seconds to achieve a uniform thickness of 50 μm. The photoresist-coated substrate was heated for 1 minute on a hot plate set at 110°C to bind the photoresist on the substrate. This coated substrate was then exposed with UV light
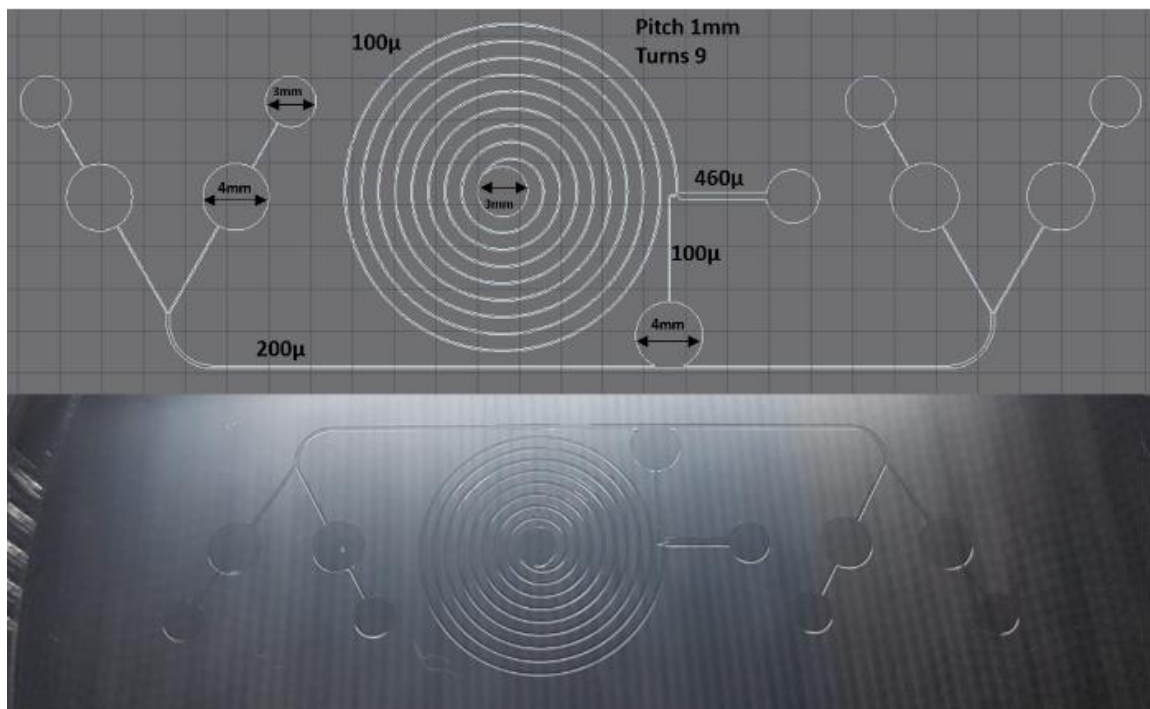
Figure 7-3: (Top) Diagram of the microfluidics pattern as designed in AutoCAD showing the dimensions of various features. (Bottom) Photograph of the master showing the microfluidics pattern embossed over Si substrate.

for pattern generation using EVG620, a semi-automatic contact photolithographic alignment and exposure tool. EVG620 was docked with the photolithography mask, photoresist coated Si substrate, and exposed in top-exposure manner with a 365 nm UV source operating at a strength of 180 mJ/cm^2. The exposed substrate was developed for 18-20 seconds using a SU-8 developer to fix the exposed areas, and undeveloped areas were removed by washing with isopropanol until the designs revealed. The developed *Master* was analyzed under a microscope to visualize complete removal of unexposed photoresist from the microfluidic patterns, and finally the substrate was hard-baked by heating at 150°C for 10 minutes to further strengthen the developed microfluidics patterns (Figure 7-3). The morphology of the generated patterns was analyzed by measuring the step height using a non-contact optical profiler (TalySurf CCI, Taylor Hobson, UK). The profiler showed a height of 50 μm across the *Master* confirming generation of a consistent pattern (Figure 7-4).
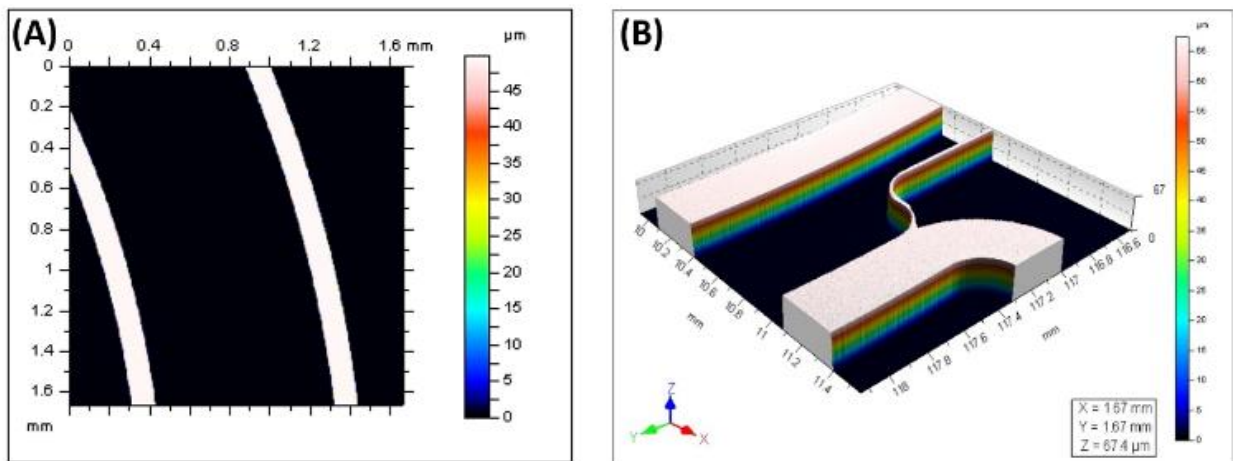
Figure 7-4: (A) Optical profiling of the microfluidics pattern showing the thickness of the photoresist. (B) Optical profiling of the microfluidics pattern showing the 3D view of separation module depicting the blood and plasma outlet channels.

7.1.4. Microfluidics device generation

Microfluidics devices were replicated from the generated microfluidics *Master* plate using a silicon-based elastomeric substrate, PDMS (poly(dimethyl siloxane)). PDMS has the ability to harden irreversibly in the presence of its curing agent, thus creating the impressions of microfluidics patterns embossed on the

Master plate. For this, PDMS elastomer and its curing agent (Sylgard 184) were taken in a ratio of 10:1 (w/w), and a homogenous mixture was generated by mixing vigorously following the manufacturer's protocol.[391] The PDMS mixture was poured on the microfluidics *Master* in a clean environment and kept under vacuum for 4 hours to remove any bubbles from the polymer. The degassed PDMS was heated at 45°C for 4 hours to polymerize the material, and then areas containing patterns were carefully removed from the *Master*. The inlets and exits were punched using a biopsy puncher (0.75 mm O.D.) and internal surface was cleaned using a scotch tape. A fresh glass slide was cleaned by sticking and stripping scotch tape and the PDMS mold was joined onto this by plasma bonding. For this, cleaned glass slide and PDMS mold were placed in a plasma bonder under vacuum and oxygen plasma was exposed for 3 minutes. The exposed mold was immediately placed on the exposed glass slide keeping the embedded designs towards the glass to create microfluidics channels. The generated device was then baked by heating at 80°C for 15 minutes to strengthen the bonding. The generated microfluidics was modified by inserting polyethylene tubing at the inlet and outlet holes and isopropanol was passed to clean the channels. An aqueous dye solution was passed through the device to visualize the construction of channels and to check the presence of any obstructions in the channels (Figure 7-5A).

7.1.5. Microfluidics-based plasma separation

The designed device was tested in its abilities to separate plasma from blood by flowing murine blood through the microfluidics channels. The device was connected with a syringe pump (New Era 2 channel programmable syringe pump, NE-4000, Figure 7-6) with a 5 mL syringe having a flow rate range of 0.08 μL/minute to 4.261 mL/minute. Murine blood was passed at different flow rates through the channels at different flow rates between 0.1 mL/minute to 4 mL/minute. The device displayed a separation of yellowish plasma even at 0.1 mL/minute flow rate although efficient separation was only observed at flow rates above 0.3 mL/minute. The separation was preliminary visualized by the appearance of RBC free yellowish plasma in the plasma channel (Figure 7-5B).
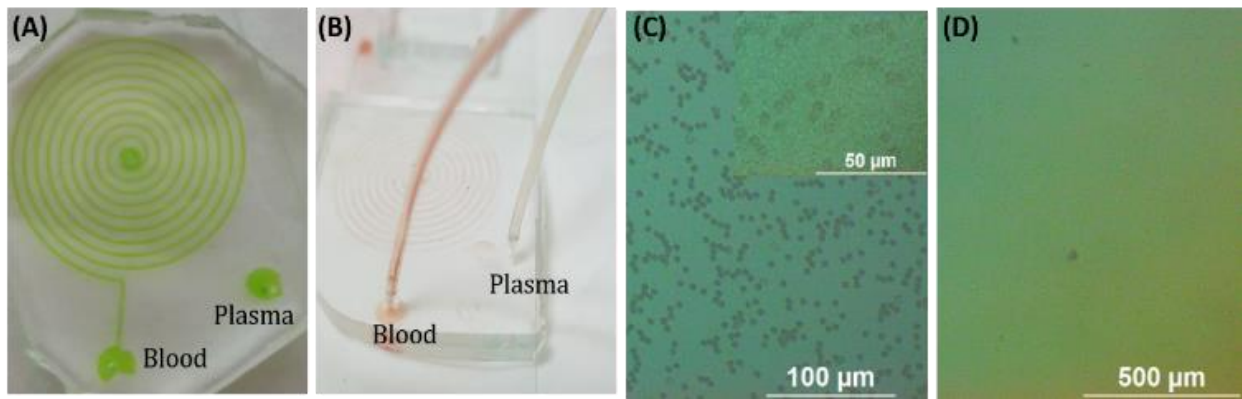
Figure 7-5: (A) PDMS mold of the device showing various microfluidics features after passing a green dye. (B) Plasma separation performance of the device with red blood in outlet labelled "Blood" and straw-yellow plasma in outlet labelled "Plasma". (C) Optical micrograph at 20× magnification of the sample collected from the "Blood" outlet showing presence of RBCs. Inset shows the optical micrograph of the same sample at 50× magnification. (D) Optical micrograph at 10× magnification of the sample collected from the "Plasma" outlet showing absence of any cellular material.

Among the fabricated devices, the separation efficacy was comparable as all the devices demonstrated equal ability for separating plasma at different flow rates. However, the extraction rate, which is the rate at which plasma is separated, was found to be highest in the device having 300 μm wide centrifugal zone. This can be due to the width of the channel that created a greater separation between the cellular components and the plasma. The device with 300 μm wide centrifugal zone was thus used for further experiments. To ascertain the separation efficiency, elutes from plasma & blood outlets were collected, and analyzed microscopically. For this, elutes were dropped on clean glass slides and visualized under a microscope (Leica DM2500 differential interference contrast fluorescence microscope) at 20× and 50× magnification. The microscopic analysis revealed presence of red blood cells in the blood channel while the samples from plasma outlet revealed a complete absence of any cellular material thus confirming complete separation of cellular materials from plasma (Figure 7-5C-D). The plasma elutes were further analyzed using an automatic blood analyzer (Sysmex

Criteria	Measured Value	Standard Value
RBC Count	$0 - 0.03 \times 10^6/\mu L$	$4 - 5 \times 10^6/\mu L$
WBC Count	$0 - 0.4 \times 10^3/\mu L$	$6 - 8 \times 10^3/\mu L$
Platelet Count	$20 - 173 \times 10^3/\mu L$	$150 - 450 \times 10^3/\mu L$
Hematocrit	$0 - 0.1\%$	$40 - 50\%$

Table 7-1: Table showing the cellular fraction in the sample collected from the plasma channel showing near complete separation efficiency of the device.

X-300) to further validate the plasma properties (Table 7-1). The biophysical analysis revealed absence of cellular components and reduction of hematocrit to 0.1%, thus establishing the developed device as an efficient tool for separating plasma from blood samples.

7.2. Generation of MoSe$_2$ nanosheets

The fabricated microfluidics-based plasma separation device was further developed into a multiplex detection device for the detection of two cardiac biomarkers. An electroactive nanomaterial made out of nanosheets of MoSe$_2$ were used as the transducing element of the electrochemical device. As found in our earlier studies (Chapter 6, Section 6.1), cationic polymer poly-L-lysine proved as an efficient exfoliation medium & conjugating linker, and thus was used as the *liquid phase* for the generation of nanosheets of MoSe$_2$. For this, 10 mg of MoSe$_2$ powder was added into 5 mL of aqueous PLL solution (0.1% w/v). The solution containing MoSe$_2$ powder was then sonicated using a horn-type probe sonicator operating at an amplitude of 30% with a pulse cycle of 5 seconds. The solution was sonicated for 1 hour, during which the color of the solution changed to brownish. The resulting suspension was centrifuged at 1500 ×g to separate large particles. The supernatant was collected and centrifuged at 10000 ×g to settle the suspending particles. The supernatant was discarded and the pellet was suspended in 5 mL of pure water by sonicating using the earlier protocol for 5 minutes. The resulting suspension was analyzed to check the presence of nanosheets.

7.3. Characterization of MoSe$_2$ nanosheets

i. Visible spectroscopic analysis

Absorption spectrum of the suspension was measured on a UV-Vis spectrophotometer (Shimadzu UV2600), which revealed absorption at 800 nm and 690 nm representing the A1 and B1 direct excitonic transitions of the material (Figure 7-6A).[347] Further, the position of the absorption peaks matched with the

literature reports for MoSe$_2$ nanosheets, suggesting the coating with PLL did not affect the characteristics of the nanomaterial.

ii. Raman Spectroscopic analysis

The Raman spectrum of the suspension was collected using a Witec Raman spectrometer (alpha300R) operating on 532 nm green laser. The sample was prepared by drop-casting 5 µL drop of the suspension on a clean Si substrate and drying at 60°C in a hot air oven. The spectrum of the suspension showed presence of signature peak at 248 cm^{-1} representing A$_{1g}$ vibrational mode which aligns with the literature reports (Figure 7-6B).[347,392] However, the weaker E^1$_{2g}$ vibrational mode appeared blue-shifted and was located around 310 cm^{-1}, which could be given to the presence of PLL over the nanosheets.
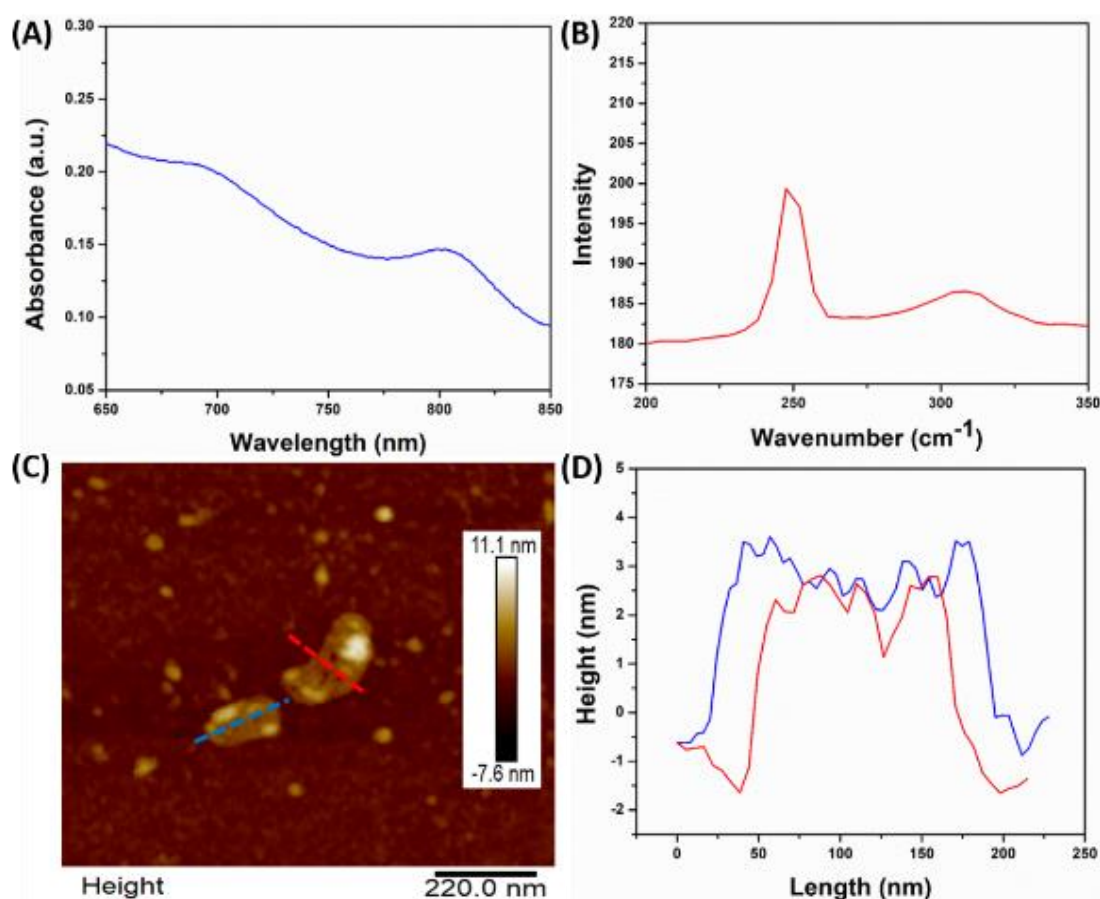
Figure 7-6: (A) Absorbance spectrum of MoSe$_2$ nanosheets showing the characteristic absorptions. (B) Raman spectrum of the MoSe$_2$ nanosheets showing signature Raman vibrational modes. (C) Atomic force micrograph of the nanomaterial showing their morphological features. (D) Height profile of the atomic force micrographs.

iii. Morphological characterization

Morphological characteristics of the nanomaterial were observed by visualizing the suspension directly under an atomic force microscope. The sample was prepared by dropping 5 μL of suspension on a clean Si substrate and incubating for 5 minutes. Thereafter the sample was washed with water, and visualized under an atomic force microscope (Multimode 8, Bruker, Germany) operating at tapping mode. The microscope showed presence of nanosheets having thickness of ~5 nm and measuring between 200-300 nm at their longest dimension on average (Figure 7-6C-D).

7.4. Validation of microfluidics device in multiplex cardiac diagnosis

7.4.1. Device design

The device was prepared by following a three-layer approach where each layer contained a separate feature of the device (Figure 7-7). The first layer containing the microfluidics patterns was synthesized of PDMS by pouring the polymer onto the microfluidics Master as given in Section 7.1.3. Layer 2 was fabricated by pouring PDMS in a glass slide and the solidified layer was harvested by cutting out the desired size. The layer was aligned with layer 1 and holes were punched to allow the passage of fluid from plasma chambers to the electrodes beneath. The layers were cleaned using scotch tape and activated by treatment with O_2 plasma to bond the layer together. The joined layers were heated at 60°C
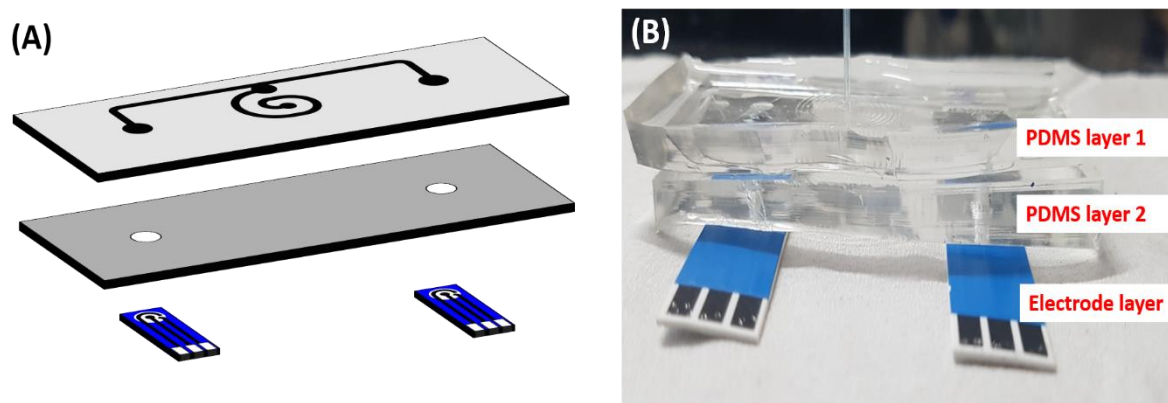
Figure 7-7: (A) Diagram showing the three-layer approach followed for the generation of the device. (B) Actual photograph showing final form and individual layers of the multiplex diagnostic device.

to strengthen the bonding further. Layer 2 acted as the floor for Layer 1 and completed the microfluidics channels. Layer 3 contained of electrodes modified with the electroactive nanomaterial, joined with the microfluidics device through a double-adhesive tape (3M Company, USA). The binding through the adhesive tape prevented any damage to the nanomaterial-modified electrodes decorated with respective aptamers and helped create a micro-reservoir for holding solutions during the operation of device.

7.4.2. Electrochemical characterization

The electrodes were prepared by modifying the screen-printed electrodes (TE100, Zensor, USA) with exfoliated nanosheets of $MoSe_2$. To find the optimum amount of $MoSe_2$ required for the preparation of sensors, cyclic voltammograms were recorded along with a stepwise increment in the nanomaterial amount. For this, 2.5 μL of $MoSe_2$ suspension was added on the working electrode of the sensor and dried at 60°C in a hot air oven. Cyclic voltammetric response of the sensor was recorded in 50 μL of Ferricyanide-Ferrocyanide electrolyte (5 mM equimolar solution prepared in phosphate buffered saline, pH 7.2). The current response showed significant improvement in comparison to bare response (Figure 7-8A). The sensor was rinsed, dried and another 2.5 μL of $MoSe_2$ suspension was added on the working electrode surface. The sensor was dried at 60°C, and current response was measured in 50 μL of electrolyte. It was observed that the current response showed maximum shift up to 5 μL of the suspension, and thereafter the
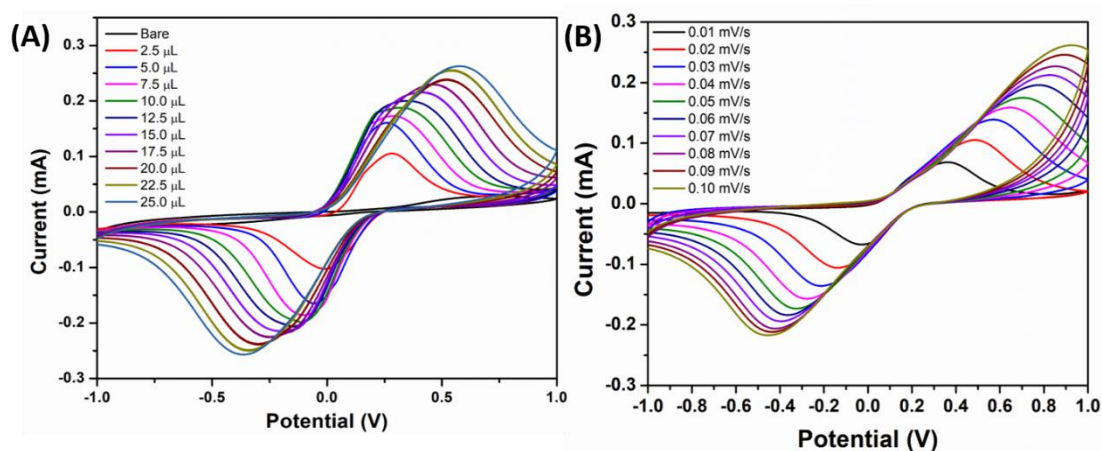
Figure 7-8: (A) CV curves showing the change in current response corresponding to nanomaterial concentration on the working electrode. (B) Scan-rate dependent cyclic voltammetric characterization of the nanomaterial-modified electrode.

144

increments were small and a shift in the cathodic and anodic peaks was observed. Thus to avoid layering effect due to the crowding of the sensor surface with very high amounts of nanomaterial, 5 µL of MoSe$_2$ suspension was chosen for further experiments. The sensor characteristics were analyzed by performing scan rate dependent cyclic voltammetry and a multi-scan cyclic voltammetry. Voltammetric measurements in the scan rate dependent were performed by varying scan rates from 0.01 V/second to 0.1 V/second and showed a linear increase in the current response as the scan rate was increased suggesting rapid electron diffusion properties (Figure 7-8B). The multi-scan measurements showed no significant variation in the current response over 50 scans, validating the highly stable nature of the generated nanostructured electrode.

7.4.3. Assay development

To create specific electrodes for the multiple diagnosis, MoSe$_2$ modified electrodes were further decorated with specific aptamers for myoglobin and troponin I. For this, 5 µL of each aptamer stock (250 µg/mL) was added on the working electrode and incubated at ambient temperature for 15 minutes. The voltammetric response from the sensors was measured that showed a decrease in the current signal suggesting decoration of aptamers on the sensor surface (Figure 7-9). The sensors were labeled as Mb-Sensor and TnI-Sensor corresponding to
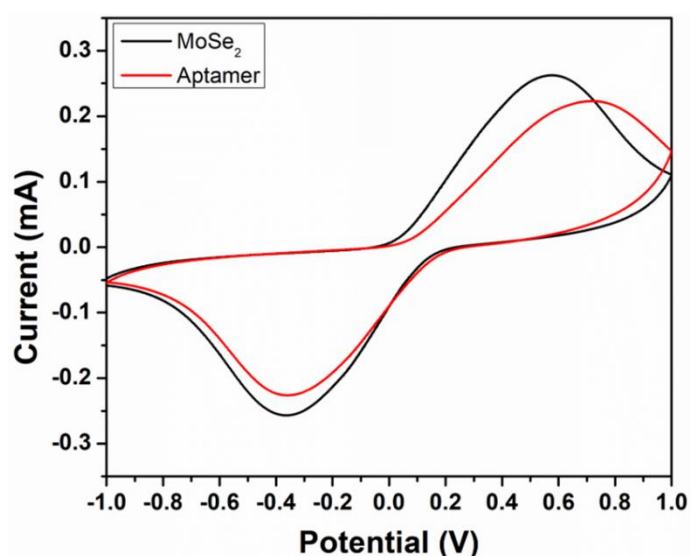
Figure 7-9: CV curves showing the decrease in the current response after the binding of aptamer on the electrode.

sensors modified with myoglobin-specific and troponin I-specific aptamers. The sensors were fixated on the microfluidics device through the double-adhesive tape, and the device was flowed with ferricyanide-ferrocyanide electrolyte solution (5 mM equimolar solution, prepared in 50 mM phosphate buffered saline, pH 7.2) and base values were recorded for the electrodes. Following this, the system was flushed with water to remove electrolyte and drained to prepare for analyte quantification. Different concentrations of myoglobin were passed through the device ranging from 1 ng/mL to 1 μg/mL. Each concentration was passed until it completely filled the micro-reservoir, and was incubated for 10 minutes. After the incubation, the device was drained, and phosphate buffer was passed through the channel to wash the channels. The electrolyte system was passed through the device and cyclic voltammetric measurements were recorded. The current response did not show significant changes corresponding to the increasing concentration of myoglobin. This was suspected to originate in the high base current due to the nanomaterial modification. To improve the Mb-sensor, the nanomaterial amount was reduced from 5 μL to 2.5 μL and the process was repeated for myoglobin detection. From the voltammograms, it was observed that the current response increased on the electrode modified with myoglobin-specific aptamer on the introduction of myoglobin to the device (Figure 7-10A). On the same device, the protocol was repeated for troponin I having concentrations ranging from 0.01 ng/mL to 10 ng/mL. Cyclic voltammetric measurements were recorded for the electrode modified with troponin-I specific aptamers. In contrast,
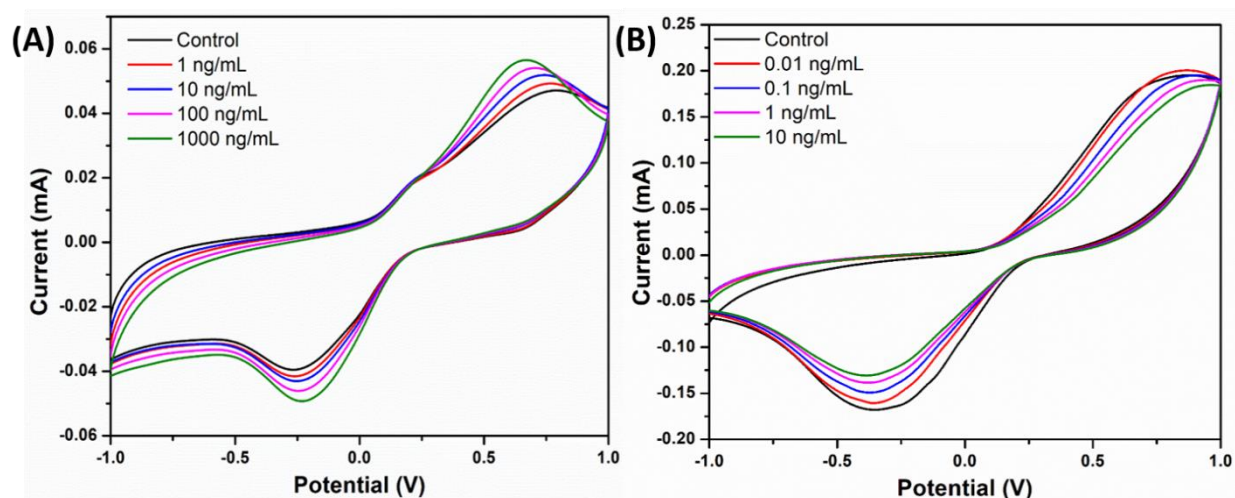
Figure 7-10: (A) CV curves showing the increase in the current signal in response to different myoglobin concentrations. (B) CV curves showing the decrease in the current signal in response to different troponin I concentrations

146

the electrode modified with troponin I showed a decrease in current in response to the binding of troponin molecules on the sensor surface (Figure 7-10B). The cross reactivity was also confirmed as the passed protein concentrations did not interfere with the current response in the opposing channel.

7.5. Conclusion

In this chapter, microfluidics-based separation of plasma from whole blood was investigated. For the purpose, a novel approach of using centrifugal forces in association with another separation technique was applied. This developed method is an approach that has never been reported as of now and the developed device possess excellent separation efficiency while maintaining high extraction rates. The device was further developed into a multi-chamber device to create a multiplex detection device. The applicability of the developed device was successfully tested on simultaneous detection of two cardiac biomarkers *viz.* myoglobin and troponin I. The device further has the potential of increasing the detection chambers to harbor and analyze more biomarkers from a single sample simultaneously.

CHAPTER 8

Conclusion & future perspectives

In this study, we have investigated various aspects of a biosensor with the aim to develop a sensitive diagnostic platform for the detection of cardiac biomarkers. It is already established that a precise cardiac diagnosis is dependent on the early detection of biochemical blood markers. The paramount requirement for an early and efficient biochemical cardiac diagnosis is the sensitivity of the biosensor that allows the user to detect the biomarkers at minute amounts and subsequently the associated disease at its initial stages. For the purpose, both components of a biosensor were explored to attain the desired sensitivities while avoiding any compromise in the specificity. As the bioreceptor, DNA-based aptamers were selected as replacement of conventional protein-based receptors. Sensitivity of the biosensors and the bioassay was compared by exploring various nanomaterials and their different properties were used to demonstrate biosensors based on different transducing approaches.

Chapter 2 of this thesis explains the development of DNA-based aptamers as biorecognition moieties. Aptamers were selected as bioreceptors than antibodies to overcome the general problems arising from the enormous sizes of antibodies. The aptamers are small molecular structures that have proven to be superior to antibodies as the biorecognition molecules on several fronts. The generation route for aptamers is a cyclic process called SELEX that has multiple variables allowing the ability to modulate the process. In this study, we experimented with the matrices and the overall generation methodology of SELEX to develop different routes that showed significant improvement over the methods available during this study. The most efficient and practical routes reported were flow-based, employing numerous solid matrices. We demonstrated that by replacing flow-based methods with an incubation-based method, the control over the process could be sufficiently enhanced. For this, we first developed a Microtitre Plate-SELEX, which used a microtitre plate surface as its stationary matrix. This allowed complete control over the retention times, and in turn over the interactions between target protein and nucleic acid sequences. Along with the developed method, we introduced a gradual expansion of reactive

surface area, achieved by increasing the number of involved wells, which created a dynamic inflation of the potential targets by relieving the selection threshold. This methodology was utilized for the development of DNA aptamers against a cardiac biomarker, myoglobin, in just 5 cycles. Subsequently, the SELEX process was further improved by introducing a single-reaction setup. The process was developed using biolayer interferometry where the sensor of the interferometer was used as the solid matrix, and was subsequently termed BLI-SELEX. The bound DNA molecules were further segregated based on their affinities by dipping in solutions with increasing dissociation strength. This method allowed the screening of specific aptamers in a single round and was used for the generation of aptamers specific to B-type natriuretic peptide and troponin I. A comparative analysis of the aptamers generated against the various cardiac biomarkers is given in tabulated from as Table 8-1.

	Anti-Myoglobin	Anti-BNP	Anti-Troponin I
T_m (°C)	56.8	51.2	54
GC content (%)	55.6	73.3	44.4
K_d (M)	0.65×10^{-10}	NA	30×10^{-8}
ΔG (kcal/mol)	-4.58	-4.90	-3.59
ΔH (kcal/mol)	-76.10	-111.50	-68.8
ΔS (cal/(K·mol))	-230.5	-343.7	-210.2

Table 8-1: Comparative table showing different characteristics and thermodynamic parameters of aptamers screened against different cardiac biomarkers.

The transducer component for the bioassays was selected by comparing different transducing approaches arising from different nanomaterials. The role of transducer was investigated by developing assays to quantify myoglobin using different nanomaterials. Chapter 3 explains the synthesis of carbon-based quantum dots as fluorescent mediums and development of optical assays based on competitive binding & direct quenching. The role of composition of quantum dots was also examined, and it was found that the incorporation of nitrogen and sulfur in the quantum dots enhanced the fluorescence of the nanomaterial. The developed assay could quantify the presence of myoglobin at a concentration range of 1 ng/mL to 100 µg/mL. The direct quenching assay was developed in Point-of-Care devices that utilized smartphones as the capturing and analyzing modules. Chapter 4 deals with the utilization of electronically active

nanomaterials as the transducers for developing electrochemical assays for the quantification of myoglobin. A van der Waals nanohybrid was synthesized from 2D reduced graphene oxide nanosheets and 1D carbon nanotubes. The nanocomposite was used as electrode material and the concentration of myoglobin was estimated by capturing the biomarker using its specific aptamers. The presence of myoglobin created an enhancement in the current signal due to its direct electron transfer property in a linear concentration-dependent manner between a concentration range of 1 ng/mL to 4 μg/mL. The assay was upgraded by replacing the nanomaterial and by introducing a more stable route of aptamer conjugation. For this, few-layered phosphorene was used as the electrode material and the aptamers were decorated onto the nanomaterial using a cationic polymer, poly-L-lysine. This directly improved the dynamic range of the bioassay, as the ability of the transducer to capture the target protein is completely dependent on the effective concentration of bioreceptor on its surface. Thus, the improved assay was able to respond to the concentrations of myoglobin in the range of 1 pg/mL to 16 μg/mL. Further, a more sensitive diagnostic platform was developed in the form of a Raman-active AuNP@WS$_2$ nanocomposite that is discussed in chapter 5. The nanocomposite was developed by utilizing the intrinsic reducing ability of exfoliated WS$_2$ nanosheets, which could reduce the gold into its nanoparticles. The nanoparticles, in turn, are decorated on the surface of the nanosheets thus generating a nanocomposite with Raman-enhancing properties. The enhancement was confirmed theoretically and experimentally using a Raman-active label probe Rhodamine 6G. The optimized platform was applied for the quantification of myoglobin through its specific aptamers and it was able to measure the cardiac protein in the concentration range of 10 fg/mL to 0.1 μg/mL. Among the developed platforms, SERS-based platform was found to be the most sensitive platform however the electrochemical platform demonstrated the widest dynamic range of detection. Therefore, electrochemical nanomaterials were chosen as the transducers for the development of the bioassays.

Based on the findings, an electrochemical platform was developed for B-type natriuretic peptide, a cardiac prognostic biomarker. For the detection of such small peptide, a sensitive electronically-active material was synthesized by exfoliating tungsten diselenide into its nanosheets. The exfoliation process was

optimized for maximum degree of delamination by experimenting with a plethora of solvents and was found that among the solvents examined, cyclohexanone was the best exfoliating agent for the generation of WSe$_2$ nanosheets. Alternatively, an aqueous solution of poly-L-lysine was also examined for its ability to convert the WSe$_2$ into its nanosheets considering the role of PLL in aptamer binding as found in our previous reports, and it was observed that PLL possessed an exfoliation ability superior to cyclohexanone. This finding was proved to originate from the ability of PLL to coat the exfoliated nanosheets, thus giving them net positive charge and preventing their aggregation. The exfoliated nanosheets were utilized in creating an impedimetric platform that was sensitive to the binding of the small cardiac peptide in a concentration range of 0.1 ng/mL to 10 µg/mL with high specificity. Table 8-2 enlists the different diagnostic platforms developed during this study against various cardiac biomarkers to provide a thorough comparative insight about the role of transducing approach towards the development of a biosensor.

Nanomaterial	Type	Transducing approach	Analyte	Limit of detection	Dynamic range	
					Lower	Upper
Carbon quantum dots	0D	Fluorescence	Myoglobin	1 ng/mL	1 ng/mL	100 µg/mL
NS-co doped Carbon dots	0D	Fluorescence	Myoglobin	10 ng/mL	10 ng/mL	100 µg/mL
rGO/CNT	1D@2D	Cyclic Voltammetry	Myoglobin	0.34 ng/mL	1 ng/mL	4 µg/mL
Phosphorene nanosheets	2D	Cyclic Voltammetry	Myoglobin	5.24 pg/mL	1 pg/mL	16 µg/mL
AuNP@WS$_2$	0D@2D	SERS	Myoglobin	10 fg/mL	10 fg/mL	0.1 µg/mL
WSe$_2$ nanosheets	2D	Impedimetry	BNP	0.1 ng/mL	0.1 ng/mL	10 µg/mL
MoSe$_2$ nanosheets	2D	Cyclic Voltammetry	Myoglobin & Troponin I	1 ng/mL (M) 10 pg/mL (T)	1 ng/mL (M) 10 pg/mL (T)	1 µg/mL (M) 10 ng/mL (T)

Table 8-2: Comparative table showing various developed diagnostic platforms.

Finally, chapter 7 deals with the generation of a microfluidics-based device as a tool for multiplex detection of cardiac biomarkers. A device functioning on whole blood can be divided into two general sections, *i.e.* a plasma separation unit and a detection unit. To generate a device with the ability to passively separate plasma from its cellular components, a novel combination approach was

employed. The device was designed to contain two separate separation dynamics to produce an enhanced separation efficiency. Further, the design contained an outward winding spiral that generated a centrifugal force on the cellular contents for their separation. The device was fabricated by photolithography and showed a remarkable RBC separation efficiency of ~99% along with an ability to function at flow rates as low as 0.1 mL/minute. The device was further designed & fabricated to house a detection unit, and was developed into a multiplex device that could process a single sample for the presence of myoglobin or troponin I by measuring the fluctuations in the current signals in voltammetric measurements on a $MoSe_2$ nanosheets-based electrochemical system.

The ability of simultaneous multiplex detection holds huge potential in clinical diagnosis as the parallel measurement of multiple biomarkers from a sample generates a self-validating response that increases the credibility of the triage, and the developments scribed in this thesis can prove revolutionary in the cardiac disease management. Further, the task of continuous & intermittent measurements to cultivate a long-term biomarker profile needed for the screening the individuals with impending disease condition relies heavily on cost-effective and portable means of detection. The methods developed for the generation of DNA aptamers are novel and present enormous improvements on the available methods. The methodologies reported in this thesis simplify the screening route while enhancing its efficacy, thus increasing the overall desirability of aptamers as biorecognition molecules while maintaining the involved costs. Furthermore, it has become evident that future diagnostics is going to benefit immensely from the improvements in the smartphone technology and the increasing capabilities of embedded camera units. The amalgamation of bioassays with small handheld units that can be attached freely with smartphones can bring a drastic frameshift in the current assay scenario as it not only provides ease-of-operation & portability, but also the power to upload, record & distribute community-wide data. Further, the advances in the miniaturization of more sophisticated biosensing techniques like mass-based cantilevers; Raman spectrometers *etc.* will highly benefit the society and economy by reducing the disease burden through identifying minute fluctuations in the proteome in the very early stages of a disease.

153

Publications

Published:

- Shorie, M.[#], Kumar, V.[#], Sabherwal, P. & Ganguli, A. K. Carbon quantum dots-mediated direct fluorescence assay for the detection of cardiac marker myoglobin. **Current Science** *108,* 1595-1596 (2015).

- Kumar, V.[#], Shorie, M.[#], Ganguli, A. K. & Sabherwal, P. Graphene-CNT nanohybrid aptasensor for label-free detection of cardiac biomarker myoglobin. **Biosensors & Bioelectronics** *72,* 56-60 (2015).

- Kumar, V., Brent, J. R., Shorie, M. *et al.* Nanostructured aptamer-functionalized black phosphorus sensing platform for label-free detection of myoglobin, a cardiovascular disease biomarker. **ACS Applied Materials and Interfaces** *8,* 22860-22868 (2016).

- Shorie, M.[#], Kumar, V.[#], Kaur, H., Singh, K., Tomer, V. K. & Sabherwal, P. Plasmonic DNA hotspots made from tungsten disulfide nanosheets and gold nanoparticles for ultrasensitive aptamer-based SERS detection of myoglobin. **Microchimica Acta** *185,* 158 (2018).

- Srinivasan, K. S., Raghavan, V. S., Shorie, M., Sabherwal, P., Gorthi, S. S., Asokan, S. & Sood, A. K. Enhanced optical sensitivity of PVA-rGO electrospun nanofiber coated etched fiber Bragg grating sensor for detection of Myoglobin a cardiac biomarker. **Advanced Photonics Research** (Just Accepted).

To be published:

- Shorie, M., Kaur, H. & Sabherwal, P. Novel biolayer interferometry BLI-SELEX (BLIS) for aptamer generation and sensitive electrochemical detection of cardiac marker BNP on few-layer WSe_2 nanosheets. (Communicated).

- Shorie, M., Kaur, H. & Sabherwal, P. Microfluidics based device for separation of plasma from blood and multiplex diagnosis of cardiac biomarkers. (Under preparation).

# Both authors contributed equally

Achievements

- National Technology Day award for "Novel nanostructures based biosensing for clinically important cardiac biomarkers" including a research funding of Rupees one lakh (2017)
- Finalist of 2nd NanoSparx Innovation competition in 9th Bangalore India Nano (2017)
- Best Poster award in Biological category in 8th Bangalore India Nano (2016)
- Finalist of 1st NanoSparx Innovation competition in 8th Bangalore India Nano (2016)
- Best Poster award in 6th MRS Trilateral symposium (2015)
- Ruchi Ram Sahni best poster award in biological category in CRIKC Nanoscience day (2015)

BIBLIOGRAPHY

1.   Tzoulaki, I., Elliott, P., Kontis, V. & Ezzati, M. Worldwide Exposures to Cardiovascular Risk Factors and Associated Health Effects: Current Knowledge and Data Gaps. *Circulation* **133**, 2314–2333 (2016).

2.   ICD-11 - Mortality and Morbidity Statistics. Available at: https://icd.who.int/browse11/l-m/en. (Accessed: 5th April 2020)

3.   Naghavi, M. *et al.* Global, regional, and national age-sex specifc mortality for 264 causes of death, 1980-2016: A systematic analysis for the Global Burden of Disease Study 2016. *Lancet* **390**, 1151–1210 (2017).

4.   Roth, G. A. *et al.* Global, Regional, and National Burden of Cardiovascular Diseases for 10 Causes, 1990 to 2015. *J. Am. Coll. Cardiol.* **70**, 1–25 (2017).

5.   Feigin, V. L. *et al.* Global burden of stroke and risk factors in 188 countries, during 1990–2013: a systematic analysis for the Global Burden of Disease Study 2013. *Lancet Neurol.* **15**, 913–924 (2016).

6.   Lozano, R. *et al.* Global and regional mortality from 235 causes of death for 20 age groups in 1990 and 2010: A systematic analysis for the Global Burden of Disease Study 2010. *Lancet* **380**, 2095–2128 (2012).

7.   Atkinson, A. J. *et al.* Biomarkers and surrogate endpoints: Preferred definitions and conceptual framework. *Clin. Pharmacol. Ther.* **69**, 89–95 (2001).

8.   Biomarkers In Risk Assessment: Validity And Validation (EHC 222, 2001). Available at: http://www.inchem.org/documents/ehc/ehc/ehc222.htm#1.0. (Accessed: 3rd April 2020)

9.   Biomarkers and risk assessment: concepts and principles (EHC 155, 1993). Available at: http://www.inchem.org/documents/ehc/ehc/ehc155.htm. (Accessed: 3rd April 2020)

10.   Bhocal, U., Saroha, B., Sabharwal, B. S. & Bhan, V. Biomarkers-Turning Failures into Success. **2**, (2014).

11.   Mayeux, R. Biomarkers: Potential Uses and Limitations. *NeuroRx* **1**, 182–188 (2004).

12.   Chau, C. H., Rixe, O., McLeod, H. & Figg, W. D. Validation of analytic methods for biomarkers used in drug development. *Clinical Cancer Research* **14**, 5967–5976 (2008).

13.   Dor, F., Dab, W., Empereur-Bissonnet, P. & Zmirou, D. Validity of biomarkers in environmental health studies: The case of PAHs and Benzene. *Critical Reviews in*

Toxicology **29**, 129–168 (1999).

14. Al-Hadi, H. A. & Fox, K. A. Cardiac markers in the early diagnosis and management of patients with acute coronary syndrome. *Sultan Qaboos Univ. Med. J.* **9**, 231–246 (2009).

15. Frank, R. & Hargreaves, R. Clinical biomarkers in drug discovery and development. *Nat. Rev. Drug Discov.* **2**, 566–580 (2003).

16. Dasgupta, A., Wahed, A., Dasgupta, A. & Wahed, A. Chapter 08 – Cardiac Markers. *Clin. Chem. Immunol. Lab. Qual. Control* 127–144 (2014). doi:10.1016/B978-0-12-407821-5.00008-5

17. Antman, E. *et al.* Myocardial infarction redefined - A consensus document of The Joint European Society of Cardiology/American College of Cardiology Committee f or the redefinition of myocardial infarction. *J. Am. Coll. Cardiol.* **36**, 959–969 (2000).

18. Singh, V., Martinezclark, P., Pascual, M., Shaw, E. S. & O'Neill, W. W. Cardiac biomarkers - The old and the new: A review. *Coron. Artery Dis.* **21**, 244–256 (2010).

19. Bhalla, N., Jolly, P., Formisano, N. & Estrela, P. Introduction to biosensors. *Essays Biochem.* **60**, 1–8 (2016).

20. Sørensen, S. Enzymstudien II: Über die Messung und die Bedeutung der Wasserstoffionenkonzentration bei enzymatischen Prozessen. *Biochem. zeit* **21**, 131–200 (1909).

21. Clark, L. C. & Lyons, C. ELECTRODE SYSTEMS FOR CONTINUOUS MONITORING IN CARDIOVASCULAR SURGERY. *Ann. N. Y. Acad. Sci.* **102**, 29–45 (2006).

22. Heineman, W. R. & Jensen, W. B. Leland C. Clark Jr. (1918–2005). *Biosens. Bioelectron.* **21**, 1403–1404 (2006).

23. Rocchitta, G. *et al.* Enzyme biosensors for biomedical applications: Strategies for safeguarding analytical performances in biological fluids. *Sensors (Switzerland)* **16**, (2016).

24. Razmi, N. *et al.* Recent advances on aptamer-based biosensors to detection of platelet-derived growth factor. *Biosens. Bioelectron.* **113**, 58–71 (2018).

25. Li, Y. L., Guo, L., Zhang, Z. Y., Tang, J. J. & Xie, J. W. Recent advances of aptamer sensors. *Sci. China, Ser. B Chem.* **51**, 193–204 (2008).

26. Sarkar, A., Sarkar, K. D., Amrutha, V. & Dutta, K. An overview of enzyme-based

biosensors for environmental monitoring. in *Tools, Techniques and Protocols for Monitoring Environmental Contaminants* 307–329 (Elsevier, 2019). doi:10.1016/b978-0-12-814679-8.00015-7

27. Liu, C. *et al.* Enzyme Biosensors for Point-of-Care Testing. in *MEMS Sensors - Design and Application* (InTech, 2018). doi:10.5772/intechopen.73249

28. Othman, A., Karimi, A. & Andreescu, S. Functional nanostructures for enzyme based biosensors: properties, fabrication and applications. *Journal of Materials Chemistry B* **4**, 7178–7203 (2016).

29. C, M. The Hybridoma Revolution: An Offshoot of Basic Research. *Bioessays* **21**, (1999).

30. Zaroff, S. & Tan, G. Hybridoma technology: The preferred method for monoclonal antibody generation for in vivo applications. *Biotechniques* **67**, 90–92 (2019).

31. Cristea, C., Florea, A., Tertis, M. & Sandulescu, R. Immunosensors. in *Biosensors - Micro and Nanoscale Applications* (InTech, 2015). doi:10.5772/60524

32. Moina, C. & Ybarr, G. Fundamentals and Applications of Immunosensors. in *Advances in Immunoassay Technology* (InTech, 2012). doi:10.5772/36947

33. Cho, I. H. *et al.* Current technologies of electrochemical immunosensors: Perspective on signal amplification. *Sensors (Switzerland)* **18**, (2018).

34. Piro, B. & Reisberg, S. Recent advances in electrochemical immunosensors. *Sensors (Switzerland)* **17**, (2017).

35. Zhu, Z. *et al.* Natural receptor-based competitive immunoelectrochemical assay for ultra-sensitive detection of Siglec 15. *Biosens. Bioelectron.* **151**, 111950 (2020).

36. Kwon, O. S., Song, H. S., Park, T. H. & Jang, J. Conducting Nanomaterial Sensor Using Natural Receptors. *Chemical Reviews* **119**, 36–93 (2019).

37. Pazos, E., Vázquez, O., Mascareñas, J. L. & Eugenio Vázquez, M. Peptide-based fluorescent biosensors. *Chemical Society Reviews* **38**, 3348–3359 (2009).

38. Damayanti, N. P., Buno, K., Voytik Harbin, S. L. & Irudayaraj, J. M. K. Epigenetic Process Monitoring in Live Cultures with Peptide Biosensors. *ACS Sensors* **4**, 562–565 (2019).

39. Barbosa, A. J. M., Oliveira, A. R. & Roque, A. C. A. Protein- and Peptide-Based Biosensors in Artificial Olfaction. *Trends in Biotechnology* **36**, 1244–1258 (2018).

40. Wasilewski, T., Szulczyński, B., Wojciechowski, M., Kamysz, W. & Gębicki, J. A

Highly Selective Biosensor Based on Peptide Directly Derived from the HarmOBP7 Aldehyde Binding Site. *Sensors* **19**, 4284 (2019).

41. Hong, P., Li, W. & Li, J. Applications of aptasensors in clinical diagnostics. *Sensors* **12**, 1181–1193 (2012).

42. Shigdar, S. *et al.* Aptamers as Theranostic Agents: Modifications, Serum Stability and Functionalisation. *Sensors* **13**, 13624–13637 (2013).

43. Amaya-González, S., de-los-Santos-Álvarez, N., Miranda-Ordieres, A. & Lobo-Castañón, M. Aptamer-Based Analysis: A Promising Alternative for Food Safety Control. *Sensors* **13**, 16292–16311 (2013).

44. Sassolas, A., Blum, L. J. & Leca-Bouvier, B. D. Electrochemical Aptasensors. *Electroanalysis* **21**, 1237–1250 (2009).

45. Martín-Fernández, B., Manzanares-Palenzuela, C. L., Sánchez-Paniagua López, M., de-los-Santos-Álvarez, N. & López-Ruiz, B. Electrochemical genosensors in food safety assessment. *Crit. Rev. Food Sci. Nutr.* **57**, 2758–2774 (2017).

46. Manzanares-Palenzuela, C. L., Martín-Fernández, B., Sánchez-Paniagua López, M. & López-Ruiz, B. Electrochemical genosensors as innovative tools for detection of genetically modified organisms. *TrAC - Trends in Analytical Chemistry* **66**, 19–31 (2015).

47. Pedrero, M., Campuzano, S. & Pingarrón, J. M. Electrochemical genosensors based on PCR strategies for microorganisms detection and quantification. *Analytical Methods* **3**, 780–789 (2011).

48. Campuzano, S., Pedrero, M. & Pingarrón, J. M. Electrochemical genosensors for the detection of cancer-related miRNAs. *Anal. Bioanal. Chem.* **406**, 27–33 (2014).

49. Damborský, P., Švitel, J. & Katrlík, J. Optical biosensors. *Essays Biochem.* **60**, 91–100 (2016).

50. Martins, T. D. *et al.* State of the Art in Biosensors - General Aspects. (2013). doi:10.5772/52330

51. Liu, R. *et al.* Design and synthesis of target-responsive aptamer-cross-linked hydrogel for visual quantitative detection of ochratoxin A. *ACS Appl. Mater. Interfaces* **7**, 6982–6990 (2015).

52. Huo, Y. *et al.* A sensitive aptasensor for colorimetric detection of adenosine triphosphate based on the protective effect of ATP-aptamer complexes on unmodified gold nanoparticles. *Biosens. Bioelectron.* **78**, 315–320 (2016).

53. Li, X. *et al.* A simple highly sensitive and selective aptamer-based colorimetric sensor for environmental toxins microcystin-LR in water samples. *J. Hazard. Mater.* **304**, 474–480 (2016).

54. Alsager, O. A. *et al.* Ultrasensitive colorimetric detection of 17-estradiol: The effect of shortening dna aptamer sequences. *Anal. Chem.* **87**, 4201–4209 (2015).

55. Tian, Y., Wang, Y., Sheng, Z., Li, T. & Li, X. A colorimetric detection method of pesticide acetamiprid by fine-tuning aptamer length. *Anal. Biochem.* **513**, 87–92 (2016).

56. Zangeneh Kamali, K. *et al.* Amalgamation based optical and colorimetric sensing of mercury(II) ions with silver@graphene oxide nanocomposite materials. *Microchim. Acta* **183**, 369–377 (2016).

57. Zhu, Y. *et al.* Building an aptamer/graphene oxide FRET biosensor for one-step detection of bisphenol A. *ACS Appl. Mater. Interfaces* **7**, 7492–7496 (2015).

58. Ling, K. *et al.* A self-assembling RNA aptamer-based graphene oxide sensor for the turn-on detection of theophylline in serum. *Biosens. Bioelectron.* **86**, 8–13 (2016).

59. Wang, B. *et al.* Aptamer induced assembly of fluorescent nitrogen-doped carbon dots on gold nanoparticles for sensitive detection of AFB1. *Biosens. Bioelectron.* **78**, 23–30 (2016).

60. Li, S. *et al.* Aptamer-molecularly imprinted sensor base on electrogenerated chemiluminescence energy transfer for detection of lincomycin. *Biosens. Bioelectron.* **91**, 687–691 (2017).

61. Zang, Y., Lei, J., Hao, Q. & Ju, H. Signal-On photoelectrochemical sensing strategy based on target-dependent aptamer conformational conversion for selective detection of Lead(II) ion. *ACS Appl. Mater. Interfaces* **6**, 15991–15997 (2014).

62. Wang, Y. *et al.* Photoelectrochemical apta-biosensor for zeatin detection based on graphene quantum dots improved photoactivity of graphite-like carbon nitride and streptavidin induced signal inhibition. *Sens Actuators, B Chem.* **257**, 237–244 (2018).

63. Wu, B. *et al.* Detection of C-reactive protein using nanoparticle-enhanced surface plasmon resonance using an aptamer-antibody sandwich assay. *Chem. Commun.* **52**, 3568–3571 (2016).

64. Yoo, S. M., Kim, D. K. & Lee, S. Y. Aptamer-functionalized localized surface plasmon resonance sensor for the multiplexed detection of different bacterial species.

Talanta **132**, 112–127 (2015).

65. Park, J. H., Byun, J. Y., Shim, W. B., Kim, S. U. & Kim, M. G. High-sensitivity detection of ATP using a localized surface plasmon resonance (LSPR) sensor and split aptamers. *Biosens. Bioelectron.* **73**, 26–31 (2015).

66. Fu, C. *et al.* Aptamer-Based Surface-Enhanced Raman Scattering-Microfluidic Sensor for Sensitive and Selective Polychlorinated Biphenyls Detection. *Anal. Chem.* **87**, 9555–9558 (2015).

67. Dong, N., Hu, Y., Yang, K. & Liu, J. Development of aptamer-modified SERS nanosensor and oligonucleotide chip to quantitatively detect melamine in milk with high sensitivity. *Sens Actuators, B Chem.* **228**, 85–93 (2016).

68. Bhamidipati, M., Cho, H.-Y., Lee, K.-B. & Fabris, L. SERS-Based Quantification of Biomarker Expression at the Single Cell Level Enabled by Gold Nanostars and Truncated Aptamers. *Bioconjug. Chem.* **29**, 2970–2981 (2018).

69. Grieshaber, D., MacKenzie, R., Vörös, J. & Reimhult, E. Electrochemical Biosensors - Sensor Principles and Architectures. *Sensors* **8**, 1400–1458 (2008).

70. Hammond, J. L., Formisano, N., Estrela, P., Carrara, S. & Tkac, J. Electrochemical biosensors and nanobiosensors. *Essays Biochem.* **60**, 69–80 (2016).

71. Cho, I. H., Kim, D. H. & Park, S. Electrochemical biosensors: Perspective on functional nanomaterials for on-site analysis. *Biomaterials Research* **24**, 1–12 (2020).

72. Dziąbowska, K., Czaczyk, E. & Nidzworski, D. Application of Electrochemical Methods in Biosensing Technologies. in *Biosensing Technologies for the Detection of Pathogens - A Prospective Way for Rapid Analysis* (InTech, 2018). doi:10.5772/intechopen.72175

73. Kurbanoglu, S. & Ozkan, S. A. A Novel Enzymatic Biosensor for the Detection of Catechol Using Multi-walled Carbon Nanotubes and Gold Nanowires. *Electrocatalysis* **9**, 252–257 (2018).

74. Dave, K., Pachauri, N., Dinda, A. & Solanki, P. R. RGO modified mediator free paper for electrochemical biosensing platform. *Appl. Surf. Sci.* **463**, 587–595 (2019).

75. Salazar, P., García-García, F. J. & González-Elipe, A. R. Sensing and biosensing with screen printed electrodes modified with nanostructured nickel oxide thin films prepared by magnetron sputtering at oblique angles. *Electrochem. commun.* **94**, 5–8 (2018).

76. Kumar, V. *et al.* Nanostructured aptamer-functionalized black phosphorus sensing platform for label-free detection of myoglobin, a cardiovascular disease biomarker. *ACS Appl. Mater. Interfaces* **8**, 22860–22868 (2016).

77. Kumar, V., Shorie, M., Ganguli, A. K. & Sabherwal, P. Graphene-CNT nanohybrid aptasensor for label free detection of cardiac biomarker myoglobin. *Biosens. Bioelectron.* **72**, 56–60 (2015).

78. Huang, K. J., Shuai, H. L. & Zhang, J. Z. Ultrasensitive sensing platform for platelet-derived growth factor BB detection based on layered molybdenum selenide-graphene composites and Exonuclease III assisted signal amplification. *Biosens. Bioelectron.* **77**, 69–75 (2016).

79. Zhou, Y. *et al.* Fabrication of an antibody-aptamer sandwich assay for electrochemical evaluation of levels of β-amyloid oligomers. *Sci. Rep.* **6**, 1–8 (2016).

80. Eissa, S. & Zourob, M. In vitro selection of DNA aptamers targeting β-lactoglobulin and their integration in graphene-based biosensor for the detection of milk allergen. *Biosens. Bioelectron.* **91**, 169–174 (2017).

81. Chen, M. *et al.* A novel aptamer- metal ions- nanoscale MOF based electrochemical biocodes for multiple antibiotics detection and signal amplification. *Sens Actuators B Chem.* **242**, 1201–1209 (2017).

82. Zdrachek, E. & Bakker, E. Potentiometric Sensing. *Analytical Chemistry* **91**, 2–26 (2019).

83. Bakker, E. & Pretsch, E. Potentiometric sensors for trace-level analysis. *TrAC - Trends Anal. Chem.* **24**, 199–207 (2005).

84. Chakraborty, A., Tibarewala, D. N. & Barui, A. Impedance-based biosensors. in *Bioelectronics and Medical Devices* 97–122 (Elsevier, 2019). doi:10.1016/B978-0-08-102420-1.00005-4

85. Kumar, L. S. S. *et al.* Label free nano-aptasensor for interleukin-6 in protein-dilute bio fluids such as sweat. *Anal. Methods* **8**, 3440–3444 (2016).

86. Fei, A. *et al.* Label-free impedimetric aptasensor for detection of femtomole level acetamiprid using gold nanoparticles decorated multiwalled carbon nanotube-reduced graphene oxide nanoribbon composites. *Biosens. Bioelectron.* **70**, 122–129 (2015).

87. Kaur, H., Shorie, M., Sharma, M., Ganguli, A. K. & Sabherwal, P. Bridged Rebar

Graphene functionalized aptasensor for pathogenic E. coli O78:K80:H11 detection. *Biosens. Bioelectron.* **98**, 486–493 (2017).

88. Wang, Q. *et al.* Label-free aptamer biosensor for thrombin detection based on functionalized graphene nanocomposites. *Talanta* **141**, 247–252 (2015).

89. Liu, X., Qin, Y., Deng, C., Xiang, J. & Li, Y. A simple and sensitive impedimetric aptasensor for the detection of tumor markers based on gold nanoparticles signal amplification. *Talanta* **132**, 150–154 (2015).

90. Zarei, S. S., Soleimanian-Zad, S. & Ensafi, A. A. An impedimetric aptasensor for Shigella dysenteriae using a gold nanoparticle-modified glassy carbon electrode. *Microchim. Acta* (2018). doi:10.1007/s00604-018-3075-0

91. Chen, Y. *et al.* Field-Effect Transistor Biosensor for Rapid Detection of Ebola Antigen. *Sci. Rep.* **7**, 1–8 (2017).

92. Xu, J. J., Luo, X. L. & Chen, H. Y. Analytical aspects of FET-based biosensors. *Frontiers in Bioscience* **10**, 420–430 (2005).

93. Vu, C. A. & Chen, W. Y. Field-effect transistor biosensors for biomedical applications: Recent advances and future prospects. *Sensors (Switzerland)* **19**, (2019).

94. Kwong Hong Tsang, D. *et al.* Chemically Functionalised Graphene FET Biosensor for the Label-free Sensing of Exosomes. *Sci. Rep.* **9**, 1–10 (2019).

95. Tsai, M. Y. *et al.* Direct correlation between potentiometric and impedance biosensing of antibody-antigen interactions using an integrated system. *Appl. Phys. Lett.* **111**, (2017).

96. Teengam, P. *et al.* Electrochemical impedance-based DNA sensor using pyrrolidinyl peptide nucleic acids for tuberculosis detection. *Anal. Chim. Acta* **1044**, 102–109 (2018).

97. Turner, A. P. F. Biosensors: sense and sensibility. *Chem. Soc. Rev.* **42**, 3184 (2013).

98. Alvarez, M., Zinoviev, K., Moreno, M. & Lechuga, L. M. Cantilever biosensors. in *Optical Biosensors* 419–452 (Elsevier, 2008). doi:10.1016/B978-044453125-4.50012-7

99. Fritz, J. Cantilever biosensors. *Analyst* **133**, 855–863 (2008).

100. Yuan, M. *et al.* Aptasensor for lead(II) based on the use of a quartz crystal microbalance modified with gold nanoparticles. *Microchim. Acta* **184**, 1397–1403 (2017).

101. Deng, Y., Yue, X., Hu, H. & Zhou, X. A new analytical experimental setup combining quartz crystal microbalance with surface enhancement Raman spectroscopy and its application in determination of thrombin. *Microchem. J.* **132**, 385–390 (2017).

102. Lian, Y., He, F., Wang, H. & Tong, F. A new aptamer/graphene interdigitated gold electrode piezoelectric sensor for rapid and specific detection of Staphylococcus aureus. *Biosens. Bioelectron.* **65**, 314–319 (2015).

103. Pohanka, M. Overview of piezoelectric biosensors, immunosensors and DNA sensors and their applications. *Materials* **11**, (2018).

104. Skládal, P. Piezoelectric biosensors. *TrAC - Trends in Analytical Chemistry* **79**, 127–133 (2016).

105. Kubicek-Sutherland, J. Z., Vu, D. M., Mendez, H. M., Jakhar, S. & Mukundan, H. Detection of lipid and amphiphilic biomarkers for disease diagnostics. *Biosensors* **7**, 25 (2017).

106. Ellington, A. D. & Szostak, J. W. In vitro selection of RNA molecules that bind specific ligands. *Nature* **346**, 818–822 (1990).

107. Dunn, M. R., Jimenez, R. M. & Chaput, J. C. Analysis of aptamer discovery and technology. *Nat. Rev. Chem.* **1**, 1–16 (2017).

108. Tuerk, C. & Gold, L. Systematic evolution of ligands by exponential enrichment: RNA ligands to bacteriophage T4 DNA polymerase. *Science* **249**, 505–10 (1990).

109. Zhuo, Z. *et al.* Recent Advances in SELEX Technology and Aptamer Applications in Biomedicine. *Int. J. Mol. Sci.* **18**, (2017).

110. Yang, Y., Yang, D., Schluesener, H. J. & Zhang, Z. Advances in SELEX and application of aptamers in the central nervous system. *Biomolecular Engineering* **24**, 583–592 (2007).

111. Setlem, K., Mondal, B., Ramlal, S. & Kingston, J. Immuno affinity SELEX for simple, rapid, and cost-effective aptamer enrichment and identification against aflatoxin B1. *Front. Microbiol.* **7**, (2016).

112. Latulippe, D. R. *et al.* Multiplexed microcolumn-based process for efficient selection of RNA aptamers. *Anal. Chem.* **85**, 3417–3424 (2013).

113. Cheng, C., Chen, Y. H., Lennox, K. A., Behlke, M. A. & Davidson, B. L. In vivo SELEX for Identification of Brain-penetrating Aptamers. *Mol. Ther. - Nucleic Acids* **2**, e67 (2013).

114. Wang, H. *et al.* In Vivo SELEX of an Inhibitory NSCLC-Specific RNA Aptamer from

PEGylated RNA Library. *Mol. Ther. - Nucleic Acids* **10**, 187–198 (2018).

115. Zhou, J. & Rossi, J. Aptamers as targeted therapeutics: Current potential and challenges. *Nature Reviews Drug Discovery* **16**, 181–202 (2017).

116. Cella, L. N. *et al.* Nano aptasensor for protective antigen toxin of anthrax. *Anal. Chem.* **82**, 2042–7 (2010).

117. Zhang, Y. *et al.* A sensitive assay based on specific aptamer binding for the detection of Salmonella enterica serovar Typhimurium in milk samples by microchip capillary electrophoresis. *J. Chromatogr. A* **1534**, 188–194 (2018).

118. Weng, C.-H., Huang, C.-J. & Lee, G.-B. Screening of Aptamers on Microfluidic Systems for Clinical Applications. *Sensors* **12**, 9514–9529 (2012).

119. Mayer, G. *et al.* Fluorescence-activated cell sorting for aptamer SELEX with cell mixtures. *Nat. Protoc.* **5**, 1993–2004 (2010).

120. Kim, E. Y. *et al.* Selection of Aptamers for Mature White Adipocytes by Cell SELEX Using Flow Cytometry. *PLoS One* **9**, e97747 (2014).

121. Li, H. *et al.* Aptamer-based microcantilever biosensor for ultrasensitive detection of tumor marker nucleolin. *Talanta* **146**, 727–731 (2016).

122. Tok, J. B. H. & Fischer, N. O. Single microbead SELEX for efficient ssDNA aptamer generation against botulinum neurotoxin. *Chem. Commun.* 1883–1885 (2008). doi:10.1039/b717936g

123. Sefah, K., Shangguan, D., Xiong, X., O'Donoghue, M. B. & Tan, W. Development of DNA aptamers using Cell-SELEX. *Nat. Protoc.* **5**, 1169–1185 (2010).

124. Catuogno, S. & Esposito, C. L. Aptamer Cell-Based Selection: Overview and Advances. *Biomedicines* **5**, 49 (2017).

125. Jayasena, S. D. Aptamers: An emerging class of molecules that rival antibodies in diagnostics. *Clin. Chem.* **45**, 1628–1650 (1999).

126. Crivianu-Gaita, V. & Thompson, M. Aptamers, antibody scFv, and antibody Fab' fragments: An overview and comparison of three of the most versatile biosensor biorecognition elements. *Biosens. Bioelectron.* **85**, 32–45 (2016).

127. Ferreira, C. S. M. & Missailidis, S. Aptamer-based therapeutics and their potential in radiopharmaceutical design. *Brazilian Arch. Biol. Technol.* **50**, 63–76 (2007).

128. Song, K.-M., Lee, S. & Ban, C. Aptamers and Their Biological Applications. *Sensors (Basel).* **12**, 612 (2012).

129. Mascini, M. Aptamers and their applications. *Anal. Bioanal. Chem.* **390**, 987–988

(2008).

130.	Barhoum, A. & Makhlouf, A. S. H. *Fundamentals of nanoparticles : classifications, synthesis methods, properties and characterization*.

131.	Balasubramanian, G. *Advances in Nanomaterials : Fundamentals, Properties and Applications*.

132.	Zhang, B. *Physical Fundamentals of Nanomaterials*. *Physical Fundamentals of Nanomaterials* (Elsevier, 2018). doi:10.1016/c2012-0-02139-4

133.	Filho, A. G. S. & Fagan, S. B. Nanomaterials Properties. in *Nanostructured Materials for Engineering Applications* 5–22 (Springer Berlin Heidelberg, 2011). doi:10.1007/978-3-642-19131-2_2

134.	Thangadurai, T. D., Manjubaashini, N., Thomas, S. & Maria, H. J. Nanomaterials, Properties and Applications. in 11–28 (Springer, Cham, 2020). doi:10.1007/978-3-030-26145-0_2

135.	Jeevanandam, J., Barhoum, A., Chan, Y. S., Dufresne, A. & Danquah, M. K. Review on nanoparticles and nanostructured materials: History, sources, toxicity and regulations. *Beilstein Journal of Nanotechnology* **9**, 1050–1074 (2018).

136.	Gajanan, K. & Tijare, S. N. Applications of nanomaterials. in *Materials Today: Proceedings* **5**, 1093–1096 (Elsevier Ltd, 2018).

137.	Chaughule, R. S. & Watawe, S. C. *Applications of nanomaterials*.

138.	Mohan, S., Oluwafemi, S. O., Kalarikkal, N. & Thomas, S. *Applications of Nanomaterials : Advances and Key Technologies*.

139.	Salata, O. V. Applications of nanoparticles in biology and medicine. *Journal of Nanobiotechnology* **2**, 3 (2004).

140.	Tiwari, J. N., Tiwari, R. N. & Kim, K. S. Zero-dimensional, one-dimensional, two-dimensional and three-dimensional nanostructured materials for advanced electrochemical energy devices. *Progress in Materials Science* **57**, 724–803 (2012).

141.	Wei, H. & Wang, E. Nanomaterials with enzyme-like characteristics (nanozymes): Next-generation artificial enzymes. *Chem. Soc. Rev.* **42**, 6060–6093 (2013).

142.	Khan, I., Saeed, K. & Khan, I. Nanoparticles: Properties, applications and toxicities. *Arabian Journal of Chemistry* **12**, 908–931 (2019).

143.	Siegel, R. W. Nanostructured Materials. in *Advanced Topics in Materials Science and Engineering* 273–288 (Springer US, 1993). doi:10.1007/978-1-4615-2842-

5_17

144. Cao, H. Synthesis, Characterization, and Applications of Zero-Dimensional (0D) Nanostructures. in *Synthesis and Applications of Inorganic Nanostructures* 21–146 (Wiley-VCH Verlag GmbH & Co. KGaA, 2017). doi:10.1002/9783527698158.ch2

145. Wu, Z., Yang, S. & Wu, W. Shape control of inorganic nanoparticles from solution. *Nanoscale* **8**, 1237–1259 (2016).

146. Raliya, R., Saha, D., Chadha, T. S., Raman, B. & Biswas, P. Non-invasive aerosol delivery and transport of gold nanoparticles to the brain. *Sci. Rep.* **7**, 1–8 (2017).

147. Huang, Y. *et al.* Mn3[Co(CN)6]2@SiO2 Core-shell Nanocubes: Novel bimodal contrast agents for MRI and optical imaging. *Sci. Rep.* **3**, 1–7 (2013).

148. Qin, Y., Lu, Y., Pan, W., Yu, D. & Zhou, J. One-pot synthesis of hollow hydrangea Au nanoparticles as a dual catalyst with SERS activity for: In situ monitoring of a reduction reaction. *RSC Adv.* **9**, 10314–10319 (2019).

149. Li, X., Rui, M., Song, J., Shen, Z. & Zeng, H. Carbon and Graphene Quantum Dots for Optoelectronic and Energy Devices: A Review. *Adv. Funct. Mater.* **25**, 4929–4947 (2015).

150. Bera, D., Qian, L., Tseng, T. K. & Holloway, P. H. Quantum dots and their multimodal applications: A review. *Materials* **3**, 2260–2345 (2010).

151. Namdari, P., Negahdari, B. & Eatemadi, A. Synthesis, properties and biomedical applications of carbon-based quantum dots: An updated review. *Biomedicine and Pharmacotherapy* **87**, 209–222 (2017).

152. Frigerio, C. *et al.* Application of quantum dots as analytical tools in automated chemical analysis: A review. *Analytica Chimica Acta* **735**, 9–22 (2012).

153. Chen, O. *et al.* Compact high-quality CdSe-CdS core-shell nanocrystals with narrow emission linewidths and suppressed blinking. *Nat. Mater.* **12**, 445–451 (2013).

154. Wang, Z. M. *One-dimensional nanostructures.* (Springer, 2008).

155. Zhai, T. & Yao, J. *One-Dimensional Nanostructures. One-Dimensional Nanostructures: Principles and Applications* (John Wiley & Sons, Inc., 2012). doi:10.1002/9781118310342

156. Huang, P. S. & Gao, T. Current development of 1D and 2D metallic nanomaterials for the application of transparent conductors in solar cells: Fabrication and

modeling. *Nano-Structures and Nano-Objects* **15**, 119–139 (2018).

157. Park, J. Y. *et al.* Nanostructures of Indium Gallium Nitride Crystals Grown on Carbon Nanotubes. *Sci. Rep.* **5**, 1–8 (2015).

158. Novoselov, K. S. *et al.* Electric field effect in atomically thin carbon films. *Science* **306**, 666–9 (2004).

159. Agarwal, V. & Chatterjee, K. Recent advances in the field of transition metal dichalcogenides for biomedical applications. *Nanoscale* **10**, 16365–16397 (2018).

160. Lin, J. *et al.* In Situ Synthesis of Vertical Standing Nanosized NiO Encapsulated in Graphene as Electrodes for High-Performance Supercapacitors. *Adv. Sci.* **5**, 1700687 (2018).

161. Koski, K. J. & Cui, Y. The new skinny in two-dimensional nanomaterials. *ACS Nano* **7**, 3739–3743 (2013).

162. Yang, G., Zhu, C., Du, D., Zhu, J. & Lin, Y. Graphene-like two-dimensional layered nanomaterials: Applications in biosensors and nanomedicine. *Nanoscale* **7**, 14217–14231 (2015).

163. Zhang, H. Ultrathin Two-Dimensional Nanomaterials. *ACS Nano* **9**, 9451–9469 (2015).

164. Tan, C. & Zhang, H. Wet-chemical synthesis and applications of non-layer structured two-dimensional nanomaterials. *Nature Communications* **6**, 1–13 (2015).

165. Song, Y. *et al.* Recent advances in electrochemical biosensors based on graphene two-dimensional nanomaterials. *Biosens. Bioelectron.* **76**, 195–212 (2016).

166. Nicolosi, V., Chhowalla, M., Kanatzidis, M. G., Strano, M. S. & Coleman, J. N. Liquid exfoliation of layered materials. *Science (80-.).* **340**, 1226419 (2013).

167. Coleman, J. N. *et al.* Two-dimensional nanosheets produced by liquid exfoliation of layered materials. *Science* **331**, 568–71 (2011).

168. Nicolosi, V., Chhowalla, M., Kanatzidis, M. G., Strano, M. S. & Coleman, J. N. Liquid exfoliation of layered materials. *Science* **340**, (2013).

169. Shehzad, K., Xu, Y., Gao, C. & Duan, X. Three-dimensional macro-structures of two-dimensional nanomaterials. *Chemical Society Reviews* **45**, 5541–5588 (2016).

170. Xu, S. *et al.* Assembly of micro/nanomaterials into complex, three-dimensional architectures by compressive buckling. *Science (80-.).* **347**, 154–159 (2015).

171. Erbay, C. *et al.* Three-dimensional porous carbon nanotube sponges for high-

performance anodes of microbial fuel cells. *J. Power Sources* **298**, 177–183 (2015).

172. Van Gough, D., Juhl, A. T. & Braun, P. V. Programming structure into 3D nanomaterials. *Materials Today* **12**, 28–35 (2009).

173. Ovsianikov, A. *et al.* Ultra-low shrinkage hybrid photosensitive material for two-photon polymerization microfabrication. *ACS Nano* **2**, 2257–2262 (2008).

174. Shir, D. *et al.* Three-dimensional nanostructures formed by single step, two-photon exposures through elastomeric Penrose quasicrystal phase masks. *Nano Lett.* **8**, 2236–2244 (2008).

175. Su, S. S. & Chang, I. Review of production routes of nanomaterials. in *Commercialization of Nanotechnologies-A Case Study Approach* 15–29 (Springer International Publishing, 2017). doi:10.1007/978-3-319-56979-6_2

176. Wang, Y. & Xia, Y. Bottom-up and top-down approaches to the synthesis of monodispersed spherical colloids of low melting-point metals. *Nano Lett.* **4**, 2047–2050 (2004).

177. Mackenzie, J. D. & Bescher, E. P. Chemical routes in the synthesis of nanomaterials using the sol-gel process. *Accounts of Chemical Research* **40**, 810–818 (2007).

178. Nizamuddin, S. *et al.* Microwave-Assisted Synthesis for Carbon Nanomaterials. in *Nanomaterials Synthesis* 121–147 (Elsevier, 2019). doi:10.1016/b978-0-12-815751-0.00005-5

179. Komiyama, H., Yamaguchi, Y. & Noda, S. Structuring knowledge on nanomaterials processing. in *Chemical Engineering Science* **59**, 5085–5090 (Pergamon, 2004).

180. N Mujawar, M. *et al.* Advanced nanomaterials synthesis from pyrolysis and hydrothermal carbonization: A review. *Curr. Org. Chem.* **21**, (2017).

181. Manawi, Y., Ihsanullah, Samara, A., Al-Ansari, T. & Atieh, M. A Review of Carbon Nanomaterials' Synthesis via the Chemical Vapor Deposition (CVD) Method. *Materials (Basel).* **11**, 822 (2018).

182. Dunne, P. W., Munn, A. S., Starkey, C. L., Huddle, T. A. & Lester, E. H. Continuous-flow hydrothermal synthesis for the production of inorganic nanomaterials. *Philosophical Transactions of the Royal Society A: Mathematical, Physical and Engineering Sciences* **373**, (2015).

183. Lyu, H. *et al.* Ball-Milled Carbon Nanomaterials for Energy and Environmental Applications. *ACS Sustainable Chemistry and Engineering* **5**, 9568–9585 (2017).

184. Ullah, M., Eaqub Ali, M. & Bee Abd Hamid, S. Structure-controlled Nanomaterial Synthesis using Surfactant-assisted Ball Milling- A Review.

185. Xu, H., Zeiger, B. W. & Suslick, K. S. Sonochemical synthesis of nanomaterials. *Chemical Society Reviews* **42**, 2555–2567 (2013).

186. Kim, J. *et al.* Direct exfoliation and dispersion of two-dimensional materials in pure water via temperature control. *Nat. Commun.* **6**, 1–9 (2015).

187. Niu, L. *et al.* Production of Two-Dimensional Nanomaterials via Liquid-Based Direct Exfoliation. *Small* **12**, 272–293 (2016).

188. Shen, J. *et al.* Surface Tension Components Based Selection of Cosolvents for Efficient Liquid Phase Exfoliation of 2D Materials. *Small* **12**, 2741–2749 (2016).

189. Bhatia, S. N. & Ingber, D. E. Microfluidic organs-on-chips. *Nature Biotechnology* **32**, 760–772 (2014).

190. Huh, D. *et al.* Reconstituting organ-level lung functions on a chip. *Science (80-.).* **328**, 1662–1668 (2010).

191. Mosig, A. S. Organ-on-chip models: New opportunities for biomedical research. *Future Science OA* **3**, (2017).

192. Pumera, M. Nanomaterials meet microfluidics. *Chem. Commun.* **47**, 5671–5680 (2011).

193. Zhang, J. & Misra, R. D. K. Nanomaterials in microfluidics for disease diagnosis and therapy development. *Materials Technology* **34**, 92–116 (2019).

194. Medina-Sánchez, M., Miserere, S. & Merkoçi, A. Nanomaterials and lab-on-a-chip technologies. in *Lab on a Chip* **12**, 1932–1943 (Royal Society of Chemistry, 2012).

195. Zhao, Z., Yang, Y., Zeng, Y. & He, M. A microfluidic ExoSearch chip for multiplexed exosome detection towards blood-based ovarian cancer diagnosis. *Lab Chip* **16**, 489–496 (2016).

196. Zheng, G., Patolsky, F., Cui, Y., Wang, W. U. & Lieber, C. M. Multiplexed electrical detection of cancer markers with nanowire sensor arrays. *Nat. Biotechnol.* **23**, 1294–1301 (2005).

197. Ortega, F. G. *et al.* Epithelial cancer biomarker EpCAM determination in peripheral blood samples using a microfluidic immunosensor based in silver nanoparticles as platform. *Sens Actuators, B Chem.* **221**, 248–256 (2015).

198. Escobedo, C. *et al.* Quantification of ovarian cancer markers with integrated microfluidic concentration gradient and imaging nanohole surface plasmon

resonance. *Analyst* **138**, 1450–1458 (2013).

199. Aćimović, S. S. *et al.* LSPR chip for parallel, rapid, and sensitive detection of cancer markers in serum. *Nano Lett.* **14**, 2636–2641 (2014).

200. Sardesai, N. P., Kadimisetty, K., Faria, R. & Rusling, J. F. A microfluidic electrochemiluminescent device for detecting cancer biomarker proteins. *Anal. Bioanal. Chem.* **405**, 3831–3838 (2013).

201. Chikkaveeraiah, B. V., Mani, V., Patel, V., Gutkind, J. S. & Rusling, J. F. Microfluidic electrochemical immunoarray for ultrasensitive detection of two cancer biomarker proteins in serum. *Biosens. Bioelectron.* **26**, 4477–4483 (2011).

202. Chikkaveeraiah, B. V., Bhirde, A. A., Morgan, N. Y., Eden, H. S. & Chen, X. Electrochemical immunosensors for detection of cancer protein biomarkers. *ACS Nano* **6**, 6546–6561 (2012).

203. Uludag, Y. & Köktürk, G. Determination of prostate-specific antigen in serum samples using gold nanoparticle based amplification and lab-on-a-chip based amperometric detection. *Microchim. Acta* **182**, 1685–1691 (2015).

204. Malhotra, R. *et al.* Ultrasensitive detection of cancer biomarkers in the clinic by use of a nanostructured microfluidic array. *Anal. Chem.* **84**, 6249–6255 (2012).

205. Wang, H. *et al.* Global, regional, and national life expectancy, all-cause mortality, and cause-specific mortality for 249 causes of death, 1980–2015: a systematic analysis for the Global Burden of Disease Study 2015. *Lancet* **388**, 1459–1544 (2016).

206. Mahmood, S. S., Levy, D., Vasan, R. S. & Wang, T. J. The Framingham Heart Study and the epidemiology of cardiovascular disease: A historical perspective. *Lancet* **383**, 999–1008 (2014).

207. DAWBER, T. R., MOORE, F. E. & MANN, G. V. Coronary heart disease in the Framingham study. *Am. J. Public Health Nations. Health* **47**, 4–24 (1957).

208. KANNEL, W. B., DAWBER, T. R., COHEN, M. E. & MCNAMARA, P. M. VASCULAR DISEASE OF THE BRAIN--EPIDEMIOLOGIC ASPECTS: THE FARMINGHAM STUDY. *Am. J. Public Health Nations. Health* **55**, 1355–1366 (1965).

209. Partamian, J. O. & Bradley, R. F. Acute myocardial infarction in 258 cases of diabetes. Immediate mortality and five-year survival. *N. Engl. J. Med.* **273**, 455–461 (1965).

210. Liebow, I. M., Hellerstein, H. K. & Miller, M. Arteriosclerotic heart disease in

diabetes mellitus. A clinical study of 383 patients. *Am. J. Med.* **18**, 438–447 (1955).

211. Garcia, M. J., McNamara, P. M., Gordon, T. & Kannell, W. B. Morbidity and mortality in diabetics in the Framingham population. Sixteen year follow up study. *Diabetes* **23**, 105–111 (1974).

212. Kannel, W. B., Hjortland, M. & Castelli, W. P. Role of diabetes in congestive heart failure: The Framingham study. *Am. J. Cardiol.* **34**, 29–34 (1974).

213. Kannel, W. B. & McGee, D. L. Diabetes and cardiovascular risk factors: The Framingham study. *Circulation* **59**, 8–13 (1979).

214. KEYS, A. & FIDANZA, F. Serum cholesterol and relative body weight of coronary patients in different populations. *Circulation* **22**, 1091–106 (1960).

215. Gordon, T., Castelli, W. P., Hjortland, M. C., Kannel, W. B. & Dawber, T. R. High density lipoprotein as a protective factor against coronary heart disease. The Framingham study. *Am. J. Med.* **62**, 707–714 (1977).

216. Kullo, I. J. & Ballantyne, C. M. Conditional risk factors for atherosclerosis. *Mayo Clinic Proceedings* **80**, 219–230 (2005).

217. Cooper, J. A., Miller, G. J. & Humphries, S. E. A comparison of the PROCAM and Framingham point-scoring systems for estimation of individual risk of coronary heart disease in the Second Northwick Park Heart Study. *Atherosclerosis* **181**, 93–100 (2005).

218. Kagen, L., Scheidt, S., Roberts, L., Porter, A. & Paul, H. Myoglobinemia following acute myocardial infarction. *Am. J. Med.* **58**, 177–182 (1975).

219. Anderson, J. L. *et al.* ACC/AHA 2007 Guidelines for the Management of Patients With Unstable Angina/Non-ST-Elevation Myocardial Infarction. A Report of the American College of Cardiology/American Heart Association Task Force on Practice Guidelines (Writing Committee to Revise the 2002 Guidelines for the Management of Patients With Unstable Angina/Non-ST-Elevation Myocardial Infarction)... *Journal of the American College of Cardiology* **50**, e1–e157 (2007).

220. VAIDYA & C., H. Myoglobin : an early biochemical marker for the diagnosis of acute myocardial infarction. *J.Clin.Immunossay* **17**, 35–39 (1994).

221. Bhayana, V., Cohoe, S., Pellar, T. G., Jablonsky, G. & Henderson, A. R. Combination (multiple) testing for myocardial infarction using myoglobin, creatine kinase-2 (mass), and troponin T. *Clin. Biochem.* **27**, 395–406 (1994).

222. Bhayana, V. & Henderson, A. R. Biochemical markers of myocardial damage. *Clinical Biochemistry* **28**, 1–29 (1995).

223. Pierce, G. F. & Jaffe, A. S. Increased creatine kinase MB in the absence of acute myocardial infarction. *Clin. Chem.* **32**, 2044–2051 (1986).

224. Katrukha, I. A. Human cardiac troponin complex. structure and functions. *Biochemistry (Moscow)* **78**, 1447–1465 (2013).

225. Sasse, S. *et al.* Troponin I gene expression during human cardiac development and in end-stage heart failure. *Circ. Res.* **72**, 932–938 (1993).

226. Bodor, G. S., Porterfield, D., Voss, E. M., Smith, S. & Apple, F. S. Cardiac troponin-I is not expressed in fetal and healthy or diseased adult human skeletal muscle tissue. *Clin. Chem.* **41**, 1710–1715 (1995).

227. Adams, J. E., Schechtman, K. B., Landt, Y., Ladenson, J. H. & Jaffe, A. S. Comparable detection of acute myocardial infarction by creatine kinase MB isoenzyme and cardiac troponin I. *Clin. Chem.* **40**, 1291–5 (1994).

228. Kullo, I. J. & Cooper, L. T. Early identification of cardiovascular risk using genomics and proteomics. *Nature Reviews Cardiology* **7**, 309–317 (2010).

229. Blair, J. E. A. *et al.* Prognostic markers in heart failure - Congestion, neurohormones, and the cardiorenal syndrome. *Acute Cardiac Care* **9**, 207–213 (2007).

230. Pascual-Figal, D. A., Caballero, L., Sanchez-Mas, J. & Lax, A. Prognostic markers for acute heart failure. *Expert Opinion on Medical Diagnostics* **7**, 379–392 (2013).

231. Dunlay, S. M. *et al.* Prognostic value of biomarkers in heart failure: application of novel methods in the community. *Circ. Heart Fail.* **2**, 393–400 (2009).

232. Wang, T. J. *et al.* Multiple Biomarkers for the Prediction of First Major Cardiovascular Events and Death. *N. Engl. J. Med.* **355**, 2631–2639 (2006).

233. Nishikimi, T., Kuwahara, K. & Nakao, K. Current biochemistry, molecular biology, and clinical relevance of natriuretic peptides. *J. Cardiol.* **57**, 131–140 (2011).

234. Mueller, T., Gegenhuber, A., Dieplinger, B., Poelz, W. & Haltmayer, M. Capability of B-Type Natriuretic Peptide (BNP) and Amino-Terminal proBNP as Indicators of Cardiac Structural Disease in Asymptomatic Patients with Systemic Arterial Hypertension. *Clin. Chem.* **51**, 2245–2251 (2005).

235. Maisel, A. S. *et al.* Rapid Measurement of B-Type Natriuretic Peptide in the Emergency Diagnosis of Heart Failure. *N. Engl. J. Med.* **347**, 161–167 (2002).

236. Dao, Q. *et al.* Utility of B-type natriuretic peptide in the diagnosis of congestive heart failure in an urgent-care setting. *J. Am. Coll. Cardiol.* **37**, 379–385 (2001).

237. Priyanka, Shorie, M., Bhalla, V., Pathania, P. & Raman Suri, C. Nanobioprobe mediated DNA aptamers for explosive detection. *Chem. Commun.* **50**, 1080–1082 (2014).

238. Sabherwal, P. *et al.* Hybrid aptamer-antibody linked fluorescence resonance energy transfer based detection of trinitrotoluene. *Anal. Chem.* **86**, 7200–7204 (2014).

239. Carlsen, C. U., Skovgaard, I. M. & Skibsted, L. H. Pseudoperoxidase activity of myoglobin: Kinetics and mechanism of the peroxidase cycle of myoglobin with H2O2 and 2,2-azino-bis(3-ethylbenzthiazoline-6-sulfonate) as substrates. *J. Agric. Food Chem.* **51**, 5815–5823 (2003).

240. Matsuo, T. *et al.* Meso-unsubstituted iron corrole in hemoproteins: Remarkable differences in effects on peroxidase activities between myoglobin and horseradish peroxidase. *J. Am. Chem. Soc.* **131**, 15124–15125 (2009).

241. Wu, L. Bin *et al.* An intramolecular disulfide bond designed in myoglobin fine-tunes both protein structure and peroxidase activity. *Arch. Biochem. Biophys.* **600**, 47–55 (2016).

242. Zuker, M. Mfold web server for nucleic acid folding and hybridization prediction. *Nucleic Acids Res.* **31**, 3406–3415 (2003).

243. Kikin, O., D'Antonio, L. & Bagga, P. S. QGRS Mapper: a web-based server for predicting G-quadruplexes in nucleotide sequences. *Nucleic Acids Res.* **34**, W676–W682 (2006).

244. FREE, A. H., ADAMS, E. C., KERCHER, M. L., FREE, H. M. & COOK, M. H. Simple specific test for urine glucose. *Clin. Chem.* **3**, 163–168 (1957).

245. Yetisen, A. K., Akram, M. S. & Lowe, C. R. Paper-based microfluidic point-of-care diagnostic devices. *Lab on a Chip* **13**, 2210–2251 (2013).

246. Zhu, H., Isikman, S. O., Mudanyali, O., Greenbaum, A. & Ozcan, A. Optical imaging techniques for point-of-care diagnostics. *Lab on a Chip* **13**, 51–67 (2013).

247. Wang, Y. & Hu, A. Carbon quantum dots: Synthesis, properties and applications. *J. Mater. Chem. C* **2**, 6921–6939 (2014).

248. Wang, X., Feng, Y., Dong, P. & Huang, J. A Mini Review on Carbon Quantum Dots: Preparation, Properties, and Electrocatalytic Application. *Frontiers in Chemistry*

7, 671 (2019).

249. Liu, Y. *et al.* Advances in carbon dots: From the perspective of traditional quantum dots. *Materials Chemistry Frontiers* **4**, 1586–1613 (2020).

250. Gomes, M. F., Gomes, Y. F., Lopes-Moriyama, A., de Barros Neto, E. L. & de Souza, C. P. Design of carbon quantum dots via hydrothermal carbonization synthesis from renewable precursors. *Biomass Convers. Biorefinery* **9**, 689–694 (2019).

251. Chai, X., He, H., Fan, H., Kang, X. & Song, X. A hydrothermal-carbonization process for simultaneously production of sugars, graphene quantum dots, and porous carbon from sugarcane bagasse. *Bioresour. Technol.* **282**, 142–147 (2019).

252. Liu, M. L., Chen, B. Bin, Li, C. M. & Huang, C. Z. Carbon dots: Synthesis, formation mechanism, fluorescence origin and sensing applications. *Green Chemistry* **21**, 449–471 (2019).

253. Xia, C., Zhu, S., Feng, T., Yang, M. & Yang, B. Evolution and Synthesis of Carbon Dots: From Carbon Dots to Carbonized Polymer Dots. *Advanced Science* **6**, (2019).

254. Wang, J., Musameh, M. & Lin, Y. Solubilization of carbon nanotubes by Nafion toward the preparation of amperometric biosensors. *J. Am. Chem. Soc.* **125**, 2408–2409 (2003).

255. Eaton, W. A. & Hofrichter, J. Polarized Absorption and Linear Dichroism Spectroscopy of Hemoglobin. *Methods Enzymol.* **76**, 175–261 (1981).

256. Eaton, W. A., Hanson, L. K., Stephens, P. J., Sutherland, C. & Dunn2b, J. B. R. *Eaton et al. / Optical Spectra of Oxy-and Deoxyhemoglobin Optical Spectra of Oxy-and Deoxyhemoglobin*.

257. Scientific, T. F. ReactiBind DNA coating solution manual. Available at: https://assets.fishersci.com/TFS-Assets/LSG/manuals/MAN0011326_Pierce_DNA_Coat_Solution_UG.pdf. (Accessed: 19th August 2020)

258. Wang, B., Yang, W., McKittrick, J. & Meyers, M. A. Keratin: Structure, mechanical properties, occurrence in biological organisms, and efforts at bioinspiration. *Progress in Materials Science* **76**, 229–318 (2016).

259. Lynch, M. H., O'Guin, W. M., Hardy, C., Mak, L. & Sun, T. T. Acidic and basic hair/nail ('hard') keratins: Their colocalization in upper cortical and cuticle cells of the human hair follicle and their relationship to 'Soft' keratins. *J. Cell Biol.* **103**, 2593–2606 (1986).

260. Gopinath, S. C. B. *et al.* Biotechnological Aspects and Perspective of Microbial Keratinase Production. (2015). doi:10.1155/2015/140726

261. Gubala, V., Harris, L. F., Ricco, A. J., Tan, M. X. & Williams, D. E. Point of care diagnostics: Status and future. *Analytical Chemistry* 84, 487–515 (2012).

262. Von Lode, P. Point-of-care immunotesting: Approaching the analytical performance of central laboratory methods. *Clinical Biochemistry* 38, 591–606 (2005).

263. Luo, J., Chen, C. & Li, Q. White blood cell counting at point-of-care testing: A review. *Electrophoresis* elps.202000029 (2020). doi:10.1002/elps.202000029

264. St John, A. & Price, C. P. Existing and Emerging Technologies for Point-of-Care Testing. *Clin. Biochem. Rev.* 35, 155–67 (2014).

265. Price, C. P. Regular review: Point of care testing. *British Medical Journal* 322, 1285–1288 (2001).

266. Liu, J., Geng, Z., Fan, Z., Liu, J. & Chen, H. Point-of-care testing based on smartphone: The current state-of-the-art (2017–2018). *Biosens. Bioelectron.* 132, 17–37 (2019).

267. Xu, X. *et al.* Advances in Smartphone-Based Point-of-Care Diagnostics. *Proc. IEEE* 103, 236–247 (2015).

268. Geng, Z. *et al.* Recent Progress in Optical Biosensors Based on Smartphone Platforms. *Sensors* 17, 2449 (2017).

269. Martinez, A. W. *et al.* Simple telemedicine for developing regions: Camera phones and paper-based microfluidic devices for real-time, off-site diagnosis. *Anal. Chem.* 80, 3699–3707 (2008).

270. Kanchi, S., Sabela, M. I., Mdluli, P. S., Inamuddin & Bisetty, K. Smartphone based bioanalytical and diagnosis applications: A review. *Biosensors and Bioelectronics* 102, 136–149 (2018).

271. Abdulbari, H. A. & Basheer, E. A. M. Electrochemical Biosensors: Electrode Development, Materials, Design, and Fabrication. *ChemBioEng Rev.* 4, 92–105 (2017).

272. Azzouz, A. *et al.* Nanomaterial-based electrochemical sensors for the detection of neurochemicals in biological matrices. *TrAC - Trends in Analytical Chemistry* 110, 15–34 (2019).

273. Manikandan, V. S., Adhikari, B. R. & Chen, A. Nanomaterial based electrochemical

sensors for the safety and quality control of food and beverages. *Analyst* **143**, 4537–4554 (2018).

274. Batool, R., Rhouati, A., Nawaz, M. H., Hayat, A. & Marty, J. L. A review of the construction of nano-hybrids for electrochemical biosensing of glucose. *Biosensors* **9**, (2019).

275. Krishnan, S. K., Singh, E., Singh, P., Meyyappan, M. & Nalwa, H. S. A review on graphene-based nanocomposites for electrochemical and fluorescent biosensors. *RSC Advances* **9**, 8778–8781 (2019).

276. Geim, A. K. & Grigorieva, I. V. Van der Waals heterostructures. *Nature* **499**, 419–425 (2013).

277. Jariwala, D., Marks, T. J. & Hersam, M. C. Mixed-dimensional van der Waals heterostructures. *Nature Materials* **16**, 170–181 (2017).

278. Novoselov, K. S., Mishchenko, A., Carvalho, A. & Castro Neto, A. H. 2D materials and van der Waals heterostructures. *Science* **353**, (2016).

279. Liu, Y. *et al.* Van der Waals heterostructures and devices. *Nature Reviews Materials* **1**, 1–17 (2016).

280. Marcano, D. C. *et al.* Improved synthesis of graphene oxide. *ACS Nano* **4**, 4806–4814 (2010).

281. Khan, M. S., Shakoor, A., Khan, G. T., Sultana, S. & Zia, A. *A Study of Stable Graphene Oxide Dispersions in Various Solvents*. *J.Chem.Soc.Pak* **37**, (2015).

282. Paredes, J. I., Villar-Rodil, S., Martínez-Alonso, A. & Tascón, J. M. D. Graphene oxide dispersions in organic solvents. *Langmuir* **24**, 10560–10564 (2008).

283. Song, M. Y., Yun, Y. S., Kim, N. R. & Jin, H. J. Dispersion stability of chemically reduced graphene oxide nanoribbons in organic solvents. *RSC Adv.* **6**, 19389–19393 (2016).

284. Johnson, D. W., Dobson, B. P. & Coleman, K. S. A manufacturing perspective on graphene dispersions. *Current Opinion in Colloid and Interface Science* **20**, 367–382 (2015).

285. Konios, D., Stylianakis, M. M., Stratakis, E. & Kymakis, E. Dispersion behaviour of graphene oxide and reduced graphene oxide. *J. Colloid Interface Sci.* **430**, 108–112 (2014).

286. Sharma, P. *et al.* Enhancing electrochemical detection on graphene oxide-CNT nanostructured electrodes using magneto-nanobioprobes. *Sci. Rep.* **2**, 1–7 (2012).

287. Andrijanto, E., Shoelarta, S., Subiyanto, G. & Rifki, S. Facile synthesis of graphene from graphite using ascorbic acid as reducing agent. in *AIP Conference Proceedings* **1725**, 020003 (American Institute of Physics Inc., 2016).

288. Zhang, J. *et al.* Reduction of graphene oxide vial-ascorbic acid. *Chem. Commun.* **46**, 1112–1114 (2010).

289. Emiru, T. F. & Ayele, D. W. Controlled synthesis, characterization and reduction of graphene oxide: A convenient method for large scale production. *Egypt. J. Basic Appl. Sci.* **4**, 74–79 (2017).

290. Srivastava, R. K. *et al.* Functionalized multilayered graphene platform for urea sensor. *ACS Nano* **6**, 168–175 (2012).

291. McAllister, M. J. *et al.* Single sheet functionalized graphene by oxidation and thermal expansion of graphite. *Chem. Mater.* **19**, 4396–4404 (2007).

292. Castellanos-Gomez, A. *et al.* Isolation and characterization of few-layer black phosphorus. *2D Mater.* **1**, 025001 (2014).

293. Khandelwal, A., Mani, K., Karigerasi, M. H. & Lahiri, I. Phosphorene – The two-dimensional black phosphorous: Properties, synthesis and applications. *Materials Science and Engineering B: Solid-State Materials for Advanced Technology* **221**, 17–34 (2017).

294. Brent, J. R. *et al.* Production of few-layer phosphorene by liquid exfoliation of black phosphorus. *Chem. Commun.* **50**, 13338–13341 (2014).

295. Castellanos-Gomez, A. Black Phosphorus: Narrow Gap, Wide Applications. *Journal of Physical Chemistry Letters* **6**, 4280–4291 (2015).

296. Jing, Y., Tang, Q., He, P., Zhou, Z. & Shen, P. Small molecules make big differences: Molecular doping effects on electronic and optical properties of phosphorene. *Nanotechnology* **26**, 095201 (2015).

297. Peng, X., Wei, Q. & Copple, A. Strain-engineered direct-indirect band gap transition and its mechanism in two-dimensional phosphorene. *Phys. Rev. B - Condens. Matter Mater. Phys.* **90**, 085402 (2014).

298. Tran, V., Soklaski, R., Liang, Y. & Yang, L. Layer-controlled band gap and anisotropic excitons in few-layer black phosphorus. *Phys. Rev. B - Condens. Matter Mater. Phys.* **89**, 235319 (2014).

299. Lv, H. Y., Lu, W. J., Shao, D. F. & Sun, Y. P. Enhanced thermoelectric performance of phosphorene by strain-induced band convergence. *Phys. Rev. B - Condens. Matter*

Mater. Phys. **90**, 085433 (2014).

300. Abell, J. L., Garren, J. M., Driskell, J. D., Tripp, R. A. & Zhao, Y. Label-Free Detection of Micro-RNA Hybridization Using Surface-Enhanced Raman Spectroscopy and Least-Squares Analysis. *J. Am. Chem. Soc.* **134**, 12889–12892 (2012).

301. Wang, P. *et al.* Label-free mapping of single bacterial cells using surface-enhanced Raman spectroscopy. *Analyst* **141**, 1356–1362 (2016).

302. Turzhitsky, V. *et al.* Picoanalysis of Drugs in Biofluids with Quantitative Label-Free Surface-Enhanced Raman Spectroscopy. *Small* **14**, 1802392 (2018).

303. Paidi, S. K. *et al.* Label-free raman spectroscopy detects stromal adaptations in premetastatic lungs primed by breast cancer. *Cancer Res.* **77**, 247–256 (2017).

304. Schie, I. W. *et al.* High-Throughput Screening Raman Spectroscopy Platform for Label-Free Cellomics. *Anal. Chem.* **90**, 2023–2030 (2018).

305. Fleischmann, M., Hendra, P. J. & McQuillan, A. J. Raman spectra of pyridine adsorbed at a silver electrode. *Chem. Phys. Lett.* **26**, 163–166 (1974).

306. Haynes, C. L., Yonzon, C. R., Zhang, X. & Van Duyne, R. P. Surface-enhanced Raman sensors: early history and the development of sensors for quantitative biowarfare agent and glucose detection. *J. Raman Spectrosc.* **36**, 471–484 (2005).

307. Huang, Z., Zhang, A., Zhang, Q. & Cui, D. Nanomaterial-based SERS sensing technology for biomedical application. *Journal of Materials Chemistry B* **7**, 3755–3774 (2019).

308. Schatz, G. C. & Van Duyne, R. P. Electromagnetic Mechanism of Surface-Enhanced Spectroscopy. in *Handbook of Vibrational Spectroscopy* (ed. Griffiths, P. R.) (John Wiley & Sons, Ltd, 2006). doi:10.1002/0470027320.s0601

309. Sharma, B., Frontiera, R. R., Henry, A. I., Ringe, E. & Van Duyne, R. P. SERS: Materials, applications, and the future. *Materials Today* **15**, 16–25 (2012).

310. Campion, A. & Kambhampati, P. Surface-enhanced Raman scattering. *Chem. Soc. Rev.* **27**, 241–250 (1998).

311. Stiles, P. L., Dieringer, J. A., Shah, N. C. & Van Duyne, R. P. Surface-Enhanced Raman Spectroscopy. *Annu. Rev. Anal. Chem.* **1**, 601–626 (2008).

312. Zhao, Y. *et al.* Au nanoflower-Ag nanoparticle assembled SERS-active substrates for sensitive MC-LR detection. *Chem. Commun.* **51**, 16908–16911 (2015).

313. Liu, K. *et al.* Porous Au-Ag Nanospheres with High-Density and Highly Accessible Hotspots for SERS Analysis. *Nano Lett.* **16**, 3675–81 (2016).

314. Yang, Y., Zhang, Q., Fu, Z.-W. & Qin, D. Transformation of Ag nanocubes into Ag-Au hollow nanostructures with enriched Ag contents to improve SERS activity and chemical stability. *ACS Appl. Mater. Interfaces* **6**, 3750–7 (2014).

315. Su, X., Wang, Y., Wang, W., Sun, K. & Chen, L. Phospholipid Encapsulated AuNR@Ag/Au Nanosphere SERS Tags with Environmental Stimulus Responsive Signal Property. *ACS Appl. Mater. Interfaces* **8**, 10201–11 (2016).

316. Nair, A. K. *et al.* Multifunctional nitrogen sulfur co-doped reduced graphene oxide – Ag nano hybrids (sphere, cube and wire) for nonlinear optical and SERS applications. *Carbon N. Y.* **132**, 380–393 (2018).

317. Huang, J. *et al.* Nanocomposites of size-controlled gold nanoparticles and graphene oxide: Formation and applications in SERS and catalysis. *Nanoscale* **2**, 2733–2738 (2010).

318. Liu, M. *et al.* Graphene oxide wrapped with gold nanorods as a tag in a SERS based immunoassay for the hepatitis B surface antigen. *Mikrochim. Acta* **185**, 458 (2018).

319. Li, Z. *et al.* 3D silver nanoparticles with multilayer graphene oxide as a spacer for surface enhanced Raman spectroscopy analysis. *Nanoscale* **10**, 5897–5905 (2018).

320. Liang, X. *et al.* Interfacial synthesis of a three-dimensional hierarchical MoS2-NS@Ag-NP nanocomposite as a SERS nanosensor for ultrasensitive thiram detection. *Nanoscale* **9**, 8879–8888 (2017).

321. Li, T. *et al.* Self-assembly of the stretchable AuNPs@MoS 2 @GF substrate for the SERS application. *Appl. Surf. Sci.* **423**, 1072–1079 (2017).

322. Zeng, L. *et al.* High-responsivity UV-Vis Photodetector Based on Transferable WS 2 Film Deposited by Magnetron Sputtering. *Sci. Rep.* **6**, (2016).

323. Zhao, J., Zhang, Z., Yang, S., Zheng, H. & Li, Y. Facile synthesis of MoS2 nanosheet-silver nanoparticles composite for surface enhanced Raman scattering and electrochemical activity. *J. Alloys Compd.* **559**, 87–91 (2013).

324. Tian, F., Bonnier, F., Casey, A., Shanahan, A. E. & Byrne, H. J. Surface enhanced Raman scattering with gold nanoparticles: Effect of particle shape. *Anal. Methods* **6**, 9116–9123 (2014).

325. Palik, E. D. *Handbook of Optical Constants of Solids*. (Academic Press, 1998).

326. Ahuja, U., Dashora, A., Tiwari, H., Kothari, D. C. & Venugopalan, K. Electronic and

optical properties of MoS2-WS2 multi-layers: First principles study. *Comput. Mater. Sci.* **92**, 451–456 (2014).

327. Tong, L., Xu, H. & Käll, M. Nanogaps for SERS applications. *MRS Bull.* **39**, 163–168 (2014).

328. Xu, H. *et al.* Interparticle coupling effects in surface-enhanced Raman scattering. in *Nanoparticles and Nanostructured Surfaces: Novel Reporters with Biological Applications* (ed. Murphy, C. J.) **4258**, 35–42 (SPIE, 2001).

329. Jensen, L. & Schatz, G. C. Resonance Raman scattering of rhodamine 6G as calculated using time-dependent density functional theory. *J. Phys. Chem. A* **110**, 5973–5977 (2006).

330. Jiang, Z. *et al.* A Label-Free Nanogold DNAzyme-Cleaved Surface-Enhanced Resonance Raman Scattering Method for Trace UO22+ Using Rhodamine 6G as Probe. *Plasmonics* **8**, 803–810 (2013).

331. Hildebrandt, P. & Stockburger, M. *Surface-Enhanced Resonance Raman Spectroscopy of Rhodamine 6G Adsorbed on Colloidal Silver. J. Phys. Chem* **88**, (1984).

332. Li, M. *et al.* Stamping surface-enhanced Raman spectroscopy for label-free, multiplexed, molecular sensing and imaging. *J. Biomed. Opt.* **19**, 050501 (2014).

333. Pristinski, D., Tan, S., Erol, M., Du, H. & Sukhishvili, S. In situ SERS study of Rhodamine 6G adsorbed on individually immobilized Ag nanoparticles. *J. Raman Spectrosc.* **37**, 762–770 (2006).

334. Barhoumi, A. & Halas, N. J. Detecting chemically modified DNA bases using surface-enhanced raman spectroscopy. *J. Phys. Chem. Lett.* **2**, 3118–3123 (2011).

335. Fan, Z., Kanchanapally, R. & Ray, P. C. Hybrid Graphene Oxide Based Ultrasensitive SERS Probe for Label-Free Biosensing. *J. Phys. Chem. Lett.* **4**, 3813–3818 (2013).

336. Frontiera, R. R., Henry, A. I., Gruenke, N. L. & Van Duyne, R. P. Surface-enhanced femtosecond stimulated Raman spectroscopy. *J. Phys. Chem. Lett.* **2**, 1199–1203 (2011).

337. Kartha, K. K., Babu, S. S., Srinivasan, S. & Ajayaghosh, A. Attogram sensing of trinitrotoluene with a self-assembled molecular gelator. *J. Am. Chem. Soc.* **134**, 4834–4841 (2012).

338. Kim, N. H., Lee, S. J. & Moskovits, M. Aptamer-mediated surface-enhanced raman spectroscopy intensity amplification. *Nano Lett.* **10**, 4181–4185 (2010).

339. Kleinman, S. L. *et al.* Single-molecule surface-enhanced raman spectroscopy of crystal violet isotopologues: Theory and experiment. *J. Am. Chem. Soc.* **133**, 4115–4122 (2011).

340. Spiro, T. G. Resonance Raman Spectroscopy as a Probe of Heme Protein Structure and Dynamics. *Adv. Protein Chem.* **37**, 111–159 (1985).

341. Sato, H., Chiba, H., Tashiro, H. & Ozaki, Y. Excitation wavelength-dependent changes in Raman spectra of whole blood and hemoglobin: comparison of the spectra with 514.5-, 720-, and 1064-nm excitation. *J. Biomed. Opt.* **6**, 366 (2001).

342. Daniels, J. S. & Pourmand, N. Label-Free Impedance Biosensors: Opportunities and Challenges. *Electroanalysis* **19**, 1239–1257 (2007).

343. Kaur, H., Shorie, M., Sharma, M., Ganguli, A. K. & Sabherwal, P. Bridged Rebar Graphene functionalized aptasensor for pathogenic E. coli O78:K80:H11 detection. *Biosens. Bioelectron.* **98**, 486–493 (2017).

344. Zhang, D., Zong, X., Wu, Z. & Zhang, Y. Ultrahigh-performance impedance humidity sensor based on layer-by-layer self-assembled tin disulfide/titanium dioxide nanohybrid film. *Sens Actuators, B Chem.* **266**, 52–62 (2018).

345. Wu, R. *et al.* Efficient capture, rapid killing and ultrasensitive detection of bacteria by a nano-decorated multi-functional electrode sensor. *Biosens. Bioelectron.* **101**, 52–59 (2018).

346. Hanlon, D. *et al.* Liquid exfoliation of solvent-stabilized few-layer black phosphorus for applications beyond electronics. *Nat. Commun.* **6**, (2015).

347. Dong, N. *et al.* Optical Limiting and Theoretical Modelling of Layered Transition Metal Dichalcogenide Nanosheets. *Sci. Rep.* **5**, 14646 (2015).

348. Gholamvand, Z. *et al.* Comparison of liquid exfoliated transition metal dichalcogenides reveals MoSe $_2$ to be the most effective hydrogen evolution catalyst. *Nanoscale* **8**, 5737–5749 (2016).

349. Li, H. *et al.* Rapid and Reliable Thickness Identification of Two-Dimensional Nanosheets Using Optical Microscopy. *ACS Nano* **7**, 10344–10353 (2013).

350. Kumar, V., Shorie, M., Ganguli, A. K. & Sabherwal, P. Graphene-CNT nanohybrid aptasensor for label free detection of cardiac biomarker myoglobin. *Biosens. Bioelectron.* **72**, 56–60 (2015).

351. Kumar, V. *et al.* Nanostructured aptamer-functionalized black phosphorus sensing platform for label-free detection of myoglobin, a cardiovascular disease

biomarker. *ACS Appl. Mater. Interfaces* **8**, 22860–22868 (2016).

352. Mielczarek, W. S., Obaje, E. A., Bachmann, T. T. & Kersaudy-Kerhoas, M. Microfluidic blood plasma separation for medical diagnostics: Is it worth it? *Lab Chip* **16**, 3441–3448 (2016).

353. Kersaudy-Kerhoas, M. & Sollier, E. Micro-scale blood plasma separation: From acoustophoresis to egg-beaters. *Lab on a Chip* **13**, 3323–3346 (2013).

354. Maria, M. S., Kumar, B. S., Chandra, T. S. & Sen, A. K. Development of a microfluidic device for cell concentration and blood cell-plasma separation. *Biomed. Microdevices* **17**, 1–19 (2015).

355. Yang, S., Ündar, A. & Zahn, J. D. A microfluidic device for continuous, real time blood plasma separation. *Lab Chip* **6**, 871–880 (2006).

356. Chung, K. H. *et al.* Magnetically-actuated blood filter unit attachable to pre-made biochips. *Lab Chip* **12**, 3272–3276 (2012).

357. Thorslund, S., Klett, O., Nikolajeff, F., Markides, K. & Bergquist, J. A hybrid poly(dimethylsiloxane) microsystem for on-chip whole blood filtration optimized for steroid screening. *Biomed. Microdevices* **8**, 73–79 (2006).

358. Moorthy, J. & Beebe, D. J. In situ fabricated porous filters for microsystems. *Lab Chip* **3**, 62–66 (2003).

359. Wang, S. Q. *et al.* Simple filter microchip for rapid separation of plasma and viruses from whole blood. *Int. J. Nanomedicine* **7**, 5019–5028 (2012).

360. Kim, J. H., Woenker, T., Adamec, J. & Regnier, F. E. Simple, miniaturized blood plasma extraction method. *Anal. Chem.* **85**, 11501–11508 (2013).

361. Crowley, T. A. & Pizziconi, V. Isolation of plasma from whole blood using planar microfilters for lab-on-a-chip applications. *Lab Chip* **5**, 922–929 (2005).

362. Lee, D.-S. *et al.* Construction of Membrane Sieves Using Stoichiometric and Stress-Reduced Si_3N_4/SiO_2/Si_3N_4 Multilayer Films and Their Applications in Blood Plasma Separation. *ETRI J.* **34**, 226–234 (2012).

363. Li, C., Liu, C., Xu, Z. & Li, J. The dual role of deposited microbead plug (DMBP): A blood filter and a conjugate reagent carrier toward point-of-care microfluidic immunoassay. *Talanta* **97**, 376–381 (2012).

364. Li, C., Liu, C., Xu, Z. & Li, J. Extraction of plasma from whole blood using a deposited microbead plug (DMBP) in a capillary-driven microfluidic device. *Biomed. Microdevices* **14**, 565–572 (2012).

365. CHEN, M. Di *et al.* Microchannel with Stacked Microbeads for Separation of Plasma from Whole Blood. *Chinese J. Anal. Chem.* **47**, 661–668 (2019).

366. VanDelinder, V. & Groisman, A. Separation of plasma from whole human blood in a continuous cross-flow in a molded microfluidic device. *Anal. Chem.* **78**, 3765–3771 (2006).

367. Fan, R. *et al.* Integrated barcode chips for rapid, multiplexed analysis of proteins in microliter quantities of blood. *Nat. Biotechnol.* **26**, 1373–1378 (2008).

368. Madadi, H., Casals-Terré, J. & Mohammadi, M. Self-driven filter-based blood plasma separator microfluidic chip for point-of-care testing. *Biofabrication* **7**, 025007 (2015).

369. Faustino, V., Catarino, S. O., Pinho, D., Lima, R. A. & Minas, G. A Passive Microfluidic Device Based on Crossflow Filtration for Cell Separation Measurements: A Spectrophotometric Characterization. *Biosensors* **8**, 125 (2018).

370. Geng, Z., Ju, Y., Wang, Q., Wang, W. & Li, Z. Multi-component continuous separation chip composed of micropillar arrays in a split-level spiral channel. *RSC Adv.* **3**, 14798–14806 (2013).

371. Kim, Y. C., Kim, S. H., Kim, D., Park, S. J. & Park, J. K. Plasma extraction in a capillary-driven microfluidic device using surfactant-added poly(dimethylsiloxane). *Sens Actuators, B Chem.* **145**, 861–868 (2010).

372. Kang, T. G., Yoon, Y.-J., Ji, H., Lim, P. Y. & Chen, Y. A continuous flow micro filtration device for plasma/blood separation using submicron vertical pillar gap structures. *J. Micromechanics Microengineering* **24**, 087001 (2014).

373. Chebbi, R. Dynamics of blood flow: modeling of the Fåhræus–Lindqvist effect. *J. Biol. Phys.* **41**, 313–326 (2015).

374. Barbee, J. H. & Cokelet, G. R. The Fahraeus effect. *Microvasc. Res.* **3**, 6–16 (1971).

375. Fung, Y. C. Stochastic flow in capillary blood vessels. *Microvasc. Res.* **5**, 34–48 (1973).

376. Yen, R. T. & Fung, Y. C. Effect of velocity distribution on red cell distribution in capillary blood vessels. *Am. J. Physiol. - Hear. Circ. Physiol.* **4**, (1978).

377. Schmid-Schönbein, G. W., Skalak, R., Usami, S. & Chien, S. Cell distribution in capillary networks. *Microvasc. Res.* **19**, 18–44 (1980).

378. Zhong, R., Wu, N. & Liu, Y. Microfluidic Human Blood Plasma Separation for Lab on Chip Based Heavy Metal Detections. in 11–16 (ECS, 2012).

doi:10.1149/1.3697855

379. Kersaudy-Kerhoas, M., Kavanagh, D. M., Dhariwal, R. S., Campbell, C. J. & Desmulliez, M. P. Y. Validation of a blood plasma separation system by biomarker detection. *Lab Chip* **10**, 1587–1595 (2010).

380. Prabhakar, A., Kumar, Y. V. B. V., Tripathi, S. & Agrawal, A. A novel, compact and efficient microchannel arrangement with multiple hydrodynamic effects for blood plasma separation. *Microfluid. Nanofluidics* **18**, 995–1006 (2015).

381. Nivedita, N. & Papautsky, I. Continuous separation of blood cells in spiral microfluidic devices. *Biomicrofluidics* **7**, (2013).

382. Sollier, E., Rostaing, H., Pouteau, P., Fouillet, Y. & Achard, J. L. Passive microfluidic devices for plasma extraction from whole human blood. *Sens Actuators, B Chem.* **141**, 617–624 (2009).

383. Sudarsan, A. P. & Ugaz, V. M. Multivortex micromixing. *Proc. Natl. Acad. Sci. U. S. A.* **103**, 7228–7233 (2006).

384. Haeberle, S., Brenner, T., Zengerle, R. & Ducrée, J. Centrifugal extraction of plasma from whole blood on a rotating disk. *Lab Chip* **6**, 776–781 (2006).

385. Gorkin, R. *et al.* Centrifugal microfluidics for biomedical applications. *Lab on a Chip* **10**, 1758–1773 (2010).

386. Kuo, J. N. & Chen, X. F. Plasma separation and preparation on centrifugal microfluidic disk for blood assays. *Microsyst. Technol.* **21**, 2485–2494 (2015).

387. Amasia, M. & Madou, M. Large-volume centrifugal microfluidic device for blood plasma separation. *Bioanalysis* **2**, 1701–1710 (2010).

388. Mack, C. *Fundamental Principles of Optical Lithography: The Science of Microfabrication. Fundamental Principles of Optical Lithography: The Science of Microfabrication* (Wiley, 2007). doi:10.1002/9780470723876

389. Cirelli, R. A., Watson, G. P. & Nalamasu, O. Optical Lithography. in *Encyclopedia of Materials: Science and Technology* 6441–6448 (Elsevier, 2001). doi:10.1016/B0-08-043152-6/01138-4

390. KING, M. C. Principles of Optical Lithography. in **1**, 41–81 (Elsevier, 1981).

391. Dow Chemical Company, T. *SYLGARD™ 184 Silicone Elastomer FEATURES & BENEFITS*. (2017).

392. Balasingam, S. K., Lee, J. S. & Jun, Y. Few-layered MoSe2 nanosheets as an advanced electrode material for supercapacitors. *Dalt. Trans.* **44**, 15491–15498

(2015).

APPENDIX

Synopsis

Aptamer Functionalized Nanobioprobe Based Sensing Platforms for Cardiovascular Diseases

Munish Shorie

PH14213

Cardiac diseases are the leading causative of mortality among non-communicable diseases in individuals falling in 30-70 years age-group, and have seen a rampant increase in the number of new cases over the years.[1] Currently, cardiovascular diseases (CVD) are responsible for ~18 million deaths, which accounts for 31% of the total annual global mortality.[2] The progression of cardiovascular diseases is slow, and may sometimes take years to develop to their lethal stages. It is believed that up to 90% of total cardiovascular-associated deaths are avoidable if the onset of the diseases is recognized and treated in the early stages.[3,4] During the development of the CVDs, certain protein molecules are released in the blood by the cardiovascular system and can purpose as characteristic beacons for the disease.[5] Such proteins, called cardiac disease biomarkers are molecules whose serum concentration can be associated with the disease stage and its severity. Sensitive quantification of such cardiac disease biomarker can reveal the onset of this otherwise silent disease, and may help in reducing the mortality & morbidity due to its lethal consequences.[6]

Currently, several cardiac biomarkers are identified as quantifiable signal molecules for the detection of cardiovascular diseases. However, their serum levels can also exceed the physiological thresholds due to some non-cardiac associated scenarios including inflammatory diseases, aggravated immune responses, certain infectious diseases, age etc., thus generating false positives.[7–10] Hence, there is a standing need for devices with abilities of multiplex diagnosis, which can generate a self-validating and reliable result for estimating the overall cardiovascular health.[11,12] Similarly, the minute concentrations of the cardiac biomarkers released during the initial phases of the disease development usually falls on the lower spectrum of diagnostic devices thus producing

false negatives.[5] Such scenarios can be averted by choosing sensitive detection platforms with the faculty to quantify the biological moieties at ultra-low levels, thus allowing the practitioners to take life-affecting decisions early and precisely.

The commercial diagnostic platforms relied on the use of antibodies as their specific bioreceptors as antibodies had established themselves over several decades of application. However, as our bioreceptors, we chose nucleic acid-based aptamers that had challenged antibodies-based platforms since their inception in the early 1990s. In several studies involving direct comparative analysis, aptamers advanced over conventional receptors owing to their superior properties involving structural stability, conformational flexibility during selection, higher melting points, and tunable *in vitro* selection methods.[13-18] Their selection method, SELEX is a simple cyclic process that enables the separation of potential targets from a diverse combinatorial library by using a target-bound stationary matrix. However, the methods reported for the selection of such aptamers either involved a very high number of cycles, usually above 20, or were single-step methodologies. Both the alternatives complicated aptamer development by inclusion of higher costs arising from high cycle number, or from sophisticated equipment. Thus, our aim was to modify the selection methodology to reduce the cycle number while maintaining its effectiveness. For this, we first developed a **Plate-SELEX**, which used a microtitre plate surface as its stationary matrix. This allowed complete control over the retention times, and in-turn over the interactions between target protein and nucleic acid sequences. Along with the developed method, we introduced a gradual expansion of reactive surface area, achieved by increasing the number of involved wells, which created a dynamic inflation of the potential targets by relieving the selection threshold. This methodology was utilized for the development of DNA aptamers against a cardiac biomarker, Myoglobin, in just 5 cycles. The developed Myoglobin-specific aptamer showed very high association with its antigen in the colorimetric characterizations. The aptamer was tested for its specificity through column chromatography, and was able to selectively recognize Myoglobin from a mixture of Myoglobin & serum albumin. To improve the SELEX process further, we developed a single-pot reaction methodology thus further reducing the reaction to one just cycle. The novel **BLI-SELEX** was based on selective screening of aptamers from a combinatorial library by an immobilized target using a bio-layer interferometer. The methodology was an advancement over other reported one-reaction SELEX methods due to the

incorporation of a differentiation step involving gradually strengthening dissociation solutions that could distinguish between aptamers differing in their binding strength for the target. The method was applied to successfully develop aptamers for B-type Natriuretic Peptide (BNP), a cardiac prognostic marker, and Troponin I, a cardiac diagnostic marker.

A biosensor has two fundamental properties, <u>Specificity</u> originating from the bioreceptor, and <u>Sensitivity</u> arising from the transducer. While a bioreceptor plays an essential role in recognizing the target antigen from a plethora of molecules, the transducer is the enabling component that decides the dynamic range of the sensor by converting the biointeraction in a readable signal. Thus, a sensitive biosensor in turn requires a sensitive transducer that can generate signal when the targets are present at very minute quantities, a quintessential feature of an early-stage detection system. With the advance of nanotechnology, several nanomaterials have been developed with remarkable transducing properties.[13] To select a suitable nanomaterial for our objective, we generated diverse number of nanomaterials to assess the role of various transducer classes and materials. Carbon-based quantum dots were generated as fluorescent probes from thermal carbonization of simple organic material. These were combined with Myoglobin-specific aptamers to develop a fluorescent assay for the detection of Myoglobin having a functional range of 1 ng/mL to 100 µg/mL. The quantum dots were modified by incorporation of Nitrogen and Sulphur to ascertain the role of dopants on fluorescent properties of the quantum dots. This was achieved by using keratin-rich materials, like nails and hair as the starting materials for quantum dots' generation. The doping resulted in an enhancement of the fluorescent properties of the nanomaterials, whereas its emission profile overlapped with the characteristic Soret absorption of Myoglobin. This allowed for the development of a direct fluorescent assay based on dynamic quenching that was further developed in a smartphone-based point-of-care (PoC) device for the quantification of Myoglobin. Further, electrochemical transducers were assessed by generating rGO/CNT based van der Waals heterostructure. The nano-hybrid demonstrated enhancement in the electronic properties compared to its starting materials, and was developed in a direct electron transfer based electrochemical assay showing a dynamic range of 1 ng/mL to 4 µg/mL. The electrochemical assay was further improved by replacing the rGO/CNT based material with few-layered Phosphorene that showed higher responses in electrochemical experiments; and with the introduction of a

cationic polymer poly-L-lysine to enhance the aptamer loading on the platform. These modifications resulted in multifold expansion of the dynamic range of developed electrochemical assay to create a faculty to quantify Myoglobin in a range of 1 pg/mL to 16 µg/mL. Furthermore, a Raman-based platform was developed, keeping in purview the excellent sensitivity of Raman spectroscopic methods. A Raman-active nanomaterial was generated from WS_2 nanosheets onto which nanoparticles of gold were decorated in an *in situ* manner. Defected nanosheets of WS_2, as generated by liquid phase exfoliation, were reported to demonstrate excellent reducing properties, and were utilized for on-site conversion of gold ions into nanoparticles, which in turn were deposited on the surface of the nanosheets. The 0D@2D AuNPs@WS_2 nano-hybrid displayed enhancement in the Raman signatures of a Raman label Rhodamine 6G, compared with unmodified nanosheets in their Raman spectrometric analysis because of the generated AuNPs hotspots. This enhancement was translated in a SERS-based platform by incorporating Myoglobin-specific aptamers, and exhibited a dynamic range of 1 fg/mL to 0.1 µg/mL. A comparative of different transducers operating on same bioreceptor & target combination (Myoglobin & Myoglobin-specific aptamer) showed Raman-based assays to deliver highest sensitivity; however, the electrochemical setups possessed a wider dynamic range and therefore the desired ability to respond at both ends of target concentrations. Thus, electrochemical transducers based platforms were developed for the remaining biomarkers. Using liquid-phase exfoliation methods, nanosheets of WSe_2 were generated for the development of impedimetric diagnostic platform for BNP.

Finally, multiplexing of cardiac biomarkers was achieved by developing a microfluidics-based device for simultaneous detection of two cardiac biomarkers. Microfluidics based devices functioning on blood samples are composed of two components *viz.* a plasma separating region & a detection region, and purely microfluidics based plasma separators further utilize various strategies like physical straining, fluid dynamics-based, and Pinch-&-Expand module. Whereas physical straining type suffers from clogging by blood cells, the remaining strategies have a limited range of allowed fluid flow-rates beyond which they tend to stop operating. Photolithography was utilized to synthesize an in-chip plasma separator by amalgamating two different techniques to create a novel centrifugal pinch-&-expand system for plasma separation from whole or diluted blood at a wider range of flowrates with 100% separation efficiency. In brief, photolithography was used to generate the desired designs onto a Si

substrate, and later transferred to PDMS substrates using standard procedures. For generating a final device, a pattern engraved PDMS slab was joined with another plain slab of PDMS that could harbor nanomaterial-modified electrodes *via* a 3M double adhesive sheet. The electrodes were modified with respective aptamers for Myoglobin and Troponin I to create two separate chambers for the detection of either protein. The device was flowed with varying concentrations of either protein, and the current response was monitored by recording voltammograms. The developed device was able to distinguish the presence of either proteins from the increase or decrease of current in the respective detection chambers for Myoglobin and Troponin I respectively. The developed microfluidics chip is a standalone device with an ability to separate plasma from blood while providing a route to detect multiple cardiac biomarkers on an electrochemical setup. The system was validated for simultaneous detection of Myoglobin and Troponin I and has the ability to be expanded for other serum-based cardiac or non-cardiac biomarkers as a parallel multiplex *lab-on-a-chip* setup.

References:

1.   Cardiovascular diseases (CVDs). Available at: https://www.who.int/news-room/fact-sheets/detail/cardiovascular-diseases-(cvds). (Accessed: 4th December 2019)

2.   Wang, H. *et al.* Global, regional, and national life expectancy, all-cause mortality, and cause-specific mortality for 249 causes of death, 1980–2015: a systematic analysis for the Global Burden of Disease Study 2015. *Lancet* **388**, 1459–1544 (2016).

3.   McGill, H. C., McMahan, C. A. & Gidding, S. S. Preventing heart disease in the 21st century: implications of the Pathobiological Determinants of Atherosclerosis in Youth (PDAY) study. *Circulation* **117**, 1216–27 (2008).

4.   O'Donnell, M. J. *et al.* Global and regional effects of potentially modifiable risk factors associated with acute stroke in 32 countries (INTERSTROKE): a case-control study. *Lancet* **388**, 761–775 (2016).

5.   De Couto, G., Ouzounian, M. & Liu, P. P. Early detection of myocardial dysfunction and heart failure. *Nature Reviews Cardiology* **7**, 334–344 (2010).

6.   Kullo, I. J. & Cooper, L. T. Early identification of cardiovascular risk using genomics and proteomics. *Nature Reviews Cardiology* **7**, 309–317 (2010).

7.   Bozbas, H., Yildirir, A. & Muderrisoglu, H. Cardiac enzymes, renal failure and renal transplantation. *Clinical Medicine and Research* **4**, 79–84 (2006).

8.   Olivieri, F. *et al.* Aged-related increase of high sensitive Troponin T and its implication in acute myocardial infarction diagnosis of elderly patients. *Mech. Ageing Dev.* **133**, 300–305 (2012).

9.   Makaryus, A. N., Makaryus, M. N. & Hassid, B. Falsely Elevated Cardiac Troponin I Levels. *Clin. Cardiol.* **30**, 92–94 (2007).

10.   DE GENNARO, L. *et al.* Increased Troponin Levels in Nonischemic Cardiac Conditions and Noncardiac Diseases. *J. Interv. Cardiol.* **21**, 129–139 (2008).

11.   May, A. & Wang, T. J. Biomarkers for cardiovascular disease: challenges and future directions. *Trends in Molecular Medicine* **14**, 261–267 (2008).

12.   Gerszten, R. E. & Wang, T. J. The search for new cardiovascular biomarkers. *Nature* **451**, 949–952 (2008).

13.   Kaur, H. & Shorie, M. Nanomaterial based aptasensors for clinical and environmental diagnostic applications. *Nanoscale Adv.* (2019). doi:10.1039/C9NA00153K

14.   Yan, Q. *et al.* Correction: Using an RNA aptamer probe for super-resolution imaging of native EGFR. *Nanoscale Adv.* **1**, 894–894 (2019).

15.   Chen, C., Zhou, S., Cai, Y. & Tang, F. Nucleic acid aptamer application in diagnosis and therapy of colorectal cancer based on cell-SELEX technology. *npj Precis. Oncol.* **1**, 37 (2017).

16.   Catanante, G., Mishra, R. K., Hayat, A. & Marty, J.-L. Sensitive analytical performance of folding based biosensor using methylene blue tagged aptamers. *Talanta* **153**, 138–144 (2016).

17.   Schlecht, U., Malavé, A., Gronewold, T., Tewes, M. & Löhndorf, M. Comparison of antibody and aptamer receptors for the specific detection of thrombin with a nanometer gap-sized impedance biosensor. *Anal. Chim. Acta* **573–574**, 65–68 (2006).

18.   Crivianu-Gaita, V. & Thompson, M. Aptamers, antibody scFv, and antibody Fab' fragments: An overview and comparison of three of the most versatile biosensor biorecognition elements. *Biosens. Bioelectron.* **85**, 32–45 (2016).

Carbon quantum dots-mediated direct fluorescence assay for the detection of cardiac marker myoglobin

Munish Shorie[†], Vinod Kumar[†], Priyanka Sabherwal* and A. K. Ganguli*

Institute of Nano Science and Technology, Mohali 160 062, India

We report here fluorescence based assay using carbon quantum dots (CQDs) for the detection of cardiac marker myoglobin (Mb). CQDs with high fluorescence properties are synthesized and functionalized with generated anti-Mb-Aptamer to develop a sensitive assay platform with a detection limit of ~1 ng/ml and a wide detection range from 1 to 10^5 ng/ml.

Keywords: Carbon quantum dots, cardiovascular diseases, fluorescence assay, myoglobin.

CARBON quantum dots (CQDs) have tremendous potential because of their superiority in water solubility, chemical inertness, low toxicity, ease of functionalization and resistance to photobleaching[1]. They have been employed as novel, ideal fluorescent probes for bioimaging and smart sensing[2]. Sensitive and specific detection of protein biomarkers plays a crucial role in proteomics, clinical diagnostics, drug screening and biodefence applications[3]. Current methods for protein biomarkers are mostly based on the use of antibodies, which are not readily available and not well adapted to a rapid, sensitive strategy[4]. Recently, aptamers have been utilized as antibody alternatives functioning in a similar fashion with molecular recognition in a variety of diagnostic formats[5]. These specific recognition molecules are usually evolved from random oligonucleotide pool by a process known as 'systematic evolution of ligands by exponential enrichment' (SELEX)[6]. The synergies of nanotechnology in synthetic macromolecules and biomolecular recognition units are promising in developing novel diagnostic platforms for clinically important biomarkers[7].

Cardiovascular diseases are the leading cause of morbidity and mortality worldwide[8]. The increase in the incidence of cardiovascular disease will be particularly dramatic in India in near future and there is a growing demand for products that can provide rapid, quantitative and cost-effective diagnostic tests in virtually all patient-care settings. Several potential cardiac biomarkers have attracted attention because of their ability to predict future cardiovascular events[9]. Serum cardiac biomarkers such as myoglobin (Mb) have become the cornerstone for risk stratification and diagnosis of patients with an acute coronary syndrome[10]. The monitoring of cardiac markers requires high-precision assays acceptable to physicians for the proper diagnosis[11]. In the present study, we have generated specific aptamers screened from oligonucleotide library by SELEX method, against the most potential cardiac biomarker Mb[12]. We report here a fluorescence-based assay using specific aptamers immobilized on microtitre plate for direct detection of Mb, as shown in Figure 1 *a*.

CQDs were synthesized by thermal carbonization process, where 0.375 g of L-glutamic acid, 5 ml of 5 M HNO_3 and optimum concentration of glycerol (45%) were heated at 300°C in an oven for 6 h. Further, 10 ml of water was added into the solution followed by stirring for 30 min with cooling at room temperature. The resulting solution was ultracentrifuged at 10,000 *g* for 1 h. The supernatant was discarded and the final product was resuspended in water containing optimized concentration of nafion (5%) to form CQDs solution, which was further used for characterization and assay development. Standard solution of Mb (4 mg/ml) was prepared in PB (100 mM) and it was added to CQDs solution with an incubation at 37°C for 2 h followed by dialysis in PB buffer for 24 h. For morphological and structural characterization, transmission electron microscopy (TEM) was used (JEOL 2100 operating at 200 kV). The results show that the CQDs exhibit an average diameter of 3 ± 0.6 nm (Figure 1 *b*) and the crystalline lattices were consistent with graphitic carbons as shown in the SAED pattern (Figure 1 *c*). Further, the elemental composition of the selected area scan as determined by the energy-dispersive X-ray spectroscopy (EDX) (Figure 1 *d*), shows the presence of carbon and fluorine, which confirms the formation of nafion-coated CQDs. The excitation and emission of the synthesized CQDs were observed at 346 and 424 nm respectively (Figure 1 *e*). For assay development Mb solution was added to nafion-coated CQDs and incubated for 1 h followed by centrifugation at 17,000 rpm for 30 min to remove unbound CQDs. The absorption spectra of Mb-coated CQDs suggest an additional peak at 400 nm due to the Soret transition, which confirms the conjugation of Mb with nafion-coated CQDs. The microtitre
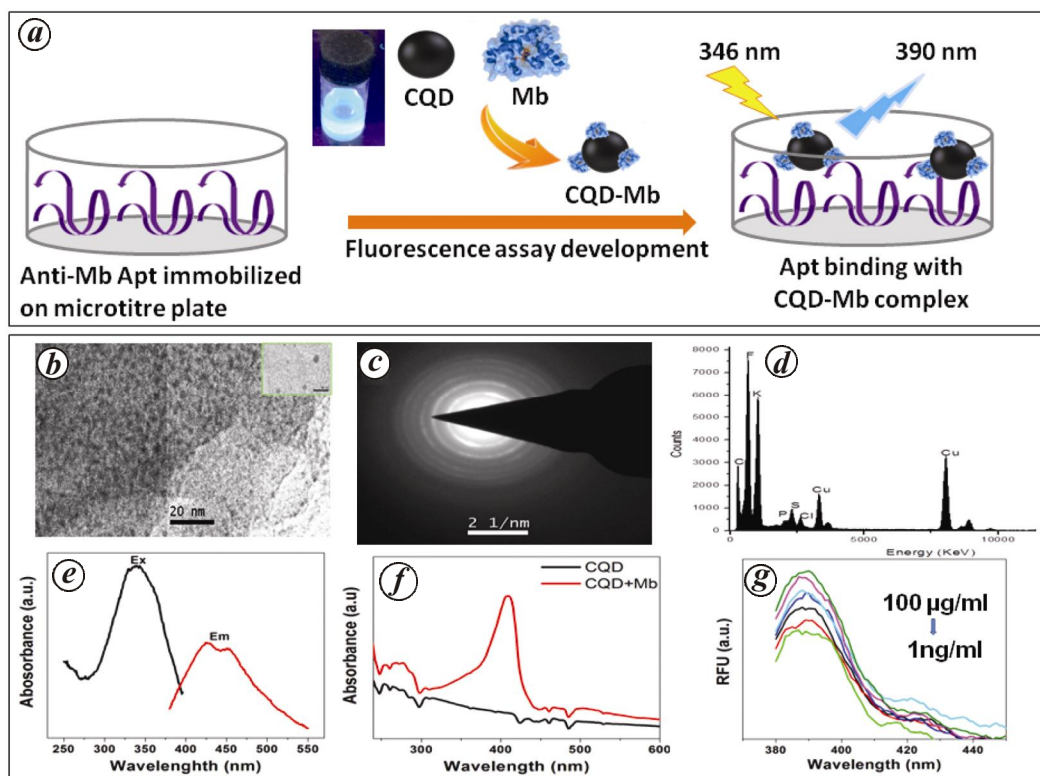
Figure 1. *a*, Schematic showing carbon quantum dots (CQDs)-mediated direct fluorescence assay for the detection of myoglobin (Mb). *b*, TEM photomicrograph showing CQDs. (Inset) Magnified view of a selected region. *c*, SAED pattern of CQDs. *d*, EDS spectra of CQDs. *e*, Excitation and emission spectra of nafion-coated CQDs. *f*, Absorption spectra of Mb-coated CQDs and CQDs. *g*, Direct fluorescence assay for Mb using varying concentrations from 1 ng/ml to 100 μg/ml.

plates were coated with anti-Mb aptamer (2 μg/ml prepared in DNA-coating solution) by incubating overnight at 4°C. Varying concentrations of Mb-conjugated nafion CQDs were added and the fluorescence spectra were recorded in the range 380–450 nm. A subsequent increase in fluorescence intensity was observed with increase in Mb concentration, suggesting the specific interaction of Mb with anti-Mb aptamer immobilized on the microtitre plate.

Conclusion

A fluorescence-based detection method is presented for the selective detection of the cardiac marker Mb. This direct method provides a wide detection range using single bioreceptor, unlike the conventional sandwich ELISA tests. The developed biosensing platform will have great potential for the early diagnosis and management of cardiac diseases.

1. Li, H., Kang, Z., Liu, Y. and Lee, S. T., Carbon nanodots: synthesis, properties and applications. *Mater. Chem.*, 2012, **22**, 24230–24253.
2. Luo, P. G. *et al.*, Carbon 'quantum' dots for optical bioimaging. *J. Mater. Chem. B*, 2013, **1**, 2116–2127.
3. Cao, L. *et al.*, Carbon dots for multiohoton bioimaging. *J. Am. Chem. Soc.*, 2007, **129**, 11318–11319.
4. Wang, L., Liu, X., Zhang, Q., Zhang, C., Liu, Y., Tu, K. and Tu, J., Selection of DNA aptamers that bind to four organophosphorus pesticides. *Biotechnol. Lett.*, 2012, **34**, 869–874.
5. Kent, A. D., Spiropulos, N. G. and Heemstra, J. M., General approach for engineering small-molecule-binding DNA split aptamers. *Anal. Chem.*, 2013, **85**, 9916–9923.
6. Shangguan, D. *et al.*, Identification of liver cancer-specific aptamers using whole live cells. *Anal. Chem.*, 2008, **80**, 721–728.
7. Moore, M. W., Babu, D. and Cotter, P. D., Challenges in the co-development of companion diagnostics. *Per. Med.*, 2012, **9**(5), 485–496.
8. Parkar, S. M., Modi, G. N. and Jani, J., Periodontitis as risk factor for acute myocardial infarction: a case control study. *Heart Views*, 2013, **14**(1), 5–11.
9. Nambi, V. *et al.*, Troponin T and N-terminal pro-B-type natriuretic peptide: a biomarker approach to predict heart failure risk-the atherosclerosis risk in communities study. *Clin. Chem.*, 2013, **59**(12), 1802–1810.
10. Lewandrowski, K. B., Cardiac markers. *Clin. Lab. Med.*, 2014, **34**(1), 31–41.
11. Sabherwal, P., Shorie, M., Pathania, P., Chaudhary, S., Bhasin, K. K., Bhalla, V. and Suri, C. R., Hybrid aptamer-antibody linked fluorescence resonance energy transfer based detection of trinitrotoluene. *Anal. Chem.*, 2014, **86**(15), 7200–7204.
12. Kumar, V., Shorie, M., Ganguli, A. K. and Sabherwal, P., Graphene-CNT nanohybrid aptasensor for label free detection of cardiac biomarker myoglobin. *Biosens. Bioelectron.*, 2015; doi: 10.1016/J.BIOS.2015.04.089.

Graphene-CNT nanohybrid aptasensor for label free detection of cardiac biomarker myoglobin

CrossMark
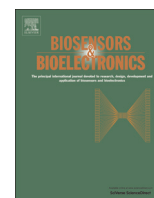
Vinod Kumar [1], Munish Shorie [1], Ashok K. Ganguli *, Priyanka Sabherwal *

Institute of Nano Science & Technology, Mohali 160062, India

A B S T R A C T

We report a label free electrochemical detection of cardiac bio-marker myoglobin (Mb) on aptamer functionalized rGO/CNT nanostructured electrodes by measuring its direct electron transfer (DET). Configured as a highly responsive aptasensor, the newly developed biosensing platform exhibits synergistic effect of the nano-hybrid functional construct by combining good electrical properties and the facile chemical functionality of nanohybrid for the compatible bio-interface development. The specific anti-Mb aptamer was generated by five iterative SELEX (Systematic evolution of ligands by exponential enrichment) rounds, showing high senstivity (K_D ~65 pM). The aptamer functionalized rGO/CNT nanostructured electrodes demonstrated a significant increase in signal response with a detection limit of ~0.34 ng/mL in the dynamic response range between 1 ng/mL and 4 μg/mL for Mb. The newly developed DET assay format presents a promising candidate in point-of-care diagnosis for routine screening of Mb in patient's samples.

© 2015 Elsevier B.V. All rights reserved.

1. Introduction

Cardiovascular diseases pose necessities for the design and development of label-free, rapid, reliable, cost effective and affinity based diagnosis (Qureshi et al., 2012). Several potential cardiac biomarkers have attracted attention because of their ability to predict future cardiovascular events and their mechanistic involvement in associated pathways (Nambi et al., 2013). Serum cardiac marker, Mb plays an important role in clinical diagnosis as its elevated level indicates myocardial damage (Stillman et al., 2011). It has also become the cornerstone for the risk stratification and diagnosis of patients with acute myocardial infarction (AMI), as it is released in biological fluids such as blood stream and urine in 4–50 h after AMI episode (Moreira et al., 2013). The expression level of Mb increases upto ~600 ng/mL in comparison to normal range i.e. from 100–200 ng/mL (Suprun et al., 2010). The quantification of Mb has been reported by several approaches including electro-analytical techniques due to their non-destructiveness, and rapid response time (Wang et al., 2005; Mishra et al., 2012). The trend in electrochemical detection is fast changing from enzyme-linked detection of redox active compounds to direct electron transfer (DET) between redox protein and electrode surface (Wang et al., 2005). Recently, DET has gained considerable

attention for understanding the complex electron transfer mechanisms in biological systems for elucidating the relationship between their structures and bio-molecular interactions (Tuteja et al., 2014). Mb has been explored as a redox active heme protein, which is used mainly as an electrode matrix to enhance electrochemical response (Li et al., 2006). Very few reports are available towards the specific and sensitive DET based detection of Mb, thereby imposing a need for proficient point-of-care diagnosis (POC), paving the way to create bedside technologies for cardiac management.

Affinity based assays using specific antibodies/aptamers offer a preferential alternate approach for biosensing in virtue of their high selectivity, sensitivity and rapidness (Priyanka et al., 2014). However, the critical part is to get high quality bioreceptors to be used as recognition/capture molecules. Aptamers have been utilized as antibody alternatives, functioning in a similar fashion with molecular recognition as target biomarker as they mimic the properties of antibodies in a variety of diagnostic formats (Wang et al., 2012). The biomolecular recognition units combined with nanomaterials are promising in the development of novel diagnostic platforms for clinically important biomarkers (Holzinger et al., 2014). The use of reduced graphene oxide/multiwalled carbon nanotubes (rGO/CNT) hybrid poses synergistic effect of the nano-hybrid functional construct by combining good electrical properties and facile chemical functionality for the development of compatible bio-interface on electrode surface (Huang et al., 2013). The present work demonstrates the effective screening of specific DNA aptamers selected from the pool of random-sequence

---

* Corresponding authors. Fax: + 91 172 2210074.
  E-mail addresses: ashok@inst.ac.in (A.K. Ganguli),
priyanka@inst.ac.in (P. Sabherwal).
  [1] Both authors contributed equally.
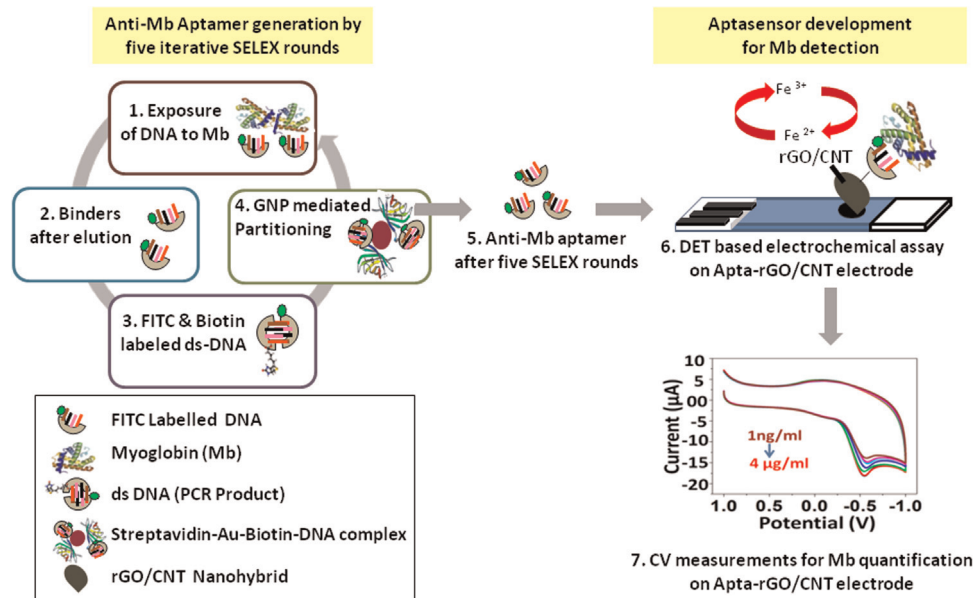
Fig. 1. Schematic showing the streptavidin labeled gold nanoprobes mediated SELEX method for specific anti-Mb aptamer generation (left) and its subsequent usage in the development of rGO/CNT modified aptasensor for the label free detection of Mb (right).

oligonucleotides and its usage in a newly developed DET based assay format for Mb detection on rGO/CNT modified aptasensor (Fig. 1). The developed sensing platform showed high sensitivity and specificity for Mb, by showing a great potential in POC diagnosis for cardiac management.

2. Experimental

2.1. Materials

Myoglobin, Graphite flakes, MWCNTs, L-ascorbic acid, hemoglobin (Hb), bovine serum albumin (BSA) and HPLC purified DNA library 5′-ATCCAGAGTGACGCAGCA-(N45)TGGACACGGTGGCTTAGT-3′ were procured from Sigma India. The sequences of the designed primers are: 5′-FITC-ATACCAGCTTATTCAATT-3′ and 5′-biotin-AGATTGCACTTAC-TATCT-3′. Reacti-Bind DNA coating solution and TMB/H_2O_2 substrate were purchased from Thermo Scientific (India).

2.2. Screening of anti-MB aptamer by modified SELEX

The specific DNA aptamers were screened from a pool of oligonucleotides with a random region of 45 nucleotides flanked by constant primer-binding region of 18 nucleotides by using modified SELEX method. Briefly, Mb (5 μg/mL prepared in 10 mM carbonate buffer pH ∼9.6) was immobilized by incubating overnight at 4 °C on microtiter plates. The single stranded DNA naive library was exposed to the immobilized target analyte, acid eluted, further amplified and partitioned to produce specific binders (Supplementary text ST1).

2.3. Characterization of generated anti-MB aptamer

The progression of SELEX rounds was monitored by measuring the absorbance values at 260 nm (for concentration), 260/280 and 260/230 ratios (for quality check) using Nanodrop spectrophotometer (Make: GE, USA, Model No. Nanovue Plus). To evaluate the specificity of selected binders with the target analyte Mb, a direct binding colorimetric assay was carried out on a microtitre plate where peroxidase activitiy of Mb was measured by taking the absorbance at 450 nm. The affinity binding SPR studies of the anti-

Mb aptamer were carried out by immobilizing Mb (100 μg/mL prepared in 50 mM sodium acetate buffer, pH ∼3.2) on carboxymethylated dextran (CMdextran) (Supplementary text ST2).

2.4. Synthesis of rGO-CNT nanohybrid

Graphene oxide (GO), the parent molecule for reduced graphene oxide (rGO) was synthesized by an earlier reported method (Priyanka et al., 2012). Briefly, 10 mg of GO was dispersed in 10 mL of double distilled water:DMF (V/V:9:1) followed by sonication for 30 min. Subsequently, 10 mg of MWCNTs were added to GO dispersion and the mixture was ultrasonicated for 1 h to get stable nanohybrid. As obtained GO/CNT hybrid was washed with double distilled water and further dried. rGO/CNT was prepared by partially reducing GO into rGO by using L-Ascorbic acid. For this, 100 mM of L-Ascorbic acid was added into the 10 mL dispersion of GO/CNTs and vigorously stirred for 4 h at 90 °C followed by washing, drying and subjected to its characterization.

2.5. Characterization of synthesized nanohybrid

The structural and morphological characterizations of rGO/CNT nanohybrid was carried out by microscopic and spectroscopic analysis. Scanning electron microscopy (SEM) was carried out on JSM-1T300 by preparing drop casted sample (2.5 μg/mL) on Si wafer. For structural analysis, Transmission Electron Microscopy (TEM) was carried out on JSM-2100 system operating at 200 kV. Conductive AFM (c-AFM, Bruker Multimode8) was carried out for electric characterization of drop casted nanohybrid on Silicon wafer and a bias voltage was applied between the sample and the cantilever. The spectroscopic characterization of the nanohybrid was carried out by Raman spectroscopy (WITEC DV401A-BV-352) using 532 nm laser. Brunauer, Emmett and Teller (BET) surface area analysis was done using Quanta Chrome Model Q2.

2.6. rGO/CNT nanostructured electrodes and assay development

Screen printed electrodes (SPE, TE 100, CH Instruments USA) were used for the electrochemical studies where 2.5 μL of rGO/CNT dispersion (1 mg/mL) was drop casted onto the working area of SPE and dried at 50 °C for 2 h. The electrochemical performance of

the nanostructured electrodes were studied with cyclic voltammetry (CV) taken in phosphate buffered saline (100 mM, pH ~7.2) at a sweeping potential ranging from 1 to –1 V with a scan rate of 100 mV/s. For assay development, 5 μL of anti-Mb DNA aptamer (250 μg/mL prepared in 10 mM Tris buffer supplemented with 50 mM NaCl and 10 mM CaCl$_2$; pH ~7.2) was drop casted over rGO/CNT nanostructured electrodes using DNA coating solution. CV response of the fabricated aptasensor at different concentrations of Mb ranging from 1 ng/mL to 4 μg/mL were carried out in PBS (100 mM, pH ~7.2).

3. Results and discussion

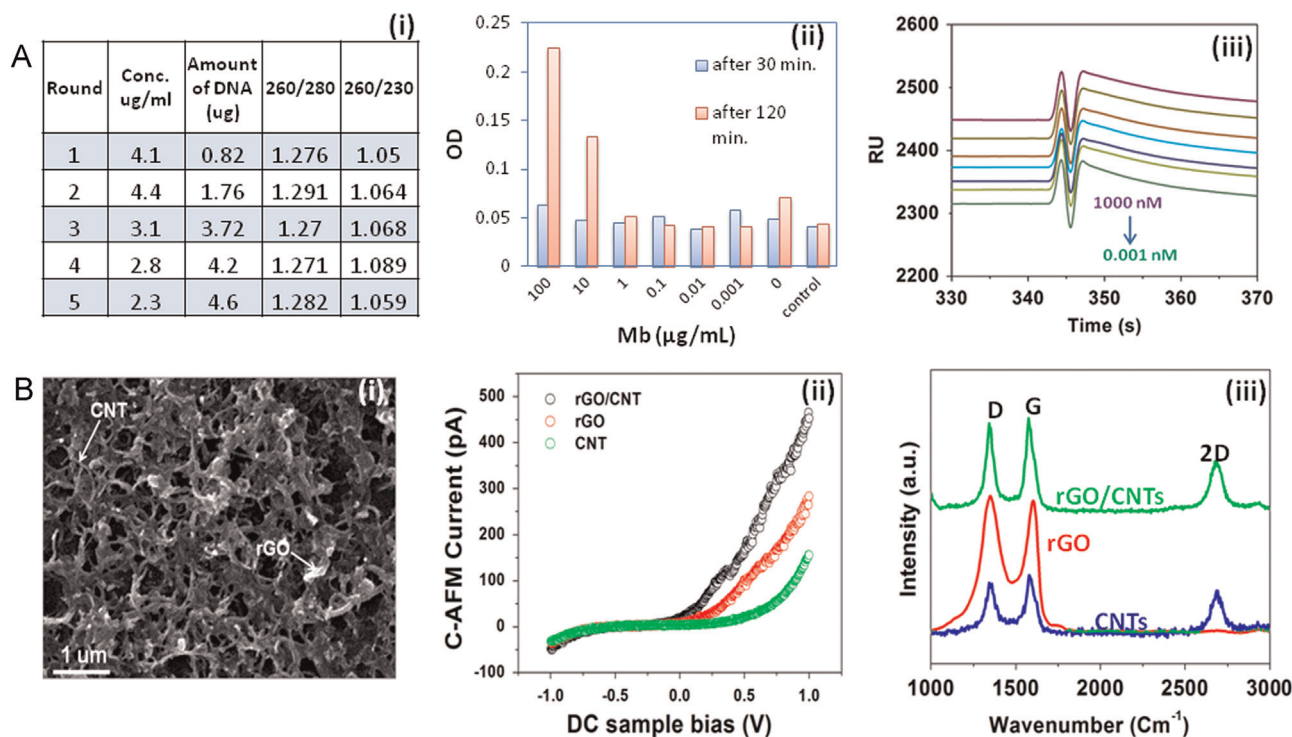### 3.1. Generation and characterization of anti-Mb aptamer

DNA aptamer specific for Mb was selected from ssDNA Library containing 45 nucleotides (random region) flanked by 18 nucleotide fixed region for PCR amplification. The oligomers from the library were exposed to the target molecule Mb immobilized on microtiter plate. Five iterative SELEX rounds involving binding, elution, amplification and partitioning were carried out to generate specific aptamers (see Supplementary ST2). To assess the quantity and purity of DNA after each SELEX round, measurements on nanodrop spectrophotometer were carried out where the absorbance values at 260 nm, 260/280 and 260/230 ratio were measured (Fig. 2A i). The concentration of DNA was also monitored by nanodrop spectrophotometer after each selection cycle.

To evaluate the specificity of selected binders, a direct assay based on peroxidase activity of Mb (Li et al., 2006) was carried out. Increased concentrations of Mb from 0.001 to 100 μg/mL were exposed on binder immobilized plates and subsequent addition of TMB/H$_2$O$_2$ as a substrate produced a gradual color change which was a indicative of specific bio-molecular interactions (Fig. 2A ii). The affinity binding SPR studies of anti-Mb aptamer on CMdextran

SPR chip shows an overlay of sensograms obtained for varying concentration (0.1–1000 nM) of Mb (Fig. 2A iii). The corresponding affinity, K_D, values calculated from the ratio between dissociation (k_d) and association (k_a) was found to be ~65 pM. The fully characterized aptamer pool was further used for the DET assay development.

3.2. rGO/CNT nanostructured electrodes

Assembling CNTs and graphene as a hybrid through noncovalent interaction via π-π stacking offers immense opportunity to collectively exploit the exceptional properties of these two excellent nanomaterials (Yen et al., 2011; Priyanka et al., 2013). In this study, rGO/CNT nanohybrid system was developed where synergistic properties of rGO and CNTs were used for sensitive detection of the analyte of interest. GO was synthesized by the oxidation of exfoliated graphite using modified Hummer's method from graphite powder as reported in the literature (Marcano et al., 2010). The morphological characterization of rGO/CNT nanocomposite by HR-TEM (see Supplementary Fig. S2a) and SEM (Fig. 2B i) displays a view of CNT bundles attached to GO layer clearly indicating the formation of the nanohybrid. c-AFM studies further give an insight into the electrical properties of the nanohybrid when various bias voltages were applied to check the influence on *I–V* characteristics of the nanohybrid (see Supplementary Fig. S2 b–d) further supported by Electrochemical impedance spectroscopic studies (see Supplementary Fig. S2e). The results showed linear *I–V* spectra indicating the good semiconducting character of the synthesized nanomaterial (Fig. 2B ii). Raman spectroscopy was used to investigate the structural aspects of rGO/CNT modification on SPE which clearly exhibits the characteristic D and G bands, at ~1350 cm^{-1} and 1600 cm^{-1} corresponding to A$_{1g}$ and E$_{2g}$ mode respectively. A red shift in G band from 1580 cm^{-1} (CNT), 1595 cm^{-1} (rGO) to 1576 cm^{-1} (rGO/CNT) was observed. A similar shift was observed in D band i.e. from

Fig. 2. (A) Aptamer characterization (i) Nanodrop measurements showing UV absorbance studies for assessing concentration and quality of DNA binders enriched after each SELEX round (1–5th). (ii) Binding characteristics of anti-Mb aptamer by employing direct assay based on peroxidase activity of Mb used in varying concentrations (0–100 μg/mL; control: without DNA). (iii) Kinetic studies showing an overlay of sensograms obtained for anti-Mb aptamers. (B) (i) SEM micrograph of synthesized nanohybrid rGO/CNT. (ii) c-AFM micrograph showing average *I–V* characteristics of rGO, CNT and rGO/CNT. (iii) Raman spectra of rGO, CNT and rGO/CNT.
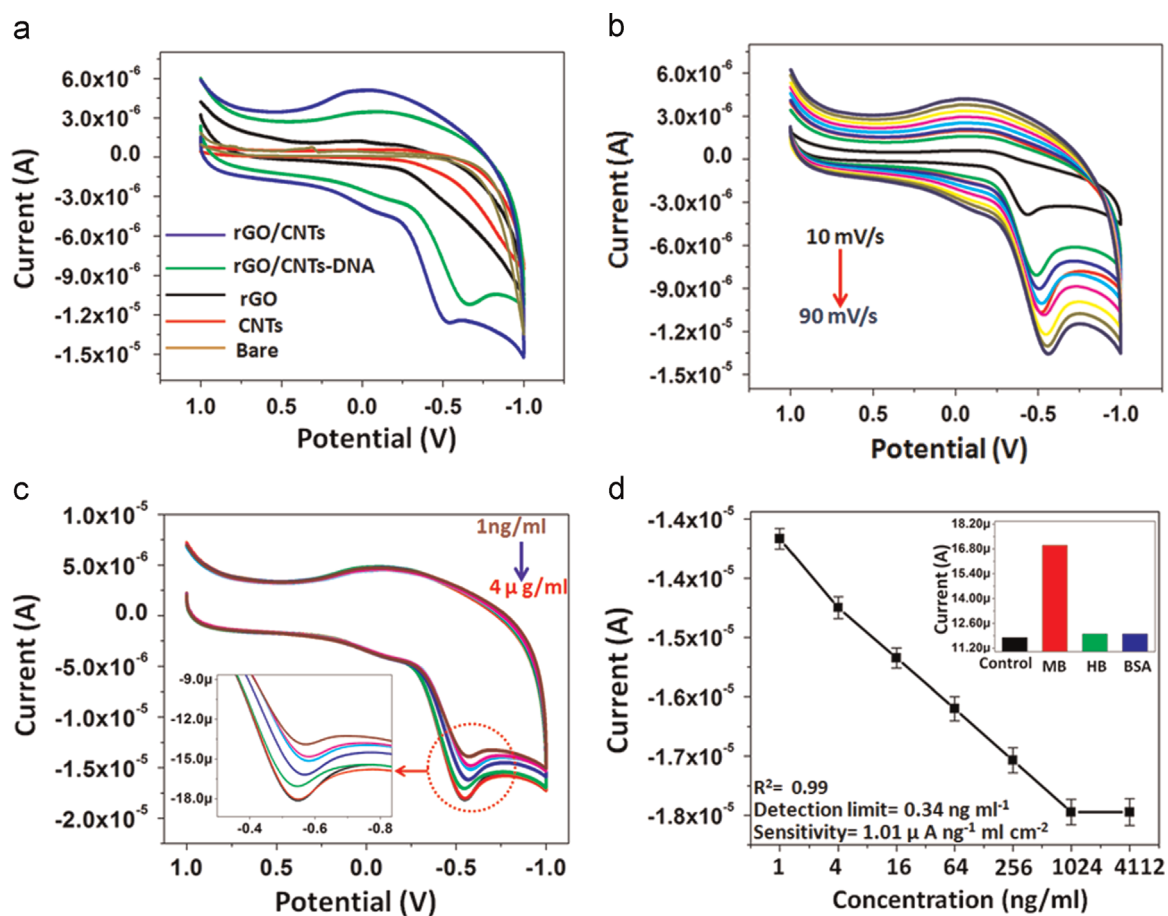
Fig. 3. (a) Electrochemical response curve of modified electrode surface with respect to bare electrode. (b) CV scans of rGO/CNT recorded at different scan rates from 10 to 90 mV/s. (c) DET response curves using varying concentration of Mb measured on apt/rGO/CNT modified SPE. Inset shows the zoom in area of the reduction peak of Mb obtained at a potential of −0.5 V (d) Calibration plot for Mb at different concentrations. Each point in the graph represents the mean of three successive measurements (n=3). Cross reactivity profile of developed sensor with Hb and BSA is shown in the inset.

1345 cm^{-1} (CNT and rGO) to 1340 cm^{-1} in nanohybrid (Fig. 2B iii and see Supplementary ST4). The Raman data suggested that, the mild reduction of GO using L-Ascorbic acid preserved adequate amount of functional groups desirable for bio-interface development. The BET surface area results suggested comparatively decreased surface area of rGO/CNT (81.3 m^2/g) with respect to parent entities CNT (18.9 m^2/g) and rGO (266.7 m^2/g). The difference in surface area of the nanohyrid may be attributed due to overlap of the exfoliated rGO sheets over CNT bundles (McAllister et al., 2007). Furthermore, a dry system would have less surface available than a solvent dispersed system as the solvent helps to maintain separation and limit agglomeration of the nanocomposite (see Supplementary Fig. S3).

From cyclic voltammograms (CV), it was confirmed that the rGO/CNT nanohybrid showed maximum current signal for cathodic peak currents as compared to GO and CNT when drop casted individually on separate electrodes (Fig. 3a). The cathodic peak observed at $\sim$ −0.5 V in rGO/CNT nanohybrid in Fig. 3(a) peak was observed due to the reduction of remaining oxygen functional groups such as hydroxyl, epoxy and carboxyl groups residing on the surface of partially reduced GO which is in accordance with earlier studies (Guo et al., 2009). A significant increase in current was observed with rGO/CNT nanohybrid in comparison to bare electrode. However, a slight decrease in current signal with a small shift in cathodic peak $\sim$0.6 V was observed due to immobilization of DNA aptamer on SPE. Different scan rate responses (25–200 mV/s at an interval of 25 mV/s) of rGO/CNT nanohybrid was also carried out as depicted in Fig. 3b. The cathodic peak current

increases linearly with increase in scan rate indicating that the process is under diffusion control (Srivastava et al., 2012). The electro-active area of nanocomposite modified electrodes was estimated to be 24.48 mm^2 (using Randles–Sevcik equation) which resulted a significant increase in signal response in the developed electrochemical assay (see Supplementary text ST6).

3.3. Electrochemical based DET assay on apt/rGO/CNT modified SPE

For the assay development anti-Mb aptamer was immobilized on rGO/CNT structured SPE and CV measurements which was recorded. A series of Mb standards were exposed to the nanostructured aptasensor and the resulting CV presented a reduction peak at a potential of −0.5 V which is in accordance with earlier reported values (Li et al., 2006). In general, Mb contains the heme group as an active site where heme-iron is in III oxidation state (ferric, Fe^{3+}) in native form which can be reduced directly at the electrode surface to its ferrous state (Fe^{2+}) by one electron transfer (Dai et al., 2009). Our results indicate that single protonation of Mb accompanies the electron transfer from ferric state to the aptamer-functionalized nanostructured electrodes. The percent amplitude of the signal increased with an increasing concentration of Mb which has been depicted in Fig. 3c. The developed assay showed excellent sensitivity in the dynamic response range between 1 ng/mL and 4 µg/mL for Mb with a detection limit of $\sim$0.034 ng/mL (Fig. 3d). The developed assay demonstrates good selectivity, high sensitivity and is capable of detecting Mb at concentration $\sim$50 times lower than that possible by other

         V. Kumar et al. / Biosensors and Bioelectronics 72 (2015) 56–60

conventional methods as shown in Table S7 (see Supplementary text ST7). In repeated experiments, the reproducibility (coefficient of variation) of the sensor for $n=3$ measurements was $\leq 3.0\%$, for 1 ng/mL Mb concentration. The cross reactivity of the developed aptasensor to structurally related protein, hemoglobin (HB) and other non-related protein, BSA showed preference in specific binding with Mb over apt/rGO/CNT functionalized electrodes.

4. Conclusions

A novel label free electrochemical sensing of cardiac marker Mb has been demonstrated for the first time where direct electron transfer of Mb was captured specifically on aptamer functionalized rGO/CNT nanostructured electrodes. The developed aptasensor exhibited high specificity and sensitivity imparted by the screened aptamers and enhanced electrochemical properties of nanohybrid construct respectively, thereby demonstrating a high detection limit of ~0.34 ng/mL for Mb in the developed aptasensor. Further studies are underway to design cost effective electrodes for real time multicardiac biomarker analysis.

Acknowledgements

Appendix A. Supplementary material

Supplementary data associated with this article can be found in the online version at http://dx.doi.org/10.1016/j.bios.2015.04.089.

References

Dai, Z., Xiao, Y., Yu, X., Mai, Z., Zhao, X., Zou, X., 2009. Biosens. Bioelectron. 24, 1629–1634.
Guo, H.L., Wang, X.F., Qian, Q.Y., Wang, F.B., Xia, X.H., 2009. ACS Nano 3, 2653–2659.
Holzinger, M., Goff, A.L., Cosnier, S., 2014. Front. Chem. 2 (63), 1–10.
Huang, T.Y., Huang, J.H., Wei, H.Y., Hoa, K.C., Chu, C.W., 2013. Biosens. Bioelectron. 43, 173–179.
Li, N., Xu, J.Z., Yao, H., Zhu, J.J., Chen, H.Y., 2006. J. Phys. Chem. B 110, 11561–11565.
Marcano, D.C., Kosynkin, D.V., Berlin, J.M., et al., 2010. ACS Nano 4 (8), 4806–4814.
McAllister, M.J., Li, J.L., Adamson, D.H., et al., 2007. Chem. Mater. 19, 4396–4404.
Mishra, S.K., Kumar, D., Biradar, A.M., Rajesh, 2012. Bioelectrochemistry 88, 118–126.
Moreira, F.T.C., Dutrab, R.A.F., Noronhad, J.P.C., Sales, M.G.F., 2013. Electrochim. Acta 107, 481–487.
Nambi, V., Liu, X., Chambless, L.E., et al., 2013. Clin. Chem. 59 (12), 1802–1810.
Priyanka, S., Bhalla, V., Dravid, V., Shekhawat, G., Jinsong, W., Prasad, E.S., Suri, C.R., 2012. Sci. Rep. 2, 877.
Priyanka, S., Tuteja, S., Bhalla, V., Shekhawat, G., Dravid, V., Suri, C.R., 2013. Biosens. Bioelectron. 39, 99–105.
Priyanka, Shorie M., Bhalla, V., Pathania, P., Suri, C.R., 2014. Chem. Commun. 50, 1080–1082.
Qureshi, A., Gurbuz, Y., Niazi, J.H., 2012. Sens. Actuators B: Chem. 171 (172), 62–76.
Srivastava, R.K., Srivastava, S., Narayanan, T.N., Mahlotra, B.D., Vajtai, R., Ajayan, P. M., Srivastava, A., 2012. ACS Nano 1, 168–175.
Stillman, A.E., Oudkerk, M., Bluemke, D., 2011. Int. J. Cardiovasc. Imaging 27, 7–24.
Suprun, E., Bulko, T., Lisitsa, A., Gnedenko, O., Ivanov, A., Shumyantseva, V., Archakov, A., 2010. Biosens. Bioelecton. 25, 1694–1698.
Tuteja, S.K., Priyanka, Bhalla, V.K., Akash Deep, Paul, A.K., Suri, C.R., 2014. Appl. Mater. Interfaces 6, 14767–14771.
Wang, L., Liu, X., Zhang, Q., Zhang, C., 2012. Biotechnol. Lett. 34, 869–874.
Wang, S.F., Chen, T., Zhang, Z.L., Shen, X.C., Lu, Z.X., Pang, D.W., Wong, K.Y., 2005. Langmuir 21, 9260–9266.
Yen, M.Y., Hsiao, M.C., Liao, S.H., Liu, P.I., Tsai, H.M., Ma, C.C.M., Pu, N.W., Ger, M.D., 2011. Carbon 49, 3597–3606.

Research Article

Nanostructured Aptamer-Functionalized Black Phosphorus Sensing Platform for Label-Free Detection of Myoglobin, a Cardiovascular Disease Biomarker

Vinod Kumar,[⊥,†] Jack R. Brent,[⊥,‡] Munish Shorie,[†] Harmanjit Kaur,[†] Gaganpreet Chadha,[†] Andrew G. Thomas,[‡] Edward A. Lewis,[‡] Aidan P. Rooney,[‡] Lan Nguyen,[‡] Xiang Li Zhong,[‡] M. Grace Burke,[‡] Sarah J. Haigh,[‡] Alex Walton,[§] Paul D. McNaughter,[§] Aleksander A. Tedstone,[§] Nicky Savjani,[§] Christopher A. Muryn,[§] Paul O'Brien,*[‡,§] Ashok K. Ganguli,*[†,∥] David J. Lewis,*[‡,§] and Priyanka Sabherwal*[†]

[†]Institute of Nano Science & Technology, Habitat Centre, Sector-64, Mohali 160062, Punjab, India
[‡]School of Materials, University of Manchester, Oxford Road, Manchester M13 9PL, United Kingdom
[§]School of Chemistry, University of Manchester, Oxford Road, Manchester M13 9PL, United Kingdom
[∥]Department of Chemistry, Indian Institute of Technology Delhi, Hauz Khas, New Delhi 110016, India

Ⓢ *Supporting Information*

ABSTRACT: We report the electrochemical detection of the redox active cardiac biomarker myoglobin (Mb) using aptamer-functionalized black phosphorus nanostructured electrodes by measuring direct electron transfer. The as-synthesized few-layer black phosphorus nanosheets have been functionalized with poly-L-lysine (PLL) to facilitate binding with generated anti-Mb DNA aptamers on nanostructured electrodes. This aptasensor platform has a record-low detection limit ($\sim$0.524 pg mL^{-1}) and sensitivity (36 μA pg^{-1} mL cm^{-2}) toward Mb with a dynamic response range from 1 pg mL^{-1} to 16 μg mL^{-1} for Mb in serum samples. This strategy opens up avenues to bedside technologies for multiplexed diagnosis of cardiovascular diseases in complex human samples.

KEYWORDS: *sensing, heart disease, myoglobin, aptamer, 2-D materials, black phosphorus*
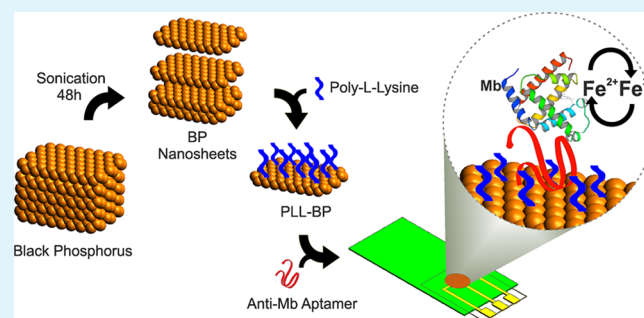
INTRODUCTION

Two-dimensional (2-D) monolayer and few-layered materials have great potential due to their altered optoelectronic and mechanical properties as compared to their multilayered bulk counterparts.[1] The archetypal 2-D material, graphene, has received enormous attention due to its high conductivity[2] and mechanical properties[3,4] which have been exploited in many applications.[5,6] Similarly, inorganic graphene analogues based on transition metal chalcogenides such as molybdenum disulfide (MoS_2)[7] have attracted attention due to their thickness-dependent semiconducting properties.[8] The utilities of these nanomaterials, however, are limited by intrinsic shortcomings, such as lack of a band gap in graphene[9] and relatively low carrier mobility in MoS_2,[10] all of which has motivated a continued search for new 2-D materials. Recently, monolayer black phosphorus (BP), also known as *phosphorene*, has emerged as an important member of this family of 2-D materials.[11] In phosphorene, each phosphorus atom forms covalent bonds with three neighboring phosphorus atoms to give a puckered honeycomb structure. Phosphorene and few-layer black phosphorus nanosheets can be synthesized by mechanical exfoliation of black phosphorus[11] or by liquid-phase exfoliation of black phosphorus in *N*-methyl-2-pyrrolidone (NMP)[12,13] and other organic solvents.[14,15] BP exhibits a direct and tunable band gap that is dependent on the number of layers (bulk, 0.3 eV; monolayer ca. 1.3 eV).[16−18] Monolayer BP has a measured free carrier mobility (ca. 1000 cm^2 V s^{-1})[11] that is superior to MoS_2 (ca. 100 cm^2 V s^{-1}).[10] Phosphorene also exhibits other fascinating and useful properties, including anisotropic electrical conductivity and optical response,[11,16,19] which distinguish it from other 2-D materials such as graphene, and transition metal chalcogenides.

Cardiovascular diseases account for ca. 30% of adult deaths in the 30−70 year age group, which is greater than the combined mortality rate from all types of cancer.[20] The ability to diagnose cardiac pathology is therefore of utmost concern to clinicians.
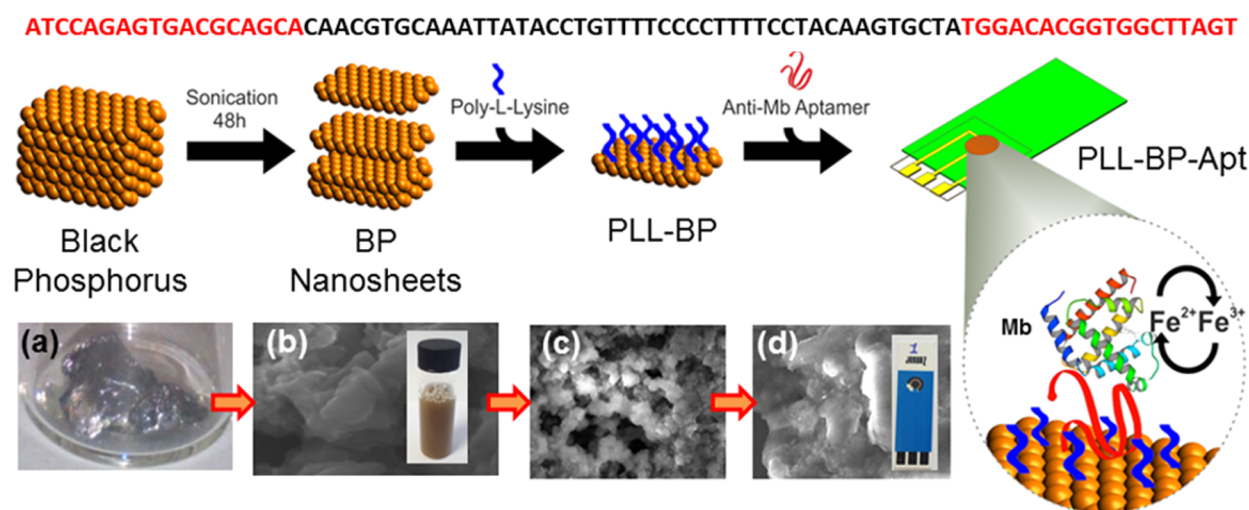
Figure 1. Schematic representation of workflow for the liquid-phase exfoliation of BP nanosheets and their surface modification for biointerface development on an electrode for Mb detection. The panels shown below the workflow scheme depict images of the real colloid, the assembled sensor, and representative secondary electron SEM images taken at each stage. (a) Bulk black phosphorus prior to liquid-phase exfoliation. (b) Representative secondary electron SEM image of exfoliated few-layer BP from aqueous 1% w/v Triton X-100 solution. Inset: Photograph of the stable colloid. (c) SEM image of few-layer BP functionalized with PLL. (d) SEM image of few-layer BP functionalized with PLL and anti-Mb aptamer (PLL-BP-Apt). Inset: Photograph of the sensing device on a screen-printed electrode as used for sensing Mb in this study. The DNA sequence of the SELEX-derived anti-Mb aptamer is shown above.

Several potential cardiac biomarkers have attracted attention because of their ability to act as signals of cardiovascular events.[21] Serum cardiac markers, especially myoglobin (Mb), play an important role in clinical diagnosis; an increased Mb level indicates myocardial damage.[22] Detection of elevated levels of Mb has become a gold standard for diagnosis in cases of acute myocardial infarction (AMI) also known as *heart attack*; Mb is released in the blood within 4−5 h after an AMI episode,[23] with the expression level in plasma serum increasing up to 600 ng mL^{-1} after AMI, over 3−6 times above the normal level expressed in healthy patients.[24] The early and rapid diagnosis of AMI is extremely important for a positive prognosis,[25] yet current Mb detection methodologies rely on analysis in centralized laboratories which are often costly and time-consuming.[26] Thus, development of proficient point-of-care (POC) diagnosis based on biochemical sensors paves the way to rapid cardiac disease management.

Affinity-based assays which use specific antibodies or nucleic acid (DNA or RNA) aptamers for a target protein or small molecule offer a facile approach to biosensing with potential for high selectivity and sensitivity.[27] Nucleic acid aptamers have been utilized as superior alternatives to antibodies due to their smaller size, molecular flexibility, *in vitro* screening, and ease of chemical modification which allows them to be superb candidates for biosensing.[28,29] Recently, the use of 2-D materials has been established in the sensitive detection of biomolecules from blood samples.[30,31] The combination of nucleic acid aptamers with nanomaterials is promising in the development of novel diagnostic platforms for clinically important biomarkers.[32] Two-dimensional nanomaterials in combination with aptamers offer the possibility of creating biosensing platforms with enhanced selectivity and unprecedented sensitivity compared with available conventional detection methods. In the present study, the exfoliation of black phosphorus to give stable few-layer BP in aqueous medium using a surfactant-mediated approach has been developed. The characterized BP nanosheets were modified with cationic polymer poly-L-lysine (PLL) which functions as a

linker for further biomolecular interactions with the underlying BP. Theoretical calculations predict that this interaction occurs through the amide functional groups in PLL. Negatively charged DNA aptamers for Mb were selected from the pool of random-sequence oligonucleotides using the systematic evolution of ligands by exponential enrichment (SELEX) method,[33] and these were immobilized on the nanosheets via Coulombic interactions between PLL and DNA. These nanostructured platforms were employed in electrochemical-based sensing for the qualitative and quantitative detection of the cardiac disease biomarker, Mb (Figure 1). The developed aptasensor showed high sensitivity and specificity for Mb and has singular potential in POC diagnosis for cardiac disease management.

EXPERIMENTAL SECTION

Materials. Black phosphorus (BP) was purchased from Smart Elements (Austria). Triton X-100, poly-L-lysine (PLL), myoglobin (Mb), hemoglobin (Hb), bovine serum albumin (BSA), DNA library 5′-ATCCAGAGTGACGCAGCA-(N45)-TGGACACGG-TGGCTTAGT-3′, and the designed primers 5′-FITC-ATCCAGAGTGACGCAGCA-3′ and 5′-biotin-ACTAAGCCA-CCGTGTCCA-3′ were procured from Sigma-Aldrich.

Instrumentation. Raman spectra were measured using Renishaw 1000 Micro-Raman System equipped with a 514 nm laser operating at 1 mW. Atomic force microscopy (AFM) was performed using Bruker Multimode 8 instrument in PeakForce QNM mode using a silicon nitride cantilever tip. Transmission electron microscope (TEM) imaging, high angle annular dark-field (HAADF) scanning transmission electron microscope (STEM) imaging, and energy dispersive X-ray (EDX) spectrum imaging were performed using a FEI Tecnai F30 TEM operated at 300 kV. HAADF STEM and electron energy loss spectroscopy (EELS) were performed using a probe side aberration corrected FEI Titan G2 80-200 S/TEM "ChemiSTEM" instrument operated at 200 kV, with a convergence angle of 18.5 mrad, a HAADF inner angle of 54 mrad, and a probe current of ∼200 pA. For the electrochemical studies, screen-printed electrodes (SPE, TE 100, CH Instruments USA) were used, and the measurements were carried out on CH660 electrochemical workstation. Optical absorption measurements were performed with a Shimadzu UV 1800 instrument. Scanning electron microscopy (SEM) was performed using a Zeiss

Sigma VP. Low voltage energy dispersive X-ray (EDX) spectroscopy was performed on a Zeiss Merlin SEM equipped with a windowless EDX system (X-Max Extreme, Oxford Instruments). In a comparison with conventional detector systems, it has low noise electronics, high resolution 100 mm^2 SDD sensor, large solid angle, and high sensitivity. EDX spectra and the respective images were analyzed using AZtec software. X-ray photoelectron spectroscopy (XPS) was performed using a Kratos Axis Ultra system.

Black Phosphorus Nanosheet Synthesis by Surfactant-Assisted Liquid-Phase Exfoliation. BP nanosheets were synthesized using an aqueous surfactant solution (1 mg mL^{-1} prepared in Triton X-100 and deionized water) which was thoroughly degassed before use. In a sealed vial, this surfactant solution (15 mL) was added to BP (100 mg, 3.2 mmol), and the vial was flushed with argon, closed, and sealed with Parafilm. Suspensions were sonicated in an Elmasonic P 70 H benchtop ultrasonic bath (820 W across four horns) operating at 37 kHz and 30% power. The temperature of the bath was maintained at 25 °C throughout via the use of a homemade cooling coil. After 36 h the dispersions were centrifuged at 1500 rpm for 45 min, and the top 10 mL of the suspension was removed. An additional 10 mL of surfactant solution was added to the remaining dispersion, and the sediment mixture was sonicated again for 12 h under the same conditions. The dispersion was centrifuged, and the supernatant was added to the previously collected dispersion.

Spectroscopic and Microscopic Characterization of Black Phosphorus Nanosheets. The dispersions of black phosphorus nanosheets were spin-coated at 2000 rpm onto 300 nm silicon-coated SiO$_2$ (SiO$_2$/Si) substrates using an Ossila spin coater for Raman and AFM analysis. For (S)TEM, imaging samples were prepared by drop casting 15 μL of dispersions onto gold-coated carbon Quantifoil grids with a hole size of 1.2 μm. Deionized water was used to wash off the excess solvent from the grids. Samples were immediately transferred to the microscope for imaging after preparation, to minimize the photo-oxidative degradation. EEL spectrum images were acquired from 20 BP flakes with large lateral dimensions (>200 nm). Measurements of t/λ (where t is the sample thickness and λ is the mean free path of inelastic electron scattering) were extracted from the spectrum images using Gatan Digital Micrograph software.

Synthesis and Characterization of PLL-Functionalized Black Phosphorus Nanosheets. The as-synthesized dispersion of exfoliated BP nanosheets in aqueous Triton-X-100 was concentrated and subsequently centrifuged at 3000 rpm to remove the surfactant. The resulting sediment was redispersed in aqueous solution of PLL (1 mg mL^{-1}) which was stirred for 1 h followed by incubation for 12 h at 4 °C. The resulting PLL-BP dispersion was characterized by Raman spectroscopy, zeta potential, and contact angle measurements to evaluate the interaction of PLL with exfoliated BP.

Generation of Specific Anti-Mb Aptamer Using Modified Systematic Evolution of Ligands by Exponential Enrichment (SELEX). The specific DNA aptamers were screened from a pool of oligonucleotides with a random region of 45 nucleotides flanked by constant primer-binding region of 18 nucleotides by using a SELEX method.[27] Briefly, Mb (10 μg mL^{-1} prepared in 50 mM carbonate buffer pH ~ 9.6) was immobilized by incubating overnight at 4 °C on microtiter plates, onto which 10^{14} molecules of ssDNA library were exposed. Harvested DNA binders were PCR amplified and partitioned to produce ssDNA. The generated DNA was subjected to iterative cycles of exposure to the immobilized Mb followed by elution, PCR amplification, and partitioning to screen highly specific DNA aptamer with a dissociation coefficient (K_d) of 65 pM (Supporting Information ST1, ST2).

Mb Detection on PLL-BP Nanostructured Electrodes. As-prepared PLL-BP (3 μL) was drop-casted onto the working area of a screen-printed electrode (SPE) and dried at 50 °C for 2 h under argon. The electrochemical performance of the PLL-BP-modified electrodes was studied with cyclic voltammetry (CV) measured in 5.0 mM potassium ferricyanide/potassium ferrocyanide solution (prepared in 100 mM phosphate buffered saline, PBS) at a sweeping potential ranging from −1 to +1 V with a scan rate of 100 mV s^{-1}. For assay development, 1 μg of anti-Mb DNA aptamer (200 μg mL^{-1} stock

prepared in 10 mM Tris buffer supplemented with 150 mM NaCl and 5 mM MgCl$_2$, pH ~ 7.2) was drop-casted over PLL-BP-modified electrodes. The CV responses of the fabricated aptasensor were recorded at different concentrations of Mb ranging from 1 pg mL^{-1} to 16 μg mL^{-1}.

■ RESULTS AND DISCUSSION

Surfactant-Assisted Liquid-Phase Exfoliation and Characterization of Few-Layer BP Nanosheets. The exfoliation of BP has been previously reported in several organic solvents[12−15] including N-methyl-2-pyrrolidone (NMP), N-cyclohexyl-2-pyrrolidone (CHP), dimethyl sulfoxide (DMSO), and N,N-dimethylformamide (DMF), all of which are biologically incompatible. This study reports the use of an aqueous medium to afford exfoliated BP nanosheets, which unlocks the direct application of the material in biological systems.

BP nanosheets were synthesized by ultrasonic exfoliation of a BP crystal in water containing 1% w/v of Triton X-100 (a nonionic surfactant). A turbid brown solution was produced (Supporting Information ST3, and Figure 1 for an example of the Triton X-100 sol). Raman spectroscopy of the exfoliated BP nanosheets revealed bands at 362, 440, and 465 cm^{-1} assigned to the A^1_g, B$_{2g}$, and A^2_g optical phonons of few-layer BP (Figure 2a). Atomic force microscopy was used to assess the thickness of nanosheets (Figure 2b−d), up to 60 nm in height. The nanosheets were also imaged using DMT modulus mapping which showed that these sheets share a modulus similar to the silicon substrate. However, dark halos were observed around the sheets, which from low voltage EDX spectroscopy measurements are revealed to be surfactant wrapped around the immobilized nanosheets. Scanning electron microscopy of the flakes revealed them to be fairly monodisperse in length (ca. 100−200 nm, Figure 2e) and electron-transparent at 6 kV (Figure 2f).

The nanosheets were further characterized by bright-field TEM and HAADF STEM imaging (Figure 3a,c). Selected area electron diffraction (SAED) of an isolated nanosheet (Figure 3b) demonstrated the crystallinity of the structure, with d-spacings of 2.6, 1.8, 1.7, 1.6, and 1.3 Å which were assigned to the (111), (121), (024), (202), and (204) reflections of black phosphorus. EDX spectroscopy of the nanosheets further confirmed that the major element present is phosphorus (Supporting Information ST4). EDX spectrum imaging of the nanosheets (Figure 3d) confirms undoubtedly that the phosphorus signal is colocalized with the spatial location of the nanosheet in the HAADF STEM image.

The thickness of the BP nanosheets was also calculated using electron energy loss spectroscopy (EELS) which provides an alternative method for local thickness estimation by determining the proportion of inelastic scattering. Although accurate thickness can also be obtained for few-layer flakes using electron diffraction data,[34] this approach generally requires flakes with uniform thickness and lateral dimensions >200 nm, and hence was found to be unreliable as liquid exfoliated flakes often have regions of restacked material, nonuniform thicknesses >10 nm, and small lateral dimensions.

Flake thickness (t) was calculated using an estimated λ (mean free path of inelastic electron scattering) value of ~144.9 nm, calculated by the Iakoubovskii method.[35] Typically, the individual flakes were found to include regions of different thickness (Figure 4) which are partly due to restacking, with smaller flakes aggregating on the surface of larger flakes either
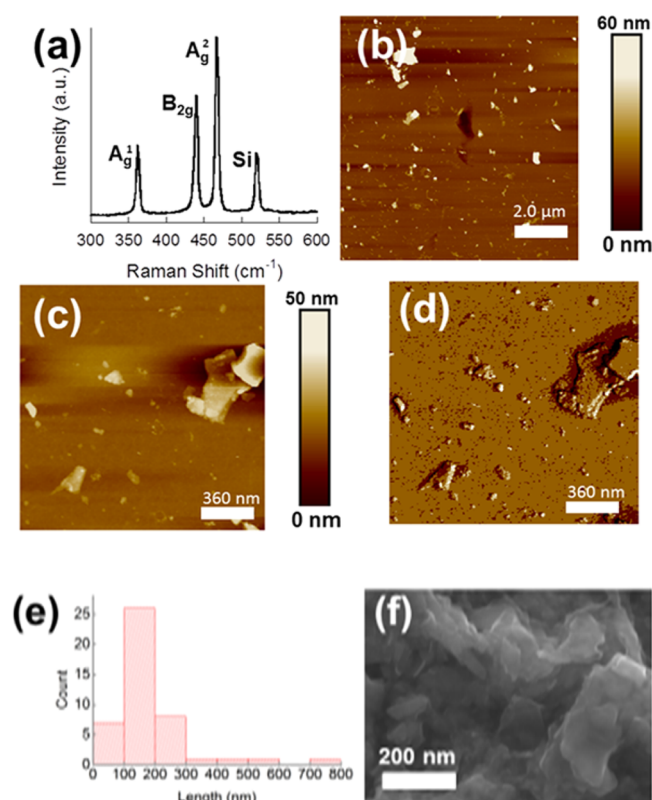
Figure 2. Characterization of liquid-phase exfoliated BP nanosheets. (a) Raman spectrum of exfoliated (in aqueous 1% w/v Triton X-100 solution) few-layer BP on SiO_2/Si substrate showing the characteristic Raman bands at 362, 440, and 465 cm^{-1} assigned to the A^1_g, B_{2g}, and A^2_g phonon modes. (b) Wide-area atomic force microscopy height profile image of few-layered BP sheets SiO_2/Si substrate. (c) Narrow-area atomic force microscopy height profile image of few-layered BP on SiO_2/Si substrate. (d) DMT elastic modulus map of the area imaged in part c. Dark halos observed around the flakes were revealed to be surfactant by low voltage EDX spectroscopy (see Supporting Information for further details). (e) Flake lateral length histogram of few-layered BP. (f) Secondary electron SEM image (6 kV) of few-layer BP. The scale bar represents 200 nm.

in solution or during the drying process. Step changes in thickness were widely observed within the flakes, often with the thinnest regions found at the edges and the thickness increasing toward the center of the flake (Figure 4), suggesting that the flakes themselves also contain terraces of different thickness features which are frequently observed in liquid exfoliated two-dimensional materials.[15,36] In order to take into consideration the range of thicknesses encountered within an individual spectrum image, both the thickest and thinnest measured regions of each flake analyzed were recorded, and the mean thickness of the flake was estimated as an average of these two values (Supporting Information ST5, Table T1). The mean thickness of 20 flakes was measured to be ~19 nm with the lateral dimensions >200 nm, which gives an estimated width/ height aspect ratio of >10:1. The thinnest areas recorded are 4−6 nm, and as the monolayer is ~0.9 nm thick, this suggests that no monolayer regions were encountered for the large flakes considered in this EELS study, but that the thinnest regions analyzed have thicknesses of 5 or more atomic layers and the thickest regions encountered correspond to >40 atomic layers. Monolayer surface steps and isolated terraces were observed on
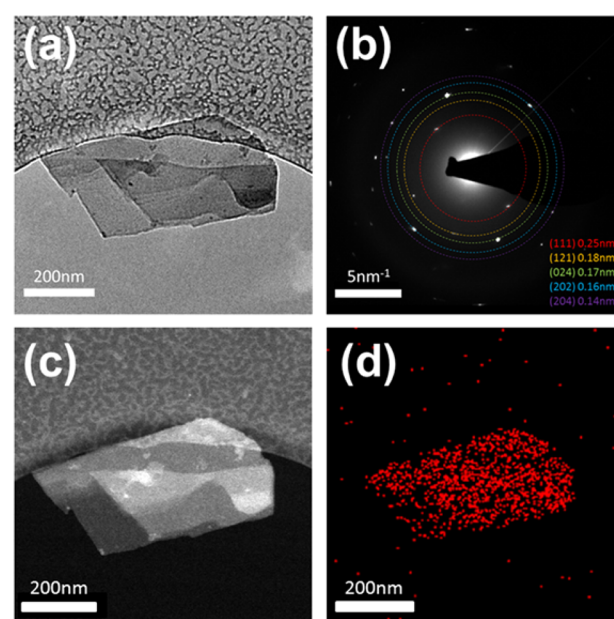
Figure 3. Characterization of an exfoliated BP nanosheet of dimensions ca. 600 nm × 400 nm, aspect ratio ca. 1.5, by TEM at 200 kV. (a) Low magnification TEM image of a BP nanosheet. (b) Selected-area diffraction pattern taken from the same region as in part a. (c) HAADF STEM image. (d) EDX spectrum image of the same BP nanosheet as in part c, showing the morphology and the distribution of phosphorus within the sheet. The flake shown here is typical in terms of aspect ratio, crystallinity, elemental analysis, and morphological features.
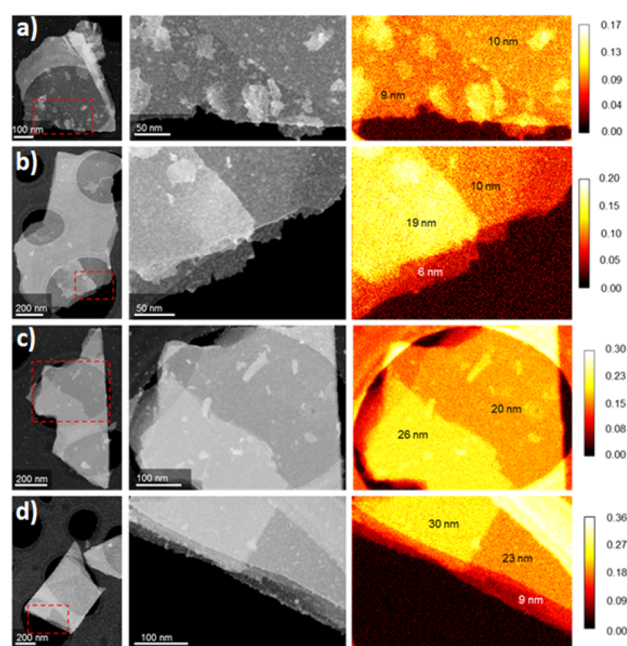
Figure 4. EELS thickness analysis of exfoliated few-layer BP. (a−d) Four typical BP flakes are shown in low magnification high angle annular dark-field (HAADF) STEM images in the left column; the dashed red box indicates the region studied by EEL spectrum imaging. The middle column shows a higher magnification HAADF image of this region, and the right column contains maps of t/λ values extracted from the EEL spectrum image. Thickness values (calculated using λ = 144.9 nm) are superimposed on the t/λ maps.
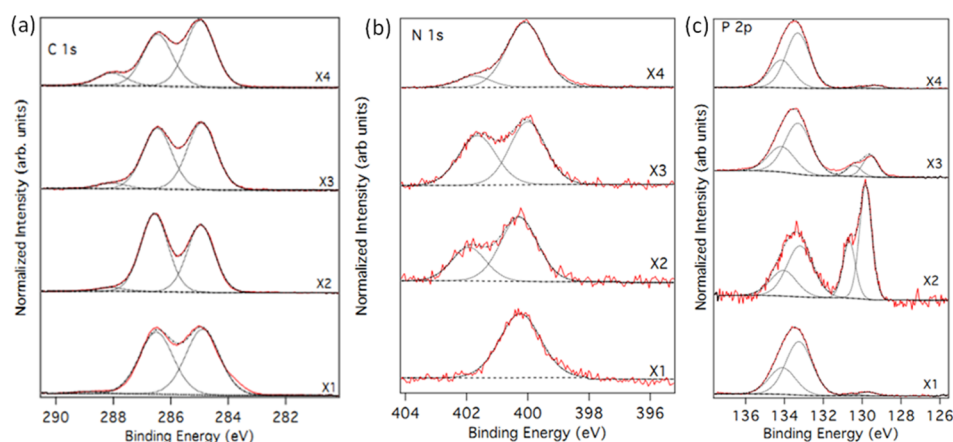
Figure 5. X-ray photoelectron (XPS) spectroscopy monitoring the layer-by-layer assembly of the aptasensor. Parts a–c show C 1s, N 1s, and P 2p comparative XPS spectra of BP nanosheets (X1), PLL-BP (X2), PLL-BP-Apt (X3), and PLL-BP-Apt-Mb (X4), respectively.

the larger flakes studied here, suggesting that monolayer material may exist for flakes with smaller lateral dimensions.

Surface Modification of Black Phosphorus Nanosheets with Poly-L-lysine. The exfoliated BP nanosheets were modified at their surface with PLL to develop an interface for DNA aptamer functionalization for specific Mb sensing. The resulting PLL-BP dispersion was characterized by various microscopic and spectroscopic techniques to evaluate the surface modifications. Low magnification SEM micrographs of PLL-BP on the electrode surface showed an increase in surface roughness (Supporting Information ST6, Figure S4a–c), and a uniform coverage with phosphorus atoms was recorded in the elemental mapping (Supporting Information ST6, Figure S4d). High magnification SEM imaging performed by modifying a Si/SiO$_2$ surface with nanosheets indicated clearly visible smooth surfaces (Supporting Information ST6, Figure S4e–h); however, the surface roughness is increased upon interaction with PLL. When DNA is immobilized over PLL-BP, the surface is completely covered, and further addition of Mb led to an altered morphology. Analysis of Raman spectra revealed a red shift in the characteristic bands of the PLL-BP conjugate from 362, 440, and 465 cm^{-1} (unmodified) to 359, 433, and 460 cm^{-1} (PLL-modified) which again are assigned to the A^1_g, B$_{2g}$, and A^2_g optical phonons, respectively (Supporting Information ST7, Figure S5).

Upon functionalization of BP with PLL, the value of zeta potential was changed from −23.4 to +13.5 mV. The characterized PLL-BP (3 μL of 1 mg mL^{-1} of colloid) was transferred onto the working area of a screen-printed electrode (SPE) and further characterized. The sensor surface characteristics play an important role toward the efficient interactions of the immobilized bioreceptors with the target analyte. The modified sensor surface characteristics (hydrophilicity/hydrophobicity) were studied by contact angle measurements which showed a decrease in mean contact angle (117.5° to 84.1°) in comparison to a bare electrode, indicating an increase in hydrophilicity. We tentatively attribute this to the sensor modification with PLL-BP having two amino groups present at α-carbon and ε-carbon along with one carboxylate group (−COO$^-$) (Supporting Information ST9, Figure S7). The interaction of PLL with the BP surface was further investigated with DFT calculations (see Supporting Information ST23 for full details).

Biointerface Development Using DNA Aptamers. Appropriate DNA aptamers which bind selectively to Mb were selected using SELEX by exposing the target molecule (Mb) immobilized on a microtiter plate to a single stranded DNA (ssDNA) library as reported previously.[33] Liquid chromatography was used to assess the binding of the developed aptamer with Mb by monitoring absorbance at 260, 280, and 409 nm (Supporting Information ST10, Figure S8). The biomolecular interactions lead to the shift of the molecular weight of standard Mb from 16.7 to 41.2 kDa suggesting its interaction with the screened aptamer having molecular weight 24.5 kDa. The characterized SELEX generated anionic aptamer was conjugated to the cationic PLL-BP by Coulombic interactions, thus creating a stable biointerface on PLL-BP as per the mechanism summarized in Figure S9. The PLL-BP nanostructure was further characterized by zeta potential measurement, where a shift of 25.6 mV in zeta potential was observed with respect to PLL-BP, which is ascribed to the electrostatic interactions of available positively charged −NH$_3^+$ groups of PLL with negatively charged DNA phosphate backbone leading to partial charge neutralization (Supporting Information ST8, Figure S6). Raman spectroscopy further supported this by revealing a comparative shift in characteristic Raman bands of PLL-BP after DNA interactions (Supporting Information ST7, Figure S5). The contact angle measurements of PLL-BP aptasensor platform reveal a decrease in contact angle value to ∼84.1° when the anti-Mb DNA aptamer was immobilized on PLL-BP nanostructured electrodes which we ascribe to its increased hydrophilicity from hosting essentially two types of charged polymers (PLL, DNA) (Supporting Information ST9, Figure S7).

Monitoring the Layer-by-Layer Assembly of Nanostructured Aptasensor Electrodes with X-ray Photoelectron Spectroscopy (XPS). XPS gave further insight on the layer-by-layer biofunctionalization strategy that we adopted (Figure 5). The peaks at lower binding energies in the XPS spectra arise due to BP, and the broader peak is due to oxidized BP (PO$_x$) and phosphorus hydroxide (P(OH)$_x$) species (Figure 5). On fitting only one doublet, the broader full width at half-maximum (fwhm) of the peaks on the PO$_x$/P(OH)$_x$ feature suggest that these are likely due to multiple components. Since it is impossible to know the precise composition of the oxidized BP, any attempt to fit multiple components would be meaningless. Following exfoliation of the
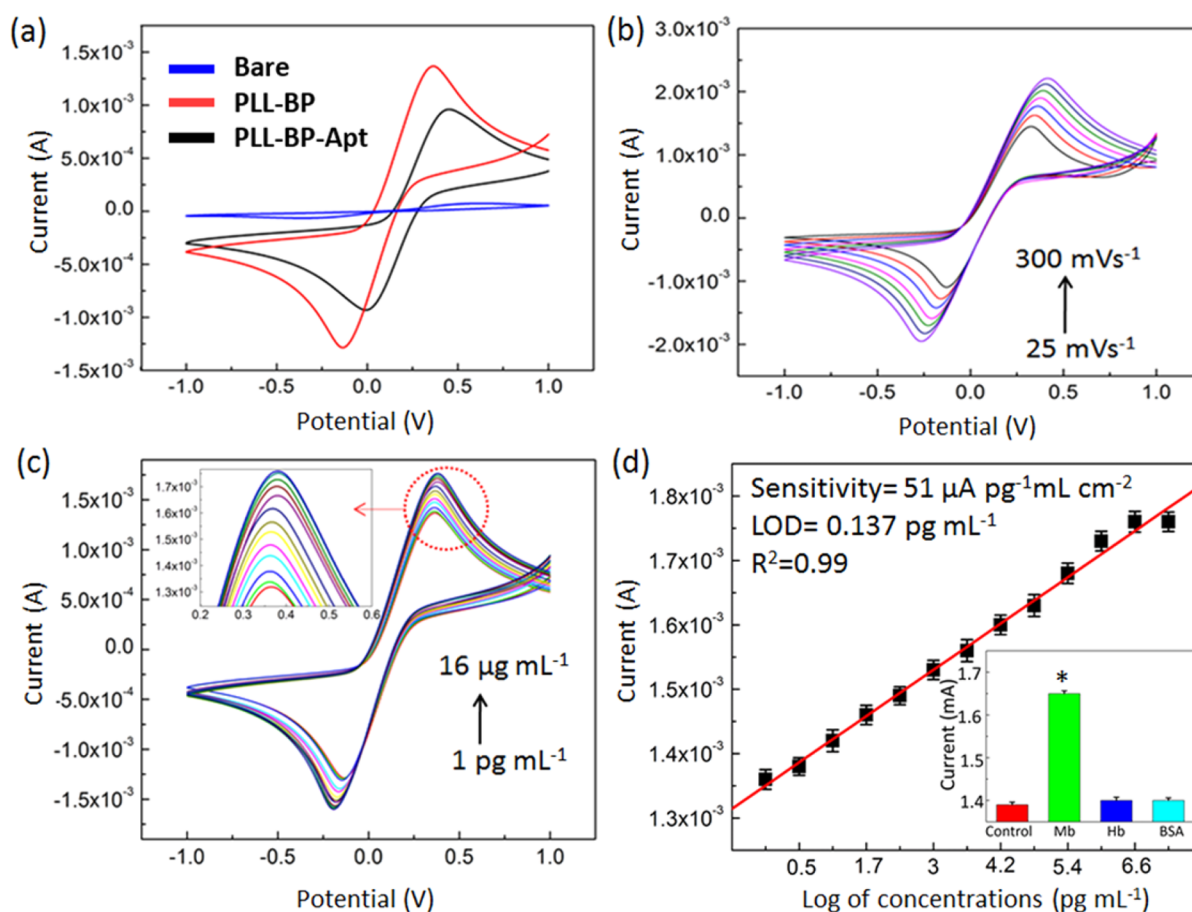
Figure 6. Sensing platform performance. (a) Electrochemical response curve of bare and PLL-BP- and PLL-BP-Apt-modified electrodes using 5 mM potassium ferricyanide/potassium ferrocyanide solution (prepared in 100 mM PBS) at a sweeping potential ranging from −1 to +1 V with a scan rate of 100 mV s^{-1}. (b) CV scans of PLL-BP nanostructured electrode, recorded at different scan rates from 25 to 300 mV s^{-1}. (c) Current response curves at varying concentration of Mb measured on PLL-BP nanostructured aptasensor. Inset shows the zoom in area of redox peak of Mb obtained. (d) Calibration plot for Mb at different concentrations. Every point in the graph represents the mean of three successive measurements ($n = 3$) at each concentration. Inset shows the cross-reactivity profile of developed sensor with a structurally related protein (Hb) and a nonrelated protein (BSA).

BP with Triton X-100, the PO$_x$ component is dominant, yet this may be expected as the sol will always contain an "equilibrium" amount of free phosphate that will dominate over the BP peak. It is likely that phosphate adsorbs to the flakes after drop casting and we cannot separate this effect from the amount of 'natural' degradation on the surface of the flakes. The C 1s peak of the Triton treated BP (Figure 5, X1) can be fitted with two components: one at 285 eV, due to C−C/C−H, and a second one at a binding energy of 286.6 eV, which is attributed to either C−O−C in the polyethylene glycol component or the surfactant. A small peak is also observed at ∼289 eV, which arises from C−OH species, also found in the surfactant. The C 1s peak is also likely to have some contribution due to the presence of adsorbed adventitious hydrocarbon since the samples have been exposed to atmospheric conditions prior to XPS analysis. A broad N 1s peak was recorded from this sample. The origin of the N 1s signal is unknown and is observed in all samples subjected to XPS analysis. Upon interaction with PLL (Figure 5, X2), a second N 1s peak is observed, which is assigned to the amine in the lysine. The BP peak is enhanced relative to the PO$_x$ peak, which suggests a large amount of adventitious phosphate from solution degradation being washed away during functionalization with PLL. Despite using the same data acquisition time it is

clear that the P 2p signal is decreased relative to C and N 1s signals, as the noise level increases. The higher binding energy feature (286.6 eV) in C 1s spectrum increases after PLL adsorption since C−N has a similar binding energy to C−O−C from the ethylene glycol. In addition, the feature at 289 eV increases slightly in intensity as more C−OH will be present from PLL. Addition of DNA (Figure 5, X3) gives rise to very little change in C 1s peaks, and the assignment of these peaks is as for PLL. The P 2p spectrum is dominated again by PO$_x$, in part due to the DNA backbone signal. Again, without prior knowledge of the precise proportion of the P-oxides and hydroxides and DNA-derived P−O components, it is impossible to meaningfully fit the PO$_x$ spectra. As expected, the signal due to amine N increases slightly upon addition of the DNA from the nucleobases. Finally, addition of Mb (Figure 5, X4) leads to almost complete suppression of the BP-derived P 2p signal (since the protein overlayer becomes comparable to the sampling depth of XPS, ca. 10 nm). A strong PO$_x$ signal, however, arises from the bound DNA. In summary XPS allowed us to observe the layer-by-layer assembly of the aptasensor.

Myoglobin Detection on the Nanostructured Aptasensor Electrodes. The modified nanostructured electrodes were employed for the detection of Mb by cyclic voltammetry.

The PLL-BP nanostructured electrodes showed a significant increase in current response (~1.3 mA) in comparison to the bare electrode (~0.64 μA) as shown in Figure 6a. The enhanced electrochemical response of the material is attributed to BP's inherent redox properties which show a significant oxidation peak at ~0.6 V (vs AgCl) corresponding to the oxidation of P^0 to P^{5+} species.[37] In our study, the electroactive area of the PLL-BP-modified electrode was estimated to be ~13.8 mm^2 using the Randles−Sevcik equation (Supporting Information ST13). A slight decrease in current signal (0.28 mA) with a small shift in the cathodic peak potential (0.11 V) was observed which is ascribed to the immobilization of DNA aptamers on PLL-BP-functionalized SPE (Figure 6a). The PLL-BP SPE showed a diffusion controlled electron transfer, evidenced by the linear increase (1.2 to 2.1 mA) in the cathodic peak intensity with increasing scan rate (25−300 mV s^{-1}) (Figure 6b). In addition, the redox peak current increases linearly with the square root of the scan rate, indicating that the redox reaction is controlled by a semi-infinite linear diffusion revealing a rapid electron transport nature.[38] The observations were further supported by scan-rate (25−300 mV s^{-1})-dependent electrical impedance spectroscopic (EIS) studies (Supporting Information ST14). The real and imaginary parts of the EIS spectra (Supporting Information Figure S11) represent Nyquist plots (Z′ vs Z″) for BP-modified SPE using 10 mM Fe(CN)$_6^{3-/4-}$ as the electrolyte. The Randles equivalent circuit model has been used to fit the experimental data where R_{sol} is electrolyte resistance, R_{ct} is charge transfer resistance, C_{dl} is double layer capacitance, and W is the Warburg impedance. The values of equivalent circuit elements were also calculated. The charge transfer process was then ascertained by measuring the charge transfer resistance (R_{ct}) at the electrode/electrolyte interface. The value of R_{ct} for the nanostructured electrode was found to be ~33.3 Ω at 25 mV s^{-1} and decreases with increasing scan rate which depends on the dielectric and insulating features at the electrode/electrolyte interface. The electrochemical stability of PLL-BP SPE was tested by repeated cyclic scanning (100 cycles), which showed insignificant change in the peak currents (Supporting Information ST15, Figure S12). DNA aptamer was drop-casted on the working area of the PLL-BP-modified electrode to a final concentration of 1 μg/electrode in order to uniformly cover the electrode surface (Supporting Information ST16, Figure S13). A series of Mb standard concentrations (prepared in phosphate-buffered saline, 10 mM, pH 7.4) were exposed to the nanostructured aptasensor, and the resulting cyclic voltammogram presented a concentration-dependent reduction peak at a potential of −0.5 V due to the redox property of Mb analyte as shown in Figure 6c. In its native form, Mb contains a heme group as an active site with an iron(II) center which can be oxidized directly at the electrode surface to iron(III) by a one-electron transfer mechanism as per the following equation:[39]

$$Mb-Fe(II) \leftrightarrow Mb-Fe(III) + e^-$$

The platform provides the label-free electrochemical detection of Mb on aptamer-functionalized PLL-BP electrodes by direct electron transfer. The calibration plot for Mb at different concentrations showed a strong linear trend (R^2 = 0.99) indicating a concentration-dependent current signal response of the DNA aptamer 2-D sensing platform. The assay showed excellent sensitivity (51 μA pg^{-1} mL cm^{-2}), in the dynamic response range between 1 pg mL^{-1} to 16 μg mL^{-1} for

Mb with a limit of detection (LOD) of ~0.137 pg mL^{-1} (Figure 6d). The cross-reactivity of the aptasensor to a structurally related protein, hemoglobin (Hb), and another nonrelated ubiquitous plasma protein, bovine serum albumin (BSA) (1 μg/mL each), showed a strong preference for the binding of Mb to the PLL-BP-Apt-functionalized electrode (inset of Figure 6d). As controls, the sensor was checked for signal response with the various modifications in this paper, namely, PLL, PLL-Apt, PLL-Apt-Mb along with BP exfoliated in Triton-X-100, BP-Apt, and BP-Apt-Mb. No significant current response change indicated the high specificity and sensitivity of the developed aptasensor imparted by the immobilized anti-Mb aptamer onto PLL-BP nanostructured electrodes (Supporting Information ST17, Figure S14). The assay was validated against serum samples spiked with varying concentrations of Mb; the aptasensor showed high sensitivity (36 μA pg^{-1} mL cm^{-2}) with a LOD of ~0.524 pg mL^{-1} for Mb in serum samples (Supporting Information ST18, Figure S15). Furthermore, the signal response of the BP nanostructured aptasensor was compared with reduced graphene oxide (rGO) under the same set of conditions used for Mb sensing (Supporting Information ST19, Figure S16). The rGO-based aptasensor shows a detection limit of ~1.3 ng mL^{-1}, with a sensitivity of 10 μA ng^{-1} mL cm^{-2} with a dynamic response range of 4 ng mL^{-1} to 16 μg mL^{-1} for Mb spiked in serum which are both inferior to the reported few-layered BP-based Mb sensor.

To assess aptasensor stability, 6 identical PLL-BP-Apt sensors were investigated by observing the current response at different time intervals, i.e., on the 0th, 1st, 3rd, 7th, 14th, and 21st day with 256 pg mL^{-1} concentration of Mb both in PBS and in serum samples. The results of these studies indicated no significant decrease in the current (within 5%) after 21 days for both Mb in PBS and in serum, revealing the excellent storage stability of the developed aptasensor (Supporting Information ST20, Figure S17). Postsensing XPS analysis of the developed sensor demonstrated that iron was retained on the electrode after use. The phosphorus P 2p high resolution spectrum of the electrode after testing was dominated by PO$_x$ species, from the DNA phosphate and possible adventitious adsorption of phosphate from the PBS buffer that the measurement was performed in (Supporting Information ST22, Figure S18). This developed 2-D sensing platform has high specificity and sensitivity along with a low limit of detection achieved by a PLL-BP nanostructured aptasensor which is superior to all previously reported Mb sensing platforms (see Supporting Information ST21 for comparison to literature).

■ CONCLUSIONS

Surfactant-assisted liquid-phase exfoliation of BP nanosheets in aqueous media is reported, and PLL was used to functionalize the surface of the nanosheets by noncovalent interactions with the underlying BP to give a PLL-modified 2-D material (PLL-BP). An indigenous modified SELEX method for enrichment of DNA aptamers that specifically targets and binds the cardiac biomarker Mb was performed. The selected DNA aptamers were bound to PLL-BP by Coulombic interactions. The PLL-BP nanostructured DNA aptasensor was found to be a label-free electrochemical sensing platform for Mb. The direct electron transfer from Mb was measured specifically onto the functionalized PLL-BP-Apt electrodes. The sensor exhibited high specificity and sensitivity imparted by the synergy of high affinity screened aptamers and the enhanced electrochemical

properties of the nanoconstruct. The sensor has a very low limit of detection of ~0.524 pg mL^{-1} with a sensitivity of 36 μA pg^{-1} mL cm^{-2} for Mb spiked in serum samples. Our study opens up numerous exciting opportunities to realize better cardiac biomarker detection for point-of-care diagnosis.

■ ASSOCIATED CONTENT

Ⓢ Supporting Information

The Supporting Information is available free of charge on the ACS Publications website at DOI: 10.1021/acsami.6b06488.

> Additional characterization details including EDX spectra, SEM characterization, Raman spectroscopy, zeta potential measurements, and other related studies (PDF)

■ AUTHOR INFORMATION

Corresponding Authors

*E-mail: paul.o'brien@manchester.ac.uk. Phone: +44 (0)-161 275 4653.
*E-mail: ashok@inst.ac.in. Phone: +91 (0)-172-2210073/75. Fax: +91-172-2210074.
*E-mail: david.Lewis-4@manchester.ac.uk. Phone: +44 (0)-7940968125.
*E-mail: priyanka@inst.ac.in. Phone: +91 (0)-172-2210073/75. Fax: +91-172-2210074.

Author Contributions

[⊥]V.K. and J.R.B. contributed equally.

Notes

The authors declare no competing financial interest.

■ ACKNOWLEDGMENTS

■ REFERENCES

(1) Miro, P.; Audiffred, M.; Heine, T. An Atlas of Two-Dimensional Materials. *Chem. Soc. Rev.* **2014**, *43* (18), 6537−6554.

(2) Novoselov, K. S.; Geim, A. K.; Morozov, S. V.; Jiang, D.; Katsnelson, M. I.; Grigorieva, I. V.; Dubonos, S. V.; Firsov, A. A. Two-dimensional Gas of Massless Dirac Fermions in Graphene. *Nature* **2005**, *438* (7065), 197−200.

(3) Lee, C.; Wei, X.; Kysar, J. W.; Hone, J. Measurement of the Elastic Properties and Intrinsic Strength of Monolayer Graphene. *Science* **2008**, *321* (5887), 385−388.

(4) Lee, J.-U.; Yoon, D.; Cheong, H. Estimation of Young's Modulus of Graphene by Raman Spectroscopy. *Nano Lett.* **2012**, *12* (9), 4444−4448.

(5) Kuilla, T.; Bhadra, S.; Yao, D.; Kim, N. H.; Bose, S.; Lee, J. H. Recent Advances in Graphene Based Polymer Composites. *Prog. Polym. Sci.* **2010**, *35* (11), 1350−1375.

(6) Akhavan, O.; Ghaderi, E.; Rahighi, R. Toward Single DNA Electrochemcial Biosensing by Graphene Nanowalls. *ACS Nano* **2012**, *6*, 2904−2916.

(7) Matte, H. S. S. R.; Gomathi, A.; Manna, A. K.; Late, D. J.; Datta, R.; Pati, S. K.; Rao, C. N. R. MoS$_2$ and WS$_2$ Analogues of Graphene. *Angew. Chem., Int. Ed.* **2010**, *49* (24), 4059−4062.

(8) Wang, Q. H.; Kalantar-Zadeh, K.; Kis, A.; Coleman, J. N.; Strano, M. S. Electronics and Optoelectronics of Two-dimensional Transition Metal Dichalcogenides. *Nat. Nanotechnol.* **2012**, *7* (11), 699−712.

(9) Castro Neto, A. H.; Guinea, F.; Peres, N. M. R.; Novoselov, K. S.; Geim, A. K. The Electronic Properties of Graphene. *Rev. Mod. Phys.* **2009**, *81* (1), 109−162.

(10) Radisavljevic, B.; Radenovic, A.; Brivio, J.; Giacometti, V.; Kis, A. Single-layer MoS2 Transistors. *Nat. Nanotechnol.* **2011**, *6* (3), 147−150.

(11) Liu, H.; Neal, A. T.; Zhu, Z.; Luo, Z.; Xu, X.; Tomanek, D.; Ye, P. D. Phosphorene: An Unexplored 2D Semiconductor with a High Hole Mobility. *ACS Nano* **2014**, *8* (4), 4033−4041.

(12) Brent, J. R.; Savjani, N.; Lewis, E. A.; Haigh, S. J.; Lewis, D. J.; O'Brien, P. Production of Few-layer Phosphorene by Liquid Exfoliation of Black Phosphorus. *Chem. Commun.* **2014**, *50* (87), 13338−13341.

(13) Kang, J.; Wood, J. D.; Wells, S. A.; Lee, J.-H.; Liu, X.; Chen, K.-S.; Hersam, M. C. Solvent Exfoliation of Electronic-Grade, Two-Dimensional Black Phosphorus. *ACS Nano* **2015**, *9* (4), 3596−3604.

(14) Yasaei, P.; Kumar, B.; Foroozan, T.; Wang, C.; Asadi, M.; Tuschel, D.; Indacochea, J. E.; Klie, R. F.; Salehi-Khojin, A. High-Quality Black Phosphorus Atomic Layers by Liquid-Phase Exfoliation. *Adv. Mater.* **2015**, *27* (11), 1887−1892.

(15) Hanlon, D.; Backes, C.; Doherty, E.; Cucinotta, C. S.; Berner, N. C.; Boland, C.; Lee, K.; Harvey, A.; Lynch, P.; Gholamvand, Z.; Zhang, S.; Wang, K.; Moynihan, G.; Pokle, A.; Ramasse, Q. M.; McEvoy, N.; Blau, W. J.; Wang, J.; Abellan, G.; Hauke, F.; Hirsch, A.; Sanvito, S.; O'Regan, D. D.; Duesberg, G. S.; Nicolosi, V.; Coleman, J. N. Liquid Exfoliation of Solvent-stabilized Few-layer Black Phosphorus for Applications Beyond Electronics. *Nat. Commun.* **2015**, *6*, 8563.

(16) Fei, R.; Yang, L. Strain-Engineering the Anisotropic Electrical Conductance of Few-Layer Black Phosphorus. *Nano Lett.* **2014**, *14* (5), 2884−2889.

(17) Rodin, A. S.; Carvalho, A.; Castro Neto, A. H. Strain-Induced Gap Modification in Black Phosphorus. *Phys. Rev. Lett.* **2014**, *112* (17), 176801.

(18) Zhu, Z.; Tomanek, D. Semiconducting Layered Blue Phosphorus: A Computational Study. *Phys. Rev. Lett.* **2014**, *112* (17), 176802.

(19) Li, L.; Yu, Y.; Ye, G. J.; Ge, Q.; Ou, X.; Wu, H.; Feng, D.; Chen, X. H.; Zhang, Y. Black Phosphorus Field-Effect Transistors. *Nat. Nanotechnol.* **2014**, *9* (5), 372−377.

(20) WHO World Health Statistics 2014, http://www.who.int/gho/publications/world_health_statistics/2014/en, (accessed May 12, 2016).

(21) Nambi, V.; Liu, X.; Chambless, L. E.; de Lemos, J. A.; Virani, S. S.; Agarwal, S.; Boerwinkle, E.; Hoogeveen, R. C.; Aguilar, D.; Astor, B. C.; Srinivas, P. R.; Deswal, A.; Mosley, T. H.; Coresh, J.; Folsom, A. R.; Heiss, G.; Ballantyne, C. M. Troponin T and N-Terminal Pro-B-Type Natriuretic Peptide: A Biomarker Approach to Predict Heart Failure Risk-The Atherosclerosis Risk in Communities Study. *Clin. Chem.* **2013**, *59* (12), 1802−1810.

(22) Stillman, A. E.; Oudkerk, M.; Bluemke, D.; Bremerich, J.; Esteves, F. P.; Garcia, E. V.; Gutberlet, M.; Hundley, W. G.; Jerosch-Herold, M.; Kuijpers, D.; Kwong, R. K.; Nagel, E.; Lerakis, S.; Oshinski, J.; Paul, J.-F.; Underwood, R.; Wintersperger, B. J.; Rees, M. R. Assessment of Acute Myocardial Infarction: Current Status and Recommendations from the North American Society for Cardiovascular Imaging and the European Society of Cardiac Radiology. *Int. J. Cardiovasc. Imaging* **2011**, *27* (1), 7−24.

(23) Moreira, F. T. C.; Dutra, R. A. F.; Noronha, J. P. C.; Sales, M. G. F. Electrochemical Biosensor Based on Biomimetic Material for Myoglobin Detection. *Electrochim. Acta* **2013**, *107*, 481−487.

(24) Suprun, E.; Bulko, T.; Lisitsa, A.; Gnedenko, O.; Ivanov, A.; Shumyantseva, V.; Archakov, A. Electrochemical Nanobiosensor for Express Diagnosis of Acute Myocardial Infarction in Undiluted Plasma. *Biosens. Bioelectron.* **2010**, *25* (7), 1694−1698.

(25) Qureshi, A.; Gurbuz, Y.; Niazi, J. H. Biosensors for Cardiac Biomarkers Detection: A Review. *Sens. Actuators, B* **2012**, *171*, 62−76.

(26) Yang, Z.; Zhou, D. M. Cardiac Markers and Their Point-of-care Testing for Diagnosis of Acute Myocardial Infarction. *Clin. Biochem.* **2006**, *39* (8), 771−780.

(27) Priyanka, S.; Shorie, M.; Bhalla, V.; Pathania, P.; Suri, C. R. Nanobioprobe Mediated DNA Aptamers for Explosive Detection. *Chem. Commun.* **2013**, *50* (9), 1080−1082.

(28) Wang, L.; Liu, X.; Zhang, Q.; Zhang, C.; Liu, Y.; Tu, K.; Tu, J. Selection of DNA Aptamers that Bind to Four Organophosphorus Pesticides. *Biotechnol. Lett.* **2012**, *34* (5), 869−874.

(29) Sabherwal, P.; Mutreja, R.; Suri, C. R. Biofunctionalized Carbon composites: New-generation Diagnostic Tools. *TrAC, Trends Anal. Chem.* **2016**, *82*, 12−21.

(30) Akhavan, O.; Ghaderi, E.; Hashemi, E.; Rahighi, R. Ultra-sensitive Detection of Leukemia by Graphene. *Nanoscale* **2014**, *6*, 14810−14819.

(31) Akhavan, O.; Ghaderi, E.; Rahighi, R.; Abdolahad, M. Spongy Graphene Electrode in Electrochemical Detection of Leukemia at Single-cell Levels. *Carbon* **2014**, *79*, 654−663.

(32) Holzinger, M.; Le Goff, A.; Cosnier, S. Nanomaterials for Biosensing Applications: A Review. *Front. Chem.* **2014**, *2*, 00063.

(33) Kumar, V.; Shorie, M.; Ganguli, A. K.; Sabherwal, P. Graphene-CNT Nanohybrid Aptasensor for Label Free Detection of Cardiac Biomarker Myoglobin. *Biosens. Bioelectron.* **2015**, *72*, 56−60.

(34) Castellanos-Gomez, A.; Vicarelli, L.; Prada, E.; Island, J. O.; Narasimha-Acharya, K. L.; Blanter, S. I.; Groenendijk, D. J.; Buscema, M.; Steele, G. A.; Alvarez, J. V.; Zandbergen, H. W.; Palacios, J. J.; van der Zant, H. S. J. Isolation and Characterization of Few-layer Black Phosphorus. *2D Mater.* **2014**, *1* (2), 025001.

(35) Iakoubovskii, K.; Mitsuishi, K.; Nakayama, Y.; Furuya, K. Thickness Measurements with Electron Energy Loss Spectroscopy. *Microsc. Res. Tech.* **2008**, *71* (8), 626−631.

(36) Savjani, N.; Lewis, E. A.; Pattrick, R. A. D.; Haigh, S. J.; O'Brien, P. MoS2 Nanosheet Production by the Direct Exfoliation of Molybdenite Minerals from Several Type-localities. *RSC Adv.* **2014**, *4* (67), 35609−35613.

(37) Wang, L.; Sofer, Z.; Pumera, M. Voltammetry of Layered Black Phosphorus: Electrochemistry of Multilayer Phosphorene. *ChemElectroChem* **2015**, *2* (3), 324−327.

(38) Tang, L.; Wang, Y.; Li, Y.; Feng, H.; Lu, J.; Li, J. Preparation, Structure, and Electrochemical Properties of Reduced Graphene Sheet Films. *Adv. Funct. Mater.* **2009**, *19* (17), 2782−2789.

(39) Shumyantseva, V. V.; Sigolaeva, L. V.; Agafonova, L. E.; Bulko, T. V.; Pergushov, D. V.; Schacher, F. H.; Archakov, A. I. Facilitated Biosensing via Direct Electron Transfer of Myoglobin Integrated Into Diblock Copolymer/Multi-walled Carbon nanotube Nanocomposites. *J. Mater. Chem. B* **2015**, *3*, 5467−5477.

CrossMark

Plasmonic DNA hotspots made from tungsten disulfide nanosheets and gold nanoparticles for ultrasensitive aptamer-based SERS detection of myoglobin

Munish Shorie[1] · Vinod Kumar[1] · Harmanjit Kaur[1] · Kulvinder Singh[1] · Vijay K. Tomer[1] · Priyanka Sabherwal[1]

Abstract
A nanohybrid mediated SERS substrate was prepared by *in-situ* synthesis and assembly of gold nanoparticles (AuNPs) on exfoliated nanosheets of tungsten disulfide (WS_2) to form plasmonic hotspots. The nanohybrid surface was functionalized with specific aptamers which imparted high selectivity for the cardiac marker myoglobin (Mb). The fabricated aptasensor was read by SERS using a 532 nm laser and demonstrated significant signal enhancement, and this allowed Mb to be determined in the 10 f. mL^{-1} to 0.1 $\mu g\ mL^{-1}$ concentration range. The study presents an approach to synergistically exploit the unique chemical and electromagnetic properties of both WS_2 and AuNPs for many-fold enhancement of SERS signals.

Keywords Cardiac biomarker · Plasmonic hotspots · SERS aptasensor · SELEX · Nanohybrid

Introduction

Myoglobin (Mb) plays an important role in clinical diagnosis of cardiovascular diseases as its elevated level indicates myocardial damage, motivating the design and development of quick, reliable, label-free and cost-effective tool for early screening of developing disease [1, 2]. Mb has become the cornerstone for the risk stratification and diagnosis of patients with acute myocardial infarction (AMI), being released in biological fluids *viz.*, blood and urine in 4–50 h after an AMI episode [3], and also wherein its expression level increases up to ~600 ng mL^{-1} in comparison to normal range *i.e.,* 100–200 ng mL^{-1} [4]. Thus, quantification of MB in the early stage of CVD progression holds great promise towards the management of disease.

✉ Priyanka Sabherwal
psnanobiotech@gmail.com

1 Institute of Nano Science and Technology, Mohali -160062, India

Single molecule Surface Enhanced Raman Scattering (sm-SERS) has emerged as a powerful technique for non-invasive, rapid and reliable sensing of chemicals and biomolecules [5, 6]. For SERS, highly localized effect occurring at sharp edges of plasmonic nanostructures or interparticle junctions, crevices or on other nano-roughnesses (~11 nm) develop hotspots and the understanding of plasmon coupling modes at hotspots is important for the development of new plasmonic nanostructures for SERS emission [7, 8]. In general, there are two prominent mechanisms that explain SERS activity; first is surface plasmon resonance effect of the plasmonic nanostructures leading to increased Raman signals due to electromagnetic enhancement (EE) of the target analyte placed in close proximity to the nanostructure [9, 10] and other is the chemical enhancement (CE) owing to the charge transfer between nanomaterials and adsorbed analyte [11, 12]. The combination of EE and CE has shown up to ~ 10^{14} times enhancement in SERS signal [13]. Thus, design and development of nanomaterials based novel SERS substrates with the combined outcomes of both EE and CE for ultrasensitive detection of disease biomarkers are receiving tremendous interest in analytical science [14, 15]. Le Ru *et al.* and Wang *et al.* have reported the combination of charge transfer property of graphene with plasmonic metal nanoparticles for SERS based detection [16, 17]. Transition metal

dichalcogenides (TMDs) possess excellent charge transfer property [18] and SERS activity of molybdenum disulfide (MoS_2) in combination with gold and silver nanoparticles have also been reported [19, 20]. Kim *et al.* reported that both MoS_2 and WS_2 can be used for direct gold decoration on their surface owing to the work functions (5.2 eV and 5.1 eV respectively) which places their Fermi levels above the reduction potential of $AuCl_4^-$. This enhancement is more profound in WS_2 in comparison to MoS_2 even with a small extent of Au decoration [21] and was explored in our study for ultra-sensitive detection. In general, the specificity imparted by these nanostructured SERS platforms without compromising their sensitivity and detection limit has been a major challenge. Therefore, fabrication of an efficient SERS active substrate is still an open area of research for ultrasensitive and label free detection.

In the current work, we report the fabrication of gold nanoparticle-tungsten disulfide (AuNP-WS_2) nanohybrid based SERS active platform for the femtomolar level detection of cardiac biomarker, Myoglobin using specific aptamers (Fig. 1). Aptamers, as capture molecules, screened by SELEX (Systematic evolution of ligands by exponential enrichment) method show high affinity to their cognate target analyte and are a good alternative to conventional immunoglobulin based systems [22, 23]. This study presents an approach to synergistically exploit unique CE and EE properties of both WS_2 and AuNP for many- fold enhancement in SERS signal leading to the specific, ultrasensitive and rapid detection desirable in clinical diagnosis.

Experimental

Materials

Tungsten disulfide powder (2 µm), Isopropyl alcohol (IPA), Myoglobin (Mb), Hydrogen tetrachloroaurate trihydrate ($HAuCl_4 \cdot 3H_2O$), and Rhodamine 6G (R6G) were purchased from Sigma-Aldrich (www.sigmaaldrich.com/india.html). N-methyl pyrrolidone (NMP), carboxy methyl cellulose (CMC) were obtained from TCI Chemicals (www.tcichemicals.com/en/in/). All chemicals were used without further purification. All aqueous solutions were prepared using ultrapure water.

Synthesis of WS_2 nanosheets

Liquid phase exfoliation of bulk WS_2 flakes was carried out following the protocol reported by Coleman *et al.* [24]. Briefly, 10 mg of bulk WS_2 flakes were dispersed in 10 mL of N-methyl pyrrolidone and isopropyl alcohol (volume ratio 3:1) and probe sonicated (30% amplitude) for 2 h (5 s pulse on, 5 s pulse off). The resultant green dispersion was centrifuged at 1000 rcf for 30 min and clear supernatant was collected.

Preparation of Au-WS_2 nanohybrid

For the preparation of gold nanoparticles (AuNP) decorated WS_2 nanohybrid, 1 mL dispersion of exfoliated WS_2 nanosheets was stirred vigorously while heating. To the solution, 500 µg CMC was added, followed by $HAuCl_4 \cdot 3H_2O$ (0.8 to 4 mM) and the solution was stirred for 30 min resulting in change in color from greenish-yellow to deep red.
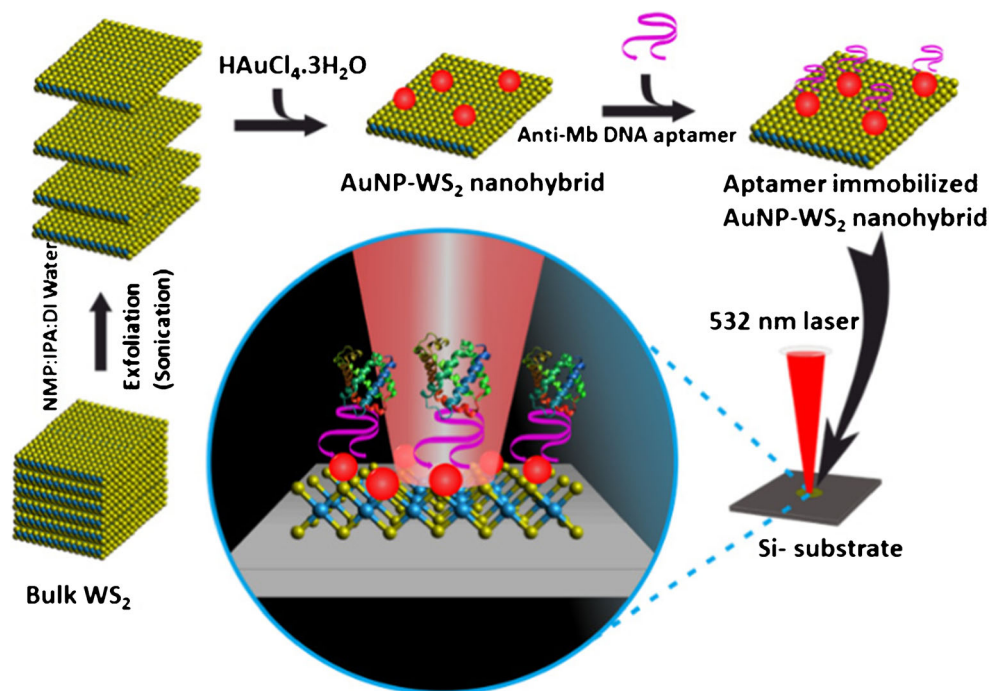
Au-WS_2 nanohybrid characterization

Powder X-ray diffraction pattern was performed using Brucker P-XRD. The UV-Vis (Shimazdu spectrophotometer UV2600) and Raman spectroscopy (WITEC DV401A-BV-352 using 532 nm Laser) were carried out to analyze the spectroscopic properties of as-synthesized nanohybrid. For morphological characterization, Transmission Electron Microscopy (TEM) was carried out on JSM-2100 system operating at 120 KV and Field-Emission Scanning Electron Microscopy (FE-SEM) was carried out using Jeol JSM-7600F.

SERS experiments

For SERS measurements, 50 µL of prepared Au-WS_2 nanohybrid was drop-casted on pre-cleaned Si substrates and dried in ambient conditions. The dried sample was washed with ultrapure water to remove any residual nanomaterial and Raman measurements were recorded to confirm nanohybrid coating. Anti-Mb DNA aptamer synthesized by modified micro-titer plate SELEX method (ST1; reported in our previous findings [25, 26]) having an exceptional $K_d = 65$ pM, was used to modify Au-WS_2 coated Si substrate. Briefly thiol-labelled single-stranded DNA (ssDNA) aptamer diluted in Binding buffer (Tris-HCl 10 mM, NaCl 150 mM, $MgCl_2$ 5 mM, pH 7.2) was immobilised on the Au-WS_2 modified Si substrate by drop-casting 10 µg DNA per 50 µL nanohybrid. The resulting sample was incubated at RT for 1 h and washed with binding buffer to remove unbound DNA molecules. Raman measurements were recorded after DNA immobilisation to confirm the fomation of the Apt-Au-WS_2 sensor (SERS aptasensor). Concentrations of Mb ranging from 0.1 fg mL^{-1} to 10 µg mL^{-1} were tested onto the nanostructured SERS aptasensor. For this, 10 µL of each Mb concentration were incubated on aptasensor surface for 15 min, washed with binding buffer and used for Raman measurements. The measurements were carried out at different positions ($n = 3$) for each sample to test the reproducibility.

**Fig. 1 Schematic Representation**: Schematic showing stepwise synthesis and fabrication of Au-WS$_2$ nanohybrid based SERS active platform

Results and discussion

Nanohybrid synthesis and characterization

The liquid phase exfoliation of bulk WS$_2$ flakes was carried out by slight modification of the method reported by Coleman *et al.* [24] to generate exfoliated WS$_2$ nanoflakes that appeared greenish-yellow in coloration (Fig. S1 A&B). For *in-situ* growth of AuNP on the surface of WS$_2$ nanosheets, WS$_2$ nanosheets were allowed to react directly with gold precursor (HAuCl$_4$) without using any external reductant and CMC was used as a stabilizing agent. The redox activity of WS$_2$ nanosheets is mainly responsible for the reduction of Au^{+3} into AuNP and the well-established interaction between gold and sulphur helps in efficient loading of AuNP over WS$_2$ nanosheets [21]. WS$_2$ formula unit formally gives more than 18 electrons for the redox reaction and it can be oxidized to W^{VI} and S^{VI} compounds, *e.g.,* hydrated WO$_3$ and SO$_4^{2-}$ *via* following reaction mechanism [27].

$$6\,HAuCl_4 + WS_2 + 12\,H_2O = 6\,Au + WO_3\,H_2O$$
$$+ 2\,H_2SO_4 + 24\,HCl$$
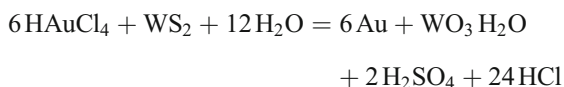
The presence of hydrated WO$_3$ and H$_2$WO$_4$ was suggested by the shift in W-4f bands in XPS measurements (Fig. S2 B). The results obtained are in accordance with the previous studies reported by Polyakov *et al.*, where they have summarized that the chemical bonding of Au and WS$_2$ increases the stability of resulting Au-WS$_2$ nanohybrid and facilitates a charge transfer between AuNP and the metal semiconductor. This suggests that in our study, the effective charge transfer between Au and WS$_2$ leads to SERS signal enhancement.

For morphological characterization, FESEM was carried on spin-coated Si wafer and micrographs suggested that the surfactant mediated exfoliation resulted into splitting of bulk lamellar structures of WS$_2$ (lateral size ranging from 50 × 100 nm) which are steadily decorated with AuNP (~29 nm) with an interparticle distance of ~10 nm (Fig. S3). The whole area energy-dispersive spectroscopy (EDS) mapping analysis (W/S/Au in red, green and blue dots respectively) and their merging exemplified the formation of Au-WS$_2$ nanohybrid structure (Fig. 4a). Furthermore, XPS analysis of Au-WS$_2$ nanohybrid confirmed the reduction of Au^{3+} over WS$_2$ nanosheets (Fig. S4 A&B). The relative molar ratio of W/S/Au depicted from EDS spectra demonstrated the desired stoichiometry of the products and was calculated to be around 20.02:63.73:16.25, which is approximately 1:3:1 (Fig. 2b). The control experiments of the parent entities in the nanohybrid were also performed for TEM, SEM and XRD analysis, showing their characteristic individual structural properties (Fig. S5).

Raman spectroscopic studies (drop-casted on to Si wafer) further gave an insight about the crystalline structure of the synthesized nanohybrid. Fig. 2c shows the two optical phonon modes E^1_{2g} (~352 cm^{-1}) and A_{1g} (~417 cm^{-1}) for WS$_2$ and Au-WS$_2$, where E^1_{2g} corresponding to in-plane optical mode and A_{1g} for out-of-plane vibration along the *c*-axis direction of the layers [20] The frequency difference between E^1_{2g} and A_{1g} varied from 63.4 cm^{-1} to 65.3 cm^{-1} when AuNPs were efficiently loaded onto the surface of WS$_2$ nanosheets. In UV-Vis analysis, appearance of plasmon band at λ_{max} 520 nm
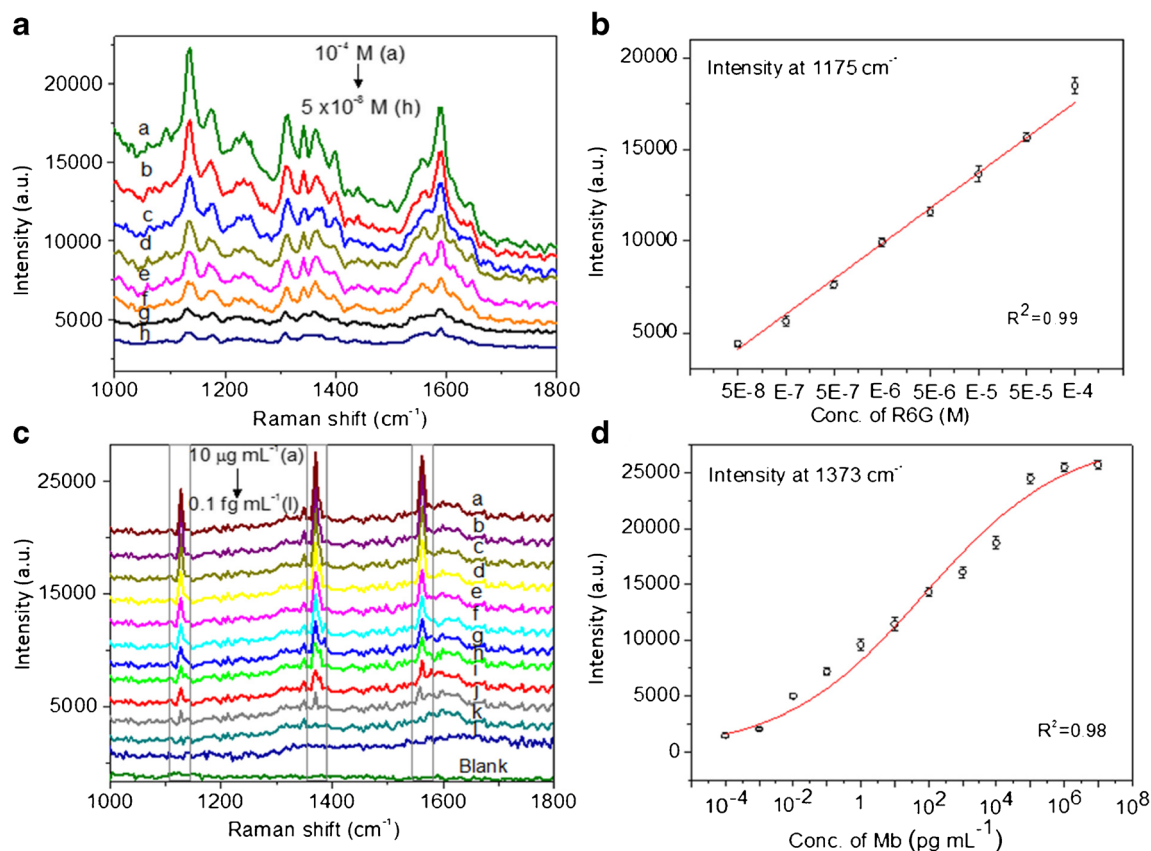
Fig. 4 Mb Detection with SERS Aptasensor: **a** SERS spectra of R6G molecules with different concentrations ranging from (a) 10^{-4} M, (b) 5×10^{-5} M, (c) 10^{-5} M, (d) 5×10^{-6} M, (e) 10^{-6} M, (f) 5×10^{-7} M, (g) 10^{-7} M, (h) 5×10^{-8} M on Au-WS$_2$–3 platform, **b** Calibration curve of R6G obtained by plotting different conc. of R6G with corresponding Raman intensity at 1175 cm^{-1}, **c** SERS spectra of Mb with different concentrations ranging from (a) 10^7 pg mL^{-1}, (b) 10^6 pg mL^{-1}, (c) 10^5 pg mL^{-1}, (d) 10^4 pg mL^{-1}, (e) 10^3 pg mL^{-1}, (f) 10^2 pg mL^{-1}, (g) 10 pg mL^{-1}, (h) 1 pg mL^{-1}, (i) 10^{-1} pg mL^{-1}, (j) 10^{-2} pg mL^{-1}, (k) 10^{-3} pg mL^{-1}, (l) 10^{-4} pg mL^{-1} (on Apta-Au-WS$_2$–3 platform), **d** Calibration curve of Mb obtained by plotting different conc. of Mb with corresponding Raman intensity at 1373 cm^{-1}

(characteristic of AuNP) along with an absorption peak at λ_{max} 667 nm of WS$_2$ nanosheets was observed in nanohybrid (Fig. 2d). A characteristic prominent exciton A band at λ_{max} 628 nm and a peak with the indirect B exciton transition at λ_{max} 525 nm was also observed in exfoliated WS$_2$ [28]. However, after centrifugation at 5000 rcf, the plasmon band at 520 nm disappeared, suggesting the formation of free gold nanoparticles in the process. A characteristic plasmonic band at 600–700 nm appeared in the re-suspended WS$_2$ nanosheets with an increase in intensity relative to the AuCl$_4^-$ concentration confirming the formation of hotspots (Fig. S1C) [29]. The recorded microscopic and spectroscopic observations confirmed the formation of a stable Au-WS$_2$ nanohybrid which was further used for fabricating SERS substrates.

Theoretical simulations of SERS ability

In SERS platforms using isotropic metallic nanostructures, the generation of plasmonic hotspots majorly depends on the inter-particle distance than orientation. To optimize the range under which Au-WS$_2$ nanohybrid efficiently produces hotspots, the plasmon of Gold nanoparticles lying on WS$_2$ nanosheets, separated by varying distances was predicted using CST microwave studio (CST studio suite, Student edition). The optical constants for Gold nanoparticles and few layer thick WS$_2$ nanosheets were taken as ϵ = 6.9; μ = 0.467 + 2.415i; and ϵ = 6.86; μ = 2.62 respectively [30, 31]. WS$_2$ sheet (500 nm × 500 nm × 10 nm) was modeled with longer axis on the x-y plane, having AuNP (30 nm) lying on top and a 532 nm light propagating along the z-axis from top (Fig. 3 *Right top*).

The inter-particle distance was varied from 1 nm to 30 nm and the generated electric field was calculated along the longer axis for WS$_2$-Au hybrid. As observed, the predicted electric field was highest when AuNP were lying in close vicinity (~1 nm) and decreased subsequently with an increase in inter-particle distance up to ~15 nm (Fig. 3 *left*). As a control, the simulations were repeated for AuNP alone to assess the role of WS$_2$ in increasing the plasmonic effect in Au-WS$_2$ hybrid (Fig. 3 *Right bottom*). In contrast to nanohybrid, the field for AuNP was calculated to be ~0.73 folds and decreased sharply to ~0.23 as the distance increased beyond
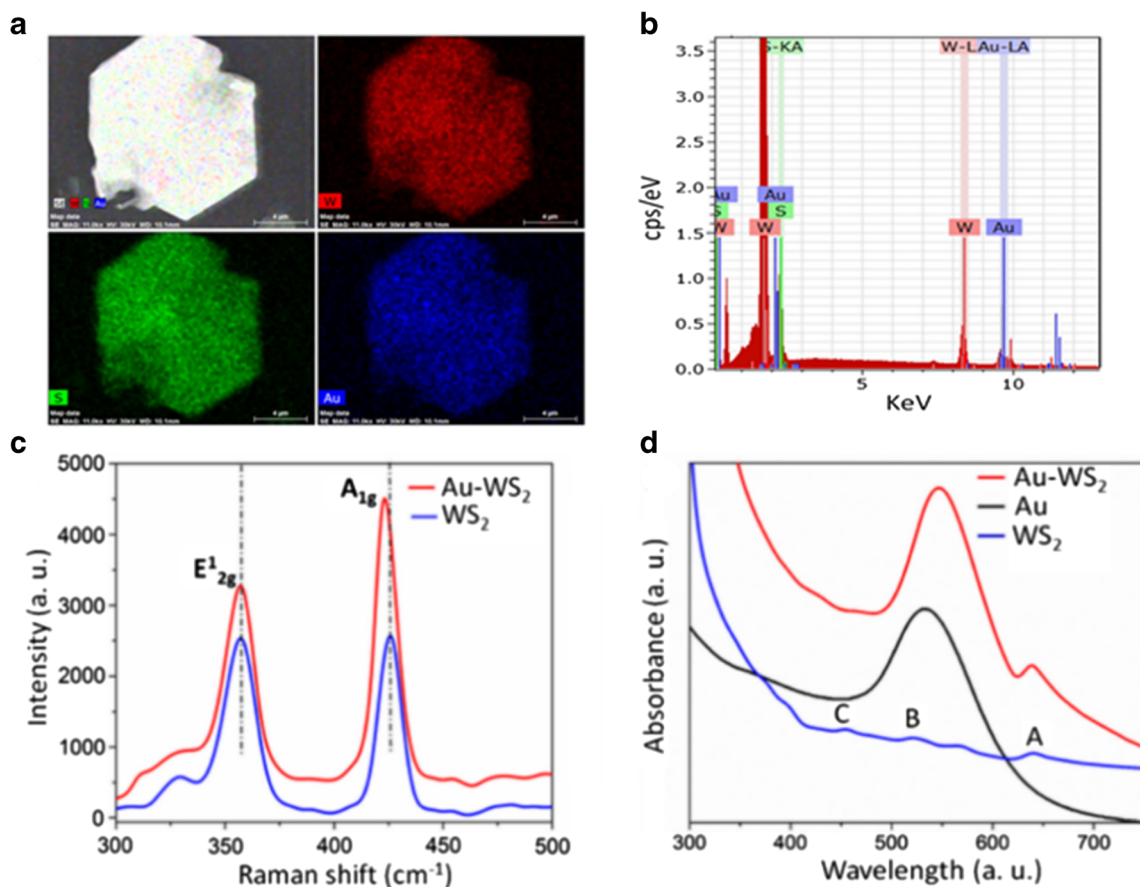
Fig. 2 Nanohybrid Characterisation: **a** EDX elemental mapping & **b** EDX spectrum and **c** Raman spectra of Au-WS$_2$ nanohybrid **d** UV-Vis absorption spectra of exfoliated WS$_2$ nanosheets and Au-WS$_2$ nanohybrid respectively

2.5 nm, thus establishing the role of WS$_2$ in enhancing the field strength ≥4 times in the nanohybrid. Furthermore, the values of localized electric field, **E$_{loc}$**, generated between the nanoparticles was calculated for the experimental conditions to be ~39×10^3 V/m for 30 nm nanoparticles separated by a distance of 10 nm (ST7) [32]. Calculated experimental **E$_{loc}$** is
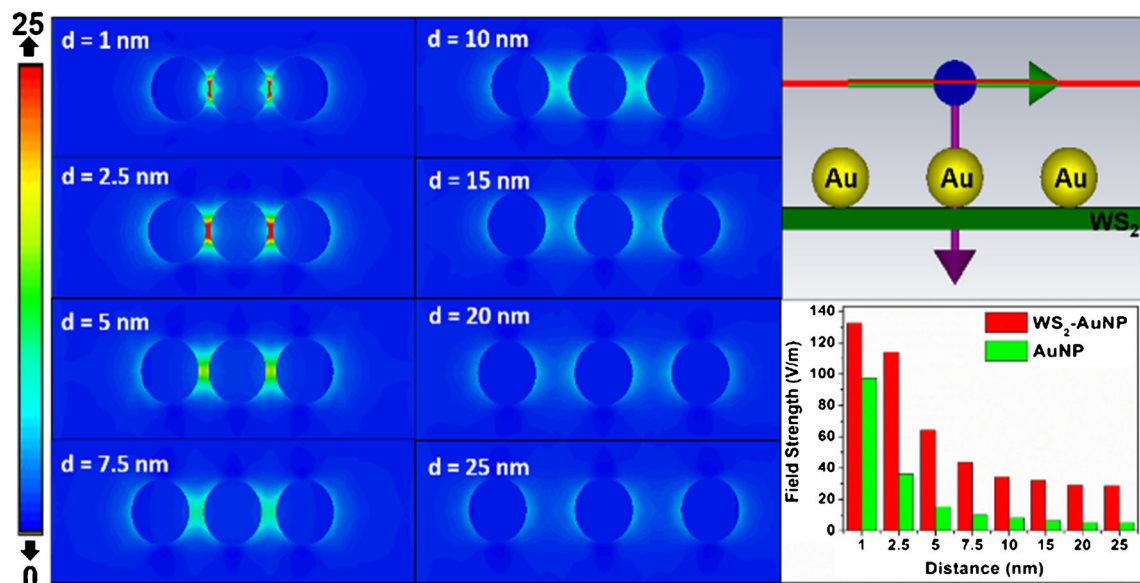
Fig. 3 Theoretical Simulations: **(Left)** 2D representation of simulated field strength of variously separated AuNP on WS$_2$ nanosheets, **(Right top)** Scheme showing simulation setup of interacting particles, **(Right bottom)**, Histogram depicting field strengths of Au-WS$_2$ in contrast to AuNP alone

Table 1 Comparative table showing various reports on the detection of Mb at low concentrations, arranged in decreasing Limits of Detection (LoD) achieved

S.No.	Nanomaterial	Technique	Specificity	LoD	RoD	Ref.
1	Glassy Carbon electrode*	Voltammetry	Molecularly Imprinted receptors	9.7 nM	60 nM- 6 μM	[37]
2	Lateral flow immunosensor chip	Optical	Antibody	58.0 pM	58 pM-0.59 μM	[38]
3	Antibody modified Magnetic particles	Mass Spectrometry	Antibody	29.0 pM	0.029–11.76 nM	[39]
4	Gold electrode*	DPV	Aptamer	27.0 pM	100 pM-40 nM	[40]
5	rGO/CNT nanohybrid	Cyclic Voltammetry	Aptamer	20.0 pM	58 pM-0.24 μM	[26]
9	TCPP-Gr/AuNPs	DPV	Aptamer	6.7 pM	20pM-0.77 μM	[41]
6	Antibody Modified AuNP	SPR	Antibody	1.0 pM	1.0 pM-20.0 nM	[42]
7	Few layer Black Phosphorus	Cyclic Voltammetry	Aptamer	80.0 fM	0.05–950.3 pM	[33]
8	Magnetic/Silica & Fluorescent Silica NPs	Fluorescence	Antibody	1.0 fM	1.0-100pM	[43]
10	*In-situ* synthesized Au-WS$_2$ nanohybrid	SERS	Aptamer	0.5 aM	0.5 aM-5.0 pM	Present Study

*: Detection platform does not use any Nanomaterial

roughly 1000 times higher than the theoretically predicted values as the simulations omit several experimental factors during calculations *viz.,* laser power, beam waist and working medium.

SERS based assay for myoglobin

For SERS measurement, the nanostructured substrates were prepared by drop-casting 50 μL dispersion of Au-WS$_2$ nanohybrid on a pre-cleaned Si wafer (5 mm × 5 mm) and dried in ambient conditions. WS$_2$ nanostructured SERS substrates of varying concentrations of AuNP were made to optimize the best SERS-active response (Fig. S6 A&B). The standard probe Rhodamine 6G (R6G) was employed to study the SERS performance on nanohybrid substrates. Fig. 4a shows the strong characteristic Raman peaks at 1136, 1175, 1311, 1343, 1362, 1589, and 1644 cm^{-1} which are in good agreement with the previous reports of pure R6G on nanomaterials-based SERS substrate [18].

Further, a significant enhancement in the Raman signal for R6G was observed within the concentration range of 10^{-4} M to 5×10^{-8} M. (Fig. 4b). Fig. S7 represents a laser power dependent comparative SERS activity of Au-WS$_2$–3 platform for R6G and it was observed that Au-WS$_2$–3 platform exhibited a significant enhancement in Raman signal for 10^{-4} M R6G at 0.2 mW of 532 nm laser. A commendable reproducibility in Raman signal enhancement was observed when measured on multiple different positions (70 spots) on nanohybrid SERS platform (Fig. S8). However, weak Raman signal of R6G was detected on individual parent entities than that of many fold enhanced signals on nanohybrid SERS platform (Fig. S9). The enhancement factor (EF = [(I_{SERS}/I_{bulk})(C_{bulk}/C_{SERS})(P_{bulk}/P_{SERS})]) was calculated from derivation of a previously reported equation [19]. From the experimental data we have estimated the enhancement factor ~6.78×10^6 for Au-WS$_2$–3 nanohybrid. (ST12), which is attributed to the synergistic effect of chemical enhancement (CE) offered by WS$_2$ nanosheets and plasmon enhancement (EE) by AuNP.

To develop an SERS based aptasensor for myoglobin (Mb), the Au-WS$_2$ SERS platform was functionalized with anti-Mb aptamer (Fig. S10) [33] and thoroughly rinsed to remove unbound aptamers to avoid any false SERS signals. Concentrations ranging from 0.1 fg mL^{-1} to 10 μg mL^{-1} of Mb were then tested (Fig. 4c), and a significant concentration dependent enhancement in Raman signal was noticed within a concentration range from 10 fg mL^{-1} to 0.1 μg mL^{-1}. The characteristic vibrational bands for Mb, positioned at 1126 cm^{-1} (due to C-N stretching) [34], 1373 cm^{-1} (oxidation marker of heme, Fe) [35] and 1560 cm^{-1} (C-C vibrations) were observed in Raman spectra. Other bands in SERS spectra of Mb at 760, 1011, 1365 and 1554 cm^{-1} arise due to numerous vibrational modes of tryptophan residues and some less intense bands at 1005 cm^{-1} and 1034 cm^{-1} were also observed due to phenylalanine residues of Mb respectively [35]. In our study, we have used specific thiolated (-SH modified) DNA aptamers which are covalently interacting with free sulfide groups of WS$_2$. Further, the DNA backbone structure is made up of electron rich

phosphate groups which are interacting with *in-situ* generated gold nanoparticles over WS_2 nanosheets. In chemical enhancement, DNA molecules are covalently attached or adsorbed at Au-WS_2 nanohybrid surface which form σ bond (S-S linkage) and induces charge-transfer between DNA and Au, leading to a large change of polarizability in the chemisorbed molecules resulting in Raman enhancement which is in accordance with the earlier report [36]. Target analyte Mb on exposure to WS_2/Au nanostructure substrate, interacts specifically with DNA *via* non-covalent interactions (*viz.* Van *der* Waals forces and hydrogen bonding) with the nucleobases, further contributing in the charge transfer mechanism.

The detection limit (LoD) was found to be 10^{-2} pg mL^{-1}, which is more than adequate for the quantification of Mb in clinical diagnosis. The formula used for the calculation is: LOD = 3σ/m, where **σ** is the standard deviation of the blank and **m** is the slope of the curve. The offered sensitivity is much better in comparison to the other existing fluorescent and electrochemical platforms for the detection of Mb which is n comparision to other protein/non-protein molecules (Table 1, Tables S1& S2). To check the specificity, a comparative study was done for the enhancement of signal in the presence of other serum proteins, Hemoglobin (Hb) and Bovine Serum Albumin (BSA) (Fig. S11). The signals produced in the presence of these protein molecules were negligible, which can be attributed to the use of screened aptamers which are highly specific to Mb. The results successfully supported the synergistic CE and EE properties of both WS_2 and AuNP for many fold enhancement in SERS signal leading to the ultrasensitive, rapid detection, desirable in clinical diagnosis for Mb detection. The key challenge of validating nanostructured aptasensor with patient samples can find new avenues in modern diagnostics, leading new avenues in point-of-care devices.

Conclusion

In conclusion, Au-WS_2 nanohybrid based SERS aptasensor has been developed for the label free detection of Myoglobin, a potent cardiac biomarker. The specific aptamers and synergistic effect of chemical enhancement offered by WS_2 nanosheets and electromagnetic enhancement by AuNPs presents a robust platform for the detection of MB. Thus, the aptasensor with its excellent performance opens new avenues for its real time applications in clinical diagnostics.

Compliance with Ethical Standards

The author(s) declare that they have no competing interests.

References

1. Qureshi A, Gurbuz Y, Niazi JH (2012) Biosensors for cardiac biomarkers detection: A review. Sensors Actuators B Chem 17:62–76
2. Stillman AE, Oudkerk M, Bluemke D, Bremerich J, Esteves FP, Garcia EV, Gutberlet M, Hundley WG, Jerosch-Herold M, Kuijpers D, Kwong RK, Nagel E, Lerakis S, Oshinski J, Paul JF, Underwood R, Wintersperger BJ, Rees MR (2011) Assessment of acute myocardial infaction: Current status and recommendations from the North American society for cardiovascular imaging and the European society of cardiac radiology. Int J Cardiovasc Imag 27:7–24
3. Moreira FTC, Dutra RAF, Noronhad JPC, Sales MGF (2013) Electrochemical biosensor based on biomimetic material for myoglobin detection. Electrochim Acta 107:481–487
4. Suprun E, Bulko T, Lisitsa A, Gnedenko O, Ivanov A, Shumyantseva V, Archakov A (2010) Electrochemical nanobiosensor for express diagnosis of acute myocardial infarction in undiluted plasma. Biosens Bioelecton 25(7):1694–1698
5. Fu X, Cheng Z, Yu J, Choo P, Chen L, Choo J (2016) A SERS-based lateral flow assay biosensor for hughly sensitive detection of HIV-1 DNA. Biosens Bioelectron 78:530–537
6. Zhao Y, Yang Y, Luo Y, Yang X, Li M, Song Q (2015) Double detection of mycotoxins based on sers labels embedded Ag@Au core-shell nanoparticles. ACS Appl Mater Interfaces 7(39):21780–21786
7. Radziuk D, Moehwald H (2015) Prospects for plasmonic hot spots in single molecule SERS towards the chemical imaging of live cells. Phys Chem Chem Phys 17:21072–21093
8. Zhang H, Ma X, Liu Y, Dua N, Wu S, Wang Z, Xu B (2015) Gold nanoparticles enhanced SERS aptasensor for simultaneous detection of Salmonella typhimurium and Staphylococcus aureus. Biosens Bioelectron 74:872–877
9. Moskovits M (2005) Surface-enhanced raman spectroscopy: A brief retrospective. J Raman Spectrosc 36:485–496
10. Halas NJ, Lal S, Chang W, Link S, Nordlander P (2011) Plasmons in strongly coupled matellic nanostructures. Chem Rev 111(6):3913–3961
11. Kelly KL, Coronado E, Zhao LL, Schatz GC (2003) The optical properties of metal nanoparticles: the influence of size, shape, and dielectric environment. J Phys Chem B 107:668–677
12. Li Z, Jiang S, Xu S, Zhang C, Qiu H, Chen P, Gao S, Man B, Yang C, Liu M (2016) Facile synthesis of large-area and highly crystalline WS_2 film on dielectric surfaces for SERS. J Alloys Compd 666:412–418
13. Kambhampati P, Child CM, Foster MC, Campion A (1998) On the chemical mechanism of surface-enhanced Raman scattering: Experiment and theory. J Chem Phys 108:5013–5026
14. Wang Y, Yan B, Chen L (2013) SERS tags: Novel optical nanoprobes for bioanalysis. Chem Rev 113(3):1391–1428
15. Feng J, Xu L, Cui G, Wu X, Ma W, Kuang H, Xu C (2016) Building SERS-active heteroassemblies for ultrasensitive Bisphenol A detection. Biosens Bioelectron 81:138–142
16. Le Ru EC, Etchegoin PG, Meyer M (2006) Enhancement factor distribution around a single surface-enhanced Raman scattering hot spot and its relation to single molecule detection. J Chem Phys 125:204701–204714
17. Wang Y, Polavarapu L, Liz-Marzán LM (2014) Reduced graphene oxide-supported gold nanostars for improved SERS sensing and drug delivery. ACS Appl Mater Interfaces 6:21798–21805
18. Chia X, Eng AYS, Ambrosi A, Tan SM, Pumera M (2015) Electrochemistry of nanostructured layered transition-metal dichalcogenides. Chem Rev 115(21):11941–11966
19. Su S, Zhang C, Yuwen L, Chao J, Zuo X, Liu X, Song C, Fan C, Wang L (2014) Creating SERS hot spots on MoS_2 nanosheets with

in-situ grown gold nanoparticles. ACS Appl Mater Interfaces 6: 18735–18741

20. Zhao J, Zhang Z, Yang S, Zheng H, Li Y (2013) Facile synthesis of Mos₂ nanosheet-silver nanoparticles composite for surface enhanced Raman scattering and electrochemical activity. J Alloys Compd 559:87–91

21. Kim J, Byun S, Smith AJ, Yu J, Huang J (2013) Enhanced electro-catalytic properties of transition-metal dichalcogenides sheets by spontaneous gold nanoparticle decoration. J Phys Chem Lett 4(8): 1227–1232

22. Chung E, Jeon J, Yu J, Lee C, Choo J (2015) Biosens Bioelectron 64:560–565

23. Kaur H, Shorie M, Sharma M, Ganguli AK, Sabherwal P (2017) Bridged Rebar Graphene functionalized aptasensor for pathogenic E. coli O78:K80:H11 detection. Biosens Bioelectron 98:486–493

24. Coleman JN, Lotya M, O'Neill A, Bergin SD, King PJ, Khan U, Young K, Gaucher A, De S, Smith RJ, Shvets IV, Arora SK, Stanton G, Kim HY, Lee K, Kim TG, Duesberg GS, Hallam T, Boland JJ, Wang JJ, Donegan JF, Grunlan JC, Moriarty G, Shmeliov A, Nicholls RJ, Perkins JM, Grieveson EM, Theuwissen K, McComb DW, Nellist PD, Nicolosi V (2011) Two-dimensional nanosheets produced by liquid exfoliation of layered materials. Science 331:568–571

25. Priyanka SM, Bhalla V, Pathania P, Suri CR (2014) Nanobioprobe mediated DNA aptamers for explosive detection. Chem Commun 50(9):1080–1082

26. Kumar V, Shorie M, Ganguli AK, Sabherwal P (2015) Graphene-CNT nanohybrid aptasensor for label free detection of cardiac biomarker myoglobin. Biosens Bioelectron 72:56–60

27. Polyakov AY, Yadgarov L, Popovitz-Biro R, Lebedev VA, Pinkas I, Rosentsveig R, Feldman Y, Goldt AE, Goodilin EA, Tenne R (2014) Decoration of WS2 nanotubes and fullerene-like MoS2 with gold nanoparticles. J Phys Chem C 118:2161–2169

28. Zeng L, Tao L, Tang C, Zhou B, Long H, Chai Y, Lu SP, Tsang YH (2016) High-responsivity UV-Vis photodetector based on transferable WS₂ film deposited by magnetron sputtering. Sci Rep 6:20343

29. Tian F, Bonnier F, Casey A, Shanahan AE, Byrne HJ (2014) Surface enhanced Raman scattering with gold nanoparticles: effect of particle shape. Anal Methods 6:9116–9123

30. Palik ED (1998) Handbook of optical constants of solids. Academic Press, San Diego

31. Ahuja U, Dashora A, Tiwari H, Kothari DC, Venugopalan K (2014) Electronic and optical properties of MoS₂-WS₂ multi-layers: First principles study. Comput Mater Sci 92:451–456

32. Tong L, Xu H, Käll M (2014) Nanogaps for SERS application. MRS Bull 39:163–168

33. Kumar V, Brent JR, Shorie M, Kaur H, Chadha G, Thomas AG, Lewis EA, Rooney AP, Nguyen L, Zhong XL, Burke MG, Haigh SJ, Walton A, McNaughter PD, Tedstone AA, Savjani N, Muryn CA, O'Brian P, Ganguli AK, Lewis DJ, Sabherwal P (2016) Nanostructured aptamer-functionalized black phosphorus sensing platform for label-free detection of myoglobin, a cardiovascular disease biomarker. ACS Appl Mater Interfaces 8(35):22860–22868

34. Spiro TG (1985) Resonance Raman spectroscopy as a probe of heme protein structure and dynamics. Adv Protein Chem 37:111–159

35. Sato H, Chiba H, Tashiro H, Ozaki Y (2001) Excitation wavelength-dependent changes in Raman spectra of whole blood and haemoglobin: Comparison of the spectra with 514.5-, 720-, and 1064-nm excitation. J Biomed Opt 6:366

36. Jiang J, Zou J, Wee ATS, Zhang W (2016) Use of single-layer g-C₃N₄/Ag hybrids for surface-enhanced Raman scattering (SERS). Sci Rep 6:34599

37. Wang Y, Han M, Ye X, Wu K, Wu T, Li C (2017) Voltammetric myoglobin sensor based on a glassy carbon electrode modified with a composite film consisting of carbon nanotubes and a molecularly imprinted polymerized ionic liquid. Microchim Acta 184(1):195–202

38. Zhu J, Zou N, Zhu D, Wang J, Jin Q, Zhao J, Mao H (2011) Simultaneous detection of high-sensitivity cardiac troponin I and myoglobin by modified sandwich lateral flow immunoassay: proof of principle. Clin Chem 57:1732–1738

39. Kwon SR, Jeon CS, Hong NY, Kim KP, Hwang I, Chung TD (2014) Gold-plated magnetic polymers for highly specific enrichment and label-free detection of biomarkers under physiological conditions. Chem Commun 50:10066–10069

40. Taghdisi SM, Danesh NM, Ramezani M, Emrani AS, Abnous K (2016) A novel electrochemical aptasensor based on Y-shape structure of dual -aptamer-complementary strand conjugate for ultrasensitive detection of myoglobin. Biosens Bioelectron 80:532–537

41. Zhang G, Liu Z, Wang L, Guo Y (2016) Electrochemical aptasensor for myoglobin-specific recognition based on porphyrin functionalised graphene-conjugated gold nanocomposites. Sensors (Basel) 16(11):1803

42. Gnedenko OV, Mezentsev YV, Molnar AA, Lisitsa AV, Ivanov AS, Archakov AI (2013) Highly sensitive detection of human cardiac myoglobin using a reverse sandwich immunoassay with a gold nanoparticle-enhanced surface plasmon resonance biosensor. Anal Chim Acta 759:105–109

43. Viswanathan K, Lee YC, Chen ZM (2014) Fluorescent dye incorporated magnetic/silica and fluorescent silica nanoparticles based myoglobin detection from whole blood samples. J Chin Chem Soc 61:533–538

Munish Shorie

Doctoral fellow

Institute of Nano Science and Technology (INST) &

Indian Institute of Science Education and Research (IISER-M), Mohali

Punjab, India.

Munish Shorie holds a graduate degree in science from Guru Nanak Dev University, Amritsar, following which he went on to earn his post-graduate degree in Science with specialization in Biotechnology from Punjab Technical University, Jalandhar. He worked as a project fellow for 1.25 years at Institute of Microbial Technology, Chandigarh under the guidance of Prof. C. Raman Suri before joining as a doctoral fellow at Institute of Nano Science and Technology, Mohali as part of its foremost batch of students. The work conducted by him under the supervision of Dr. Priyanka Sabherwal has been presented and awarded at several national & international forums. His work was awarded National Technology Day award with a research grant of rupees one lakh, best poster awards at 8th Bangalore India Nano, 6th MRS trilateral symposium & CRIKC Nanoscience day, and he was selected as finalist in the NanoSparx Innovation competition in 8th & 9th Bangalore India Nano. The research work is published under several peer-reviewed journals (Elsevier, Springer, Wiley & American Chemical Society) of international repute with a cumulative impact factor of 81.6. He has amassed around 450 citations from his work and has an H-index of 9. He holds interests in the development of optical/electrochemical biosensors for clinical biomarkers and environmental pollutants with keen indulgence in the amalgamation of nanotechnology with DNA technology.